Advancing DNA nanotechnology using single molecule fluorescence methodologies

By

Amani Assadallah Hariri

A thesis submitted to McGill University in partial fulfillment of the requirements for the degree of

Doctor of Philosophy

Department of Chemistry, McGill University

Montréal, Québec, Canada

April 2016

I dedicate this thesis

***T**o my family: my father Assadallah, my mother Najwa, my sister Farah, my brothers Hamoudi and Ali, my grandfather Fayoub and my grandmother Samira, for your constant support and love.*

***T**o the memory of my grandparents Alia & Hariri.*

Abstract

By taking it out of its biological role, DNA has served as a robust, reliable and programmable nanofabrication building block for the assembly of a variety of two- and three-dimensional discrete nanometer-sized structures with arbitrary shapes and designs. These molecularly addressable materials could serve as platforms for the site-specific hybridization with nanometer precision. Besides structural complexity, DNA objects evolved to comprise an intrinsic dynamic character allowing them to respond to surrounding stimuli in a predictable manner. Many researchers have previously constructed nanostructures using methods that rely on the spontaneous assembly of DNA in solution, in which case the more complex the assembly design is, the more error-prone the product becomes. This constitutes a major problem for the application of DNA-based structures in dynamic devices such as machines, motors, robots, and computers, where even small errors in assembly can drastically affect performance. Therefore, quantitative tools for analysing structures and dynamics of complex DNA nanostructures are critical. Single molecule fluorescence techniques have been transformative to the field of nanoscience and have played a leading role in providing a mature understanding and an informative feedback on the building blocks and final products of self-assembly.

This thesis demonstrates how different single molecule fluorescence methodologies can be utilized to study and advance the structure, dynamics and integrity of DNA-assemblies, specifically those shaped as nanotubes. Conceptually, this research can be divided into four main parts: (i) synthesis optimization, (ii) structural characterization, (iii) monitoring dynamic structures, and (iv) studying structural dynamics. First, a solid-phase synthesis strategy and its visualization through single-molecule spectroscopy was devised to assemble DNA nanotubes in a stepwise fashion, with a full control over their size and sequence pattern. This method paves the way for the production of custom-made DNA nanotubes with fewer structural flaws than the spontaneous-assembly method. Second, single molecule photobleaching and two-color colocalization approaches were uniquely combined to provide a systematic way of assessing the polydispersity, stoichiometry and degree of defectiveness of different DNA nanotubes structures. These approaches will be of significant importance for many research groups synthesizing large supramolecular structures or studying naturally occurring ones, such as protein clusters, amyloids, etc. Third, *in situ* single molecule immobilization-based fluorescence microscopy was employed to introduce structural changes into DNA nanotubes by dynamically adjusting one or several of

the edge lengths between the building blocks using a combination of strand displacement and loops. This is interesting for sensing applications, especially when the analyte produces large scale, detectable structural changes, and also for creating molecular muscles, capable of extension and contraction under external control. Lastly, dynamics and robustness of DNA nanotubes, reconfigured in response to site-specific deletion of DNA strands, were investigated using two-color single molecule microscopy. This strategy enables to develop a better understanding of the collective structural changes within DNA structures in response to modifications in their repeat unit.

Together, the different methods developed in this thesis underline the importance of single molecule techniques as powerful tools which can advance the field of DNA nanotechnology by enabling the production of well-defined high-quality objects that can meet the designer's compositional and dynamic specifications.

Résumé

Au-delà de son rôle biologique, l'ADN a servi comme un matériau de nanofabrication robuste, fiable, et programmable pour l'assemblage d'une variété de structures nanométriques, adoptant des formes arbitraires en deux et en trois dimensions. Ces nanostructures adressables au niveau moléculaire, pourraient servir comme des plates-formes d'hybridation site-spécifique, précise à l'échelle nanométrique. Outre la complexité structurelle, les objets d'ADN ont évolué pour intégrer un caractère dynamique intrinsèque qui leur permet de réagir à des stimuli environnants de manière prévisible. De nombreux chercheurs ont déjà construit des nanostructures en utilisant des méthodes qui reposent sur l'assemblage spontané des brins d'ADN en solution, durant lequel des erreurs pourraient se produire surtout dans des modèles de plus en plus complexes. Ceci constitue un problème majeur pour l'application des structures à base d'ADN dans des dispositifs dynamiques tels que des machines, des moteurs, des robots et des ordinateurs, où même des erreurs minimes d'assemblage peuvent considérablement affecter la performance du dispositif. Par conséquent, le développement d'outils quantitatifs dans le but d'analyser les structures et la dynamique des objets d'ADN complexes est essentiel. La technique de microscopie de fluorescence de molécules uniques a joué un rôle principal dans la transformation du domaine de la nanoscience en fournissant une compréhension mature et informative des différents matériaux de nanofabrication et des produits finaux de l'auto-assemblage.

Cette thèse démontre la façon dont différentes méthodologies simplifiées de fluorescence de molécules uniques peuvent être utilisées pour étudier et développer la structure, la dynamique et l'intégrité des assemblages d'ADN, en particulier ceux en forme de nanotubes. Conceptuellement, cette recherche peut être divisée en quatre parties principales: (i) l'optimisation de la synthèse, (ii) la caractérisation structurale, (iii) la surveillance des structures dynamiques et (iv) la dynamique structurelle. En premier lieu, une stratégie de synthèse en phase solide et sa visualisation par microscopie de molécules uniques a été conçue pour assembler des nanotubes d'ADN de manière progressive, avec un contrôle total sur leur taille et leur séquence modèle. Cette méthode va permettre la production de nanotubes d'ADN faits sur mesure ayant l'avantage de présenter des défauts structurels minimes comparativement à ceux résultants de la méthode d'assemblage spontané en solution. En deuxième lieu, une technique

de microscopie de fluorescence qui utilise le photoblanchiment de molécules uniques, a été combiné avec une méthode de colocalisation de deux couleurs, fournissant une façon systématique pour évaluer la polydispersité et la stœchiométrie de différents nanotubes d'ADN. Cet outil sera d'une grande importance pour de nombreux groupes de recherche qui synthétisent différentes structures supramoléculaires ou qui étudient celles d'origine naturelle comme des groupes de protéines, des amyloïdes, etc. En troisième lieu, un protocole *in situ* utilisant la microscopie de fluorescence à base d'immobilisation de molécules uniques a été utilisé pour introduire des changements structurels dans les nanotubes d'ADN. Dans ce but, une combinaison de déplacement de brin d'ADN et de boucles d'ADN a été adoptée afin d'ajuster de façon dynamique une ou plusieurs des longueurs d'arêtes entre les différents blocs. Cette approche est intéressante pour les applications de détection, en particulier lorsque les analytes génèrent des changements structurels détectables et à large échelle, ainsi que pour la création de muscles moléculaires, capables d'extension et de contraction suite à un stimulus externe. Enfin, la dynamique et la fidélité de la structure des nanotubes d'ADN, reconfigurés suite à la délétion site-spécifique de brins d'ADN, ont été étudiées à l'aide de la microscopie de fluorescence de molécules uniques à deux couleurs. Cette stratégie permet d'acquérir une meilleure compréhension des changements structurels collectifs au sein des nanostructures d'ADN en réponse à des modifications dans leur unité de répétition.

Collectivement, les différents procédés développés dans cette thèse soulignent l'importance des techniques de microscopie de fluorescence de molécules uniques comme outils puissants qui pourraient être exploités afin de progresser le domaine de la nanotechnologie de l'ADN. Ces méthodes vont permettre la fabrication d'objets bien définis, de haute qualité, pouvant répondre de manière pratique à des spécifications dynamiques et de composition.

Acknowledgments

"If I have seen further than others, it is by standing on the shoulders of giants"

Isaac Newton

I am very grateful to the many people who helped me throughout my Ph.D. at McGill, both in and out of the lab. First of all I would like to thank both of my supervisors, Prof. Gonzalo Cosa and Prof. Hanadi Sleiman, for their constant guidance and support throughout my research and for ensuring a nice balance of supervision to get the best out of the collaboration. Gonzalo was always there to motivate and encourage me when I needed it the most and provide me with a constant and outstanding feedback. His great expertise, wide knowledge, innovative ideas, intelligence, "eagle eye" and curiosity, were instrumental in helping me get my projects rolling and grow as a scientist. I was equally lucky to have Hanadi as my co-supervisor. It was always a pleasure meeting with Hanadi for a brainstorm, listen and learn from her. Her creativity, enthusiasm, and constructive criticism were a source of inspiration that greatly impacted my achievements. They both were amazing mentors, Hanadi being the architect who brilliantly designs and Gonzalo the engineer who meticulously develop, and I am evermore grateful for their confidence in my capabilities as the apprentice.

I would never have had the sense of perseverance in research, and positivity to pursue challenging problems was it not for my great experience at the American University of Beirut, I would like to acknowledge in particular Prof. Rabih Sultan who introduced me to the world of scientific research with the statement "*A priori*, things don't work at the beginning and you'll have to figure it out" which was greatly helpful during my Ph.D. where even when things got frustrating, I just stuck to it. Indeed, a Ph.D. isn't about what works, but about why things aren't working (at least mine).

From before I ever arrived, helping me with every step of my move to make it smoother, answering all my questions and concerns, introducing me to friends and family, taking me on from day one and training me, I will be forever thankful to Dr. Karam (The Hakim). He taught me so much, and was the big brother in Montreal, Thank you Hakim for all your effort, care and honourable title "Hakim junior"!

Throughout our collaboration, he endured the horrors of looking at my gels, solving bands that he never encountered before (and will probably never), watching his buffers getting emptied but

fortunately winning the bets on a Hockey game, I am extremely grateful to Dr. Hamblin for a great and fruitful collaboration, for being always there when I needed to solve a DNA-related problem, I may never forget his timing at giving me 10 samples to image the night before my vacation (always), but will always trust his judgment and expertise.

I would also like to thank all the past and current members of the Cosa and Sleiman lab for their help and support, thank you all for the wonderful and unforgettable journey! I especially thank the past and current Corridor members: Ryan Markovnikov the PCC, Mathieu the old man, Christina the dear wife (with a common future project W.R.), Yasser the Yassman (made with love and full of FRET) and Victoria (Vickels pickels but brighter with Nickel) for being amazing citizens under the reign of the general (except for Yasser, a bit revolutionary); with all the insightful and fruitful discussions, you guys made me "enjoy life and research" as a Ph.D. student, thank you! I also want to thank Ricky for enduring the craziness of the general, Lana (and Will) for her constant support to the general's dynasty, Andres Durantini for being the best perro (que quere beludo?), Mayra for her constant smile and positivity, Mei for her amazing cooking skills (and is almost my height!) Casey the turtle (a nice, smart and tough cookie indeed!), Roberto for understanding my Spanish (partire a londro), Katarina for being my lab neighboor (..after midnight).

I want to particularly thank Johano (BioBarca politics expert and apple-steve hater), Kim (the master spider cookie chef), Ilton (the great Gordo), Kevin (the mean Suisse guy) and Hsiao-Wei (best roommate and broccoli-maker ever) for being great, helpful and supportive post-docs and friends. I also want to thank Justin Conway, for always putting the smile on my face even when my gels were failing or when my passport got lost..; Tom Edwardson for teaching me all the tricks to make better gels and how to apply those skills in nature, Dodo for being my best French friend ever, Karina for her Brazilian charisma, Dan Dan (the dabdoub) for encouraging me to sing, Kai for her stretching tips (and yes one day she will quit smoking), Pongphak for being the nicest person I've ever known (keep smiling, it makes everyone around you happy), Katherine for her awesomeness and positive spirit, Nicole for her amazing voice (and yes I will attend your concert one day), Janano tech for his Lebanese pride (The shawarmaman), Violeta for her lovely and sweet presence, and last but not least all the new group members who joined in the recent year (with a special hug for Tuan), you've all been amazing and extremely kind and nice to me, thank you all!

I would also like to thank all the students I supervised including James, Jack (Jerkels) and Jesse who taught me how to become a better teacher and mentor (Ana, Bri and Xavier too!). I have also had the pleasure to work with people in various other laboratories and would like to thank Gina for her turbulent, active and enthusiastic personality steering up new ideas for experiments every week and Jean-francois (Printintin) for all the fruitful discussions, skype meetings and hot chocolate.

I am forever grateful to Prof. Masad Damha (chair) for his instrumental role in my Ph.D. and more particularly in my review meetings where he provided me with insightful advices, refined ideas and assisted in setting up rational objectives for my projects that lead to successful outcomes.

Special thanks to Tony Mittermier and Amy Blum for being actively involved in my committee and giving me a great feedback. I want to also thank the Mittermier group members, in particular Robby Harkness (son and father), for being my official personal gym trainer and did a transformative change in my life, and more importantly for being my good and caring friend (but I will still call security!), and Spanky Ditrani, my Italian teddy bear, liquored friend (I'll get you a muffin) and Farah el Turk (including Noah and Tante Khaldiye) who was my ex-childhood neighbour and became a dear friend.

I am grateful to Petr Fiurasek for his help in organizing CSACS meetings (and non-stop jokes and Tim Horton coffees and Csacs lunch!), and Chantal Marotte for making all of the hard things in grad student life easy from the beginning to the end. Karen and Sandra for helping out in all the travel awards, room booking, Gonzalo's lost keys etc. Special thanks to Mr. Robello, for his cheerful smile, his care and joyful French conversations at 3pm every day.

Life in Montreal would not have been the same without a solid group of friends. I would not have survived my thesis writing, my gym classes with Keena without the support of my departmental besties Hala and Caroline, and I am forever grateful sweetest ladies for turning my negative energy with a positive one and listening to all my complains! Special thanks also to my departmental mother Antisar who was constantly present to hear all my Ph.D. adventures, to give me fruits when I am weak and always take good care of me, come back soon! I also want to thank Saul (Jare), for being a great friend, a hero, a pilot, an adventurer who makes any outing activity more fun, what a friend! The sweetest Serene, thank you for being a great friend and amazing

listener, it's always a pleasure talking to you, complaining and joking! I also want to thank Ghada for her sweet talks and amazing laughs (yes amazing!!).

Outside the department, I had also a great family supporting me throughout my years in Montreal. I would like to thank my best friends who were like brothers and sisters to me, giving me support even from a long distance: Lili (m3alem Alameh), Hiba Canada (Hibamania), Ahmad (Lezem), Hiba jarti, Nannousse (including David, Alex and Gab), Gloria, Iman, Larita, Bitaro, Nader Lamaa, Zizi Moussa, Mohamed-Gabriel Alameh, Jons Kanso, Aline, Feddo, Nourita, Betty, Nermin (Gizam), Sado, Bahaa, Nader (and co.), Chraim, Alain, Nastasia, Karim (Tison), The Basha team. Also, I would like to thank my uncle Bassem, my aunt Rima, Maha, and my cousins Wissam and Maya for their constant support and care.

To my boyfriend Max (Mon atoutou, a moi seulement), who made my last Ph.D. year a very special one by introducing me to all the fun in the city, but more importantly endured the highest stress levels (i.e. complains, nagging, depression, tears, anger) from a Ph.D. survivor, I am forever grateful for all the nights you have spent working with me at Second cup just to keep me company, for all your motivational speeches, confidence in my capabilities, boosting my self-esteem and all the chocolate, bike trips, festivals, dinners, gifts, movies, and crazy moments that made me a happier person. I would also like to thank Lyne and Ray for being amazing hosts during the writing of thesis introduction, and Marcel and Jeff for being great family companions.

Last of all, I owe everything to my family, to my giants, my mother, my father, my sister and brothers. They were always there for me, regardless of distance, for every high and low. Hearing the voice of my mother and father every morning, witnessing the success of my sister and achievements of my brothers meant the world to me. Their unconditional love, care, support, inspiration and motivation were the source of my smiles, positivity and energy. It may take a lifetime to thank you enough!

Table of content

List of Figures

List of Tables

List of abbreviations

1D : One-dimensional

2D : Two-dimensional

3D : Three-dimensional

A : Adenine

AFM : Atomic force microscopy

AGE : Agarose gel electrophoresis

APD : Avalanche photodiode

Ar+ : Argon-ion laser

ATP : Adenosine triphosphate

AuNP : Gold nanoparticle

BM: Blink Microscopy

Bp : Base pair

BSA : Bovine serum albumin

C : Cytosine

C6 : Hexanediol spacer insertion

Ca^{2+} : Calcium

$CaCl_2$: Calcium Chloride

CCD : Charge-coupled device

Cox : Cholesterol oxidase

CP : Conjugated polymer

CPE : Conjugated polyelectrolyte

CPG :Controlled pore glass solid support

Cryo-EM : Cryogenic electron microscopy

Cy3 : Cyanine 3

Cy5 : Cyanine 5

DLS : Dynamic light scattering

DMT : Dimethoxytrityl

DNA : Deoxyribonucleic acid

dNTP : Deoxynucleotide triphosphates

ds : Double-stranded

DX : Double-crossover

EDTA : Ethylenediaminetetraacetic acid

EMCCD : Electron multiplied charge coupled device

ExoVII : Exonuclease VII

FAD : Flavin adenine dinucleotide

$FADH_2$: Flavin Adenine Dinucleotide (hydroquinone form)

FIONA : Fluorescence Imaging with One Nanometer Accuracy

FLIM : Fluorescence Lifetime Imaging Microscopy

FRET : Förster resonance energy transfer

G : Guanine

GFP : Green fluorescent protein

H_2O_2 : Hydrogen peroxide

H_2SO_4 : Sulfuric acid

HCR : Hybridization chain reaction

HCV : Hepatitis C Virus

HeLa : Cervical cancer cell line

HOPG : Highly ordered pyrolytic graphite

HPLC : High-performance liquid chromatography

HQ : High Quality non-sputtered exciter or emitter

IDL : Interactive Data Language

IR : Infrared

Kb: Kilobase

LP : Longpass filter

MES : Morpholino ethanesulfonic acid

M_n : Number average molecular weight

M_W : Weight average molecular weight

n : Refractive index

N_2 : Nitrogen

NA : Numerical aperture

Na^+ : Sodium

NaCl : Sodium chloride

$NaHCO_3$: Sodium bicarbonate

NMR : Nuclear magnetic resonance

NS5B : Nonstructural protein 5B

NSOM : Near-field scanning optical microscope

OD: Optical density

PAGE : Polyacrylamide gel electrophoresis

PA-GFP : Photoactivatable green fluorescent protein

PALM : Photoactivated localization microscopy

PBS : Phosphate buffered saline

PCR : Polymerase chain reaction

PDI : Polydispersity Index

PEG : Poly(ethylene glycol)

PIFE : Protein induced fluorescence enhancement

R_0 : Förster distance

RCA : Rolling circle amplification

RDC : Reflection dichroic reflection

RNA : Ribonucleic acid

SM-FRET : Single-molecule Förster resonance energy transfer

SMS : Single molecule spectroscopy

ss : Single Stranded

STED : Stimulated emission depletion microscopy

STM : Scanning tunneling microscope

STORM : Stochastic optical reconstruction microscopy

SVA : Succinimidyl valerate

TEM : Transmission electron microscopy

TIRF : Total internal reflection fluorescence

ε : Absorption extinction coefficient

θc : Critical angle

θi : Incident angle

λ : Wavelength

Φ : Emission quantum yield

Author Contributions

Gonzalo Cosa and Hanadi F. Sleiman provided funding, research objectives, and intellectual guidance for all of the projects described in this thesis.

Chapter 2

Reproduced with permission from: "Stepwise growth of surface-grafted DNA nanotubes visualized at the single-molecule level", **Amani A. Hariri**, Graham D. Hamblin, Yasser Gidi, Hanadi F. Sleiman & Gonzalo Cosa, Nature Chemistry **7**, 295–300 (2015). Author Contributions: Single molecule experiments and analysis were carried out by **Amani A. Hariri** in addition to the finalized gels presented in this section and co-wrote the paper. DNA sequence design, synthesis and purification were carried out in collaboration with **Graham D. Hamblin.** STORM experiments were carried out in close collaboration with **Yasser Gidi**. **Prof. H.F. Sleiman** and **Prof. G. Cosa** designed the project, guided interpretation of data, discussion of results and concepts and co-wrote the paper. Journal cover was accomplished by **Melanie Burger**.

Chapter 3

Author contributions: **Amani A. Hariri** performed the single molecule photobleaching measurements and carried the data analysis. **Amani A. Hariri** designed experiments and wrote the manuscript with **Prof. H.F. Sleiman** and **Prof. G. Cosa**. **Jean Francois DesJardens** built the automated MATLAB routine for the photobleaching step counting. **John Hardwick** assisted **Amani A. Hariri** in the optimization of the photobleaching steps, characterization and purification of the foundation rung. **Amani A. Hariri** and **Graham Hamblin** carried out DNA synthesis. **Robert Godin** performed the MATLAB simulations on nanotubes with different labelling efficiencies. **Prof. P. Wiseman**, **Prof. H. F. Sleiman** and **Prof. G. Cosa** designed the project, guided interpretation of data, discussion of results and concepts and co-wrote the paper. *(Manuscript to be submitted)*

Chapter 4

Reproduced in part with permission from: "Dynamic DNA Nanotubes: Reversible Switching between Single and Double-Stranded Forms, and Effect of Base Deletions", Janane F. Rahbani, **Amani A. Hariri**, Gonzalo Cosa & Hanadi F. Sleiman, ACS nano **2015**, *9* (12), pp 11898–11908. Author Contributions: DNA sequence design, synthesis and purification were carried out by **Janane F. Rahbani.** Single molecule experiments were carried out by **Amani A. Hariri**. The DNA nanotubes structural schemes were generated by **Alex Rousina-Webb. Prof. H.F. Sleiman** and **Prof. G. Cosa** designed the project, guided interpretation of data, discussion of results and concepts and co-wrote the paper.

Chapter 5

Author Contributions: Single molecule protocols and experimental design were developed by **Amani A. Hariri** in assistance with **Jesse Gordon** (summer student, 2015). Single molecule experiments were carried by **Amani A. Hariri** in assistance with **Jesse Gordon** and **Casey Platnich**. Data analysis was interpreted by **Amani A. Hariri** with the help of **Prof. G. Cosa, Prof. H.F. Sleiman** and **Yasser Gidi**. DNA sequence design, nanotube synthesis and purification were carried out by **Janane F. Rahbani. Amani A. Hariri** designed experiments and co-wrote the manuscript**. Prof. G. Cosa** and **Prof. H. F. Sleiman** designed the project, guided interpretation of data, discussion of results and concepts and co-wrote the paper *(Manuscript in preparation).*

"[...] Deep in the sea
all molecules repeat
the patterns of one another
till complex new ones are formed.
They make others like themselves
and a new dance starts.

Growing in size and complexity
living things
masses of atoms
DNA, protein
dancing a pattern ever more intricate.

Out of the cradle
onto dry land
here it is
standing:
atoms with consciousness;
matter with curiosity.

Stands at the sea,
wonders at wondering: I
a universe of atoms
an atom in the universe."

Richard Feynman

1 Introduction

1.1 Nanoscience: A Big step for Small!

"We'll have more power in the volume of a sugar cube than exists in the entire world today"

Ralph Merkle

Nanoscience involves the study, design, characterization and manipulation of materials at atomic, molecular and macromolecular scales (1-100 nm length scale). Working in the nano-regime opens the door for many attractive opportunities in that nanosized systems often have novel properties due to a significant reduction in dimensionality. Another important aspect of nanoscience is the high complexity of nanostructures. Indeed, hundreds of thousands of atoms or molecules make up systems with exceptional configurations, which are complex enough to give rise to an 'emergent behaviour'.[1] In these systems, electronic, optical, structural, biological and chemical potentials can all become shape and size dependent when entities are smaller than 100 nm. At the moment, nanoscience applications are widespread and are present in a variety of areas including information and communication technology, energy harvesting and environment, healthcare and medicine, food and nutrition, biotechnology and agriculture and optics, to name a few.[2] To give few examples, today's nanotechnology-enabled products range from tennis rackets to catalysts for refining crude oil and ultrasensitive detection of toxins.[3] Not to mention that nanoscale transistors may lead to faster and more powerful computers. Nanomaterials hold the potential to exponentially increase information storage capacity; soon the computer's entire memory may be stored on a single tiny chip. In the energy arena, nanotechnology may enable high-efficiency, low-cost batteries and solar cells. Many more fields have also found uses for nanotechnologies such as antibacterial odour-reducing nanoparticles in clothing, waste water treatment strategies and light materials for bicycles and other vehicles.[4] Notably, nanotechnology can provide the right tools and technologies to create the next generation of advances in healthcare.[5] Similarly to how the internet revolutionized the information industry, we are on the verge of a global revolution in healthcare enabled by nanoscience (Figure 1.1).[6]

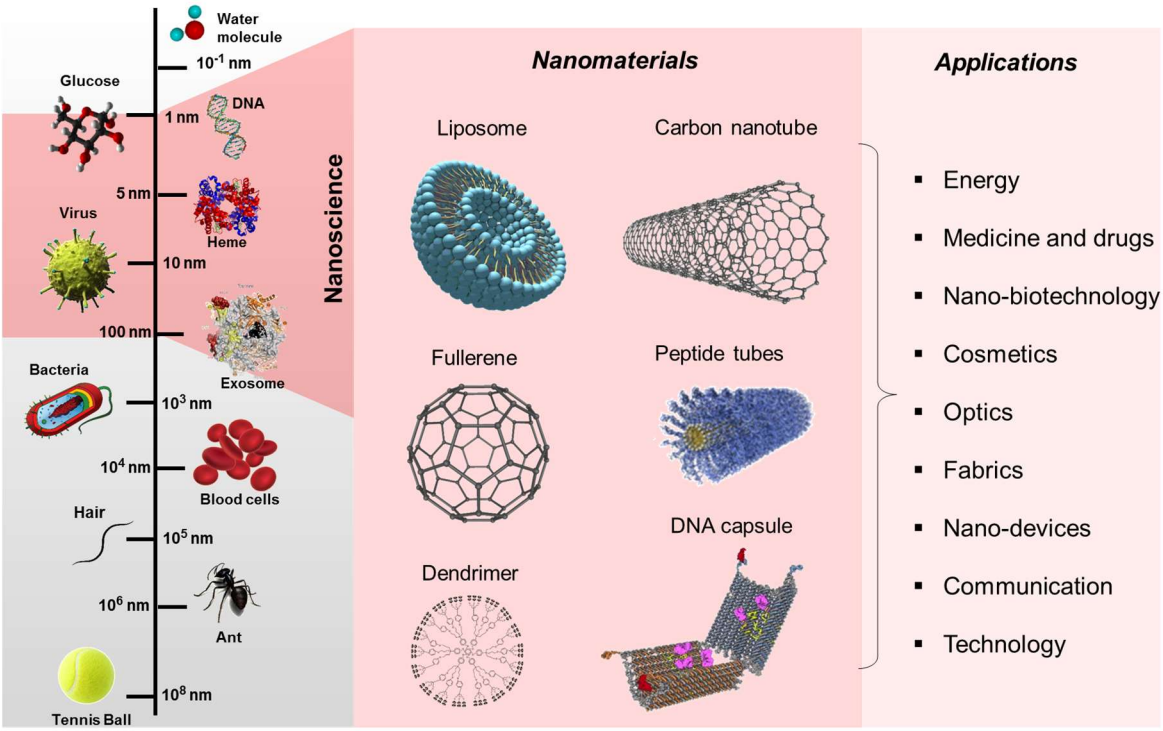

Figure 1.1: Length scale showing the nanometer in context. The length scale of interest for nanoscience and nanotechnology is expanded in red (from 100 nm down to atomic scale of 0.2 nm) to show examples of nanomaterials developed during the past decades along with the potential applications in many different fields.

A wide variety of approaches are available for fabricating nanomaterials with various degrees of complexity, precision, speed and cost. These manufacturing approaches fall into two categories: 'top-down' and 'bottom-up'.[7] 'Top-down' manufacturing involves reducing larger pieces of material to the required dimensions and patterns by means of external assembling tools. Micropatterning techniques, such as photolithography and inkjet printing belong to this category. 'Bottom-up' nanofabrication takes advantage of molecular self-assembly in which atoms or molecules arrange themselves spontaneously into nanostructures. Using this approach, self-assembly is typically directed through noncovalent interactions such as hydrogen bonding, metal coordination, van der Waals forces, π-π interactions, and/or electrostatic, as well as electromagnetic interactions. Common examples of self-assembled structures include vesicles, micelles, lipid-bilayers, double helical DNA and protein quaternary structure.[8] This method is much cheaper and easier to scale up in comparison to the top-down approach.

Much attention is being focused on self-assembly for constructing nanodevices with high level of precision and complexity, integrating order and dynamics, to achieve useful functions such as stimuli-responsiveness, recognition, transport, and catalysis. Indeed, among the most outstanding examples of man-made nanostructures are DNA-based nanomachines. However, imperfectly assembled DNA-structures may produce nonreactive and malfunctioning devices. For this reason, quantitatively "*seeing*" and "*inspecting*" these nanostructures is crucial for the successful development of materials with potential applications.

1.2 Nanoscopy: "Seeing is believing"

"It is only with the heart that one can see rightly, what's essential is invisible to the eye"

The Little Prince

The development of tools which allow atoms and molecules to be examined and probed with great precision (i.e., "nanoscopy") was pivotal to increasing our understanding of the nanoworld.[9] In fact, it was the invention of the scanning tunneling microscope[10] (STM) in the 1980's and the atomic force microscopy (AFM) shortly after, that stimulated the early advances of nanoscience.[11] These instruments enabled the molecular-scale characterization of the structure and composition of nanoscale objects and further helped to build a detailed understanding of their optical, magnetic and electronic properties. Shortly after, detecting single molecules using optical microscopy and more precisely the near-field scanning optical microscope (NSOM) brought the additional advantage of in-depth and non-invasive visualization and control of small structures. It was subsequently demonstrated that with careful sample preparation and optimal detection, single molecule studies could be conducted at room temperature with far-field techniques such as wide-field epifluorescence, confocal and total internal reflection fluorescence microscopies.[12] Recently, ground-breaking developments in fluorescence microscopy have led to the so-called super-resolution imaging with nanometer scale resolution, which were otherwise not possible with conventional tools limited by the ~200 nm diffraction limit. These novel techniques have completely unraveled new insights into the nano-universe and could provide a window into nanoscale interactions with intrinsic access to time-dependent changes.[13]

1.3 A marriage of fields: Single molecule imaging to advance DNA nanotechnology

Single molecule spectroscopy has been transformative to the field of nanoscience and has played a leading role in providing a quantitative and informative feedback on the building blocks and final products of self-assembly. From this perspective, the main focus of this thesis is the development of single molecule fluorescence methodologies for structural characterization and optimization of DNA nanostructures. Importantly, this work demonstrates how these particular imaging techniques can uniquely assist in probing and understanding dynamic DNA structures and structural dynamics at the finest level. This thesis starts with a general introduction of the field of DNA nanotechnology and highlights the recent developments in structural DNA self-assembly (static and dynamic) along with the potential emerging applications. The following Chapters (2 – 6) provide an in-depth description of the different single molecule fluorescence (SMF) tools that we have developed or adopted to guide the advancement of DNA-based devices, in terms of design, manufacture and evaluation.

1.4 DNA nanotechnology

1.4.1 The DNA molecule: a biological building block goes exotic

"See the undersurfaces of the spiral treads, and the spaces in between.. for she is the staircase.. constructed as a model with matches and a ribbon tape"

May Swenson

Deoxyribonucleic acid (DNA) is the fundamental 'molecule of life' as it plays the essential role of carrying our entire genetic code. Beyond its biological functions, DNA possesses fascinating properties that make it a versatile material for nano-engineering. For instance, the DNA double helix is inherently well-defined on the nanometer scale.[14] It has a diameter of approximately 2 nm, a helical repeat of 3.4 nm (10.5 base pairs) and a persistence length of approximately 50 nm (Figure 1.2). More importantly, this simple biopolymer, composed of a sugar-phosphate backbone and nucleobases, displays some of the most predictable and programmable interactions of any known molecule, natural or synthetic. The two strands of the double helix are held together by Watson-

Crick base pairing of complementary nucleobases (Adenine (A) with Thymine (T), Cytosine (C) with Guanine (G)) through a combination of hydrogen bonding, π-π stacking, electrostatic interactions as well as the hydrophobic effect. In addition, DNA can be conveniently synthesized with a nearly infinite number of sequences using automated methods combined with a large toolbox of DNA-acting enzymes, which can further tune and modify its basic structure.

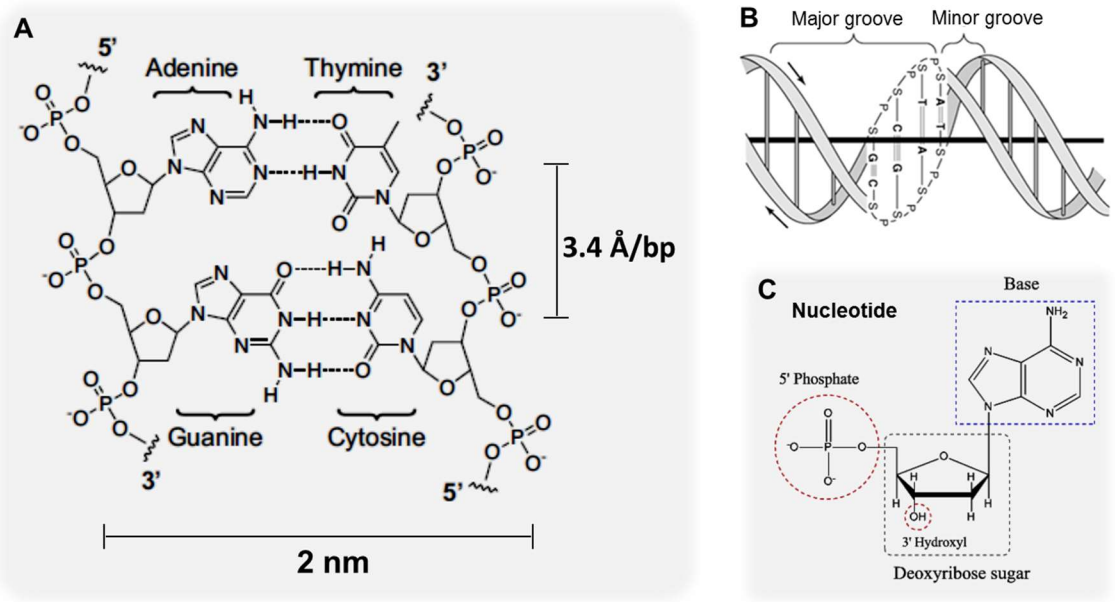

Figure 1.2: Structure of a DNA molecule. (A) Sugar-phosphate backbone links together individual nucleobases with 5'→ 3' directionality is shown with the Watson-Crick base-pairs A:T and C:G along with the dimensions of duplex DNA in the B-form. (B) Scheme of the B-form of DNA. (C) Nucleotide composition: Phosphate + sugar + Base.

1.4.2 DNA synthesis: a solid phase thinking

" ... I wonder what made me think that this approach would ever succeed. But from the outset I had a strong conviction that this was a good idea, and I am glad that I stayed with it long enough"

Bruce Merrifield

The concept of solid-phase synthetic chemistry was first introduced by Bruce Merrifield as an ingenious technique for the preparation of peptides in the 1960s.[15] Extension of this method to include a wide panorama of organic synthetic transformations was conceived later for oligonucleotides and oligosaccharides in addition to the field of combinatorial chemistry.[16] An in depth discussion of this approach is beyond the scope of this thesis, however a brief description of

oligonucleotide synthesis in particular will be presented, as its application to the creation of sequence-defined DNA nanotubes, which is an major underlying theme in the presented work.

Generally, solid-phase synthesis relies on preparing sequence-defined segments by connecting monomer units with orthogonally protected functional groups one-by-one using iterative chemical steps (Figure 1.3A). In this simple approach, the growing oligomers are covalently bound to a solid-support, typically in the form of controlled-pore glass or polystyrene beads. These can greatly improve and facilitate purification protocols. Moreover, the automation of this chemical process has proven to significantly reduced reaction times. For oligonucleotide synthesis, many strategies of coupling chemistry have been explored, with the phosphoramidite method as the most widely used at the time-being. Phophoramidite synthesis begins with the 3'-terminal nucleotide and proceeds through a series of cycles composed of four steps that are repeated until the 5'-terminal nucleotide is attached. These four main steps are deprotection, coupling, capping, and finally oxidation.

Deprotection (or deblocking) easily removes the dimethoxytrityl protecting group from the 5' hydroxyl under acidic conditions (dichloroacetic acid). Coupling brings in the next monomer as a 5' DMT-protected deoxynucleoside (2-cyanoethyl-N,N-diisopropyl) phosphoramidite, under acidic conditions and uses tetrazole derivatives as a reaction 'activator'. Next, the capping step is performed by treating the solid support-bound material with a mixture of acetic anhydride and 1-methylimidazole. This capping mixture acetylates, to a large extent, any unreacted 5'-hydroxy groups. This step is important to reduce side-products caused by unreacted 5' hydroxyl groups, since free "uncapped" 5' hydroxyl groups could participate in the next coupling cycle and produce a complex mixture of products, which complicates the purification process. Next, the oxidation step converts the phosphite triester to a phosphate triester. The process is repeated until the desired product is fully synthesized on the solid support. Lastly, treatment with aqueous ammonia releases the oligonucleotides from the solid support and removes the base-labile nucleobase and cyanoethyl protecting groups, giving the crude oligonucleotide polymer ready for purification. (Figure 1.3B)

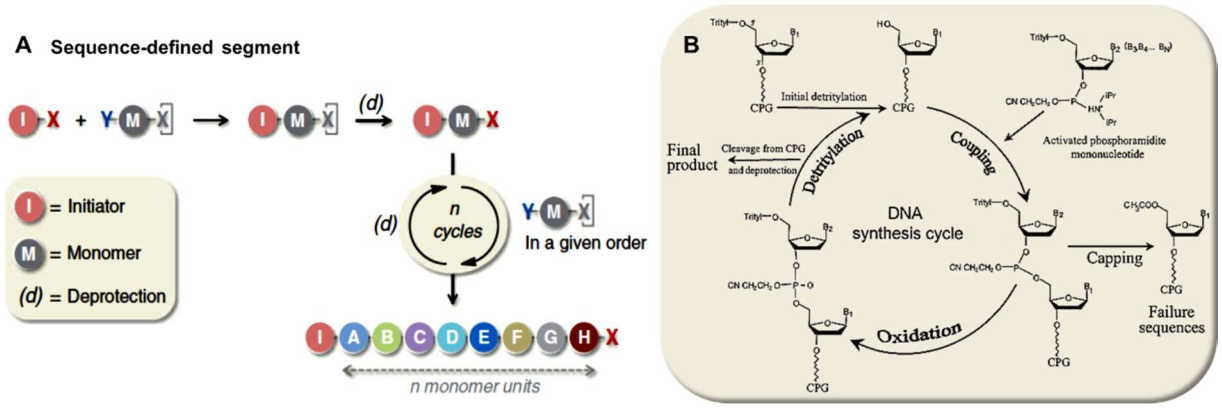

Figure 1.3: Solid phase synthesis. (A) Scheme showing how monomer units connect one-by-one through iterative chemical steps which generate sequence-defined segments. Adapted with permission from reference [16] (The American Association for the Advancement of Science, 2013). (B) Scheme showing the different steps involved in a DNA synthesis cycle.

The unique self-assembly properties and ease of synthesis of DNA made it an intriguing material for building complex nanoscale structures.[17] However, the matter remains that linear DNA lacks the complexity and flexibility needed for nano-construction. For this reason, different approaches have been developed over the past two decades in order to introduce branching points within the DNA structure in efforts to create different geometric definitions. These approaches include: *DNA tile self-Assembly*, *DNA origami* and *supramolecular DNA assembly*, which will be discussed in more detail in the following sections, to show how they enabled the exponential growth of the field of DNA nanotechnology, as illustrated in figure 1.4.

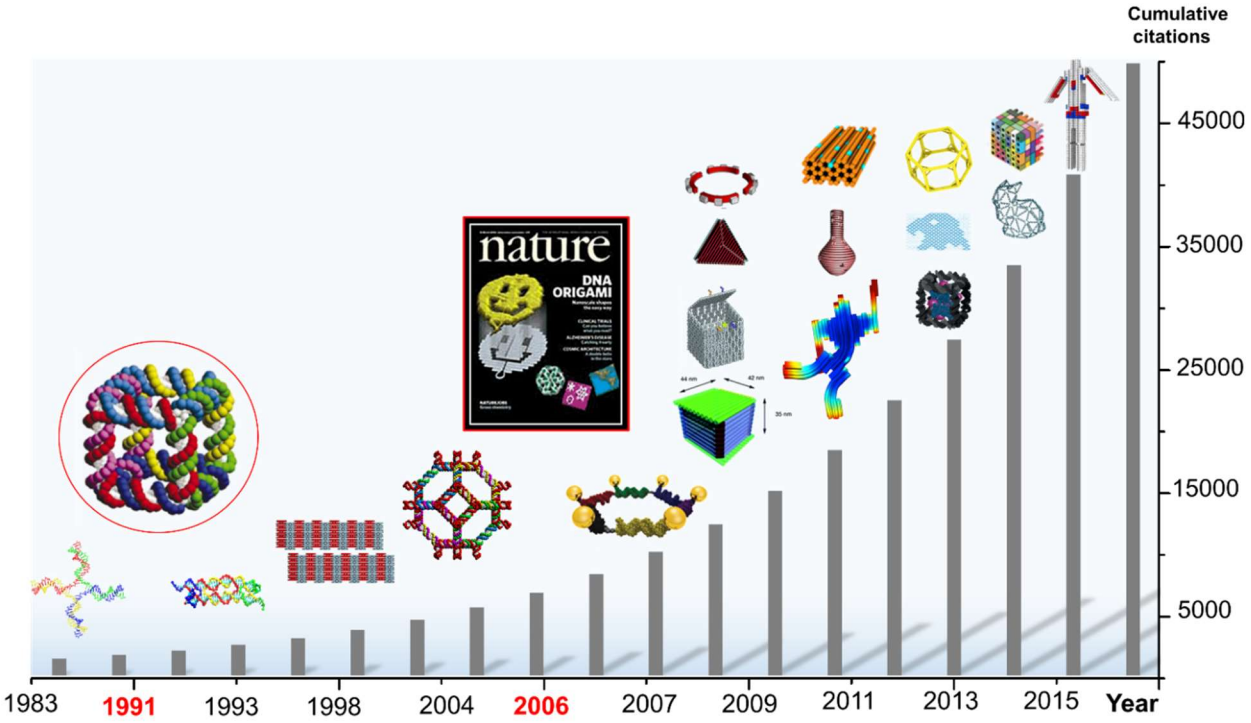

Figure 1.4: Illustration of the design space expansion and the growth of structural DNA nanotechnology. From left to right, bottom to top: immobile DNA junction. DNA object with cube connectivity. DNA double crossover (DX) molecule. 2D crossovers tiles and lattice formation. DNA octahedron. DNA origami smiley face. DNA hexagon. Box shaped DNA origami. DNA box with opening lid. DNA tetrahedron. Curvature in DNA origami. 3D DNA robot. 3D DNA vase. 3D multilayer DNA origami. DNA cage. 2D tiles. DNA Polygon meshes (rabbit). The lego DNA. Shape complementary 3D DNA nanodevice.

1.4.3 DNA tile self-assembly: just like nature

"I regard…DNA nanotechnology to be an outgrowth of crystallography and crystallographic thinking"

Nadrian Seeman

Inspired by the six-finned fish in the Escher painting, in 1980 Nadrian Seeman conceptualized the use of branched junctions of DNA which can then deliberately assemble together using base pairing interactions into a crystalline material, where proteins may be bound and therefore crystallized. His innovative idea set the foundations of the field of DNA nanotechnology.[18] Among natural DNA primitives with branched junctions, the Holliday junction is a transient arrangement of four strands that occurs during homologous recombination (Figure 1.5).[19] However, in nature, these sequences are geometrically flexible and unstable, constantly undergoing branch migration

due to the sequence symmetry of their arms (homologous sequences). Hence, it is extremely difficult to assemble large arrays from these tiles. To address this problem, Seeman and co-workers specifically introduced immobile junctions in their structures by rendering the arms sequences unique. Once equipped with matching sticky-ends (complementary single stranded DNA portions), multiple junctions could then associate together. Subsequent ligation would then generate the first example of a three-dimensional DNA-based object; with the connectivity of a cube.[20] Additionally, Seeman's group reported in 1993 the design of more rigid building blocks using paired four-arm junctions, known as crossovers, where DNA double helices are linked together by two strands exchanges instead of a single exchange as involved in the Holliday junction.[21] The resulting molecules can hold the structures tightly in one focal plane, restricting motion and enforcing stability and geometric rigidity which is required to initiate the assembly of larger nanostructures.

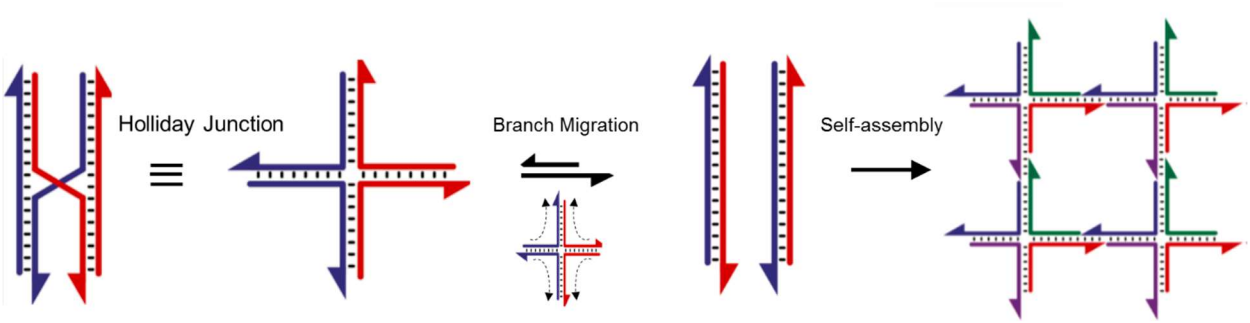

Figure 1.5: Holliday junction. A mobile Holliday junction prone to branch migration is shown. Using sequence asymmetry, an immobile branched junction is created which can conceptually produce extended 2D networks via sticky end cohesion.

More complex tile designs have been produced recently, such as the triple crossover motifs, paranemic crossover and cross-motifs. Through their addressable sticky ends, these stable DNA building blocks gave rise to a wide variety of structures, such as periodic two-dimensional (2D) lattices, DNA nanoribbons, nanotubes and complex helix bundles, etc.[22] Interestingly, Winfree showed that using a nucleating strand of defined sequence, algorithmic tiles (Wang tiles) which are squares of different colors (color = DNA sequence) can grow into a periodic 2D crystals (Figure 1.6A-B).[23] Mao et al. reported the generation of symmetric 3D DNA polyhedra, such as tetrahedral or icosahedra (Buckyball), relying on the association of identical and symmetrical DNA three or five point star tiles (Figure 1.6D).[24] Alternatively, a single unique DNA component can produce highly controlled and complex products. Peng Yin has developed extended 2D arrays and 3D tubes

using a single self-complementary strand (Figure 1.6B-C).[25] More recently, the same group invented a novel, simple and robust approach to make structures from DNA bricks.[26] With an almost limitless range of 32 nucleotide bricks available, they were able to construct myriad three-dimensional structures by sticking the bricks together (Figure 1.6E).

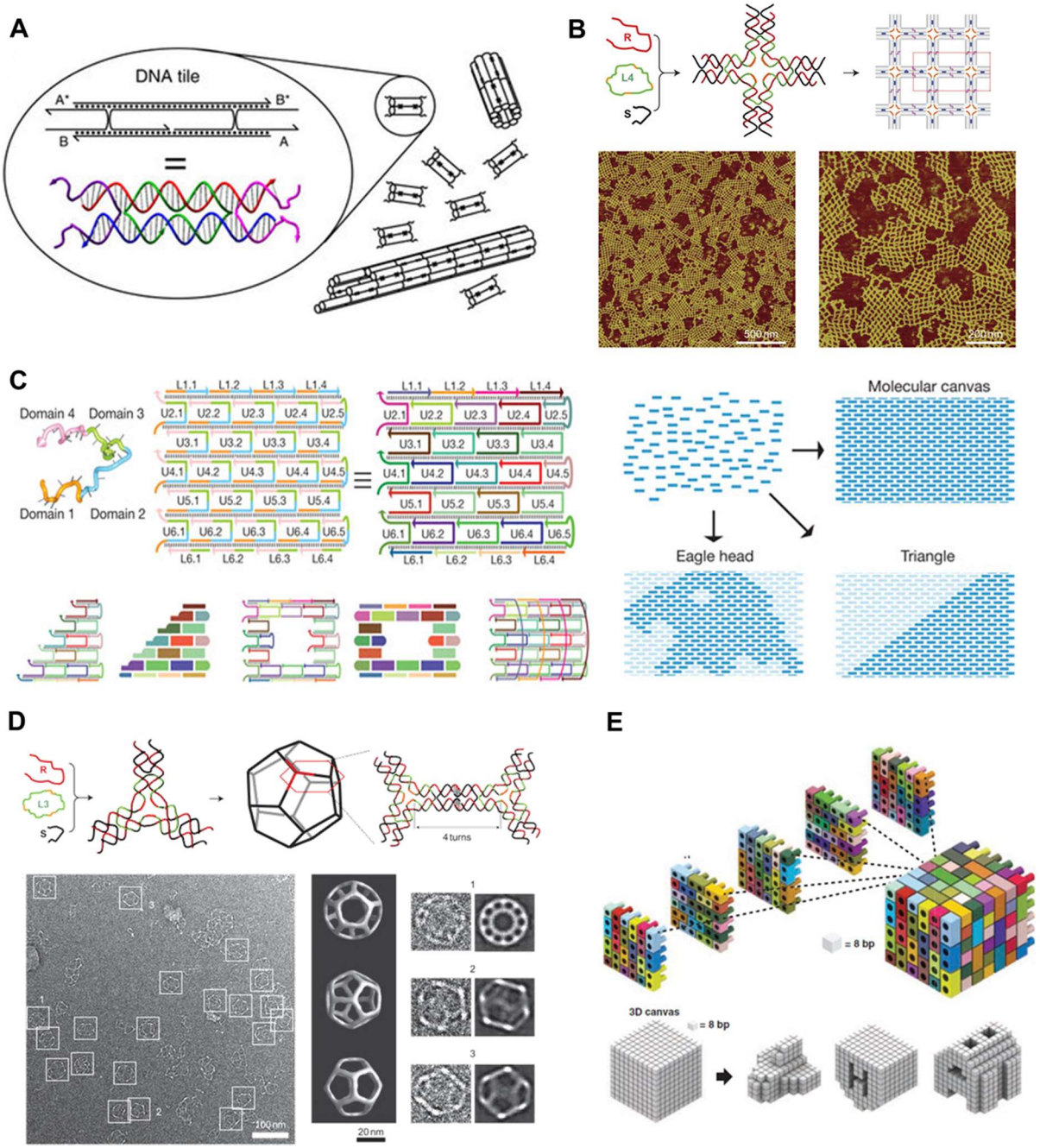

Figure 1.6: Tile-based assemblies. (A) DNA nanotubes constructed by assembling sheets of DX tiles. Adapted with permission from reference [22] (American Chemical Society, 2004) (B) Four-way tiles to make extended 2D networks. Adapted with permission from reference [23] (The American Association for the Advancement of Science, 2003). (C) Single stranded tile which can create sheets that roll into tubes (palindromic sequences), and into other specific 2D extended arrangements (non-palindromic sequences). Adapted with permission from reference [25] (Nature Publishing Group, 2012). (D) A three-point star tile with "DX-like" crossover points from which various 3D geometries can be generated. Adapted with permission from reference [24] (Nature Publishing Group, 2008). (E) Assembly of 3D nanostructures from single stranded tiles (SSTs), each SST has a unique position in the final structures represented by different colored bricks. Adapted with permission from reference [26] (Nature Publishing Group, 2014).

1.4.4 DNA origami: stapling a smiley

"It's like being able to bake a cake and not pay attention to the ingredient ratios"

Paul Rothemund

Tile self-assembly nanotechnology can produce large and well-defined supramolecular structures but the resulting structures are periodic or symmetrical. This assembly method requires strictly balanced stoichiometry, and the possible structural outcomes are often limited by the length of the DNA which can be synthesized. For this reason, a new scaffold-based self-assembly approach was introduced in 2004 by Shih and co-workers.[27] Scaffold-based self-assembly uses a long single-stranded DNA (ssDNA) as a molecular backbone where multiple small 'staple' strands can fold the scaffold into the desired shape. By adopting a virus-derived 1.7 kb ssDNA fragment as the scaffold, a three-dimensional (3D) octahedron with only five DNA 'staples' was built. A general and more powerful approach appeared in Nature in 2006 by Paul Rothemund. This strategy, known as DNA origami, uses a 7.3 kb single-stranded M13 viral genome and about 200 DNA staples to knit together selected parts of the long backbone piece (Figure 1.7).[28] By programming the locations of these interactions, the scaffold could be folded into a variety of non-periodic 2D architectures, such as rectangles, squares, snowflakes, stars, smiley faces and many more deliberately designed patterns (Figure 1.8A).

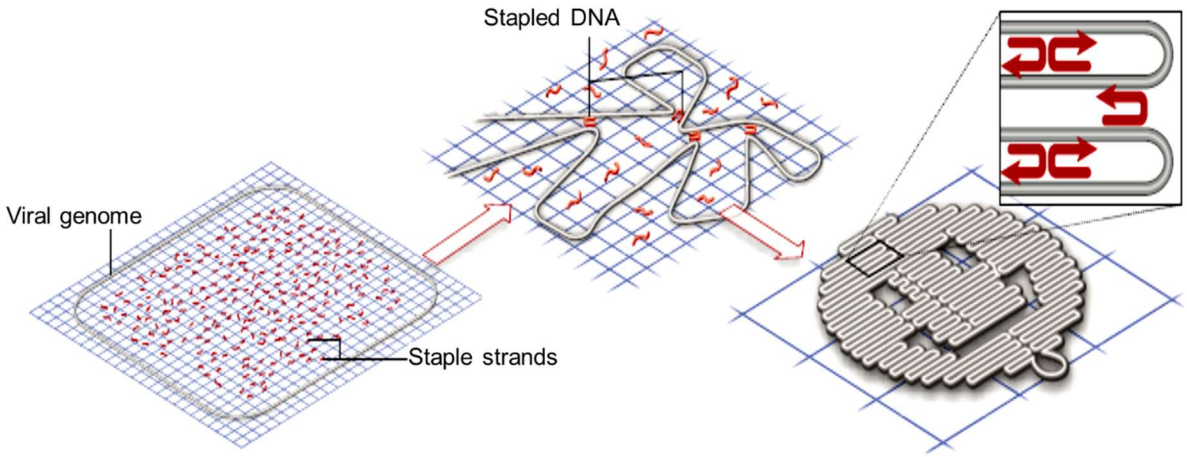

Figure 1.7: DNA origami. A long genomic scaffold strand (black rectangle) is folded into a smiley face shape via hybridization to many short "staple" strands. Adapted with permission from reference [28] (Nature Publishing Group, 2006).

This approach transformed the landscape of DNA nanotechnology in terms of its complexity, rigidity, aperiodicity and ease of self-assembly. Without the need for purification, a large stoichiometric excess of the staple strands would drive efficient product formation. More importantly, origami scaffolds of folded DNA are packed with known sequences (200 sites) that could be used to position DNA-binding cargos just a few nanometres apart (Figure 1.8). This type of precision engineering opens the door for scientists aiming to position components on nano-electronic circuits or exploring the placement of proteins in close, accurate proximity to one another using a reliable self-assembly approach. Shortly after the introduction of DNA origami, research groups exploited this method to engineer 3D nanostructures. Andersen *et al*. constructed a DNA box with a well-defined shape and internal cavities.[29] This was achieved by assembling six DNA origami faces and then connecting them via staple strands at the edges. Shih and coworkers established a general method of rolling DNA origami into a range of discrete 3D structures. To achieve this, the viral backbone was folded with staple strands to create a honeycomb lattice where parallel DNA duplexes were connected by crossovers at specific locations.[30] The group also demonstrated the assembly of twisted DNA bundles, which are curved shapes with well-defined bent angles (Figure 1.8C).[31] Yin *et al.* designed a stiff three arm-junction DNA origami tile motif with precisely controlled angles and arm lengths for hierarchical assembly of polyhedral (Figure 1.8D).[32] Unlike conventional origami designs built from close-packed helices, Högberg and co-

workers created nanostructures of unprecedented complexity.[33] They achieved this by finding a DNA strand path through wireframe shapes using an approach based on graph theory (Figure 1.8E). These structures have a more open conformation with one helix per edge and are therefore stable under the ionic conditions usually used in biological assays. Similarly, Yan and colleagues established a methodology to produce complex wireframe DNA origami nanostructures with multi-arm junction vertices starting with a large set of 2D wireframe structures, then 3D wireframe structures in the form of an Archimedean solid cuboctahedron and a snub cube.[34]

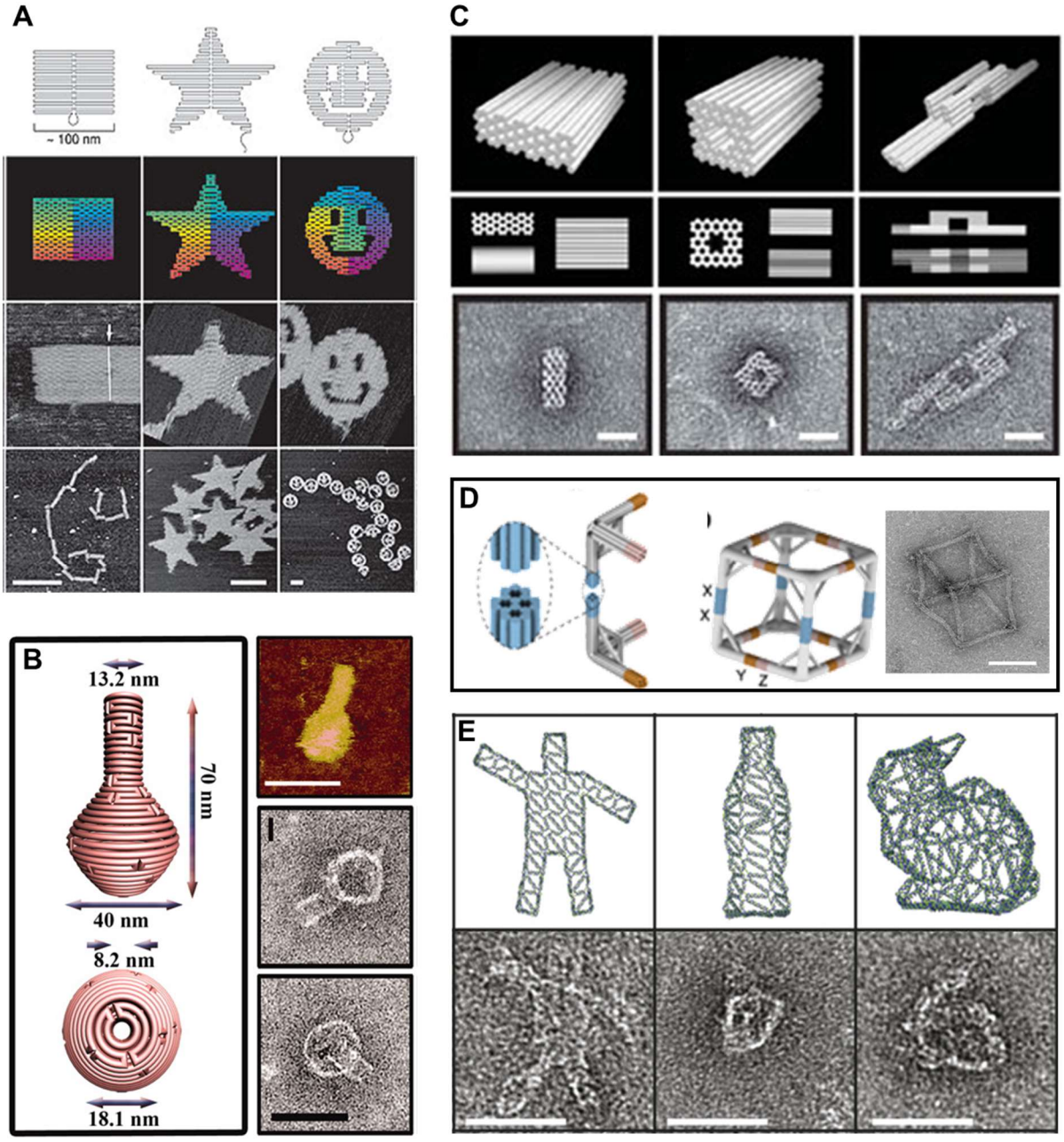

Figure 1.8: Examples of structures created with DNA Origami. (A) Highly rigid and well-defined product created from DNA origami including a rectangle, a star and smiley faces. Adapted with permission from reference [28]. (Nature Publishing Group, 2006). (B) Introducing curvature to DNA origami using unequal arrangements of crossover points between neighbouring helices to generate 2D and 3D products such as a DNA nanovase. Adapted with permission from reference [35]. (The American Association for the Advancement of Science, 2011). (C) 3D DNA origami using hexagonally packed helix bundles showing a number of target geometries. Adapted with permission from reference [31]. (Nature Publishing Group, 2009). (D) Polyhedra self-assembled from DNA tripods with tunable inter-arm angles the tetrahedron and cube designs represented. Adapted with permission from reference [32]. (The American Association for the Advancement of Science, 2014). (E) Different views of the 3D meshes provided as starting points for the automated design process: a waving stickman, a bottle and a version of the Stanford bunny. Adapted with permission from reference [33]. (Nature Publishing Group, 2015).

A variety of complex curved origami assemblies was reported by the same group, including DNA origami spheres, ellipsoids, nanovases and many more (Figure 1.8B).[35] However, challenges such as the length limit of the scaffold strand (origami structures fall below 100 nm in size) in addition to the need for hundreds of strands of different sequences, may indeed be problematic for this approach. Thus, one would need to develop reliable and low cost methods for enzymatic amplification of DNA strands which would make possible the custom-design of DNA nanostructures of 1 gigadalton in mass.

1.4.5 Supramolecular DNA assembly: it takes two to tango!

"What if you bring all of the tools of chemistry into DNA… towards a molecular partnership?"

Hanadi F. Sleiman

In order to overcome the challenges of the origami approach mentioned above, an alternative route to achieve higher order nanostructures of DNA involves the use of synthetic organic and inorganic molecules (Figure 1.9A-E). For instance, DNA building blocks can be blended with supramolecular motifs such as rigid junctions, amphiphilic moieties and ligands, in order to bring additional interactions thus expanding the chemical space and potentially achieving more branching or enhanced structural definition. For example, in the pioneering work by Shi and Bergstrom, the assembly of DNA rings was achieved by incorporating arylethynylaryl moieties (Figure 1.9A).[36] The Sleiman group further studied the directed assembly of DNA polygons with m-terphenyl synthetic corner units[37] and showed that they can self-assemble into well-defined 3D cages and nanotubes using appropriately sequenced linking strands (Figure 1.9B-E).[38] An in depth characterization of these nanotubes will be presented in this thesis. Additionally, Tanaka et al.

showed that azobenzene molecules can be inserted into the sticky ends of three-point-star motifs which facilitated their assembly into nanocapsules with increased stability.[39] Using a different approach, Sleiman and co-workers also demonstrated the assembly of metal-linked branched DNA motifs and produced various metal-nucleic acid 3D nanocages.[40] Shionoya, Schultz and Carrell have also reported the replacement of DNA bases with metal-binding ligands to create metal-mediated base-pairs (Figure 1.9C-D).[41]

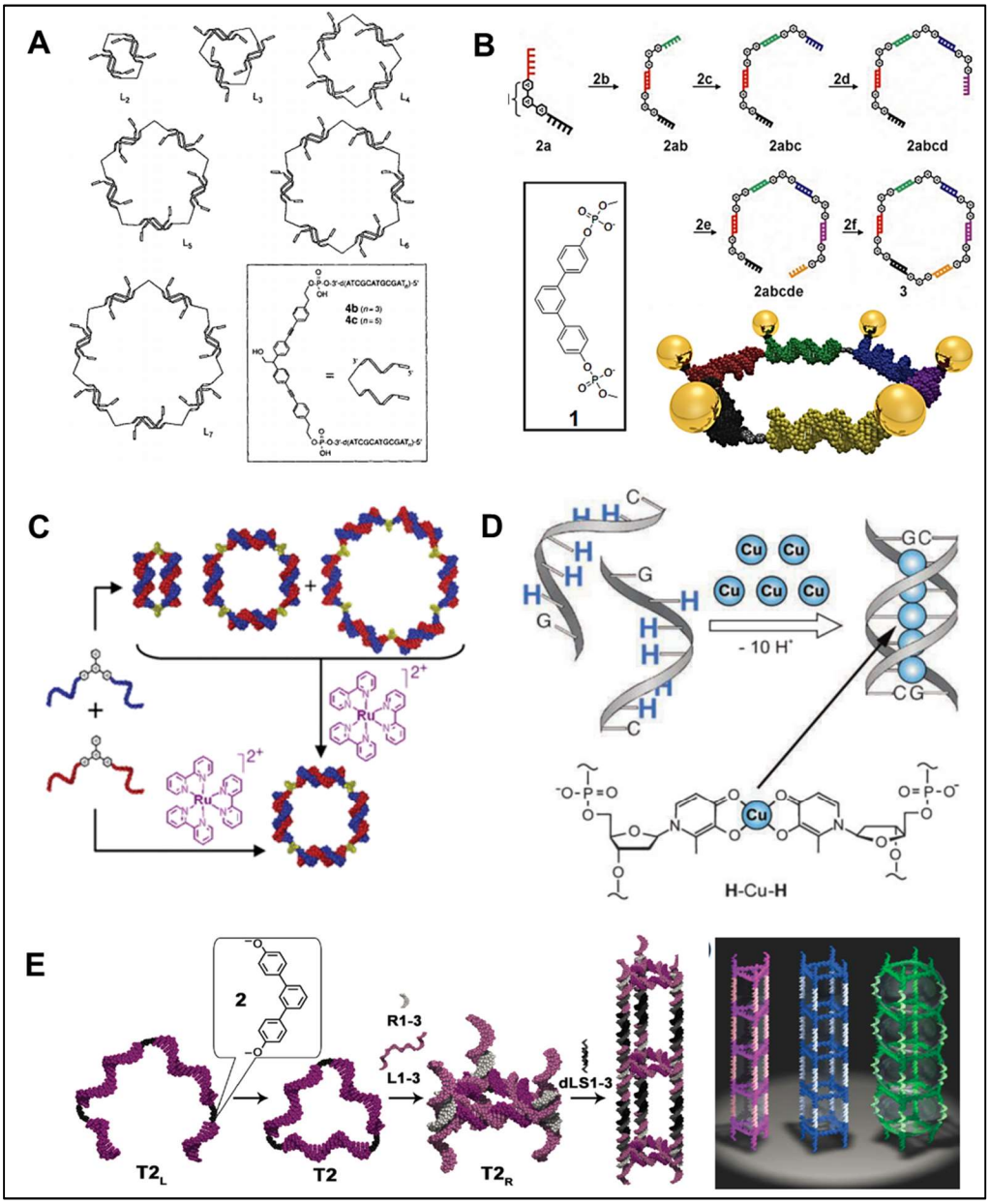

Figure 1.9: Supramolecular self-assembly examples. (A) Two copies of a self-complementary DNA strand joined by a tetrahedral organic vertex. A distribution of macrocycles results from

hybridization of the DNA components. Adapted with permission from reference [36]. (John Wiley and Sons, 1997). (B) Asymmetric DNA building blocks with organic vertices are used to prepare discrete hexagons that can assemble gold nanoparticles. Adapted with permission from reference [37]. (John Wiley and Sons, 2006). (C) The molecule $Ru(bpy)_3^{2+}$affects the self-assembly outcome of two symmetric DNA building blocks and selectively mediates the assembly of a single product, a DNA square. Adapted with permission from reference [40]. (American Chemical Society, 2009). (D) Assembly of a duplex containing five stacked Cu^{2+} ions consisting of a short palindromic oligonucleotide containing five consecutive hydroxypyridone ligands flanked by only one natural nucleobase on both ends. Adapted with permission from reference [41]. (John Wiley and Sons, 2007). (E) A DNA strand with triaryl vertices can be used to construct a rung, by adding complementary and rigidifying strands to the cyclic DNA template. Multiple rungs are stacked vertically via the appropriate double-stranded linkers creating a nanotube of different shapes depending on the template. Adapted with permission from reference [38] (Nature Publishing Group, 2009).

Beyond providing simple structural definition, synthetic molecules and transition metal insertions into the interior of the DNA provide an increased stability and cooperativity to the generated DNA structures without the need for hundreds of different strands. In this regard, another area of tremendous promise involves creating amphiphilic block copolymers from DNA. Block copolymers can be organized into predictable morphologies such as micelles, vesicles, toroids, bilayers and many more long-range assemblies. Combining these materials with DNA can result in unique folding patterns. Very Recently, Sleiman et al. have used DNA-polymer conjugates to create hydrophobic pockets within 3D-DNA cubes, hence mimicking protein coiled-coil motifs.[42]

Supramolecular DNA assembly has been employed to create a variety of nanostructures with additional handles, in efforts to bring the field a step closer to producing active components. Thus, this area has the potential to revolutionize the field of nanotechnology. The synthetic strategies of such hybrid structures, however, will need to be simplified and more effort will be required to scale up the synthesis.

1.4.6 Dynamic DNA nanostructures: a dancing partner

"He who would learn to fly one day must first learn to stand and walk and run and climb and dance; one cannot fly into flying."

Friedrich Nietzsche

As described in the previous sections, by taking it out of its biological role, DNA has served as a robust and versatile building block to assemble a variety of 2D and 3D discrete nanometer-sized structures with controlled shapes and designs as dictated by the designer. In addition to designing objects with increasing structural complexity, the development of DNA nanotechnology has evolved along the lines of building an intrinsic dynamic character into the assembly and function of the resulting structures. Possible dynamic modes include extension-contraction, opening-closing and reversible rotations. A seminal work by Yurke and Turberfield[43] in 2000 adopted the fundamental concept of toehold-mediated strand displacement[44] in artificial DNA nanostructures (Figure 1.10A). For instance, if a strand is bound to a structure, but contains an unbound overhang segment (toehold), a fully complementary strand (fuel strand) can bind the toehold and rapidly displace the other strand from its original location, and leading to the formation of a more stable duplex.[45] This strategy can be combined with static structures to execute active reconfigurations in DNA nanodevices. Notable examples of dynamic assemblies controlled by DNA include nanotubes for controlled release of gold nanoparticles, a DNA box that can be opened in the presence of externally supplied DNA 'keys'[29] and DNA walkers moving autonomously along a track[46] (Figure 1.10C). Other methods to make dynamic DNA nanostructures use stimuli-responsive systems based on i-motifs (pH-responsive)[47], G-quadruplexes (cation-responsive)[48], azobenzene moieties (light-responsive)[49], aptamers (ligand-responsive)[50] and more recently nucleotide base-stacking interactions (temperature and cation-responsive)[51] (Figure 1.10B-C).

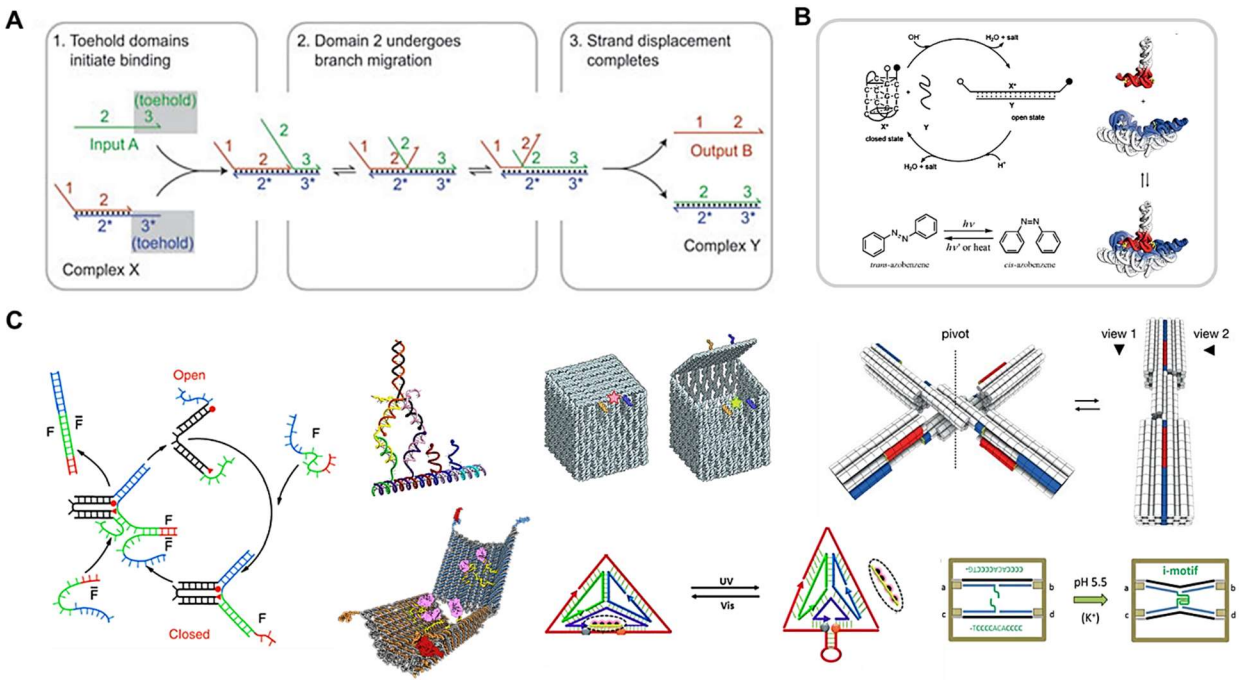

Figure 1.10: DNA dynamic systems. (A) Schematic of the strand displacement reaction, a key concept in dynamic DNA nanotechnology. Adapted with permission from reference [45]. (Nature Publishing Group, 2011). (B) Unusual folding motifs (pH responsive), Azobenzene (photo-responsive), DNA shape complementarity. Adapted with permission from reference [47] (American Chemical Society, 2005), reference [51] (The American Association for the Advancement of Science, 2015). (C) Examples of dynamic DNA nanodevices such as DNA tweezers, DNA walker, DNA origami capsule, DNA box, photocontrollable DNA nanostructure using azobenzenes, DNA switch object with one rotational degree of freedom in the open and closed conformations, DNA frames with inter-strand i-motif formation. Adapted with permission from reference [46] (Nature Publishing Group, 2010), reference [46] (American Chemical Society, 2004), reference [40] (Royal Society of Chemistry, 2011), reference [50] (The American Association for the Advancement of Science, 2012), reference [29] (Nature Publishing Group, 2009), reference [51] (The American Association for the Advancement of Science, 2015), reference [48] (American Chemical Society, 2015).

A particularly exciting possibility would be to interface DNA based-devices with biological circuits, catalytic amplifiers or molecular computing in order to achieve mechanical systems that can process and generate information. This concept will be described in depth in the following section.

1.4.7 DNA nanotechnology at work: more than a pretty face!

"Form ever follows function."

Louis Sullivan

The unique sequence and spatial addressability of DNA nanostructures offer unparalleled precision in positioning proteins, nanoparticles, carbon nanotubes and other nanomaterials into pre-designed arrangements with sub-10 nm features, which surpasses by far the resolution of current top-down fabrication methodologies. In turn, the resulting products of these DNA-directed assemblies have led to improved functional properties. For example, the increased enzyme-cascade activities as was shown in the pilot work of Niemeyer and co-workers where they assembled two enzymes (NAD(P)H : FMN oxidoreductase and luciferase) using ssDNA as a guide.[52] Additionally, Yan *et al.* have used DNA nanostructures as chaperones to align and organize protein molecules using different approaches such as biotin-streptavidin, aptamer-target interactions and ligand-engineered.[53] Shih and co-workers recently designed a DNA origami nanotube that can serve as a detergent-resistant alignment medium in NMR-based protein structure determination.[54] The Turberfield's group used periodic 2D DNA crystals as templates to arrange proteins and subsequently used cryo-EM to solve their structures.[55] DNA nanostructures were also used to organize various organic chromophores and conjugated polymers into artificial light-harvesting complexes with control over cascading unidirectional energy transfer. In addition to revealing the fundamental physics underlying the collective properties of nanomaterials, these hybrid materials will certainly play an essential role in future devices such as solar cells, light emitting diodes, electronic and photonic circuits, etc. For instance, Gothelf *et al.* self-assembled recently individual synthetic polymer wires containing short oligonucleotides into predesigned routings on both two- and three-dimensional DNA origami templates (Figure 1.11A).[56]

DNA-mediated self-assembly of inorganic nanomaterials such as quantum dots, nanowires, metal nanoparticles and organic chromophores, have enabled a systematic investigation of their emerging photophysical properties.[57] In one example, Liedl and co-workers constructed a spiral and chiral arrangement of gold nanoparticles at regular intervals.[58] His group also demonstrated, in a very recent work, the creation of reconfigurable 3D plasmonic metamolecules, which execute DNA-regulated conformational changes at the nanoscale. This work showed how DNA scaffolding can be used to control the precise structural arrangement of metal nanoparticles,

allowing scientists to tailor surface Plasmon resonance and its interaction with visible light.[59] Tinnefeld used DNA origami nanotube to position a pair of gold nanoparticles and create an "antenna" (Figure 1.11B). By achieving a fine control of optical fields at the nanometre scale between the particles, the absorption and emission of local emitters was significantly enhanced.[60]

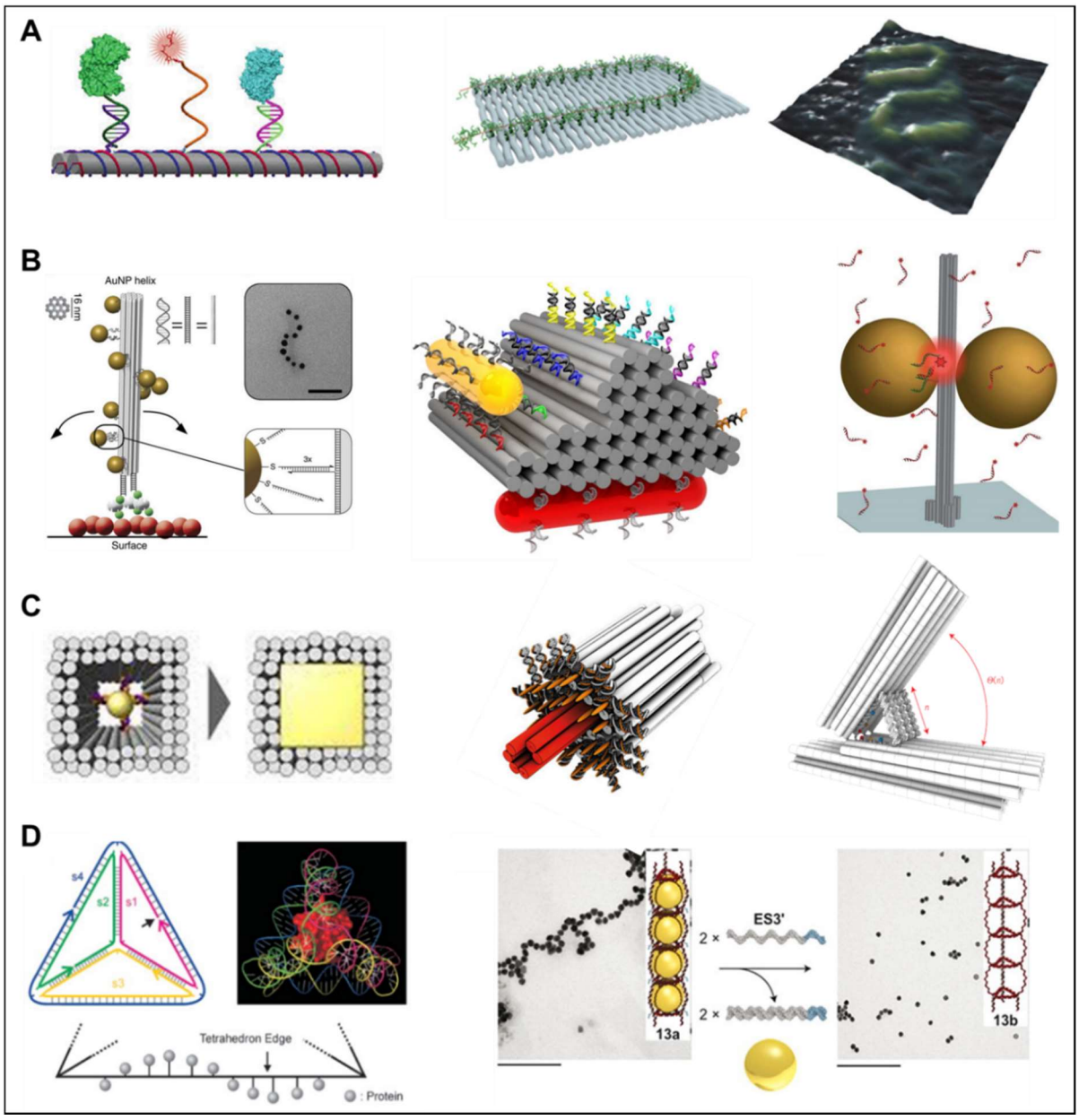

Figure 1.11: Applications of DNA nanodevices. (A) Multi-enzyme complexes and conjugated polyelectrolytes on DNA scaffolds. Adapted from reference [53] (Nature Publishing Group, 2014), reference [56] (Nature Publishing Group, 2015). (B) Gold nanoparticles arranged in a secondary left-handed helix on the DNA origami structure, plasmonic DNA-based walker and nanoantenna. Adapted with permission from reference [58] (Nature Publishing Group, 2013), reference [59]

(Nature Publishing Group, 2015), reference [60] (The American Association for the Advancement of Science, 2012), reference [59] (Nature Publishing Group, 2015). (C) DNA mold, lipid membrane DNA nanochannel, a high-resolution DNA positioning device. Adapted with permission from reference [61] (The American Association for the Advancement of Science, 2014), reference [62] (The American Association for the Advancement of Science, 2012). (D) DNA tetrahedron for protein encapsulation and DNA nanotubes for gold nanoparticles delivery. Adapted with permission from reference [67] (Nature Publishing Group, 2012), reference [65] (Nature Publishing Group, 2010).

The ability to create arrays of nano-entities with nanometre scale spacing makes DNA materials ideal for nanomedicine[61] and even more so for applications in biosensing and detection.[62] In fact, many detection systems have been built taking advantage of the hybridization power of linear DNA, such as molecular beacons and colorimetric detection systems. Among many reported models, Yan and co-workers developed 2D barcoding nanoarray[63] used as a platform where multiple aptamers are attached as the signalling units. The same grid was employed for the construction of a multiplexed sensing array, where its tiles are labelled with either one of the two encoding dyes (red and green) or the detection probes carrying a blue dye.[64] By using this system, they were able to detect severe acute respiratory syndrome virus, human immunodeficiency virus, and protein targets such as thrombin and adenosine triphosphate simultaneously. Moreover, many research groups have started to explore the possibility of employing complex 3D nanocontainers as delivery vehicles. In addition to the selective release of gold nanoparticles in DNA nanotubes[65], Sleiman confirmed the penetration of wireframe cages into cells without the aid of transfection agents, and in greater efficiency in comparison to ss and ds DNA.[66] Turberfield and co-workers demonstrated the encapsulation of cytochrome C within a DNA tetrahedral cage, where the protein molecule is conjugated to the 5′-end of one of the component DNA strands via a surface amine (Figure 1.11D).[67] This could open the door for a new kind of delivery of oligonucleotide therapeutics. More recently, Stupp showed that DNA nanotubes functionalized with RGD peptides (ArginylGlycylAspartic acid) can enhance significantly the differentiation of neural stem cells into neurons.[68]

1.5 Single molecule fluorescence methodologies

1.5.1 Nanoscale imaging techniques: just look at the thing!

"A picture is worth a thousand words"

Napoleon Bonaparte

All the above mentioned examples of applications providing tools for targeted delivery, plasmonic devices, light harvesting and diagnostic systems, are among the various proof of concept studies accomplished so far in the field of DNA nanotechnology. However, a number of technical challenges need to be addressed including improving stability and scalability, achieving simplicity in design, reducing the costs and high error rate of self-assembly, and more importantly, devising new quantitative tools and implementing existing ones to analyze the structures at the finest possible level of detail. Without the ability to validate whether one has produced the nanostructures aimed for, there can be no experimental feedback to help rational development of the field.[69] Currently, the most commonly used analytical tools to characterize the size and stability of DNA constructs include gel electrophoresis, atomic force microscopy (AFM) and transmission electron microscopy (TEM).[70] However, these techniques require large amount of DNA (μM concentration and more), long acquisition times (more than two hours processing time), and are not *in situ*, which could lead to sample damage during the reconditioning to the measurement environment. More recently, single molecule fluorescence techniques have played a leading role in observing nanometer size structures while avoiding/minimizing the challenges mentioned above.[12]

1.5.2 Single molecule fluorescence imaging: watching a small world in motion

"*If you judge a fish by its ability to climb a tree, it will live its whole life believing that it is stupid"*

Albert Einstein

Optical spectroscopy at the ultimate resolution of a single molecule has grown over the past decades into a powerful technique for observing the behavior of individual molecules in their complex local (nanoscale) environments. Observing one molecule at a time removes the ensemble averaging, and provides unique access to hidden heterogeneity and dynamics in complex condensed phases with unprecedented details. Among different single-molecule techniques, fluorescence-based detection is the most widely-used method due to its high spatial and temporal resolution, high contrast against background, non-destructiveness and ease in instrumentation.[71]

The beginning of this research field may be traced back to the optical detection of single pentacene molecules inside an organic crystal by Moerner in 1989 using absorption spectroscopy. Shortly after, Orrit reported the detection of fluorescence from individual pentacene molecules within a p-terphenyl crystal in 1990. This was followed by the development and optimization of many successful microscopic methods including near-field scanning optical microscopy (NSOM), epifluorescence, total internal reflection, and confocal microscopies. Given that each single fluorophore acts as a single light source (1 nm in size), conventional microscopy cleverly combined with the active control of the number of emitting molecules within a light-pumped volume.[72] This then led to the proposal and demonstration of super-resolution imaging by Eric Betzig and others, a new frontier for optical microscopy beyond the diffraction limit resolution.[13]

The next section includes an overview the fundamentals of fluorescence in addition to the different factors involved in single molecule fluorescence detection such as brightness, background and resolution, with a specific focus on single molecule TIRF microscopy. This is followed by a description of the different quantitative analyses obtained from single molecule fluorescence methodologies which can help access the details of the nano-world and in particular the structure and dynamics of DNA nanostructures.

1.5.3 Fluorescence and fluorophores: *let there be photons!*

Fluorescence is the emission of light from the singlet excited state of a molecule as it relaxes back to the singlet ground state.[73] The photophysical processes that can occur for a molecule following electronic excitation (e.g. absorption of a photon) can be conveniently illustrated in a Jablonski diagram (named after Professor Alexander Jablonski, Figure 1.12B). The process of fluorescence starts with the instantaneous (~10^{-15} s) absorption of a photon by the molecule. The energy provided by the photon excites an electron from the singlet ground state of the molecule (S0) to some vibrational energy level in a higher singlet excited state (e.g., S1). Upon excitation to a higher energy state, the electron can relax and dissipate the excess energy through a variety of pathways. Typically, the first process following excitation is called internal conversion, where the excited electron rapidly relaxes to the lowest vibrational energy level of S1. Finally, fluorescence occurs when the excited electron in S1 returns to S0 via the emission of a photon (ca. 10^{-8} s). Another common deactivation pathway for S1 involves non-radiative decay concomitant with heat

dissipation (i.e., internal conversion). This process typically competes with fluorescence and is characterized by rate constants in the range of 1×10^{15} - 1×10^{8} s^{-1}.

An excited electron in S1 can alternatively undergo spin conversion to an excited triplet state, (e.g., T1). This process is called intersystem crossing. Although quantum mechanically a "forbidden" transition, relaxation of the excited electron from T1 to S0 can still take place, resulting in the emission of a photon in a process known as phosphorescence (10^{-3} – 100 s). Once the molecule crosses over to the triplet state manifold, the excited fluorophore has a much longer timeframe to undergo chemical reactions with surrounding molecules, potentially resulting in chemical modifications of the fluorophore backbone. Although triplet states are efficiently quenched by oxygen, this happens at the expense of sensitizing singlet oxygen, a strongly oxidizing species that may rapidly react with its sensitizer, leading to permanent photobleaching of the fluorophore.[74] Therefore, two commonly employed strategies to remove molecular oxygen can help minimize photobleaching such as employing an enzymatic oxygen scavenger system or equilibrating the sample with an inert gas such as argon or nitrogen.[75]

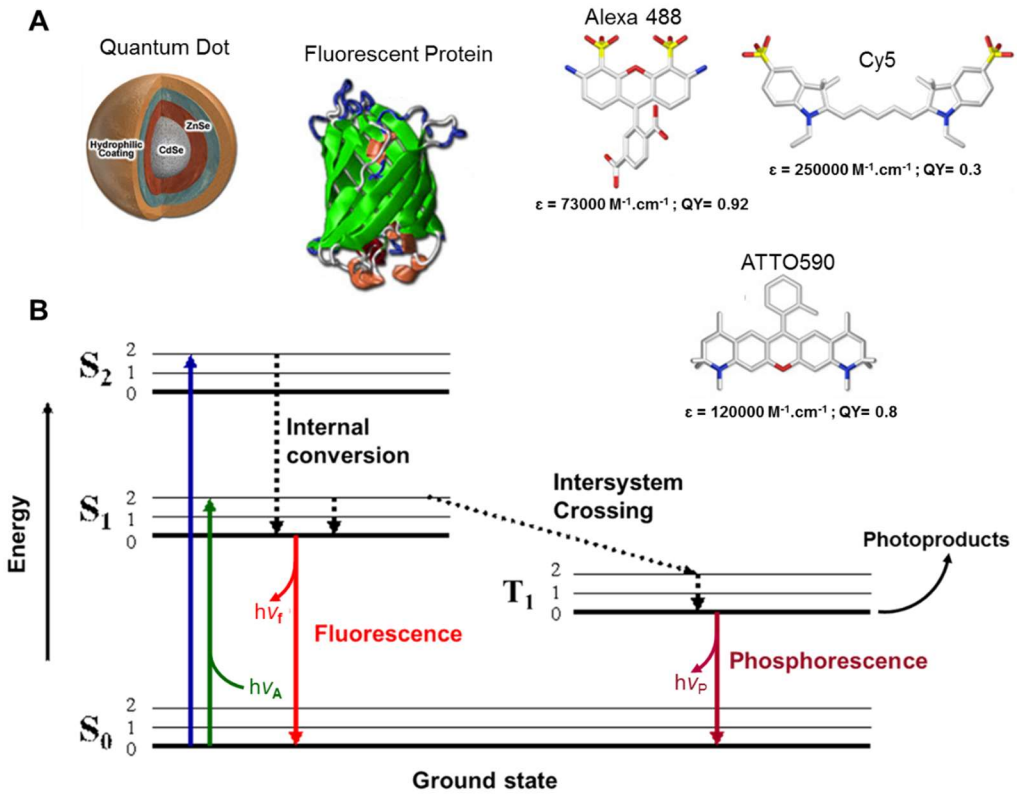

Figure 1.12: Fluorescent probes and Jablonski diagram. (A) Quantum Dot, Fluorescent protein and organic fluorophores including Alexa 488, Cy5 (cyanine) and ATTO590 with their respective extinction coefficient and quantum yield (image not to scale). (B) Jablonski diagram showing the various electronic and molecular processes that occur upon the excitation of a molecule.

Emitting species suitable for single-molecule detection fall into several categories, including organic fluorophore labels (such as cyanine dyes like Cy3, Alexa dyes, etc.), quantum dots and fluorescent protein labels that can be attached to the biomolecule of interest (which may be a protein, lipid, or an oligonucleotide). A suitable emissive species needs to have: (i) high brightness, given by the product of the absorption of the fluorophore (extinction coefficient) at the excitation wavelength (ideally >100,000 M^{-1} cm^{-1}) and the fluorescence quantum yield (ratio of emitted to absorbed photons) at the emission wavelength (ideally it would be >10%), (ii) a relatively short excited-state lifetime (in the order of few nanoseconds) to quickly replenish the ground state, (iii) a large Stokes shift to reject scattered excitation light, and (iv) stable photophysical properties (high photostability and low probability of dark states).[76] Depending on their molecular structure and local environment, some molecules can photobleach after absorbing only a few photons, whereas more robust molecules can undergo tens or hundreds of millions of absorption/emission cycles before photobleaching occurs. The following are typical photophysical parameters for the three main categories of emitters: (i) Green fluorescent protein: 10^4-10^5 photons, 0.1-1 second lifetime), (ii) typical organic dye: 10^5-10^6 photons, 1-10 second lifetime, and (iii) CdSe/ZnS Quantum dot: 10^8 photons, > 1000 second lifetime (Figure 1.12A).

Importantly, in the context of single molecule fluorescence microscopy, the concentration of the labeled molecules must be kept low such that individual molecules can be resolved and no background from molecules (out of focus) is picked up by the detectors. A key requirement for single molecule experiments is to maximize the fluorescence emission rate of the molecule under investigation while strictly reducing the background. Additionally, to obtain a large signal, a very small focal volume is needed to irradiate the sample on a typically transparent substrate. This will help eliminating background fluorescence from outside the focal plane and will improve the spatial resolution. The next section describes different microscopic strategies to achieve this goal.

1.5.4 Total Internal Reflection Fluorescence (TIRF) Microscopy:

"It shines better when everything has darken."

Rabindranath Tagore

The idea of using total internal reflection to illuminate a small volume of a sample contacting the surface of the glass coverslip was first described by E.J. Ambrose in 1956 and then extended by Daniel Axelrod at the University of Michigan in the early 1980s.[77] The total internal reflection fluorescence microscopy (TIRFM, also called 'evanescent wave microscopy') is provided by an incident light beam that undergoes TIR at the interface between a high and a low refractive index material. This generates a very thin (approx. 100 – 200 nm) evanescent field that penetrates the low refractive index material. As the intensity of an evanescent field decreases exponentially with distance to the interface, only fluorophores in a close proximity to the coverslip surface are excited, thus reducing the background from out of focus emitters in solution (Figure 1.13A-B).[78] For angles of incidence measured from the interface normal (θ) above the critical angle, the evanescent field intensity (I) drops off with a distance z into the lower-index medium according to equations (1) and (2):

$$I_{(z)} = I_{(0)}\, e^{-z/d} \qquad [1]$$

$$d = \frac{\lambda_0}{2\pi}(n_2^2\, sin^2\theta - n_1^2)^{-1/2} \qquad [2]$$

Where *d* is the distance, λ_0 is the wavelength of the excitation light in vacuum, and n_1 and n_2 are the indices of refraction at the interface of liquid and glass, respectively (e.g. n_1= 1.33 for water; n_2= 1.52 for glass). This allows the creation of images with outstanding signal-to-background ratio, as fluorophores from regions farther from the surface are hardly excited. Two general configurations of TIRFM are commonly used: prism-type and through-objective TIRFM. In the prism-type configuration, TIR is implemented by coupling a microscope slide to a prism with a refractive index matching fluid (quartz prism is used instead of glass in order to minimize background autofluorescence).[79] A laser beam is coupled into the prism above the critical angle to achieve TIR. In the through-objective mode, a very high numerical aperture objective (NA ≥1.4) is used to couple an input laser beam at a super-critical angle in order to generate an evanescent field in the sample at the cover-slip–sample interface. In this latter approach, the sample is more easily accessible from the open side of the microscope to e.g. manipulate it. The higher NA

objectives can allow for increased lateral resolution. Emission from the sample is collected back through the objective and is typically focused on a back-illuminated electron multiplied charge coupled device (EMCCD camera) to acquire a real-time series of images. It is important to note the diffraction limit equation here: the focal spot of the excitation beam cannot be made smaller than l/(2NA) where NA is the numerical aperture of the microscope. In the visible spectrum, this limit corresponds to approximately 250 nm which results in a dramatic contrast between the size of the focal spot and the size of the fluorescence labels, which are typically a few nm in length or smaller (Figure 1.13A-B).

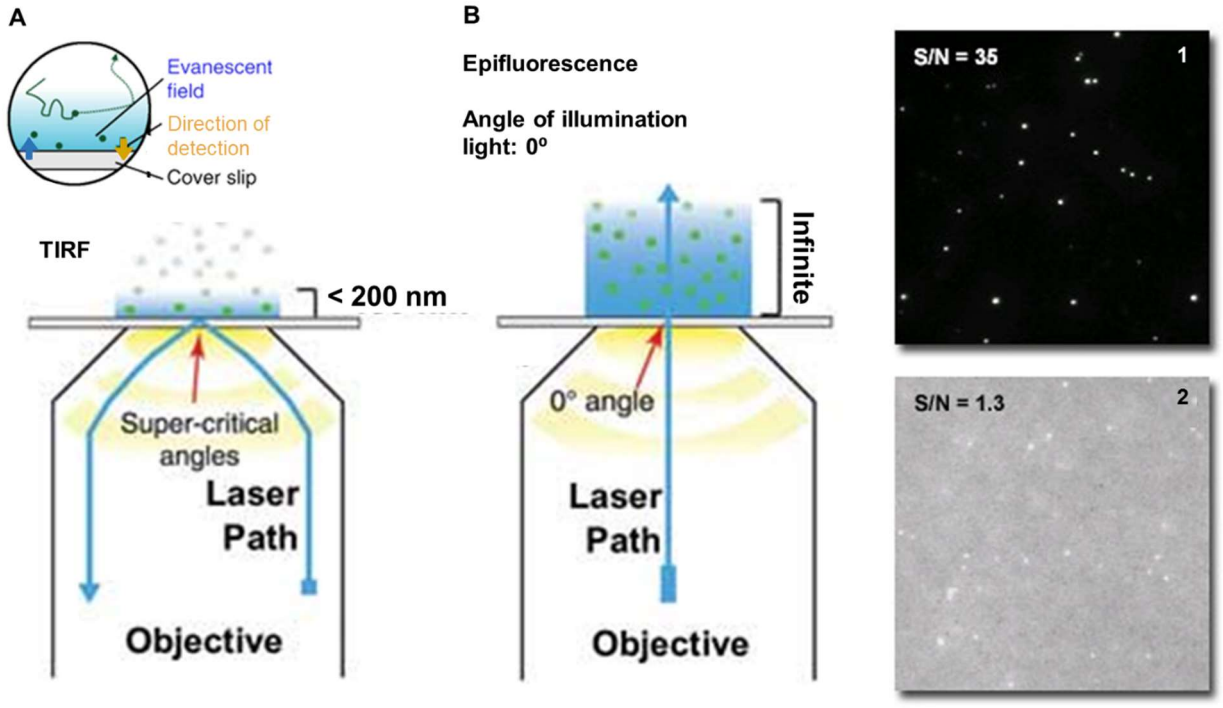

Figure 1.13: Single molecule imaging microscopes. A cartoon illustrating the illuminated (blue) and observed (orange) region within a sample for each of the two microscopy schemes (A) TIRF microscopy and (B) Epifluorescence imaging set-up. On the right, typical images showing a comparison between the signal to noise obtained with a TIRF set-up (1) versus epifluorescence (2). Adapted with permission from reference [79] Nature Publishing Group, 2015).

In one of the first examples of TIRF experiments with the capability to conduct real-time single-molecule fluorescence imaging, Yanagida and co-workers developed a system to detect single ATP turnover events catalyzed by a single-headed myosin sub-fragments.[80] Soon after, the Xie's group reported real-time observation of single turnovers catalyzed by cholesterol oxidase enzymes, which are flavoenzymes that catalyze the oxidation of cholesterol using molecular oxygen.[81] They monitored the appearance and disappearance (on-off) of flavin adenine dinucleotide (FAD) fluorescence, present at the redox center of the enzyme's active site. These proof of principle experiments provided new insight into a seemingly well-characterized and well-understood system and thus were an important step to prove the power of being able to monitor fluorescence trajectories of single molecules on a biologically relevant time scale.[82] For instance, visualization of RNA polymerase in real time as it searches for promoters, at the submicroscopic scale, was demonstrated by Greene et al. using TIRFM[83] (Figure 1.14A-E). More recently, single DNA nanotubes were observed by TIRF microscopy when the DNA strands are partially conjugated with fluorescein, a green fluorescence dye. The Mao group showed that the size distributions of the structures obtained agreed with the AFM data, the advantage of fluorescence imaging being that it was easy and possible to conduct in solution in a time efficient manner.[84] In another example, Winfree and co-workers used TIRF microscopy to monitor DNA nanotube polymerization in real time at the single filament level over a wide range of free monomer concentrations and temperatures.[85] This is a step forward towards understanding the design principles of dynamic tubular architectures (Figure 1.14F).

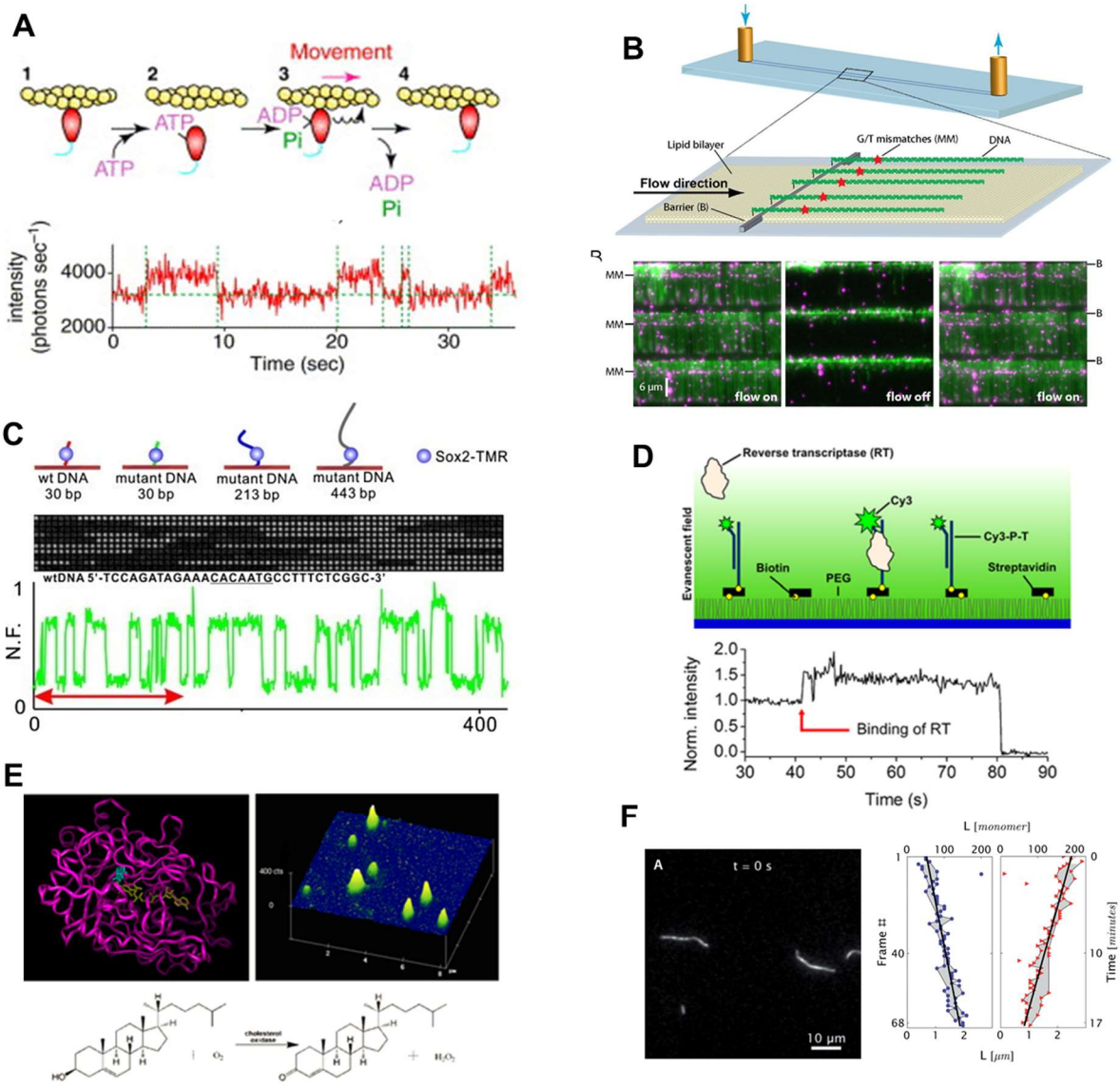

Figure 1.14: Single molecule TIRF imaging examples. (A) Detection of single ATP turnover events catalyzed by a single-headed myosin sub-fragments using TIRF microscopy. Adapted with permission from reference [80] (Nature Publishing Group, 1994) (B) Single-molecule DNA-curtain assay for promoter-specific binding by RNA polymerase. Adapted with permission from reference [83] (Nature Publishing Group, 2013) (C) Study the dynamic behavior of transcription factors both in vitro and in live cells using SM-TIRF system. Adapted with permission from reference [82] (Nature Publishing Group, 2015) (D) A total internal reflection fluorescence microscopy setup combined with surface-immobilized Cy3-labeled primer-template (Cy3-P-T) was employed for the SM-PIFE measurements. Adapted with permission from reference [86] (American Chemical Society, 2013), (E) Real-time observation of single turnovers catalyzed by cholesterol oxidase enzymes. Adapted with permission from reference [81] (The American Association for the Advancement of Science, 2012) (F) Imaging single tile-based DNA nanotubes polymerization using TIRF microscopy. Adapted with permission from reference [85] (Royal Society of Chemistry, 2015).

Using single molecule TIRFM, and depending on the experimental design, as will be described in the next section, information on different state parameters such as intensity, lifetime, polarization and energy transfer, can be measured for each individual molecule over time.[86]

1.5.5 Single molecule FRET: emission impossible… or possible?

"There can be only one sun at a time. Never obscure the sunlight, or rival the sun's brilliance; rather, fade into the sky and find ways to heighten the master star's intensity"

Robert Greene

Published in the 1940s, Theodor Förster's ground-breaking theory on Förster Resonance Energy Transfer (FRET) has been employed over the years as a powerful tool in several scientific fields such as material sciences, drug development and medicine.[87] The phenomenon of FRET is based on non-radiative energy transfer between a donor and acceptor dye molecules via dipole-dipole interactions.[88] FRET results in a decrease in donor emission intensity and a concomitant increase in acceptor emission.[89] The rate of energy transfer between a donor and acceptor (k_T) is given by equation (3):

$$k_T(r) = \frac{1}{\tau_D}\left(\frac{R_0}{r}\right)^6 \qquad [3]$$

Where τ_D is the fluorescence lifetime of the donor (i.e., the average time the donor spends in the excited state before emitting a photon), r is the distance between the donor and acceptor, and R_0 is the Förster radius: the distance between the donor and acceptor that gives 50% energy transfer. R_0 is calculated as described in equation (4) (Figure 1.15A):

$$R_0 = \left(\frac{9\ln(10)\varphi_D\kappa^2 J(\nu)}{128\pi^5 N_A n^4}\right)^{\frac{1}{6}} \qquad [4]$$

Where Φ is the emission quantum yield of the donor, κ is a factor describing the spatial orientation of the donor and acceptor, N_A is Avogadro's number, and J(ν) is an integral describing the spectral overlap between the donor emission and acceptor absorption spectra. We note that FRET occurs when the emission spectrum of the donor dye overlaps with excitation spectrum of the acceptor dye (Figure 15B).

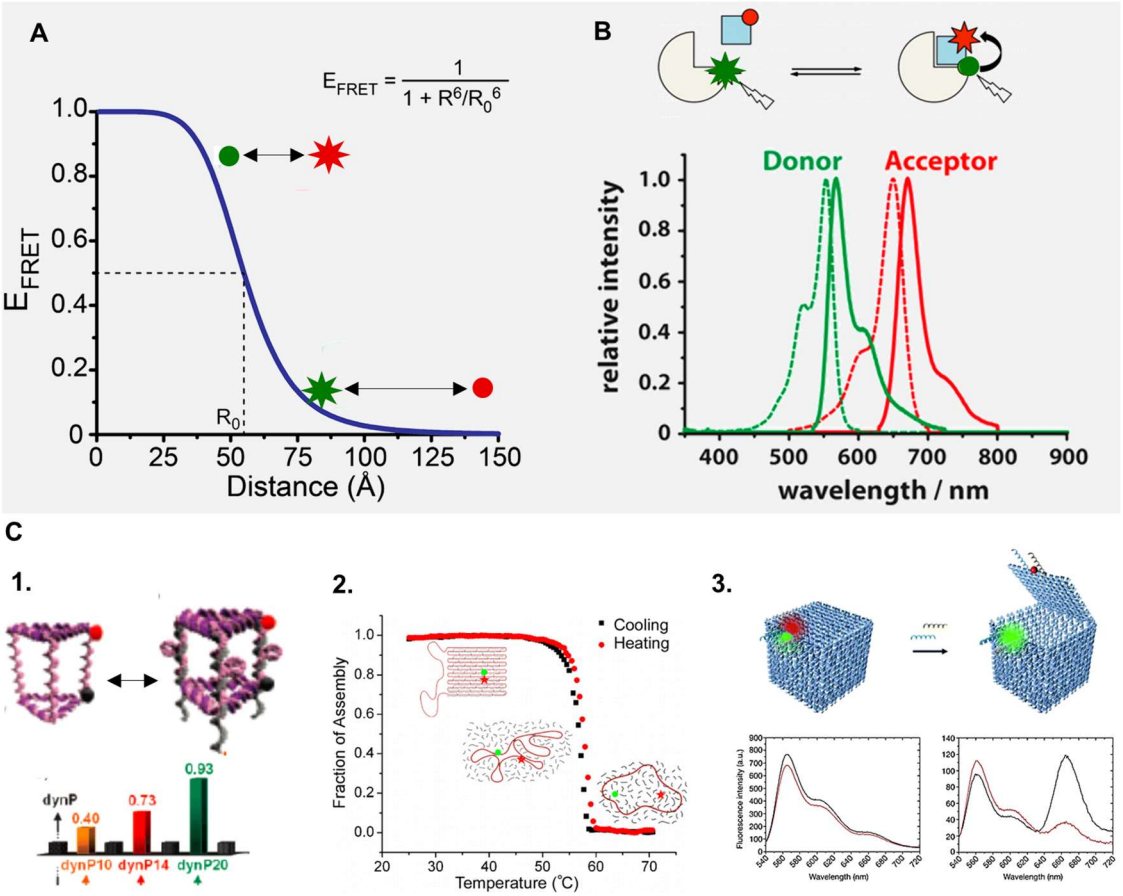

Figure 1.15: Single molecule FRET. (A) FRET efficiency, E, as a function of inter-dye distance (R) for a R_0 = 50 Å. Donor dye directly excited with incident laser either fluoresces or transfers energy to acceptor dye, depending upon its proximity. At R = R_0, E = 0.5, but at smaller distances, it is >0.5 and vice versa, according to the function shown on the right. (B) FRET occurs when the emission spectrum of the donor dye (green continuous line) overlaps with excitation spectrum of the acceptor dye (red dashed line). (C) 1) Structural switching cycle of 3D DNA object confirmed by FRET. 2) Mapping the thermal behavior of DNA Origami nanostructures using FRET-based measurements. 3) Monitoring the controlled opening and closing of a DNA box lid using ensemble FRET measurements. Adapted with permission from reference [90] (American Chemical Society, 2007), ((The American Association for the Advancement of Science, 2018).

Ensemble FRET techniques were commonly used to study nanostructures in solutions and elucidate their dynamics.[90] However, the heterogeneous nature of the samples is hidden in bulk systems (Figure 1.15C). For this reason, single-molecule Förster resonance energy transfer (SM-FRET) can be used to report on inter- and intramolecular dynamics/kinetics of biomolecules by exploiting the distance-dependent energy transfer between a donor and acceptor fluorophores. In 1996, Ha et al. described the first detection of SM-FRET[91], however it did not take long for the

widespread adoption of SM-FRET as a tool to study and gain insights into many complex biochemical processes[92], such as RNA and protein folding, protein and nucleic acid conformational dynamics, DNA unwinding, homologous recombination, and translation.[93]

Given that the ultimate goal of DNA nanotechnology is to develop dynamic nanomachines, SM-FRET would naturally emerge as the method of choice to characterize the dynamics within complex 3D DNA architectures. For instance, application of SM-FRET methods has revealed the kinetics of reconfigurable DNA nanochambers upon the extension and contraction of an inner cavity and showed that it is highly dependent on the actuator sequence.[94] In another example, the method has enabled the confirmation that thermodynamics and kinetics of oligonucleotide target hybridization onto patterned 2D arrays on DNA origami nano-pegboards are significantly dependant on the density of the probe.[95] (Figure 1.16A-F)

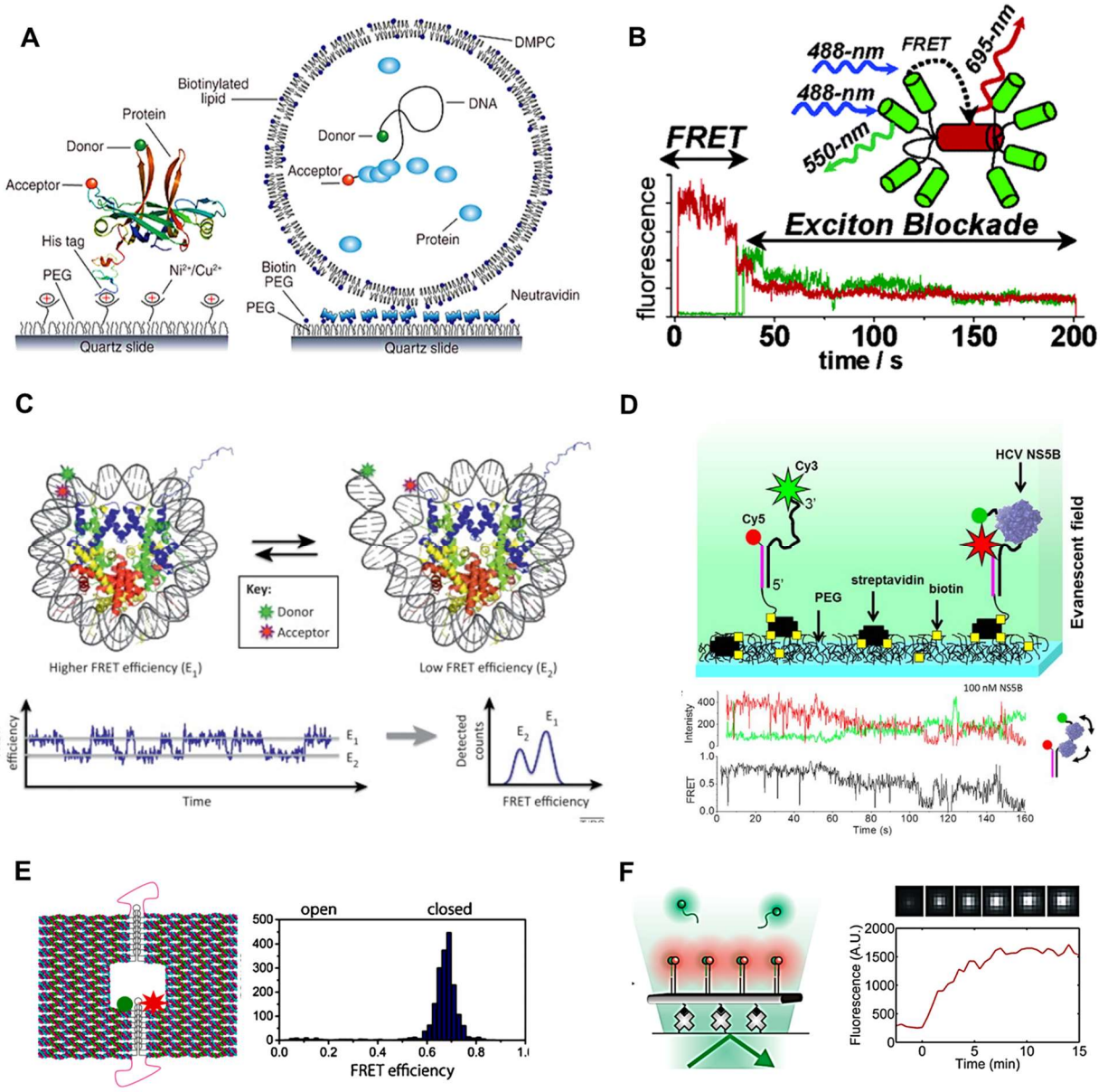

Figure 1.16: Examples of single molecule FRET applications. (A) Surface immobilization strategies for smFRET experiments. Adapted with permission from reference [89] (Nature Publishing Group, 2008). (B) Intramolecular directional Förster Resonance Energy Transfer at the single-molecule level in a dendritic system. Adapted from reference [92] (American Chemical Society, 2003). (C) Single-molecule fluorescence resonance energy transfer (FRET) studies on the structure and structural dynamics of nucleosomes. Adapted with permission from reference [92] (Elsevier Ltd., 2012) (D) TIRF experiment monitoring HCV NS5B binding to a 3' RNA overhang from which single molecule fluorescence intensity time and FRET fluctuation trajectories are extracted. Adapted with permission from reference [92] (The American Society for Biochemistry and Molecular Biology, 2014) (E) Reversible reconfiguration of DNA origami nanochambers monitored by Single-Molecule FRET. Adapted from reference [94] with permission (John Wiley and Sons, 2015). (F) Kinetics of hybridization of oligonucleotide probes into patterned two-

dimensional arrays on DNA origami nanopegboards. Adapted from reference [95] (American Chemical Society, 2013).

1.5.6 Single molecule photobleaching: turn obstacles into opportunities!

"One step at a time… everything is possible"

Lady climbing a pyramid (Coba, 2016)

TIRF microscopy has been recently utilized towards counting the subunit stoichiometry in fluorescently labelled complexes via the recording and monitoring of photobleaching steps in single particle intensity-time trajectories. Upon prolonged laser illumination, molecules will undergo a photoreaction leading to structural modifications, which lead to an irreversible loss of fluorescence.[96] Photobleaching is a stochastic process which, under constant irradiation power, occurs with a given probability for each excitation–emission cycle. The probability of photobleaching will be related to the irradiation power, the concentration of O_2, the presence of triplet excited state scavengers in the solution etc. Due to the stochastic nature of the process, when working with a large number of fluorophores (at least >10 dyes), photobleaching is perceived as an exponential decay of sample intensity. At the single molecule level, a discrete and complete loss of emission from each individual fluorescent molecule can be observed, resulting in a single step in the intensity-time trajectory (Figure 1.17). Though undesirable in most fluorescence applications, the photobleaching process can be exploited beneficially in certain applications.[97]

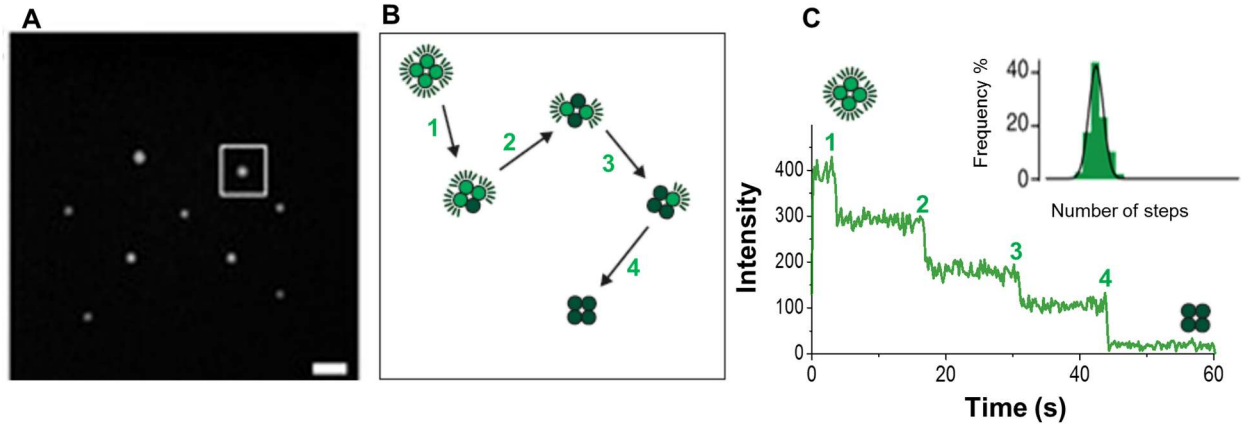

Figure 1.17: Single molecule photobleaching method. (A) Typical TIRF image of single molecules on the surface (Scale bar 5µm) (B) Scheme showing the different stages of the single molecule photobleaching over time: Extracting intensity time trajectory of a single molecule on the surface and a histogram of the number of steps counted from the total obtained traces.

The stepwise bleaching allows for the identification and counting of multiple fluorescent tags within a composite. Based on this principle, many researchers have employed this method to define stoichiometry of a variety of macromolecules with previously unknown subunit numbers. Isacoff described a single-molecule technique for counting subunits of proteins in live cell membranes by observing bleaching steps of GFP fused to a protein of interest.[98] Another example is included in the work of Bayley and coworkers where they applied the subunit-counting approach to the β-barrel-forming toxins α-hemolysin.[99] The method has been also combined with binomial distribution analysis to clarify the stoichiometry of the phi29 DNA packaging motor and many other systems as shown in Figure 1.18.

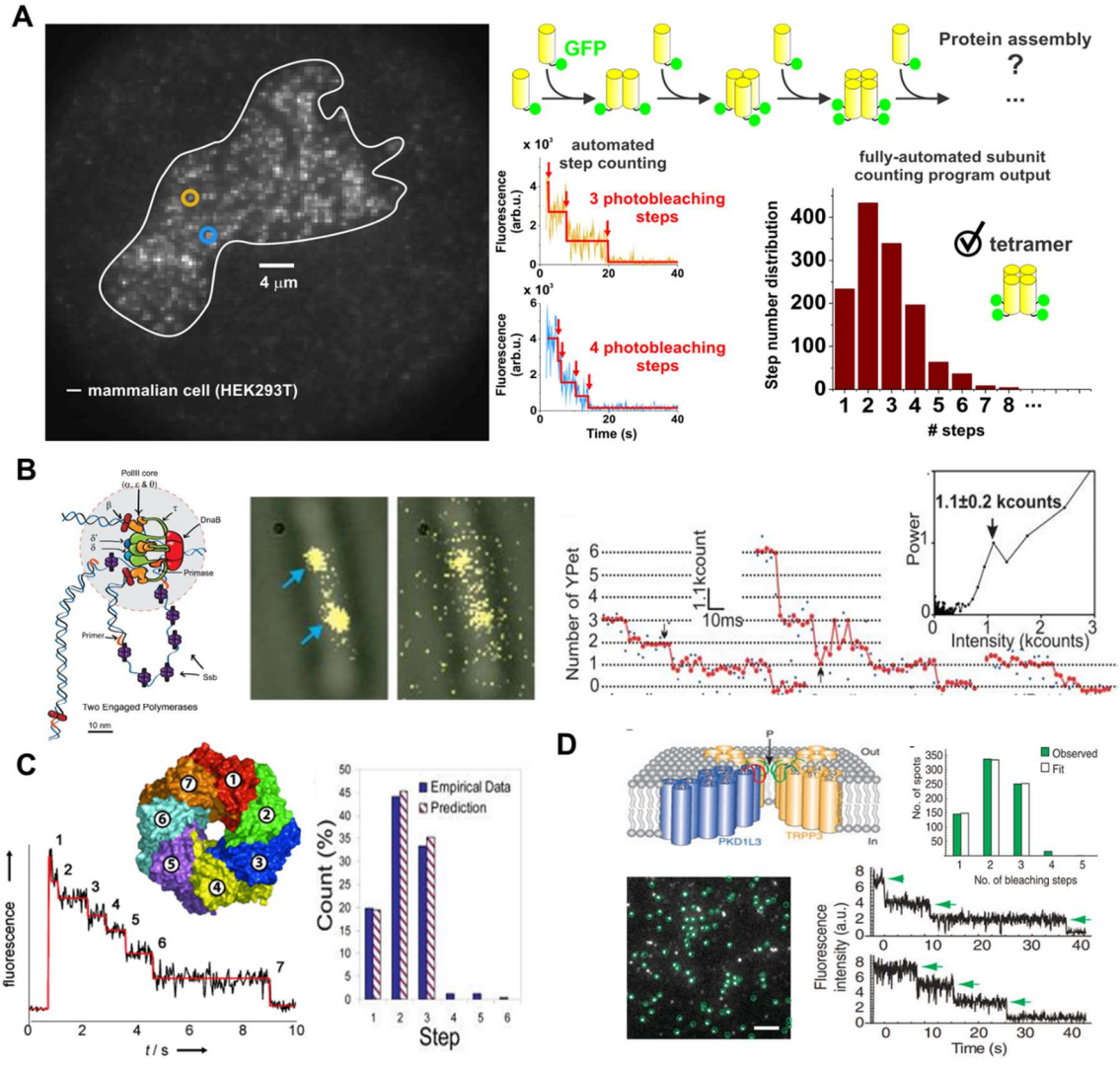

Figure 1.18: Single molecule photobleaching applications. (A) Single Subunit Counting of Membrane Proteins in Mammalian Cells. Adapted with permission from reference [97] (The

American Society for Biochemistry and Molecular Biology, 2012). (B) Stoichiometry of active DNA replication machinery in Escherichia coli. Adapted with permission from reference [97] (The American Association for the Advancement of Science, 2010). (C) Stoichiometry of membrane protein α-haemolysin and leucocidin. Adapted with permission from reference [99] (John Wiley and Sons, 2007). (D) Subunit counting of acid-sensing receptor ion channel complex. Adapted with permission from reference [97] (Nature Publishing Group, 2012)

Despite the considerable power of the technique, many technical reasons complicate the counting of bleaching steps and may cause a deviation of the experimental results from theoretical predictions.[100] Specifically, non-optimal labelling of the structure of interest with the corresponding fluorescent tag. This outcome will give rise to a non-fluorescent fraction in the sample resulting in an underestimation of the subunit number. By counting the bleaching steps of many individual units in the bleached area, a histogram can be constructed, with the number of bleaching steps per particle. In parallel, and upon knowledge of the labeling efficiency, one may estimate the expected distribution of photobleaching steps per particle via the binomial model.[101] The theoretical estimate for the distribution of the dyes attached to the structure can be obtained by solving the following equation:

$$f(n; M, P) = \binom{M}{n} P^n (1-P)^{M-n} = \left(\frac{M!}{n!(M-n)!}\right) P^n (1-P)^{M-n} \qquad [5]$$

Given n_{block}, the probability of n_{dye} attached is:

$$f(n_{dye}; n_{block}, P_{dye}) = \binom{n_{block}}{n_{dye}} {P_{dye}}^{n_{dye}} (1-P_{dye})^{n_{block}-n_{dye}} \qquad [6]$$

Where n_{block} is the number of building blocks in a structure (n_{blocks}= 1, 2,…6), n_{dye} is the number of bleaching steps (number of dyes), and P_{dye} is the experimentally determined labeling efficiency based on the measured absorbance and reported extinction coefficient of the dye-labeled DNA.

Although impossible theoretically, in practice one could observe a small fraction of events with a larger number of bleaching steps than the structure actually has subunits. This could be caused by two complexes “dimerizing” on the surface which can be eliminated by lowering the surface density. It might also be a misassembled structure with extra units or an aggregated structure. Finally, a small movement of the complex (in the case that it is flexible) would change its distance from the surface, translating into changes in illumination intensity experienced by the fluorophore given the exponential decay of the evanescent field with distance (TIR). The movement of

fluorophores will thus introduce additional noise and fluctuations into the recorded traces and will hamper the discrimination of distinct intensity levels.

In order to obtain good trajectories with discrete, clearly observable steps, two requirements must be fulfilled: (i) a long enough time interval should exist prior to a photobleaching event, and (ii) intensity should be large enough such that each photobleaching step may be distinguishable from noise fluctuations.[102] To this end, it is crucial to maximize photon collection, in a given time period, while minimizing possible saturation in the image. Optimizing parameters such as excitation power, exposure time, camera gain, camera frame rate, fluorophore choice, and antifading agents is thus of paramount importance and is discussed in great detail in Chapters 2 and 3.

With organic dyes that display a high intensity and slow photobleaching rates, up to ten bleaching steps can be reliably counted (as demonstrated in Chapter 2 and 3). The limitation of ten steps is due to the fact that the likelihood of missing an event increases exponentially with the number of molecules in a structure. The upper limit for the number of countable molecules can be extended using mathematical aids. Many algorithms have been developed to extract stepwise changes from the intensity traces of fluorescent spots.[97b, 103] One approach towards estimating the number of photobleaching steps is to measure the steps that are visible, calculate the step size of bleaching a single fluorophore using a gamma distribution, and then divide the starting intensity by the step size. However, most of the algorithms encounter difficulty in accounting for the restrictions mentioned above while attempting to extract step-like changes from traces. Since the nature of the restrictions are often unique to each set of data, manual identification of photobleaching steps remains more reliable than an automated approach.

When more complex structures can assemble in variable stoichiometries and in different patterns, it becomes difficult to decrypt their assembly patterns using only one type of dye. They can be discriminated more easily if two or more tags are available, based on the number of bleaching steps, or differential emission intensity of the tags. Clearly, a requisite condition for the analysis of interactions by the colocalization of two colors is a high probability that both fluorophores are present (high labeling efficiency).[104] Non-specific dye binding to the coverslip surface is not very problematic, given that it will not be present in both colors and be then readily excluded during the analysis. Based on the analysis of the intensity histogram, Leake and

coworkers determined the stoichiometry of the components in the DNA replication machinery of the Escherichia coli bacterium.[97c, 105] Also, by developing a single-molecule fluorescence colocalization method Isacoff's group focused on the plasma membrane to simultaneously determine the subunit composition for hundreds of individual protein complexes within an optical patch on a live cell.[97d, 106] (Figure 1.19)

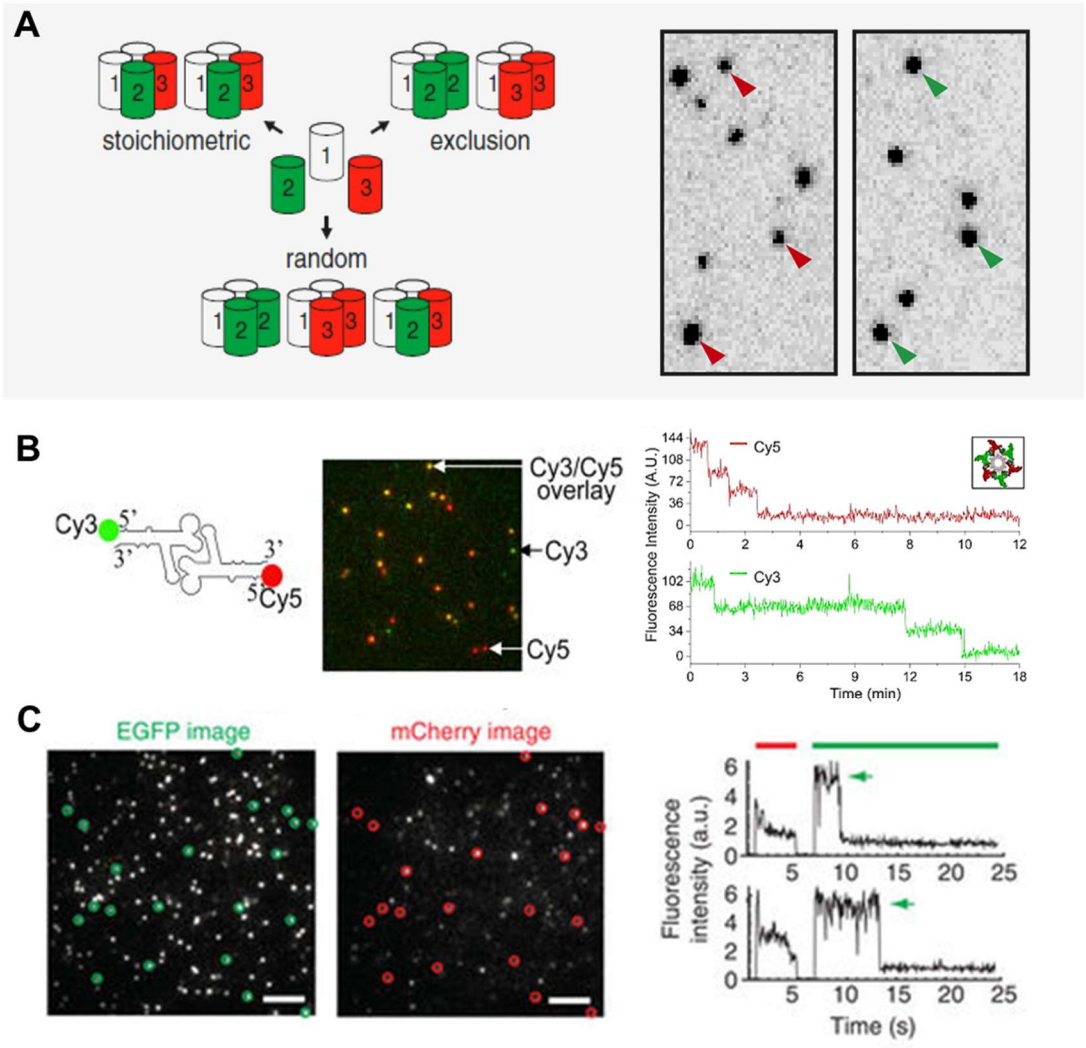

Figure 1.19: Two color photobleaching analysis. (A) Colocalization of green and red in the subunits receptors with different assembly rules: Stoichiometric, random, and exclusive. Adapted with permission from reference [104] (eLife Open Access, 2015) (B-C) 2-color single molecule photobleaching analysis of the DNA replication motor and an acid-sensing receptor ion channel complex. Adapted with permission from reference [106] (Nature Publishing Group, 2012).

1.5.7 Intensity-based analysis: The bigger, the brighter!

For larger structures, the identification of bleaching steps is not always possible, particularly when the noise is high and the time between steps is not sufficiently long to distinguish between them. A straightforward approach for counting subunits in this case would be to measure the ratio of the fluorescence intensities of a complex to a standard dye that, ideally, is similar to the structure of interest and imaged under the same conditions for proper comparison purposes.[107] The main condition required to achieve accurate measurements is a homogeneous illumination across the whole field. Laser power, room and microscope temperature, camera, and image acquisition settings should be all kept constant during such an experiment. The only variable parameter is the exposure time (the fluorescence intensity recorded by the camera is directly proportional to the exposure time within the linear range of the camera) which may be corrected to keep the signal to noise ratio high and more importantly to avoid saturation.[108] The ratio method of quantification can be used to count the changing number of building blocks present over time as a result of their accumulation or dispersal and thus to extract kinetic information. Time-lapse quantification requires correction for the photobleaching over time. Thus, the number of molecules of each complex and their relative stoichiometries can be obtained using the ratio method at one or many time points. If a sufficiently large number of events are collected, the average intensity levels, representing the distinct numbers of fluorescent tags and their occupancies, can be extracted from the histogram of the measured emission intensities. In essence, with this method a much greater number of subunits can be counted compared to the photobleaching method. This approach was used by many groups to evaluate protein composition and stoichiometry. For example, the number of Cse4p proteins (modified histone) in microtubule kinetochore clusters have been measured using three different fluorescent standards. These included the in vitro use of individual EGFP (enhanced green fluorescent protein) molecules to measure the mean number Cse4-GFPs, as well as representative proteins for inner and outer kinetochore complexes within a budding yeast kinetochore (Figure 1.20).[107a]

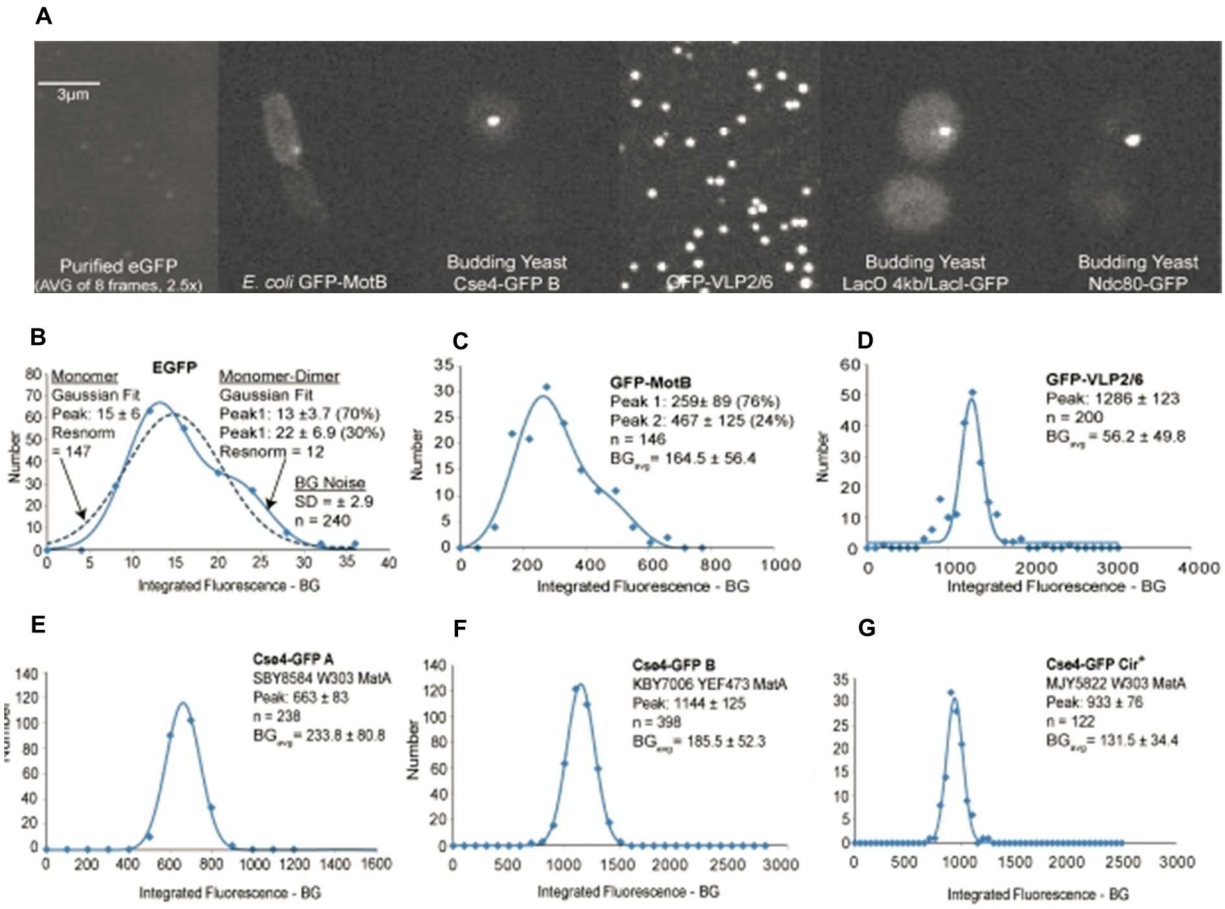

Figure 1.20: Fluorescence intensity of Cse4-GFP within a cluster of kinetochores at anaphase compared with the standards and potential standards, and Ndc80-GFP used in our experiments. (A) Images are sorted by increasing brightness. Bar, 3 µm. (B–G) Mean values ± SD obtained from Gaussian curve fits to histograms of measured values of integrated fluorescent intensity**.** Adapted with permission from reference [107] (The Rockefeller University Press, 2011)

Until recently, ordinary fluorescence imaging methods have not played a major role in the investigation of DNA nanostructures, simply because these structures are usually much smaller than the diffraction limit. This has changed, however, with the advancement of super-resolution microscopy or 'nanoscopy' as will be discussed in the next section.

1.5.8 Super-resolution techniques: a revolution in resolution

In the early 1990s, many theoretical studies were proposed to ultimately allow imaging beyond the classical diffraction limit using far-field fluorescence microscopy.[109] The principle of super-resolution imaging is based on a clever combination of two capabilities: (i) estimating the center position of single molecules with a precision well beyond the diffraction limit by fitting the point

spread function (PSF) of the fluorescent spot. Here, the precision of the localization scales with the inverse square of the number of detected photons and (ii) the actively controlled switching and sampling of sparse subsets of the fluorescent labels such that the PSFs of individual molecules do not overlap.[110] This switching behaviour allows the fluorescent labels to be localized consecutively over time (Figure 1.21A). Some approaches require new technologies such as STED microscopy, while others, such as STORM and PALM microscopies, rely on existing ones while utilizing stochastic blinking.

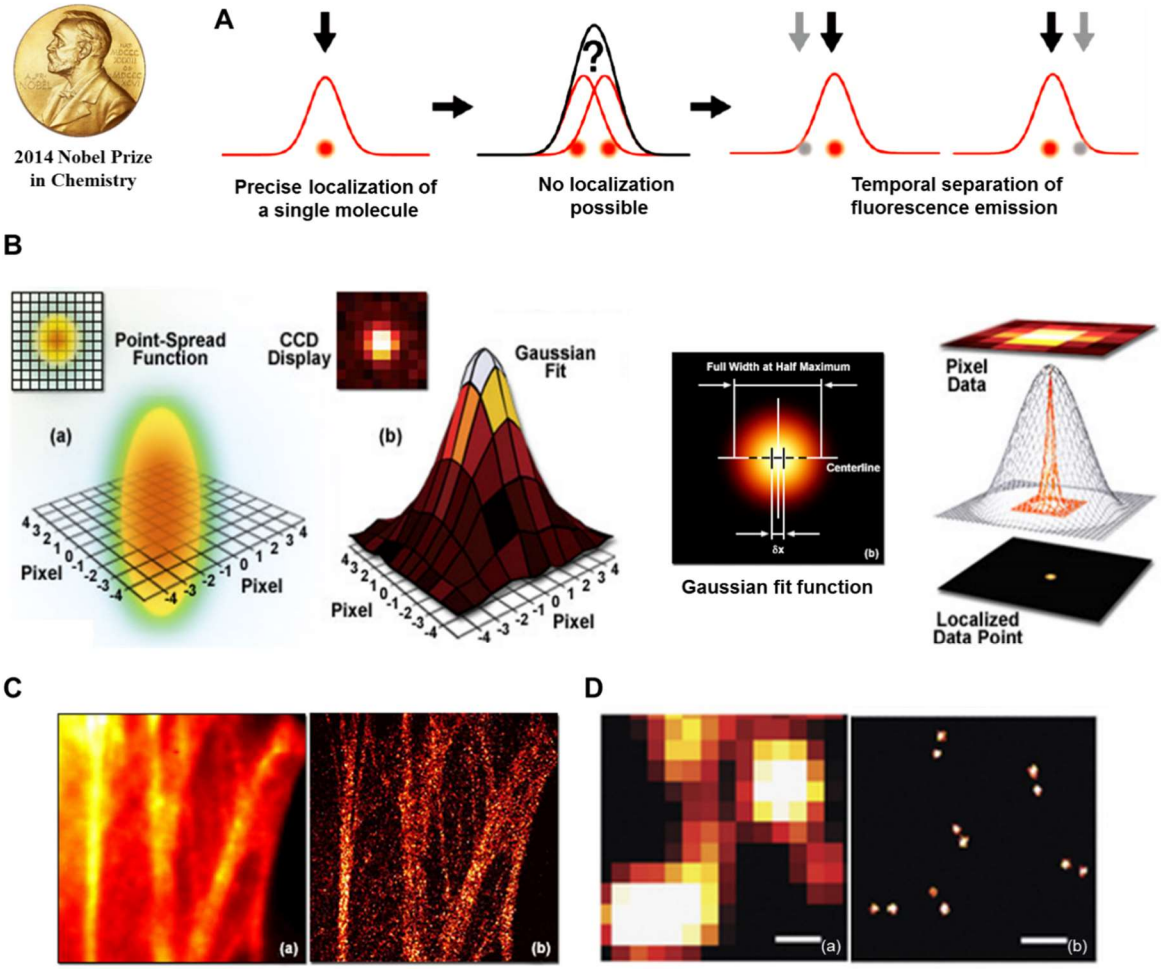

Figure 1.21: Super-resolution imaging. (A) Stochastic readout principle for super-resolution fluorescence microscopy. Using temporal separation of fluorescence emission by stochastically switching fluorescence between ON and OFF states, the locations of the molecules can be reconstructed in a super-resolved image. (B) Illustrated in this figure are the steps involved in localizing single molecules with high precision by fitting the point-spread function to a Gaussian function. (C-D) Representative TIRF images and the corresponding super-resolution images of actin filaments (C) and DNA origami (D) as test structures. (Scale bar 300 nm) Adapted with permission from reference [121] (Nature Publishing Group, 2014).

One of the early examples of a super-resolution technique is stimulated emission depletion (STED) microscopy.[111] Using a laser-scanning microscope, each spot of the image is illuminated by an excitation laser overlaid by another, red-shifted laser which has a doughnut-shaped intensity profile. This second laser suppresses fluorescence emission from fluorophores located in the doughnut area and thus 'focuses' the active excitation area below the diffraction limit. This allows imaging with a lateral resolution of approximately 20 nm.[112]

In 2006, Eric Betzig and Harald Hess used photoactivatable green fluorescent proteins (PA-GFP) along with other photo-switchable fluorescent proteins as an active control mechanism and termed the method Photo Activated Localization Microscopy (PALM).[113] Simultaneously, other stochastic reconstruction methods quickly appeared such as stochastic optical reconstruction microscopy (STORM)[114], point accumulation for imaging in nanoscale topography (PAINT)[115], blink microscopy (BM)[116], and nanometer accuracy by stochastic chemical reactions (NASCA) microscopy[117]. All of these methods rely on stochastic photoswitching of fluorophores such as cyanine dyes between ON and OFF states and localization of single molecules within a diffraction-limited area (Figure 1.21B).[118] Another area of interest is the extension of super-resolution microscopy beyond two spatial transverse dimensions to include three dimensions. Some researchers have pursued astigmatic imaging, multi-plane imaging or more recently pupil-plane optical Fourier processing 3D microscopy.[119] All of these developments allowed the resolution of the 2D and 3D morphology of nanoscopic cellular substructures including the molecular organization of proteins within structures such as actin and microtubule networks.[120]

The application of super-resolution microscopy methods to the arena of DNA nanotechnology has only started recently. In fact, the nanometer-precise addressability of DNA nanostructures makes them extremely attractive substrates for super-resolution imaging.[121] In 2009, Steinhauer et al. were the first to use super-resolution fluorescence microscopy to image single-layer DNA origami rectangle modified with two single fluorophores at a distance of approximately 90 nm (Figure 1.21C-D).[122] Very recently, Yin and co-workers used DNA-PAINT microscopy to visualize the designed 3D patterns of vertices in DNA-based polyhedra which had expected heights suggesting that the solution shape of the structures is maintained during surface immobilization and imaging.[123] In essence, DNA-PAINT uses thermally-driven binding and unbinding of engineered DNA sequences to induce fluorophore blinking, which ultimately yields images with

sub-10-nm spatial resolution. Of course, the imaging remains time-sequential and best for quasi-static structures or fixed cells, but indeed significant progress has been made in order to increase the imaging speed and be able to extend these methods to elucidate dynamics within nanostructures.

1.6 Context and scope of this thesis

"firmitas, utilitas, venustas….solid, useful, beautiful"

Louis Sullivan

DNA is a powerful, reliable and programmable nanofabrication building block. Taking advantage of its nanoscale features, researchers have used it extensively to generate complex 2D, 3D and reconfigurable assemblies with a number of recent potential applications. *Could much more complex DNA-nanostructure designs be made in the future?* Yes, but many technical challenges shall be first overcome, the most significant of which is the high error rate of self-assembly. Indeed, the more complex the assembly design is, the more error-prone is the product. This constitutes a major problem for the application of DNA-based structures in dynamic devices such as machines, motors, robots, and computers, where even small errors in assembly can drastically affect performance. Therefore, quantitative tools for analysing defect occurrence in complex DNA nanostructures are needed.

Fluorescence-based techniques offer a unique set of capabilities to study supramolecular structures and would enable the rational development of DNA-made devices. However, valuable information regarding side products, non-reactive and malfunctioning devices is often lost in bulk measurements. Single molecule fluorescence (SMF) is thus the method of choice for the *in situ* study of structure, dynamics, integrity, and operation of DNA-made devices. The research covered in this thesis is specifically focused on demonstrating how different single molecule fluorescence methodologies can be utilized to provide a quantitative and informative feedback on the building blocks and final products of DNA self-assembly. It is also focused on implementing SMF methods towards gaining a mature understanding of the kinetics and structural dynamics within and between the DNA building blocks. Conceptually, this research can be divided into four main parts: (i) synthesis optimization (Chapter 2), (ii) structural characterization (Chapter 3), (iii) monitoring dynamic structures (Chapter 4) and (iv) structural dynamics (Chapter 5).

In Chapter 2, bottom-up self-assembly methods developed in SMF were used to control the positioning of rungs along the backbone of the nanotubes, minimize the polydispersity in their manufacture and reduce the building costs. SMF was used in parallel to visualize and characterize the new architectures. Specifically, a solid-phase synthesis methodology was realized, in which distinct rungs can be incorporated in a predetermined manner, through a cyclic scheme starting from a 'foundation rung' specifically bound to the surface. Each rung is orthogonally addressable. Using fluorescently tagged rungs, SMF studies demonstrated the robustness and structural fidelity of the constructs and confirmed the incorporation of the rungs in quantitative yield at each step of the cycle. When combined, the solid-phase synthesis strategy and its visualization through SMF provide good promise for the production of custom-made DNA nanotubes.

In Chapter 3, a SMF method was developed to assign polydispersity, sequence pattern and stoichiometry for different DNA nanotubes systems. Working with fluorescence intensity-time trajectories acquired for doubly labelled DNA nanotubes bearing a green Cy3 and red Cy5/or ATTO647N emissive dyes along their backbone, and upon monitoring single photobleaching steps in both colors; key structural parameters were successfully retrieved of four DNA nanotube systems differing in their preparation method. An algorithm that automatically counts photobleaching steps in both channels and assigns them to a given nanotube was developed to facilitate the selection and interpretation of data. Automation allowed analysis of large two-color datasets consisting of hundreds of nanotubes monitored in parallel over time through thousands of frames. This approach allows the selection and isolation of every nanostructure with its molecular profile. In addition, it provides a rapid and systematic way of accurately assessing the outcome of synthetic work building supramolecular systems. The method described herein, while developed for DNA nanotubes, will be instrumental to many research groups synthesizing large supramolecular structures or studying naturally occurring ones.

In Chapter 4, SM-based TIRF microscopy methods was employed to investigate the programmable introduction of DNA structural changes within the dye-labelled repeat units of DNA nanotubes designed and synthesized in the Sleiman lab. Using single molecule photobleaching studies on surface-immobilized surface nanotubes, the number of Cy3-tagged repeat units was first quantified within a nanotube structure at the initial (open tube) and the final

(fully assembled tube) steps of the tube-assembly, to shed light on a plausible assembly mechanism. Second, the effect of base-deletion on the nanotube structure was investigated. DNA strands were site-specifically introduced to shorten two sides of the nanotubes, while keeping intact and strain free the length of the third side. Possibly, a length mismatch in each repeat unit could induce distortion/bending of the nanotubes generated in solution, until it is significant enough to compromise the stability and shorten the nanotube, as measured by photobleaching experiments. Using two-color single molecule photobleaching studies and strand displacement experiments, the presence of the loop strand within the structures was validated, and the possibility that an initially long single-stranded nanotube can be fragmented and shortened upon addition of length mismatched strands was verified.

In Chapter 5, SMF methodologies were used to investigate the dynamics and analyze defect occurrence within DNA nanostructures. Two types of structures including DNA nanotube dimers and oligomers (described in Chapter 4) were chosen for this study. The unique structure of the utilized nanotubes can be reversibly switched from a ds to a ss DNA form using strand displacement strategies. TIRF microscopy was employed to examine, in real time, the "peeling off" of the linking strands from a surface-bound DNA nanotube. Survival lifetimes studies and two-color colocalization intensity analysis uncovered the structural cooperativity and evaluated the robustness of the DNA assembly. This demonstrates how SMF methodologies are uniquely poised to understand and tackle the vexing dynamic nature of DNA strand-displacement-based devices; to enable a continuous and systematic fabrication of potential actuators, amplifiers and computational tools with improved performances.

1.7 References

1. Biju, V., Chemical modifications and bioconjugate reactions of nanomaterials for sensing, imaging, drug delivery and therapy. *Chemical Society Reviews* **2014,** *43* (3), 744-764.
2. Lee, J.; Mahendra, S.; Alvarez, P. J. J., Nanomaterials in the Construction Industry: A Review of Their Applications and Environmental Health and Safety Considerations. *ACS Nano* **2010,** *4* (7), 3580-3590.
3. Hobson, D. W., Commercialization of nanotechnology. *Wiley Interdisciplinary Reviews: Nanomedicine and Nanobiotechnology* **2009,** *1* (2), 189-202.
4. Gondal, M. A.; Dastageer, M. A.; Khalil, A., Synthesis of nano-WO3 and its catalytic activity for enhanced antimicrobial process for water purification using laser induced photo-catalysis. *Catalysis Communications* **2009,** *11* (3), 214-219.
5. (a) Heath, J. R., Nanotechnologies for biomedical science and translational medicine. *Proceedings of the National Academy of Sciences* **2015,** *112* (47), 14436-14443; (b) Holzinger, M.; Le Goff, A.; Cosnier, S., Nanomaterials for biosensing applications: a review. *Frontiers in Chemistry* **2014,** *2*, 63.
6. Hashimoto, M.; Tong, R.; Kohane, D. S., Microdevices for Nanomedicine. *Molecular Pharmaceutics* **2013,** *10* (6), 2127-2144.
7. Chong, T. C.; Hong, M. H.; Shi, L. P., Laser precision engineering: from microfabrication to nanoprocessing. *Laser & Photonics Reviews* **2010,** *4* (1), 123-143.
8. (a) Kim, J.; Piao, Y.; Hyeon, T., Multifunctional nanostructured materials for multimodal imaging, and simultaneous imaging and therapy. *Chemical Society Reviews* **2009,** *38* (2), 372-390; (b) Hickey, R. J.; Haynes, A. S.; Kikkawa, J. M.; Park, S.-J., Controlling the Self-Assembly Structure of Magnetic Nanoparticles and Amphiphilic Block-Copolymers: From Micelles to Vesicles. *Journal of the American Chemical Society* **2011,** *133* (5), 1517-1525.
9. Betzig, E., Single Molecules, Cells, and Super-Resolution Optics (Nobel Lecture). *Angewandte Chemie International Edition* **2015,** *54* (28), 8034-8053.
10. Binnig, G.; Rohrer, H.; Gerber, C.; Weibel, E., Surface Studies by Scanning Tunneling Microscopy. *Physical Review Letters* **1982,** *49* (1), 57-61.
11. Custance, O.; Perez, R.; Morita, S., Atomic force microscopy as a tool for atom manipulation. *Nat Nano* **2009,** *4* (12), 803-810.
12. Moerner, W. E.; Fromm, D. P., Methods of single-molecule fluorescence spectroscopy and microscopy. *Review of Scientific Instruments* **2003,** *74* (8), 3597-3619.
13. Möckl, L.; Lamb, D. C.; Bräuchle, C., Super-resolved Fluorescence Microscopy: Nobel Prize in Chemistry 2014 for Eric Betzig, Stefan Hell, and William E. Moerner. *Angewandte Chemie International Edition* **2014,** *53* (51), 13972-13977.
14. Seeman, N. C., DNA in a material world. *Nature* **2003,** *421* (6921), 427-431.
15. Merrifield, B., Solid phase synthesis. *Bioscience Reports 5* (5), 353-376.
16. (a) Lutz, J.-F.; Ouchi, M.; Liu, D. R.; Sawamoto, M., Sequence-Controlled Polymers. *Science* **2013,** *341* (6146); (b) Goldberg, M., BioFab: Applying Moore's Law to DNA Synthesis. *Industrial Biotechnology* **2013,** *9* (1), 10-12.
17. Aldaye, F. A.; Palmer, A. L.; Sleiman, H. F., Assembling Materials with DNA as the Guide. *Science* **2008,** *321* (5897), 1795-1799.
18. Seeman, N. C., Nucleic acid junctions and lattices. *Journal of Theoretical Biology* **1982,** *99* (2), 237-247.

19. Kallenbach, N. R.; Ma, R.-I.; Seeman, N. C., An immobile nucleic acid junction constructed from oligonucleotides. *Nature* **1983,** *305* (5937), 829-831.
20. Chen, J.; Seeman, N. C., Synthesis from DNA of a molecule with the connectivity of a cube. *Nature* **1991,** *350* (6319), 631-633.
21. Fu, T. J.; Seeman, N. C., DNA double-crossover molecules. *Biochemistry* **1993,** *32* (13), 3211-3220.
22. Rothemund, P. W. K.; Ekani-Nkodo, A.; Papadakis, N.; Kumar, A.; Fygenson, D. K.; Winfree, E., Design and Characterization of Programmable DNA Nanotubes. *Journal of the American Chemical Society* **2004,** *126* (50), 16344-16352.
23. Yan, H.; Park, S. H.; Finkelstein, G.; Reif, J. H.; LaBean, T. H., DNA-Templated Self-Assembly of Protein Arrays and Highly Conductive Nanowires. *Science* **2003,** *301* (5641), 1882-1884.
24. He, Y.; Ye, T.; Su, M.; Zhang, C.; Ribbe, A. E.; Jiang, W.; Mao, C., Hierarchical self-assembly of DNA into symmetric supramolecular polyhedra. *Nature* **2008,** *452* (7184), 198-201.
25. Wei, B.; Dai, M.; Yin, P., Complex shapes self-assembled from single-stranded DNA tiles. *Nature* **2012,** *485* (7400), 623-626.
26. Ke, Y.; Ong, L. L.; Sun, W.; Song, J.; Dong, M.; Shih, W. M.; Yin, P., DNA brick crystals with prescribed depths. *Nat Chem* **2014,** *6* (11), 994-1002.
27. Shih, W. M.; Quispe, J. D.; Joyce, G. F., A 1.7-kilobase single-stranded DNA that folds into a nanoscale octahedron. *Nature* **2004,** *427* (6975), 618-621.
28. Rothemund, P. W. K., Folding DNA to create nanoscale shapes and patterns. *Nature* **2006,** *440* (7082), 297-302.
29. Andersen, E. S.; Dong, M.; Nielsen, M. M.; Jahn, K.; Subramani, R.; Mamdouh, W.; Golas, M. M.; Sander, B.; Stark, H.; Oliveira, C. L. P.; Pedersen, J. S.; Birkedal, V.; Besenbacher, F.; Gothelf, K. V.; Kjems, J., Self-assembly of a nanoscale DNA box with a controllable lid. *Nature* **2009,** *459* (7243), 73-76.
30. Shih, W. M.; Lin, C., Knitting complex weaves with DNA origami. *Current opinion in structural biology* **2010,** *20* (3), 276-282.
31. Douglas, S. M.; Dietz, H.; Liedl, T.; Hogberg, B.; Graf, F.; Shih, W. M., Self-assembly of DNA into nanoscale three-dimensional shapes. *Nature* **2009,** *459* (7245), 414-418.
32. Iinuma, R.; Ke, Y.; Jungmann, R.; Schlichthaerle, T.; Woehrstein, J. B.; Yin, P., Polyhedra Self-Assembled from DNA Tripods and Characterized with 3D DNA-PAINT. *Science* **2014**.
33. Benson, E.; Mohammed, A.; Gardell, J.; Masich, S.; Czeizler, E.; Orponen, P.; Hogberg, B., DNA rendering of polyhedral meshes at the nanoscale. *Nature* **2015,** *523* (7561), 441-444.
34. Zhang, F.; Jiang, S.; Wu, S.; Li, Y.; Mao, C.; Liu, Y.; Yan, H., Complex wireframe DNA origami nanostructures with multi-arm junction vertices. *Nat Nano* **2015,** *10* (9), 779-784.
35. Han, D.; Pal, S.; Nangreave, J.; Deng, Z.; Liu, Y.; Yan, H., DNA Origami with Complex Curvatures in Three-Dimensional Space. *Science* **2011,** *332* (6027), 342-346.
36. Gothelf, K. V.; LaBean, T. H., DNA-programmed assembly of nanostructures. *Organic & Biomolecular Chemistry* **2005,** *3* (22), 4023-4037.
37. Aldaye, F. A.; Sleiman, H. F., Sequential Self-Assembly of a DNA Hexagon as a Template for the Organization of Gold Nanoparticles. *Angewandte Chemie International Edition* **2006,** *45* (14), 2204-2209.
38. Aldaye, F. A.; Lo, P. K.; Karam, P.; McLaughlin, C. K.; Cosa, G.; Sleiman, H. F., Modular construction of DNA nanotubes of tunable geometry and single- or double-stranded character. *Nat Nano* **2009,** *4* (6), 349-352.

39. Tanaka, F.; Mochizuki, T.; Liang, X.; Asanuma, H.; Tanaka, S.; Suzuki, K.; Kitamura, S.-i.; Nishikawa, A.; Ui-Tei, K.; Hagiya, M., Robust and Photocontrollable DNA Capsules Using Azobenzenes. *Nano Letters* **2010,** *10* (9), 3560-3565.
40. Aldaye, F. A.; Sleiman, H. F., Guest-Mediated Access to a Single DNA Nanostructure from a Library of Multiple Assemblies. *Journal of the American Chemical Society* **2007,** *129* (33), 10070-10071.
41. Clever, G. H.; Kaul, C.; Carell, T., DNA–Metal Base Pairs. *Angewandte Chemie International Edition* **2007,** *46* (33), 6226-6236.
42. Edwardson, T. G. W.; Carneiro, K. M. M.; McLaughlin, C. K.; Serpell, C. J.; Sleiman, H. F., Site-specific positioning of dendritic alkyl chains on DNA cages enables their geometry-dependent self-assembly. *Nat Chem* **2013,** *5* (10), 868-875.
43. Yurke, B.; Turberfield, A. J.; Mills, A. P.; Simmel, F. C.; Neumann, J. L., A DNA-fuelled molecular machine made of DNA. *Nature* **2000,** *406* (6796), 605-608.
44. Nielsen, P.; Egholm, M.; Berg, R.; Buchardt, O., Sequence-selective recognition of DNA by strand displacement with a thymine-substituted polyamide. *Science* **1991,** *254* (5037), 1497-1500.
45. Zhang, D. Y.; Seelig, G., Dynamic DNA nanotechnology using strand-displacement reactions. *Nat Chem* **2011,** *3* (2), 103-113.
46. Shin, J.-S.; Pierce, N. A., A Synthetic DNA Walker for Molecular Transport. *Journal of the American Chemical Society* **2004,** *126* (35), 10834-10835.
47. Liedl, T.; Simmel, F. C., Switching the Conformation of a DNA Molecule with a Chemical Oscillator. *Nano Letters* **2005,** *5* (10), 1894-1898.
48. Endo, M.; Xing, X.; Zhou, X.; Emura, T.; Hidaka, K.; Tuesuwan, B.; Sugiyama, H., Single-Molecule Manipulation of the Duplex Formation and Dissociation at the G-Quadruplex/i-Motif Site in the DNA Nanostructure. *ACS Nano* **2015,** *9* (10), 9922-9929.
49. Han, D.; Huang, J.; Zhu, Z.; Yuan, Q.; You, M.; Chen, Y.; Tan, W., Molecular engineering of photoresponsive three-dimensional DNA nanostructures. *Chemical Communications* **2011,** *47* (16), 4670-4672.
50. Douglas, S. M.; Bachelet, I.; Church, G. M., A Logic-Gated Nanorobot for Targeted Transport of Molecular Payloads. *Science* **2012,** *335* (6070), 831-834.
51. Gerling, T.; Wagenbauer, K. F.; Neuner, A. M.; Dietz, H., Dynamic DNA devices and assemblies formed by shape-complementary, non–base pairing 3D components. *Science* **2015,** *347* (6229), 1446-1452.
52. Niemeyer, C. M.; Koehler, J.; Wuerdemann, C., DNA-Directed Assembly of Bienzymic Complexes from In Vivo Biotinylated NAD(P)H:FMN Oxidoreductase and Luciferase. *ChemBioChem* **2002,** *3* (2-3), 242-245.
53. Fu, J.; Yang, Y. R.; Johnson-Buck, A.; Liu, M.; Liu, Y.; Walter, N. G.; Woodbury, N. W.; Yan, H., Multi-enzyme complexes on DNA scaffolds capable of substrate channelling with an artificial swinging arm. *Nat Nano* **2014,** *9* (7), 531-536.
54. Bellot, G.; McClintock, M. A.; Chou, J. J.; Shih, W. M., DNA Nanotubes for NMR Structure Determination of Membrane Proteins. *Nature protocols* **2013,** *8* (4), 10.1038/nprot.2013.037.
55. Malo, J.; Mitchell, J. C.; Vénien-Bryan, C.; Harris, J. R.; Wille, H.; Sherratt, D. J.; Turberfield, A. J., Engineering a 2D Protein–DNA Crystal. *Angewandte Chemie International Edition* **2005,** *44* (20), 3057-3061.
56. Knudsen, J. B.; Liu, L.; Bank Kodal, A. L.; Madsen, M.; Li, Q.; Song, J.; Woehrstein, J. B.; Wickham, S. F. J.; Strauss, M. T.; Schueder, F.; Vinther, J.; Krissanaprasit, A.; Gudnason, D.; Smith, A. A. A.; Ogaki, R.; Zelikin, A. N.; Besenbacher, F.; Birkedal, V.; Yin, P.; Shih, W. M.;

Jungmann, R.; Dong, M.; Gothelf, K. V., Routing of individual polymers in designed patterns. *Nat Nano* **2015,** *10* (10), 892-898.
57. Sun, W.; Boulais, E.; Hakobyan, Y.; Wang, W. L.; Guan, A.; Bathe, M.; Yin, P., Casting inorganic structures with DNA molds. *Science* **2014,** *346* (6210).
58. Schreiber, R.; Luong, N.; Fan, Z.; Kuzyk, A.; Nickels, P. C.; Zhang, T.; Smith, D. M.; Yurke, B.; Kuang, W.; Govorov, A. O.; Liedl, T., Chiral plasmonic DNA nanostructures with switchable circular dichroism. *Nat Commun* **2013,** *4*.
59. Zhou, C.; Duan, X.; Liu, N., A plasmonic nanorod that walks on DNA origami. *Nat Commun* **2015,** *6*.
60. Acuna, G. P.; Möller, F. M.; Holzmeister, P.; Beater, S.; Lalkens, B.; Tinnefeld, P., Fluorescence Enhancement at Docking Sites of DNA-Directed Self-Assembled Nanoantennas. *Science* **2012,** *338* (6106), 506-510.
61. (a) Langecker, M.; Arnaut, V.; Martin, T. G.; List, J.; Renner, S.; Mayer, M.; Dietz, H.; Simmel, F. C., Synthetic Lipid Membrane Channels Formed by Designed DNA Nanostructures. *Science* **2012,** *338* (6109), 932-936; (b) Lee, H.; Lytton-Jean, A. K. R.; Chen, Y.; Love, K. T.; Park, A. I.; Karagiannis, E. D.; Sehgal, A.; Querbes, W.; Zurenko, C. S.; Jayaraman, M.; Peng, C. G.; Charisse, K.; Borodovsky, A.; Manoharan, M.; Donahoe, J. S.; Truelove, J.; Nahrendorf, M.; Langer, R.; Anderson, D. G., Molecularly self-assembled nucleic acid nanoparticles for targeted in vivo siRNA delivery. *Nat Nano* **2012,** *7* (6), 389-393.
62. Funke, J. J.; Dietz, H., Placing molecules with Bohr radius resolution using DNA origami. *Nat Nano* **2016,** *11* (1), 47-52.
63. Yan, H.; LaBean, T. H.; Feng, L.; Reif, J. H., Directed nucleation assembly of DNA tile complexes for barcode-patterned lattices. *Proceedings of the National Academy of Sciences* **2003,** *100* (14), 8103-8108.
64. Lin, C.; Liu, Y.; Yan, H., Self-Assembled Combinatorial Encoding Nanoarrays for Multiplexed Biosensing. *Nano Letters* **2007,** *7* (2), 507-512.
65. Lo, P. K.; Karam, P.; Aldaye, F. A.; McLaughlin, C. K.; Hamblin, G. D.; Cosa, G.; Sleiman, H. F., Loading and selective release of cargo in DNA nanotubes with longitudinal variation. *Nat Chem* **2010,** *2* (4), 319-328.
66. Fakhoury, J. J.; McLaughlin, C. K.; Edwardson, T. W.; Conway, J. W.; Sleiman, H. F., Development and Characterization of Gene Silencing DNA Cages. *Biomacromolecules* **2014,** *15* (1), 276-282.
67. Erben, C. M.; Goodman, R. P.; Turberfield, A. J., Single-Molecule Protein Encapsulation in a Rigid DNA Cage. *Angewandte Chemie* **2006,** *118* (44), 7574-7577.
68. Stephanopoulos, N.; Freeman, R.; North, H. A.; Sur, S.; Jeong, S. J.; Tantakitti, F.; Kessler, J. A.; Stupp, S. I., Bioactive DNA-Peptide Nanotubes Enhance the Differentiation of Neural Stem Cells Into Neurons. *Nano Letters* **2015,** *15* (1), 603-609.
69. Pinheiro, A. V.; Han, D.; Shih, W. M.; Yan, H., Challenges and opportunities for structural DNA nanotechnology. *Nat Nano* **2011,** *6* (12), 763-772.
70. Deniz, A. A.; Mukhopadhyay, S.; Lemke, E. A., Single-molecule biophysics: at the interface of biology, physics and chemistry. *Journal of The Royal Society Interface* **2008,** *5* (18), 15-45.
71. Tsukanov, R.; Tomov, T. E.; Liber, M.; Berger, Y.; Nir, E., Developing DNA Nanotechnology Using Single-Molecule Fluorescence. *Accounts of Chemical Research* **2014,** *47* (6), 1789-1798.
72. Moerner, W. E., Nobel Lecture: Single-molecule spectroscopy, imaging, and photocontrol: Foundations for super-resolution microscopy*. *Reviews of Modern Physics* **2015,** *87* (4), 1183-1212.

73. Wolf, D. E., Chapter 4 - Fundamentals of Fluorescence and Fluorescence Microscopy. In *Methods in Cell Biology*, Greenfield, S.; David, E. W., Eds. Academic Press: 2013; Vol. Volume 114, pp 69-97.
74. Glembockyte, V.; Lincoln, R.; Cosa, G., Cy3 Photoprotection Mediated by Ni2+ for Extended Single-Molecule Imaging: Old Tricks for New Techniques. *Journal of the American Chemical Society* **2015,** *137* (3), 1116-1122.
75. Aitken, C. E.; Marshall, R. A.; Puglisi, J. D., An Oxygen Scavenging System for Improvement of Dye Stability in Single-Molecule Fluorescence Experiments(). *Biophysical Journal* **2008,** *94* (5), 1826-1835.
76. Zheng, Q.; Juette, M. F.; Jockusch, S.; Wasserman, M. R.; Zhou, Z.; Altman, R. B.; Blanchard, S. C., Ultra-stable organic fluorophores for single-molecule research. *Chemical Society Reviews* **2014,** *43* (4), 1044-1056.
77. Axelrod, D., Total Internal Reflection Fluorescence Microscopy in Cell Biology. *Traffic* **2001,** *2* (11), 764-774.
78. Trache, A.; Meininger, G. A., Total Internal Reflection Fluorescence (TIRF) Microscopy. In *Current Protocols in Microbiology*, John Wiley & Sons, Inc.: 2005.
79. Krieger, J. W.; Singh, A. P.; Bag, N.; Garbe, C. S.; Saunders, T. E.; Langowski, J.; Wohland, T., Imaging fluorescence (cross-) correlation spectroscopy in live cells and organisms. *Nat. Protocols* **2015,** *10* (12), 1948-1974.
80. Funatsu, T.; Harada, Y.; Tokunaga, M.; Saito, K.; Yanagida, T., Imaging of single fluorescent molecules and individual ATP turnovers by single myosin molecules in aqueous solution. *Nature* **1995,** *374* (6522), 555-559.
81. Lu, H. P.; Xun, L.; Xie, X. S., Single-Molecule Enzymatic Dynamics. *Science* **1998,** *282* (5395), 1877-1882.
82. (a) Chen, J.; Zhang, Z.; Li, L.; Chen, B.-C.; Revyakin, A.; Hajj, B.; Legant, W.; Dahan, M.; Lionnet, T.; Betzig, E.; Tjian, R.; Liu, Z., Single-molecule Dynamics of Enhanceosome Assembly in Embryonic Stem Cells. *Cell* **2014,** *156* (6), 1274-1285; (b) Peterson, E. M.; Manhart, M. W.; Harris, J. M., Single-Molecule Fluorescence Imaging of Interfacial DNA Hybridization Kinetics at Selective Capture Surfaces. *Analytical Chemistry* **2016,** *88* (2), 1345-1354.
83. Wang, F.; Redding, S.; Finkelstein, I. J.; Gorman, J.; Reichman, D. R.; Greene, E. C., The promoter-search mechanism of Escherichia coli RNA polymerase is dominated by three-dimensional diffusion. *Nat Struct Mol Biol* **2013,** *20* (2), 174-181.
84. Liu, H.; Chen, Y.; He, Y.; Ribbe, A. E.; Mao, C., Approaching The Limit: Can One DNA Oligonucleotide Assemble into Large Nanostructures? *Angewandte Chemie* **2006,** *118* (12), 1976-1979.
85. Hariadi, R. F.; Yurke, B.; Winfree, E., Thermodynamics and kinetics of DNA nanotube polymerization from single-filament measurements. *Chemical Science* **2015,** *6* (4), 2252-2267.
86. Marko, R. A.; Liu, H.-W.; Ablenas, C. J.; Ehteshami, M.; Götte, M.; Cosa, G., Binding Kinetics and Affinities of Heterodimeric versus Homodimeric HIV-1 Reverse Transcriptase on DNA–DNA Substrates at the Single-Molecule Level. *The Journal of Physical Chemistry B* **2013,** *117* (16), 4560-4567.
87. Forster, T., Energiewanderung und Fluoreszenz. *Naturwissenschaften 33* (6), 166-175.
88. Sun, Y.; Wallrabe, H.; Seo, S.-A.; Periasamy, A., FRET microscopy in 2010: The legacy of Theodor Förster on the 100th anniversary of his birth. *Chemphyschem : a European journal of chemical physics and physical chemistry* **2011,** *12* (3), 462-474.

89. Roy, R.; Hohng, S.; Ha, T., A Practical Guide to Single Molecule FRET. *Nature methods* **2008,** *5* (6), 507-516.
90. (a) Saccà, B.; Meyer, R.; Feldkamp, U.; Schroeder, H.; Niemeyer, C. M., High-Throughput, Real-Time Monitoring of the Self-Assembly of DNA Nanostructures by FRET Spectroscopy. *Angewandte Chemie International Edition* **2008,** *47* (11), 2135-2137; (b) Sacca, B.; Meyer, R.; Niemeyer, C. M., Temperature-dependent FRET spectroscopy for the high-throughput analysis of self-assembled DNA nanostructures in real time. *Nat. Protocols* **2009,** *4* (3), 271-285; (c) Ye, Y.; Blaser, G.; Horrocks, M. H.; Ruedas-Rama, M. J.; Ibrahim, S.; Zhukov, A. A.; Orte, A.; Klenerman, D.; Jackson, S. E.; Komander, D., Ubiquitin chain conformation regulates recognition and activity of interacting proteins. *Nature* **2012,** *492* (7428), 266-270; (d) Marini, M.; Piantanida, L.; Musetti, R.; Bek, A.; Dong, M.; Besenbacher, F.; Lazzarino, M.; Firrao, G., A Revertible, Autonomous, Self-Assembled DNA-Origami Nanoactuator. *Nano Letters* **2011,** *11* (12), 5449-5454; (e) Wei, X.; Nangreave, J.; Jiang, S.; Yan, H.; Liu, Y., Mapping the Thermal Behavior of DNA Origami Nanostructures. *Journal of the American Chemical Society* **2013,** *135* (16), 6165-6176; (f) Aldaye, F. A.; Sleiman, H. F., Modular Access to Structurally Switchable 3D Discrete DNA Assemblies. *Journal of the American Chemical Society* **2007,** *129* (44), 13376-13377.
91. Ha, T.; Enderle, T.; Ogletree, D. F.; Chemla, D. S.; Selvin, P. R.; Weiss, S., Probing the interaction between two single molecules: fluorescence resonance energy transfer between a single donor and a single acceptor. *Proceedings of the National Academy of Sciences of the United States of America* **1996,** *93* (13), 6264-6268.
92. (a) Zhuang, X.; Bartley, L. E.; Babcock, H. P.; Russell, R.; Ha, T.; Herschlag, D.; Chu, S., A Single-Molecule Study of RNA Catalysis and Folding. *Science* **2000,** *288* (5473), 2048-2051; (b) Karam, P.; Powdrill, M. H.; Liu, H.-W.; Vasquez, C.; Mah, W.; Bernatchez, J.; Götte, M.; Cosa, G., Dynamics of HCV RNA-dependent RNA Polymerase NS5B in Complex with RNA. *Journal of Biological Chemistry* **2014**.
93. (a) Hohlbein, J.; Craggs, T. D.; Cordes, T., Alternating-laser excitation: single-molecule FRET and beyond. *Chemical Society Reviews* **2014,** *43* (4), 1156-1171; (b) Evans, G. W.; Hohlbein, J.; Craggs, T.; Aigrain, L.; Kapanidis, A. N., Real-time single-molecule studies of the motions of DNA polymerase fingers illuminate DNA synthesis mechanisms. *Nucleic Acids Research* **2015,** *43* (12), 5998-6008; (c) Didenko, V. V., DNA Probes Using Fluorescence Resonance Energy Transfer (FRET): Designs and Applications. *BioTechniques* **2001,** *31* (5), 1106-1121; (d) Choy, J. S.; Lee, T.-H., Structural dynamics of nucleosomes at single-molecule resolution. *Trends in Biochemical Sciences 37* (10), 425-435; (e) Cotlet, M.; Gronheid, R.; Habuchi, S.; Stefan, A.; Barbafina, A.; Müllen, K.; Hofkens, J.; De Schryver, F. C., Intramolecular Directional Förster Resonance Energy Transfer at the Single-Molecule Level in a Dendritic System. *Journal of the American Chemical Society* **2003,** *125* (44), 13609-13617; (f) Schuler, B.; Lipman, E. A.; Eaton, W. A., Probing the free-energy surface for protein folding with single-molecule fluorescence spectroscopy. *Nature* **2002,** *419* (6908), 743-747.
94. Saccà, B.; Ishitsuka, Y.; Meyer, R.; Sprengel, A.; Schöneweiß, E.-C.; Nienhaus, G. U.; Niemeyer, C. M., Reversible Reconfiguration of DNA Origami Nanochambers Monitored by Single-Molecule FRET. *Angewandte Chemie International Edition* **2015,** *54* (12), 3592-3597.
95. Johnson-Buck, A.; Nangreave, J.; Jiang, S.; Yan, H.; Walter, N. G., Multifactorial Modulation of Binding and Dissociation Kinetics on Two-Dimensional DNA Nanostructures. *Nano Letters* **2013,** *13* (6), 2754-2759.

96. Soper, S. A.; Nutter, H. L.; Keller, R. A.; Davis, L. M.; Shera, E. B., THE PHOTOPHYSICAL CONSTANTS OF SEVERAL FLUORESCENT DYES PERTAINING TO ULTRASENSITIVE FLUORESCENCE SPECTROSCOPY. *Photochemistry and Photobiology* **1993,** *57*, 972-977.
97. (a) Ulbrich, M. H., Counting Molecules: Toward Quantitative Imaging. In *Far-Field Optical Nanoscopy*, Tinnefeld, P.; Eggeling, C.; Hell, W. S., Eds. Springer Berlin Heidelberg: Berlin, Heidelberg, 2015; pp 263-291; (b) McGuire, H.; Aurousseau, M. R. P.; Bowie, D.; Blunck, R., Automating Single Subunit Counting of Membrane Proteins in Mammalian Cells. *The Journal of Biological Chemistry* **2012,** *287* (43), 35912-35921; (c) Reyes-Lamothe, R.; Sherratt, D. J.; Leake, M. C., Stoichiometry and architecture of active DNA replication machinery in Escherichia coli. *Science (New York, N.Y.)* **2010,** *328* (5977), 498-501; (d) Yu, Y.; Ulbrich, M. H.; Li, M.-h.; Dobbins, S.; Zhang, W. K.; Tong, L.; Isacoff, E. Y.; Yang, J., Molecular mechanism of the assembly of an acid-sensing receptor ion channel complex. *Nature communications* **2012,** *3*, 1252-1252.
98. Ulbrich, M. H.; Isacoff, E. Y., Subunit counting in membrane-bound proteins. *Nature methods* **2007,** *4* (4), 319-321.
99. Das, S. K.; Darshi, M.; Cheley, S.; Wallace, M. I.; Bayley, H., Membrane Protein Stoichiometry Determined from the Step-Wise Photobleaching of Dye-Labelled Subunits. *ChemBioChem* **2007,** *8* (9), 994-999.
100. Coffman, V. C.; Wu, J.-Q., Counting protein molecules using quantitative fluorescence microscopy. *Trends in biochemical sciences* **2012,** *37* (11), 499-506.
101. Hastie, P.; Ulbrich, M. H.; Wang, H.-L.; Arant, R. J.; Lau, A. G.; Zhang, Z.; Isacoff, E. Y.; Chen, L., AMPA receptor/TARP stoichiometry visualized by single-molecule subunit counting. *Proceedings of the National Academy of Sciences* **2013,** *110* (13), 5163-5168.
102. Waters, J. C., Accuracy and precision in quantitative fluorescence microscopy. *The Journal of Cell Biology* **2009,** *185* (7), 1135-1148.
103. (a) Liesche, C.; Grußmayer, Kristin S.; Ludwig, M.; Wörz, S.; Rohr, K.; Herten, D.-P.; Beaudouin, J.; Eils, R., Automated Analysis of Single-Molecule Photobleaching Data by Statistical Modeling of Spot Populations. *Biophysical Journal* **2015,** *109* (11), 2352-2362; (b) Wang, X.; Li, X.; Deng, X.; Luu, D.-T.; Maurel, C.; Lin, J., Single-molecule fluorescence imaging to quantify membrane protein dynamics and oligomerization in living plant cells. *Nat. Protocols* **2015,** *10* (12), 2054-2063.
104. Wu, R. A.; Dagdas, Y. S.; Yilmaz, S. T.; Yildiz, A.; Collins, K., Single-molecule imaging of telomerase reverse transcriptase in human telomerase holoenzyme and minimal RNP complexes. *eLife* **2015,** *4*, e08363.
105. Leake, M. C., Shining the spotlight on functional molecular complexes: The new science of single-molecule cell biology. *Communicative & Integrative Biology* **2010,** *3* (5), 415-418.
106. Chen, Y.; Bharill, S.; Isacoff, E. Y.; Chalfie, M., Subunit composition of a DEG/ENaC mechanosensory channel of Caenorhabditis elegans. *Proceedings of the National Academy of Sciences* **2015,** *112* (37), 11690-11695.
107. (a) Lawrimore, J.; Bloom, K. S.; Salmon, E. D., Point centromeres contain more than a single centromere-specific Cse4 (CENP-A) nucleosome. *The Journal of Cell Biology* **2011,** *195* (4), 573-582; (b) Gadd, J. C.; Fujimoto, B. S.; Bajjalieh, S. M.; Chiu, D. T., Single-Molecule Fluorescence Quantification with a Photobleached Internal Standard. *Analytical chemistry* **2012,** *84* (24), 10522-10525.
108. Verdaasdonk, J. S.; Lawrimore, J.; Bloom, K., Determining absolute protein numbers by quantitative fluorescence microscopy. *Methods in cell biology* **2014,** *123*, 347-365.

109. Huang, B.; Bates, M.; Zhuang, X., Super resolution fluorescence microscopy. *Annual review of biochemistry* **2009,** *78*, 993-1016.
110. Schermelleh, L.; Heintzmann, R.; Leonhardt, H., A guide to super-resolution fluorescence microscopy. *The Journal of Cell Biology* **2010,** *190* (2), 165-175.
111. Schönle, A.; Hänninen, P. E.; Hell, S. W., Nonlinear fluorescence through intermolecular energy transfer and resolution increase in fluorescence microscopy. *Annalen der Physik* **1999,** *8* (2), 115-133.
112. Hell, S. W., Toward fluorescence nanoscopy. *Nat Biotech* **2003,** *21* (11), 1347-1355.
113. Betzig, E.; Patterson, G. H.; Sougrat, R.; Lindwasser, O. W.; Olenych, S.; Bonifacino, J. S.; Davidson, M. W.; Lippincott-Schwartz, J.; Hess, H. F., Imaging Intracellular Fluorescent Proteins at Nanometer Resolution. *Science* **2006,** *313* (5793), 1642-1645.
114. Rust, M. J.; Bates, M.; Zhuang, X., Sub-diffraction-limit imaging by stochastic optical reconstruction microscopy (STORM). *Nat Meth* **2006,** *3* (10), 793-796.
115. Jungmann, R.; Avendano, M. S.; Woehrstein, J. B.; Dai, M.; Shih, W. M.; Yin, P., Multiplexed 3D cellular super-resolution imaging with DNA-PAINT and Exchange-PAINT. *Nat Meth* **2014,** *11* (3), 313-318.
116. Steinhauer, C.; Itano, M. S.; Tinnefeld, P., Super-Resolution Fluorescence Imaging with Blink Microscopy. In *Nanoimaging: Methods and Protocols*, Sousa, A. A.; Kruhlak, J. M., Eds. Humana Press: Totowa, NJ, 2013; pp 111-129.
117. Cremer, G. D.; Sels, B. F.; Vos, D. E. D.; Hofkens, J.; Roeffaers, M. B. J., NASCA Microscopy: Super-Resolution Mapping of Chemical Reaction Centers. In *Far-Field Optical Nanoscopy*, Tinnefeld, P.; Eggeling, C.; Hell, W. S., Eds. Springer Berlin Heidelberg: Berlin, Heidelberg, 2015; pp 245-261.
118. Fernandez-Suarez, M.; Ting, A. Y., Fluorescent probes for super-resolution imaging in living cells. *Nat Rev Mol Cell Biol* **2008,** *9* (12), 929-943.
119. (a) Huang, B.; Wang, W.; Bates, M.; Zhuang, X., Three-dimensional Super-resolution Imaging by Stochastic Optical Reconstruction Microscopy. *Science (New York, N.Y.)* **2008,** *319* (5864), 810-813; (b) Abrahamsson, S.; Chen, J.; Hajj, B.; Stallinga, S.; Katsov, A. Y.; Wisniewski, J.; Mizuguchi, G.; Soule, P.; Mueller, F.; Darzacq, C. D.; Darzacq, X.; Wu, C.; Bargmann, C. I.; Agard, D. A.; Dahan, M.; Gustafsson, M. G. L., Fast multicolor 3D imaging using aberration-corrected multifocus microscopy. *Nat Meth* **2013,** *10* (1), 60-63.
120. Kner, P.; Chhun, B. B.; Griffis, E. R.; Winoto, L.; Gustafsson, M. G. L., Super-resolution video microscopy of live cells by structured illumination. *Nat Meth* **2009,** *6* (5), 339-342.
121. Schmied, J. J.; Raab, M.; Forthmann, C.; Pibiri, E.; Wünsch, B.; Dammeyer, T.; Tinnefeld, P., DNA origami–based standards for quantitative fluorescence microscopy. *Nat. Protocols* **2014,** *9* (6), 1367-1391.
122. Steinhauer, C.; Jungmann, R.; Sobey, T. L.; Simmel, F. C.; Tinnefeld, P., DNA Origami as a Nanoscopic Ruler for Super-Resolution Microscopy. *Angewandte Chemie International Edition* **2009,** *48* (47), 8870-8873.
123. (a) Jungmann, R.; Avendano, M. S.; Woehrstein, J. B.; Dai, M.; Shih, W. M.; Yin, P., Multiplexed 3D Cellular Super-Resolution Imaging with DNA-PAINT and Exchange-PAINT. *Nature methods* **2014,** *11* (3), 313-318; (b) Jungmann, R.; Steinhauer, C.; Scheible, M.; Kuzyk, A.; Tinnefeld, P.; Simmel, F. C., Single-Molecule Kinetics and Super-Resolution Microscopy by Fluorescence Imaging of Transient Binding on DNA Origami. *Nano Letters* **2010,** *10* (11), 4756-4761.

2 Stepwise growth of surface-grafted DNA Nanotubes visualized at the single-molecule Level

Reproduced with permission from: "Stepwise growth of surface-grafted DNA nanotubes visualized at the single-molecule level", **Amani A. Hariri**, Graham D. Hamblin, Yasser Gidi, Hanadi F. Sleiman & Gonzalo Cosa, Nature Chemistry **7**, 295–300 (2015).

Author Contributions: Single molecule experiments and analysis were carried out by **Amani A. Hariri** in addition to the finalized gels presented in this section. DNA sequence design, synthesis and purification were carried out in collaboration with **Graham D. Hamblin.** STORM experiments were carried out in close collaboration with **Yasser Gidi**. Cover was accomplished by **Melanie Burger**.

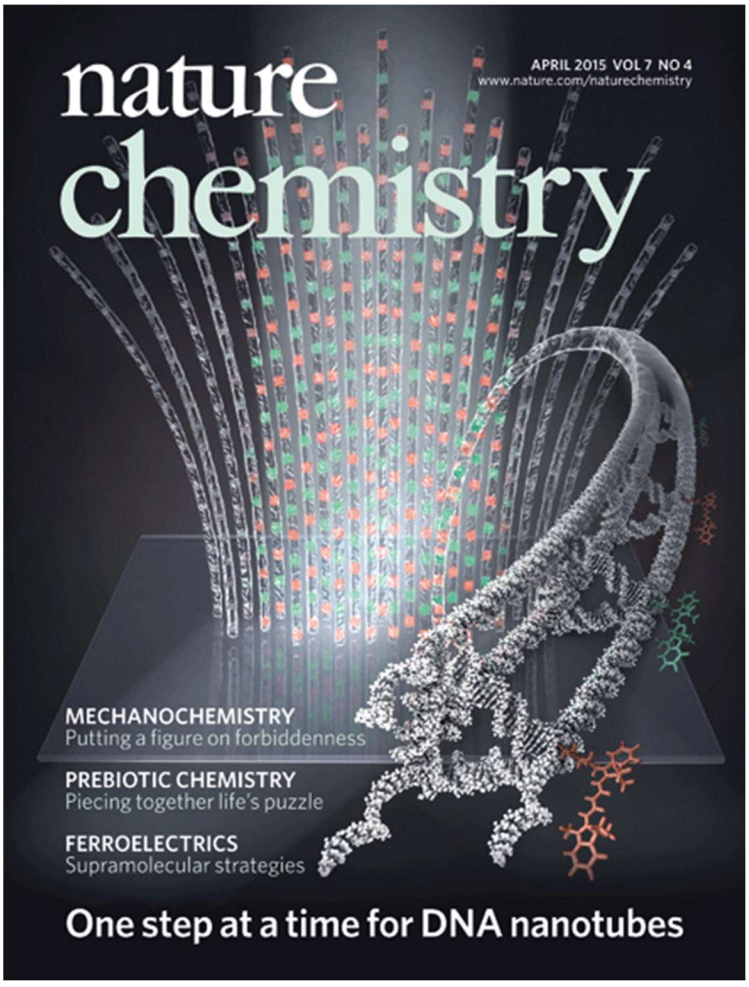

2.1 Abstract

DNA nanotubes offer a high aspect ratio and rigidity, attractive attributes for the controlled assembly of hierarchically complex linear arrays. It is highly desirable to control the positioning along the nanotube backbone, minimize the polydispersity in their manufacture and reduce the building costs. We report here a solid-phase synthesis methodology in which, starting from a 'foundation rung' specifically bound to the surface, we are able to incorporate, through a cyclic scheme, distinct rungs laid out in a predetermined manner. Each rung is orthogonally addressable. Using fluorescently tagged rungs, single-molecule fluorescence studies demonstrated the robustness and structural fidelity of the constructs and confirmed the incorporation of the rungs in quantitative yield (>95%) at each step of the cycle. Prototype structures that consisted of up to 20 repeat units, about 450 nm in contour length, were constructed. Combined, the solid-phase synthesis strategy described and its visualization through single-molecule spectroscopy show good promise for the production of custom-made DNA nanotubes.

2.2 Introduction

DNA nanotubes are promising one dimensional[1] self-assembled nanostructures with an ever expanding range of applications that stems from their high aspect ratio, rigidity, biocompatibility, encapsulating potential and addressable structure.[2] The latter quality offers a programmable lateral and longitudinal design control upon exploitation of base-pair-mediated sequence recognition.[3-6]

Crucial to unravel fully the potential of DNA nanotubes is the ability to optimize their preparation; significant efforts have thus been invested towards this goal.[7-11] The assembly of DNA nanotubes originally relied on either aligning DNA duplexes into a curved motif followed by its closure, or on rolling and cyclizing a two-dimensional DNA origami array.[12,13] Most recently we developed a modular construction through the incorporation in solution of prefabricated building blocks that consist of DNA rungs and DNA linkers.[3,14,15]

Here we show the construction of surface-grafted DNA nanotubes that exploits an assembly methodology reminiscent of the principles and methods of solid-phase synthesis.[16] Starting from

a ‘foundation rung’ specifically bound to the surface, we were able to incorporate serially, in a cyclic scheme, prefabricated DNA rungs and linkers, and thus demonstrate the possibility of preparing custom-made modular DNA nanotubes bearing the desired rung sequence along their backbone. The modular repeat units are delivered in a sequence that involves the flowing, incubation and washing of rungs first and linkers next (Fig. 2.1). This strategy offers the opportunity to modulate the shape, size and sequence of a nanotube backbone, one rung at a time.

2.3 Results and discussions

Key to our experiments is the adaptation of state-of-the-art single-molecule fluorescence methodologies[17-19] to visualize and characterize the assembly process. Single-molecule photobleaching and two-colour imaging experiments enabled us to characterize unequivocally the step growth of surface-grafted DNA nanotubes in imaging chambers. These experiments report the robustness and structural fidelity of the constructs. Combined, the assembly strategy described and its visualization through single-molecule spectroscopy pave the way for the production of custom-made DNA nanotubes with distinct orthogonally addressable rungs laid out in a predetermined manner.

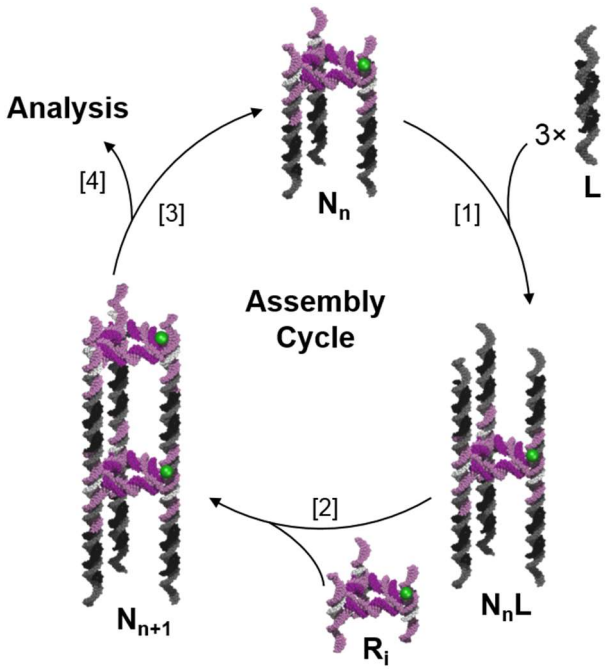

Figure 2.1: Schematic representation of the stepwise assembly of a triangular-shaped DNA nanotube (N). The time-programmed cyclic sequence involves the sequential addition first of prefabricated DNA linkers (**L**) (step 1) and then of triangular rungs ($\mathbf{R_{i+1}}$) (step 2)—both consisting of duplex DNA—to the nanotube $\mathbf{N_n}$ through flowing, incubating and washing. This cycle goes on to be subjected to the same process (step 3) to produce the desired nanotube ($\mathbf{N_{n+1}}$), which is then characterized by single-molecule spectroscopy (step 4).

2.3.1 Assembly of the DNA nanostructures

Our DNA nanotubes were assembled from two types of repeating units, namely triangular DNA rungs (R) and linker pillars (L) of duplex DNA (Figs 2.1 and 2.2; also see Experimental Section, Tables 1 and 2, which list the sequences of all the oligomers used in constructing R and L, respectively). The DNA rungs were built from a closed triangular single-stranded DNA scaffold characterized by orthogonal sequences in each of its three sides. The rung was completed after the hybridization of three strands, each complementary to a triangle side and presenting an extended non-complementary region at the ends for subsequent functionalization along the vertices ('sticky ends', Fig. 2.2, step 1). Next, three rigidifying strands were hybridized at the vertices to render the rung sticky ends better oriented in space (step 2). For the fluorescence analysis, one of the rigidifying strands was labelled with a fluorophore (Cy3, Cy5 or Atto647N). Individual DNA rungs and linker pillars were prepared separately (Figs 2.1 and 2.2) and stored until further use.[3,14]

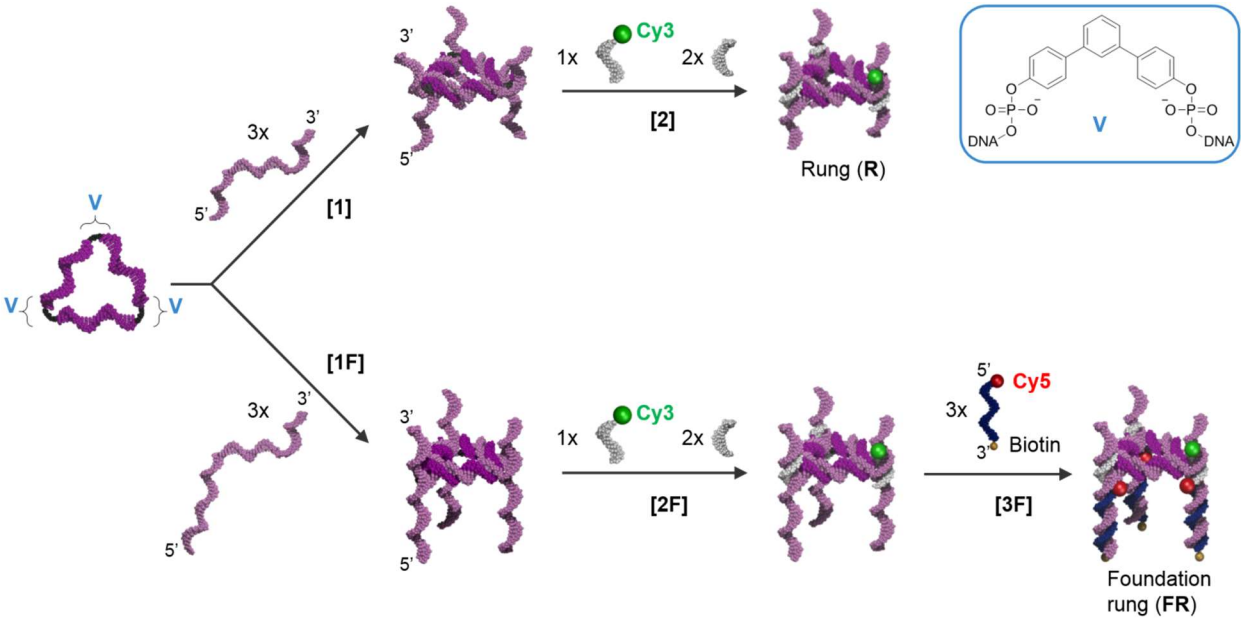

Figure 2.2: Schematic representation of the assembly of the DNA rung (R) and the foundation rung (FR). A triangular DNA strand (shown in dark purple) that bears synthetic aromatic corner units (V) at the three vertices to yield orientation and rigidity is first prepared as previously described[14]. The sequences for each side of the triangle are designed to be orthogonal to each other. Each side is then hybridized to give a complementary sequence (shown in light purple); see step 1 for **R** (or step 1F for **FR**). The complementary strands bear long overhang segments at both ends. They are arranged so that their 3′ end is above the triangular scaffold plane and their 5′ end is below it. In the next step (2 or 2F), the overhangs are partially hybridized to three short single-stranded DNA rigidifying segments (shown in light grey). One of these contains a fluorophore of choice (Cy3 in this figure). The remaining single-stranded regions of the overhangs provide the rung **R** and **FR** with sticky ends above and below the triangular plane, which enable connection of the rungs to the linker pillars **L** (see Fig. 2.1)[14]. In the case of **FR** the three sticky ends below the triangular plane are hybridized with three 18-mer single-stranded DNA sequences (shown in dark blue) that are functionalized at their 3′ end with a biotin moiety, which enables grafting to a substrate through biotin–streptavidin interactions. The 18-mer single-stranded DNAs are also labelled at their 5′ end with a Cy5 fluorophore (step 3F).

2.3.2 Foundation rungs and surface-immobilization strategies

To initiate the stepwise assembly of surface-grafted DNA nanotubes, we first prepared a foundation rung (FR) that bore biotin moieties to enable its specific surface immobilization through biotin–streptavidin interactions[7]. This rung constituted the nucleation site from which the nanotube was extended. The foundation rung was built in a similar manner to R, but using a unique series of three strands complementary to the triangle (Fig. 2.2, steps 1F and 2F). These strands hybridized at their 5′ end (below the triangle plane, Fig. 2.2) with short 18-mer segments of DNA, which were labelled at their 5′ and 3′ ends with a Cy5 fluorophore and a biotin molecule, respectively. As for the normal rung, the foundation rung bore three rigidifying strands, including one with a Cy3 tag (Experimental Section, Table 3 lists the sequences of all the components of FR). The FR structure thus obtained was roughly 13.5 nm tall with sides of 6.8 nm (Experimental Section, Fig. 2.8). Our design provides three points of immobilization to ensure a resilient surface grafting. Successful formation of the foundation rung in solution was confirmed by gel electrophoresis (Experimental Section, Figs 2.7 and 2.9).

The foundation rungs were next immobilized in flow-through chambers[20] on top of glass coverslips through biotin–streptavidin interactions (Fig. 2.3a). Surfaces were preconditioned with a 100/1 mole ratio mixture of polyethylene glycol (PEG) and PEG–biotin to avoid any

nonspecific adsorption.[17,21] A solution of streptavidin was next incubated on the surface followed by grafting of the foundation rung from an approximately 100 pM solution. Controls ruled out any nonspecific binding of the rungs (Experimental Section, Fig. 2.10).

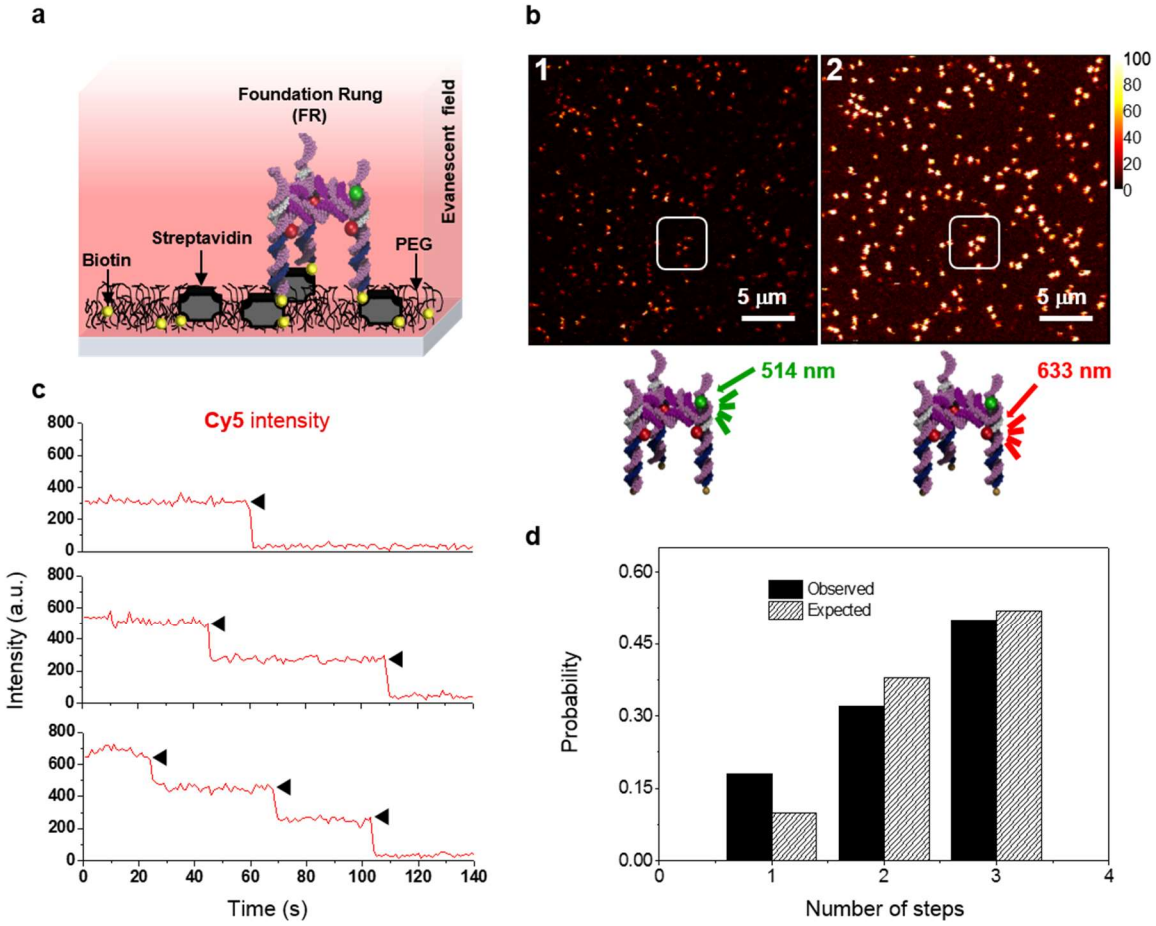

Figure 2.3: Single-molecule characterization of surface-grafted foundation rungs. **a**. Schematic illustration of the details for the imaging experiment; the bottom-up self-assembly materials are shown, together with a Cy3- and Cy5-labelled foundation rung (FR). **b**. Fluorescence scanning confocal images obtained for the foundation rung. **i**. Green-channel image acquired on excitation with the 514 nm output of an Ar+ laser and collecting the emission between 555 and 625 nm. **ii**. Red channel image acquired on exciting the previous region with the 633 nm output of a HeNe laser and collecting the emission between 645 and 725 nm. The colour bar on the right illustrates the counts per millisecond per pixel. Geometric figures assist in qualitatively visualizing the colocalization, quantified with homebuilt software. **c**. Representative intensity–time trajectories recorded for Cy5 in our TIRFM set-up on excitation of the foundation rungs. The panels show trajectories that exhibit one, two and three photobleaching steps. **d**. The experimentally obtained probability distribution for the number of Cy5 dyes (and photobleaching steps) per foundation rung compared with the theoretical expectations.

2.3.3 Single molecule characterization of the foundation rung

Single-molecule fluorescence spectroscopy studies enabled us to characterize individual foundation rungs and provide information on their structural fidelity as well as on the grafting robustness over time. A confocal fluorescence microscope was employed to visualize the constructs. Images were acquired on the independent direct excitation of the Cy3 and Cy5 dyes with the 514 nm output of an Ar+ laser and the 633 nm output of a HeNe laser, respectively (Fig. 2.3b). Two detection channels (green and red) were employed to record independently the emissions of Cy3 and Cy5, respectively. Colocalization of Cy3 and Cy5 emissions on their simultaneous excitation was observed, which confirms that foundation rungs assemble on the surface as integral units. A larger number of units were detected in the red channel than in the green channel, however (see Fig. 2.3bi, bii for the green and red channel images, respectively). Thus, whereas all the units observed in the green channel had a counterpart emission in the red channel, 13% of the molecules observed in the red channel lacked a corresponding Cy3 emission. The result is anticipated considering the theoretical one-third molecular ratio for Cy3/ Cy5 in a rung, and on correction for the labelling efficiency of Cy3 and Cy5 on their DNA constructs (86 and 90%, respectively, experimentally determined based on the measured absorbance and reported extinction coefficient of the dye-labelled DNA). Thus, 14% of the foundation rungs are expected to have a rigidifying strand that actually lacks its Cy3 fluorophore, in good agreement with the 13% discrepancy observed experimentally. However, the probability may be estimated at 0.13 (that is, ~0.1%) for the odds that a foundation rung does not show Cy5 emission, as this would require all three of its 18-mer DNAs to be mislabelled. The surface-grafted foundation rungs were observed to remain pristine in the imaging chambers for prolonged periods that spanned more than two hours subjected to intermittent flow. This result underlines the resilience of these structures and the grafting robustness under our experimental conditions. Importantly, we designed the inter-dye distance in the foundation rung to minimize the occurrence of Förster resonance energy transfer (FRET).

Through fluorescence single-molecule photobleaching we determined the number of Cy5 dyes per foundation rung. We used a total internal reflection fluorescence microscope

(TIRFM) for our studies. Regions were excited with an evanescent field employing the 641 nm output of a continuous wave (CW) diode laser. An electron-multiplied CCD (charge-coupled device) camera was used to record images of a $\sim 70 \times 70\ \mu m^2$ region at a frame-acquisition frequency of 5 Hz. Individual intensity–time trajectories arising from hundreds of foundation rungs were extracted from the images. Photobleaching events were thus recorded for hundreds of units visualized simultaneously.

The fluorescence intensity for any given foundation rung was observed to decrease stepwise over time to give rise to a 'staircase' pattern with a measurable number of discrete intensity levels, ranging from three to one, which we assign to units that have three, two and one Cy5 dyes, respectively (see Fig. 2.3c). By manually counting the number of intensity steps recorded for each of the ~300 foundation rungs, we built the probability distribution histogram for the number of Cy5 dyes per rung. We observed that 50, 32 and 18% of the foundation rungs exhibited three, two and one photobleaching steps, respectively. Next, the projected probability distribution of the number of dyes/steps per foundation rung was estimated with a binomial distribution analysis (see Experimental Section) based on the 90% experimentally determined labelling efficiency of the 18-mer strands with Cy5. A good correlation was observed between the experimental outcome and the calculated distribution (Fig. 2.3d). Taken together, the colocalization, FRET and photobleaching analysis results enabled us to build a detailed characterization and extract quantitative information about the assembly, structural fidelity and robustness of the foundation rung.

2.3.4 Stepwise assembly of surface-grafted DNA nanotubes at the single molecule level

Next, the assembly of surface-grafted DNA nanotubes was achieved in our flow-through imaging chambers, building from the immobilized foundation rung, which serves as a nucleation point. A time-programmed cyclic sequence was implemented that involved flowing and incubation of the DNA linker pillars L, at a concentration of 120 nM, for five minutes followed by washing of any residual unbound reagent. Then the process was repeated with the DNA rungs R at a concentration of 40 nM, thus completing the cycle (Fig. 2.1). Such a cyclical protocol prevented uncontrolled polymerization of the rungs in both directions in solution. The

controlled addition of both L and R to the nanotube resulted in step increases of ~24.5 nm after each addition cycle (Experimental Section, Fig. 2.11).

Labelling of the incoming DNA rungs with Cy3 enabled the nanotube growth to be monitored at each step utilizing a TIRFM set-up equipped with a 532 nm CW diode laser. A line scan on the images acquired prior to and after the first addition cycle clearly shows a doubling of the intensity for most of the molecules visualized (Experimental Section, Fig. 2.12a,b, respectively). Although appealing for following the nanotube growth in real-time, a major drawback of this imaging procedure is the rapid photobleaching of the Cy3 dyes (see also Experimental Section, Fig. 2.15), which prevents an accurate estimation of the number of rungs incorporated in subsequent cycles.

We next used single-molecule photobleaching of Cy3 to monitor the number of rungs incorporated after a programmed sequence of additions. A series of images was acquired at 5 Hz frequency after completing one up to five addition cycles (Fig. 2.4a). A new region was monitored in each case as the experiment relied on photobleaching all the Cy3 dyes in the probed region. The subsequent analysis involved manually counting the intensity steps in the individual intensity–time trajectories recorded for each unit.

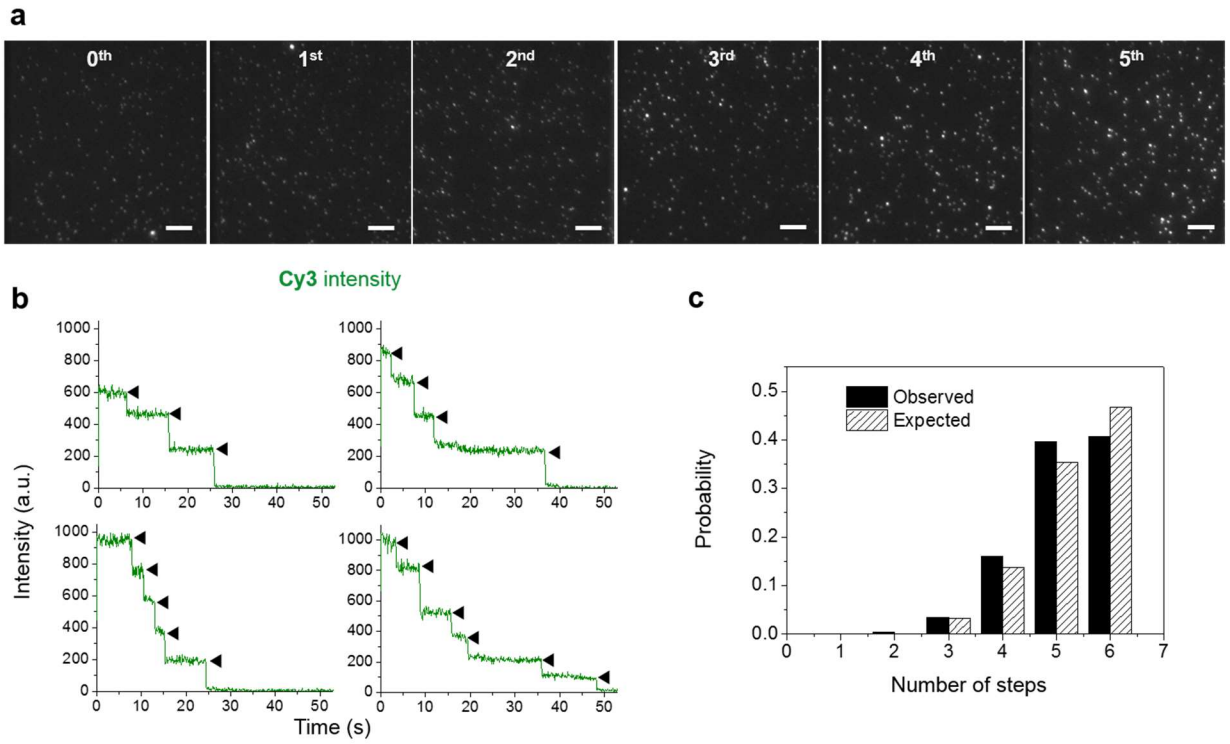

Figure 2.4: Single-molecule imaging of nanotubes prepared after an increasing number of addition cycles, each incorporating a Cy3-tagged rung. a. Series of images acquired in a TIRFM set-up equipped with a 532 nm excitation source after the addition of the foundation rung and an increasing number of addition cycles up to five. Scale bars, 5 μm. **b**. Representative Cy3 intensity–time trajectories acquired for individual surface-grafted DNA nanotubes after five addition cycles. Trajectories with three, four, five and six photobleaching steps are illustrated. **c**. The experimentally obtained probability distribution for the number of Cy3 dyes (and photobleaching steps) per surface-grafted DNA nanotube after five addition cycles compared with the theoretical expectations.

In Fig. 2.4a, one may qualitatively appreciate an increase in the observed intensity of the imaged nanotube units with an increase in the number of cycles executed. Given the 86% Cy3 labelling efficiency we encountered for the rigidifying strand, there is a possibility of recording intensity–time trajectories in which the number of intensity steps (dyes) is smaller than the maximum expectation, which is given by the total number of cycles plus one. Representative intensity–time trajectories after five addition cycles are shown in Fig. 2.4b. As observed in the four panels displayed, units typically exhibited six, but also five, four and three intensity steps. The experimentally determined probability distribution histograms after one to five addition cycles are compared with theoretical expectations based on the measured labelling efficiency and a binomial distribution model in Fig. 2.4c (for five additions) and in Experimental Section, Fig. 2.13a–d (for one to four additions, respectively). There is a good agreement between both distributions. The outcome of single-molecule photobleaching experiments and their agreement with expectations underline that the structures neither suffer from branching during their formation (more dyes would then be expected per addition cycle) nor suffer from polydispersity that arises from a low yield assembly at each cycle. One may conclude that the incorporation of rungs on individual nanotubes starting from the foundation rung occurs in a high yield and fidelity at each step of the cyclic assembly.

To confirm that nanotubes grow specifically from the surface-grafted foundation rung we further studied the colocalization of emission from Cy3 that arises from the repeat units along the nanotube and from Cy5 that arises from the foundation rung. As shown in Fig. 2.14 (Experimental Section), a good correlation exists between the Cy3 and Cy5 positions after five addition cycles, which indicates that the growth of nonspecifically bound nanotubes lacking a foundation rung may be ruled out.

2.3.5 Assembly of surface-grafted DNA nanotubes with alternating patterns

To demonstrate the assembly of long structures with positional control along their backbone, we next performed a proof-of-concept experiment. We built DNA nanotubes bearing 20 rungs labelled with green (Cy3) and red (Atto647N) dyes in an alternating pattern (Fig. 2.5a). The choice of ten rungs bearing either dye arises from the requisite to distinguish individual photobleaching steps in intensity–time trajectories. More than ten steps may be difficult to recognize and assign given the intensity dynamic range and the increasing probability of simultaneous photobleaching events. We designed two-colour, single-molecule photobleaching experiments to count the number of green and red emitters, and the overall number of rungs in a given nanotube. Regions were excited with an evanescent field employing the 641 nm output of a diode laser first and the 532 nm output of a second diode laser next (Fig. 2.5b). This sequential recording of the photobleaching events minimized artefacts that arise from the bleeding of Atto647N emission into the green channel and of Cy3 emission into the red channel. We selected Atto647N over Cy5 given its longer survival time, which results in trajectories with long intervals of steady intensity between photobleaching steps (see also Experimental Section, Fig. 2.15).

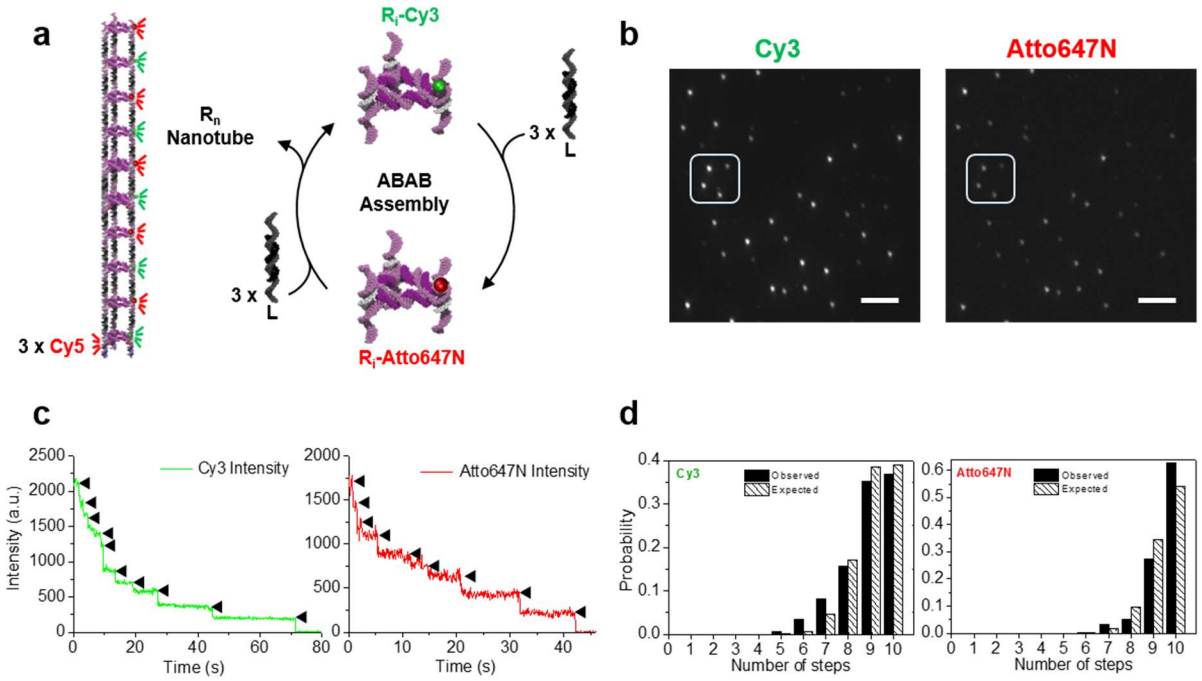

Figure 2.5: Single-molecule imaging of long DNA nanotubes bearing 20 rungs with alternating Cy3 and Atto647N dyes. a. Cyclic scheme showing the stepwise assembly of the nanotubes prepared by incorporating DNA rungs labelled with green (Cy3) and red (Atto647N) dyes in an alternating pattern ('ABAB assembly'). A structure that bore 20 rungs was fabricated, but for clarity a ten-rung nanotube is shown here. **b**. Typical TIRFM images of surface-grafted nanotubes, which show colocalization of Cy3 (green) and Atto647N (red) dyes. Scale bars, 5 μm. **c**. Typical intensity–time trajectories acquired for a single nanotube (arrows indicate bleaching events). **d**. The experimentally obtained probability distribution for the number of either Cy3 or Atto647N dyes per surface-grafted long DNA nanotube compared with the theoretical expectation.

Representative intensity–time trajectories for nanotubes 20 rungs long are shown in Fig. 2.5c. Considering the experimentally determined labelling efficiencies of 91% both for Atto647N and for Cy3, there is a good correlation between the probability distribution histogram obtained from photobleaching curves and the theoretical expectation based on labelling efficiencies (Fig. 2.5d). A good correlation was also obtained in a second sample prepared with rigidifiers labelled with Cy3 at a labelling efficiency of 80% (Experimental Section, Fig. 2.16). It may be speculated that a poor growth efficiency during each step of the nanotube assembly, rather than an incomplete functionalization of fluorophores to the rigidifying strand in DNA, accounts for the experimentally obtained distribution of either Cy3 or Atto647N. Considering the good correlation between the experimental distributions for Atto647N and Cy3 incorporation and the theoretical estimates based on a 91% efficiency, one may then safely set the minimum yield of stepwise additions at this value. Such an assignment would, however, disregard the experimentally determined labelling efficiencies. Even if considering a 5% error in the labelling-efficiency determination (95% labelling efficiency for both dyes), we obtain a quantitative yield (>95%) per rung addition. Utilizing the 95% yield per rung addition as a lower bound, it is then possible to estimate that, after 44 rung-addition cycles, the yield of the full-length product (expected contour length of 1.1μm) would be ~10%, which sets a realistic limit to the number of rungs that may be added.

2.3.6 3D STORM imaging of surface-grafted DNA nanotubes

We next devised stochastic optical reconstruction microscopy (STORM)-based super-resolution imaging experiments on newly constructed nanotubes 20 rungs long.[30-33] We prepared the nanotubes as described above, but replaced Atto647N with Cy5 because the blinking duty cycle of the latter has been shown to surpass amply that of the former towards achieving well-resolved structures in STORM experiments.[30] Figure 2.17 (Experimental Section) displays an image that superimposes the super-resolution STORM image of the nanotubes obtained on photoexciting Cy5 along a nanotube over the image achieved on photoexciting Cy3 on the same nanotube. These data confirm the presence of large, isolated surface-bound nanotubes.

We provide a methodology for the synthesis of DNA nanotubes that relies on their assembly from prefabricated building blocks delivered and removed in a flow-through chamber in a controlled fashion. Single-molecule fluorescence imaging further provides unique opportunities to inspect and validate the assembly process. Our synthetic strategy exploits an assembly methodology reminiscent of the principles and methods of solid-phase synthesis. The sequential introduction, in controlled amounts, of prefabricated building blocks provides a unique opportunity to customize the backbone sequence one rung at a time. We may fully exploit the hierarchical control of information/organization in which the base sequence for component strands is dictated by the design constraints that require the strands to hybridize and form rungs and linkers, and for which the nanotube code along its backbone may be dictated a priori by the controlled sequential delivery of predesigned rungs. Our proof-of-concept experiments, rooted in the exploitation of single-molecule fluorescence photobleaching and STORM, show a high yield (>95% per rung-addition cycle) and fidelity in the nanotube structure when up to 19 cycles are executed (building on a foundation rung), which produces structures 450 nm long in contour length. Our results further show the formation of a highly resilient structure.

2.4 Conclusion

We believe that the method described herein to construct and visualize DNA nanotubes one rung at a time will pave the way towards the production of custom-made materials scaffolded onto DNA nanotubes that bear distinct orthogonally addressable rungs laid out in a predetermined manner. This method may be extended to the construction of other DNA or macromolecular nanostructures assembled in a stepwise, controlled manner, rather than relying

on their spontaneous assembly in solution. The ability to analyse the fidelity and incorporation at each stage of the assembly will, in turn, allow an in-depth analysis of the growth mechanism of the new structures.

2.5 Methods

All the materials and methods, including DNA-strand preparation, foundation rung (FR), Cy3-tagged rung (R) and double-stranded linker (L) assembly and characterization are included in the experimental section. Also in the experimental section are ensemble and single-molecule methodologies, including single-molecule sample preparation and imaging, microscopy and image analysis, STORM imaging and data analysis.

2.6 References

1. Seeman, N.C. An overview of structural DNA Nanotechnology. *Mol. Biotechnol.* **37**, 246-257 (2007).
2. Aldaye, F.A., Palmer, A.L. & Sleiman, H.F. Assembling materials with DNA as the guide. *Science* **321**, 1795-1799 (2008).
3. Lo, P.K. et al. Loading and selective release of cargo in DNA nanotubes with longitudinal variation. *Nat Chem* **2**, 319-328 (2010).
4. Dutta, P.K. et al. DNA-Directed Artificial Light-Harvesting Antenna. *J. Am. Chem. Soc.* **133**, 11985-11993 (2011).
5. Kuzyk, A. et al. DNA-based self-assembly of chiral plasmonic nanostructures with tailored optical response. *Nature* **483**, 311-314 (2012).
6. Wei, B., Dai, M.J. & Yin, P. Complex shapes self-assembled from single-stranded DNA tiles. *Nature* **485**, 623-626 (2012).

7. Wilner, O.I. et al. Self-assembly of DNA nanotubes with controllable diameters. *Nat Commun* **2**, 540 (2011).

8. Hamblin, G.D., Carneiro, K.M., Fakhoury, J.F., Bujold, K.E. & Sleiman, H.F. Rolling circle amplification-templated DNA nanotubes show increased stability and cell penetration ability. *J. Am. Chem. Soc.* **134**, 2888-2891 (2012).

9. O'Neill, P., Rothemund, P.W.K., Kumar, A. & Fygenson, D.K. Sturdier DNA nanotubes via ligation. *Nano Lett.* **6**, 1379-1383 (2006).

10. Yin, P. et al. Programming DNA tube circumferences. *Science* **321**, 824-826 (2008).

11. Rothemund, P.W.K. et al. Design and Characterization of Programmable DNA Nanotubes (vol 126, pg 16344, 2004). *J. Am. Chem. Soc.* **135**, 2864-2864 (2013).

12. Liu, D., Park, S.H., Reif, J.H. & LaBean, T.H. DNA nanotubes self-assembled from triple-crossover tiles as templates for conductive nanowires. *Proc. Natl. Acad. Sci. USA* **101**, 717-722 (2004).

13. Douglas, S.M., Chou, J.J. & Shih, W.M. DNA-nanotube-induced alignment of membrane proteins for NMR structure determination. *Proc. Natl. Acad. Sci. USA* **104**, 6644-6648 (2007).

14. Aldaye, F.A. et al. Modular construction of DNA nanotubes of tunable geometry and single- or double-stranded character. *Nature Nanotechnology* **4**, 349-352 (2009).

15. Hamblin, G.D. et al. Simple design for DNA nanotubes from a minimal set of unmodified strands: rapid, room-temperature assembly and readily tunable structure. *Acs Nano* **7**, 3022-3028 (2013).

16. Zhang, Y. & Seeman, N.C. Construction of a DNA-Truncated Octahedron. *J. Am. Chem. Soc.* **116**, 1661-1669 (1994).

17. Roy, R., Hohng, S. & Ha, T. A practical guide to single-molecule FRET. *Nat Meth* **5**, 507-516 (2008).

18. Joo, C., Balci, H., Ishitsuka, Y., Buranachai, C. & Ha, T. Advances in Single-Molecule Fluorescence Methods for Molecular Biology. *Annu. Rev. Biochem* **77**, 51-76 (2008).

19. Weiss, S. Fluorescence Spectroscopy of Single Biomolecules. *Science* **283**, 1676-1683 (1999).

20. Karam, P., Ngo, A.T., Rouiller, I. & Cosa, G. Unraveling electronic energy transfer in single conjugated polyelectrolytes encapsulated in lipid vesicles. *Proc. Natl. Acad. Sci. USA* **107**, 17480-17485 (2010).

21. Ngo, A.T., Karam, P., Fuller, E., Burger, M. & Cosa, G. Liposome Encapsulation of Conjugated Polyelectrolytes: Toward a Liposome Beacon. *J. Am. Chem. Soc.* **130**, 457-459 (2007).

22. Ha, T. et al. Probing the interaction between two single molecules: fluorescence resonance energy transfer between a single donor and a single acceptor. *Proc. Natl. Acad. Sci. USA* **93**, 6264-6268 (1996).

23. Ulbrich, M.H. & Isacoff, E.Y. Subunit counting in membrane-bound proteins. *Nat. Methods* **4**, 319-321 (2007).

24. Casanova, D. et al. Counting the number of proteins coupled to single nanoparticles. *J. Am. Chem. Soc.* **129**, 12592-12593 (2007).

25. Jain, A. et al. Probing cellular protein complexes using single-molecule pull-down. *Nature* **473**, 484-488 (2011).

26. Blunck, R., McGuire, H., Hyde, H.C. & Bezanilla, F. Fluorescence detection of the movement of single KcsA subunits reveals cooperativity. *Proc. Natl. Acad. Sci. USA* **105**, 20263-20268 (2008).

27. Harms, G.S. et al. Single-molecule imaging of l-type Ca(2+) channels in live cells. *Biophys. J.* **81**, 2639-2646 (2001).

28. Shu, D., Zhang, H., Jin, J. & Guo, P. Counting of six pRNAs of phi29 DNA-packaging motor with customized single-molecule dual-view system. *EMBO J* **26**, 527-537 (2007).

29. Ha, T. & Tinnefeld, P. Photophysics of Fluorescent Probes for Single-Molecule Biophysics and Super-Resolution Imaging. *Annu. Rev. Phys. Chem.* **63**, 595-617 (2012).

30. Dempsey, G.T., Vaughan, J.C., Chen, K.H., Bates, M. & Zhuang, X.W. Evaluation of fluorophores for optimal performance in localization-based super-resolution imaging. *Nat. Methods* **8**, 1027-1036 (2011).

31. Huang, B., Wang, W., Bates, M. & Zhuang, X. Three-Dimensional Super-Resolution Imaging by Stochastic Optical Reconstruction Microscopy. *Science* **319**, 810-813 (2008).

32. Rust, M.J., Bates, M. & Zhuang, X.W. Sub-diffraction-limit imaging by stochastic optical reconstruction microscopy (STORM). *Nat. Methods* **3**, 793-795 (2006).

33. Schmied, J.J. et al. DNA Origami Nanopillars as Standards for Three-Dimensional Superresolution Microscopy. *Nano Lett.* **13**, 781-785 (2013).

2.7 Experimental Section

2.7.1 Materials and Methods

Acetic acid, boric acid, cyanogen bromide (5M in acetonitrile), EDTA, urea, 4-morpholineethanesulfonic acid (MES), magnesium chloride, StainsAll and tris(hydroxymethyl)-aminomethane (Tris) were purchased from Aldrich. 1000Å nucleoside-derivatized LCAA-CPG solid support with loading densities of 25-40 μmole/g, Sephadex G-25 (super fine DNA grade) and reagents for automated DNA synthesis were used as purchased from BioAutomation. 1000Å Phosphate-CPG was purchased from ChemGenes. Exonuclease VII (ExoVII, source: recombinant) was used as purchased from BioLynx Incorporated. 40% acrylamide/bis-acrylamide 19:1 solution and agarose were purchased from BioShop. Cy3-tagged DNA strand was purchased from IDT, and Cy5-Biotin DNA strand was purchased from TriLink Biotechnologies. 1xTBE buffer is composed of 90 mM Tris and boric acid, 1.1 mM EDTA, with a pH of ~8.3. 1xTAMg buffer is composed of 45 mM Tris, 7.6 mM $MgCl_2$, with pH adjusted to 8.0 using glacial acetic acid. 1xMESMg buffer is composed of 250 mM MES, 20 mM $MgCl_2$, with pH 7.6.

Listed below in Tables 1-3 are the sequences utilized in constructing the foundation rung as well as rungs and linkers used as repeating units.

Table 2.1: Sequences for all the oligomers used in constructing the Cy3-tagged DNA rung (R).

Name	Sequences (5'-3')
Triangular DNA scaffold (**T**)[a,b]	←TATTGGTTTG-**v**-TGACCAATAACACAAATCGG-**v**-TCAGTAATCTCTTGAAGGTA-**v**-GGAAACGACA→
Complementary **S**trands to the triangular scaffold (**CS#**)[b,c]	**CS1** **CTCAGCAGCGAAAA** ACCGCTTTAC TACCTTCAAGAGATTACTGA GTCTTGGAGT **CGGATTGAGC**
	CS2 **TCGGCAGACT** CTACTTGGTG CAAACCAATATGTCGTTTCC AGCATAGGAC **GGCGGCGTTAAATA**
	CS3 **CGGTGCATTT** AGTCGTGTCG CCGATTTGTGTTATTGGTCA CGCGAATCAT **GCGTACTCGT**
Rigidifying **S**trands[d]	**RS1** ACTCCAAGAC **TT** CGACACGACT **RS1-*ATTO647N*** /ATTO647NN/ ACTCCAAGAC **TT** CGACACGACT
	RS2 ATGATTCGCG **TT** CACCAAGTAG **RS2** **/5Cy3/**ATGATTCGCG **TT** CACCAAGTAG
	RS3 GTCCTATGCT **TT** GTAAAGCGGT

[a]The linear strand shown is subsequently hybridized into a triangle using a complementary DNA strand, and then it is chemically ligated using cyanogen bromide to yield the single-stranded DNA template. Arrows in the sequence indicate the ligation point, whereas "v" indicates the triangle vertices (1,3-bis-(4-hydroxyphenyl)benzene) incorporated along the sequence to facilitate bending.[1,2] [b]Regions are color-coded where complementary sections between **T** and **CS#** are found. [c]Bold text marks complementary sections to **LS#** (see Table 2 below). [d]The TT region provides flexible non-base pairing sections.

Table 2.2: Sequences for all the oligomers used in constructing the DNA linker pillars (L).

Name	Sequences (5'-3')
Linking **S**trands[a]	**LS1** TTTTCGCTGCTGAG TGAACCAGAAAGTGGTCCTGTA TATTTAACGCCGCC
	LS2 AGTCTGCCGA GCTACCAGGTGAATTTCAAACGCAATTACG ACGAGTACGC
	LS3 AAATGCACCG GCTACCAGGTGAATTTCAAACGCAATTACG GCTCAATCCG
Double **S**tranded Linking Strands[a]	**DS1** TACAGGACCACTTTCTGGTTCA
	DS2 and DS3 CGTAATTGCGTTTGAAATTCACCTGGTAGC

[a]Regions are color-coded where complementary sections between **LS#** and **DS#** are found.

Table 2.3: Sequences for all the oligomers used in constructing the foundation rung (FR).

Name	Sequences (5'-3')
Triangular DNA scaffold (**T**)[a,b]	←TATTGGTTTG-**v**-TGACCAATAACACAAATCGG-**v**-TCAGTAATCTCTTGAAGGTA-**v**-GGAAACGACA→
Complementary **S**trands-(**cap**ped) to the triangular scaffold (**CS#-cap**)[b,c]	**CS1-cap TGGCGACGGTCGCGAGGT** ACCGCTTTAC TACCTTCAAGAGATTACTGA GTCTTGGAGTCGGATTGAGC
	CS2-cap TGGCGACGGTCGCGAGGT CTACTTGGTG CAAACCAATATGTCGTTTCC AGCATAGGACGGCGGCGTTAAATA
	CS3-cap TGGCGACGGTCGCGAGGT AGTCGTGTCG CCGATTTGTGTTATTGGTCA CGCGAATCATGCGTACTCGT
Rigidifying **S**trands (**RS#**)[d]	**RS1** ACTCCAAGAC **TT** CGACACGACT
	RS2 /**5Cy3**/ATGATTCGCG **TT** CACCAAGTAG
	RS3 GTCCTATGCT **TT** GTAAAGCGGT
Biotin-Cy5 strands	(**Cy5**) (C6-NH) ACCTCGCGACCGTCGCCA (Biotin BB)

[a]The linear strand shown is subsequently hybridized into a triangle using a complementary DNA strand, and then it is chemically ligated using cyanogen bromide to yield the single-stranded DNA template. Arrows in the sequence indicate the ligation point, whereas "v" indicates the triangle vertices (1,3-bis-(4-hydroxyphenyl)benzene) incorporated along the sequence to facilitate bending.[1,2] [b]Regions are color-coded where complementary sections between **T** and **CS#** are found. [c]Bold text marks complementary sections to the biotin-Cy5 strand. [d]The TT region provides flexible non-base pairing sections.

2.7.2 DNA Sample Preparation

DNA synthesis was performed on a 1 µmole scale, and deprotection carried out in concentrated ammonium hydroxide (55˚C, 16 hours). Crude products were purified on 12-19% polyacrylamide/8M urea polyacrylamide gels (PAGE; up to 20 OD260 of crude DNA per gel) at constant current of 30 mA for 1-2 hours, using 1xTBE running buffer. Following electrophoresis, the plates were wrapped in plastic and placed on a fluorescent TLC plate and illuminated with a UV lamp (254 nm) (Figure 2.6). The bands were quickly excised, and the gel pieces were crushed and incubated in 10 mL of sterile water at 55˚C for 16 hours. Samples were then dried to 1.5 mL, desalted using size exclusion chromatography (Sephadex G-25), and quantified.

A cyclic single stranded DNA triangular scaffold was synthesized and chemically ligated following a previously reported protocol.[1,2]

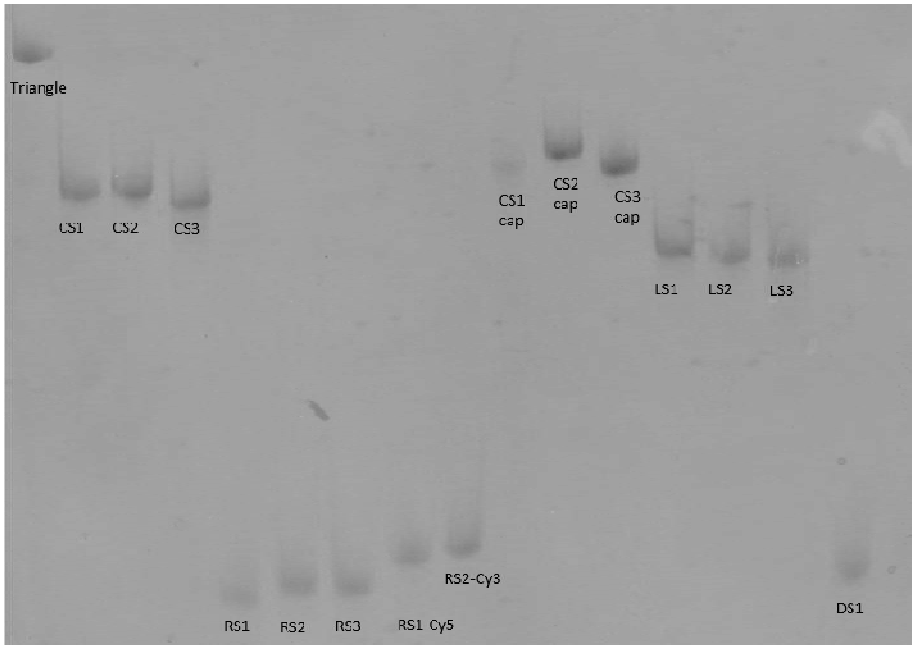

Figure 2.6: Denaturing urea-polyacrylamide gel electrophoresis of all the DNA strands used to form the DNA rung and foundation rung.

2.7.2.1 Foundation Rung (FR) Assembly and Characterization

This rung was generated upon the equimolar combination of triangular DNA scaffold strands (**T**), complementary-(capped) strands to the triangular scaffold **CS1-cap** to **CS3-cap**, and rigidifying strands **RS1** to **RS3** at a final concentration of 2.0 μM in 1xTAMg. This mixture was hybridized from 95°C to 4°C over 3.5 hours to maximize clean product formation. An excess of the Cy5-biotin DNA strand is then added to the pre-fabricated DNA rung at room temperature and incubated for 30 min. Native PAGE (8%, 1xTAMg running buffer, stained with StainsAll®) confirmed the hybridization of each product (Figure 2.7).

Figure 2.8 below provides a cartoon with relevant dimensions of the foundation rung including height, and distance between Cy3 and Cy5 dyes. We designed the inter-dye distance in the foundation rung to minimize the occurrence of Förster resonance energy transfer (FRET) between Cy3 and Cy5 dyes. The Cy3 in the rigidifying strand along a vertex is positioned at

~7.5nm from the closest Cy5 dye, tagged to the 18 mer strand sharing the same vertex. The remaining Cy5 dyes at the opposite two vertices are at a larger distance (*ca.* 10 nm, see Fig. 2.3). FRET efficiency between Cy3 and Cy5 was estimated at 8% and 1.7%, respectively and was not experimentally observed upon excitation of Cy3 by the 514 nm laser line in our single molecule confocal experiments (Fig. 2.3b).

A native PAGE of our sample (2x) was prepared to isolate the desired foundation rung product (top band in the gel) and dispose of the excess of biotinylated Cy5 strands. This is required given that we used an excess of the Cy5-Biotin strand in our hybridization protocol which may next bind to steptavidin in the imaging chamber providing for false foundation rung positives. Using a Typhoon Gel scanner (CIAN, McGill), we followed the emission of the Cy3 and Cy5 dyes present in the sample upon exciting with the 532 nm and 633 nm lasers respectively. An image of the gel was obtained (Figure 2.9) and the desired band was excised. This fraction is crushed gently in a 15ml falcon tube to which 1 ml of 1x TAMg buffer was added. The solution was next incubated for ~17 hours. A filter unit of 0.22μm pore size was used (Millex GV, Durapore) to purify the solution and eliminate the gel particles in addition to other impurities. A centrifugal filter (Amicon Ultra, 0.5ml, 3K) was used to concentrate the sample from a 1ml to a 50μL solution (20x).

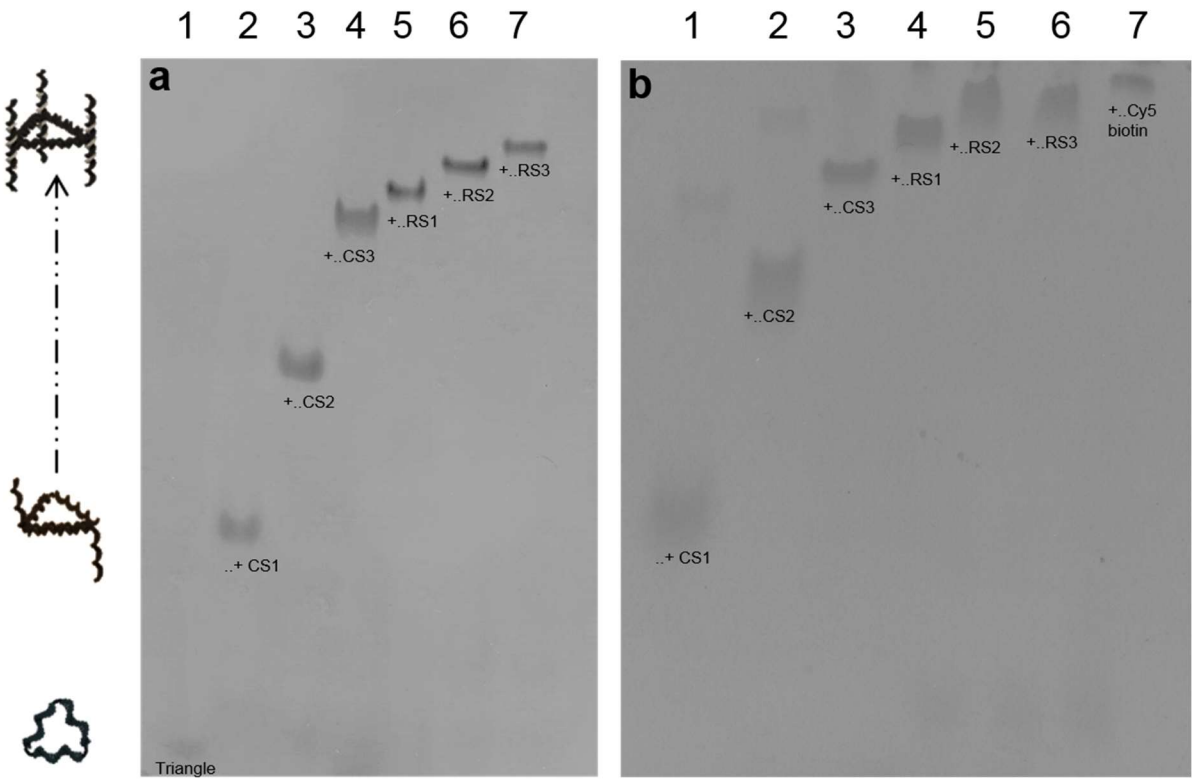

Figure 2.7: Native PAGE analysis revealing the assembly of the foundation rung and the Cy3-tagged DNA rungs. a. The single stranded DNA triangular scaffold is sequentially titrated with the complementary strands CS1-CS3 (lanes 2-4, respectively), and with the RS1-RS3 strands to generate a fully assembled triangular Cy3-tagged DNA rung (lane 7). **b.** The single stranded triangle is sequentially titrated with the capped complementary strands CS1-cap to –CS3-cap (lanes 1-3, respectively), and with the RS1-RS3 strands to generate a fully assembled triangular rung (lane 6). An excess of the Cy5-Biotin strand is added to hybridize to the sticky ends of the rung to form a Cy3-Cy5 labeled rung functionalized with biotin (lane 7).

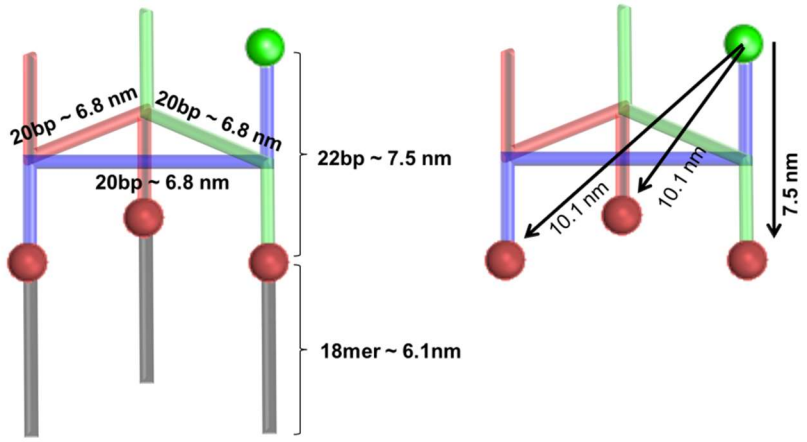

Figure 2.8: Cartoon illustrating the dimensions of the foundation rung. Note that for simplicity the cartoon portrays in color (green, red and blue) the double-stranded segments of **CS#-cap** hybridized to the triangular DNA scaffold **T** and rigidifying strands **RS#**. The gray segments illustrate the sticky ends of **CS#-cap** in **FR** hybridized to the 18 mer Biotin-Cy5 strands. Not shown are the 10 base-long single-stranded DNA sticky ends of the foundation rung at the top of the structure.

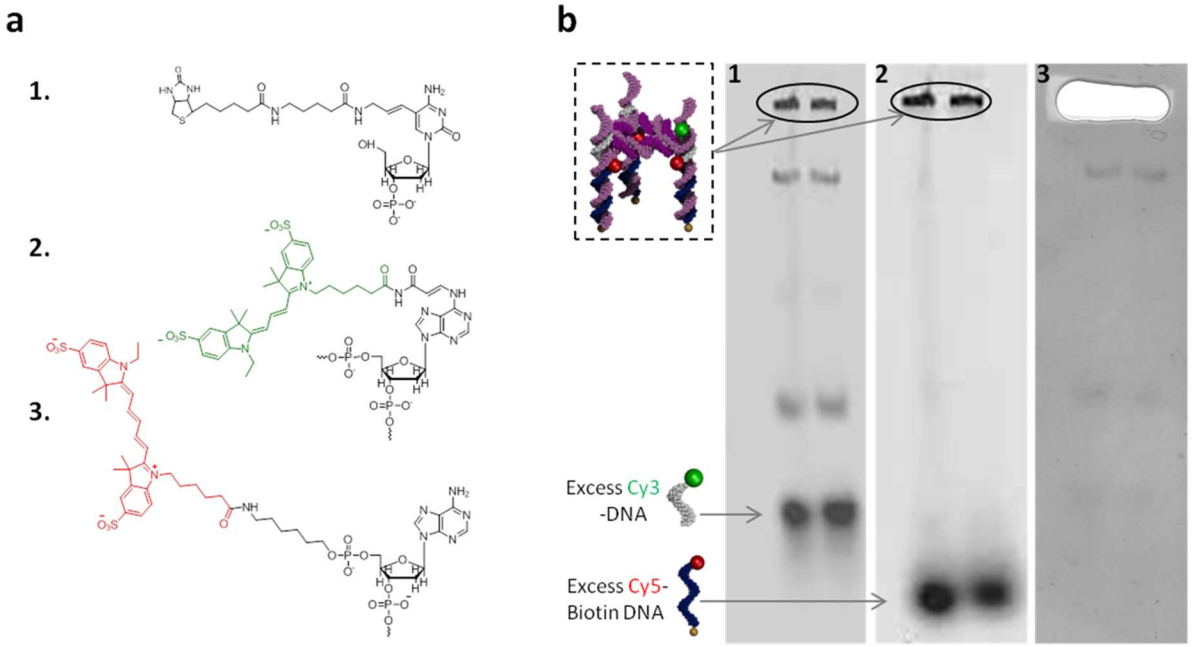

Figure 2.9: a. Structure of the various dye conjugates utilized, Cy3 appears in green and Cy5 in red. **a1.** Corresponds to the biotin conjugation to the cytosine base of the DNA strand. **a2.** Corresponds to the Cy3 conjugation to the adenine base of the DNA strand. **a3.** Corresponds to the Cy5 conjugate at the 5' end of the DNA strand. **b.** Native PAGE analysis showing the assembly of the foundation rung. **b1.** Emission of the Cy3 dye following a 532 nm excitation. **b2.** Emission of the Cy5 dye following a 633 nm excitation. **b3.** DNA stained with StainsAll after excision of the desired bands.

2.7.2.2 Cy3/Cy5/Atto647N tagged Rung (R) Assembly and Characterization

This rung is generated upon the equimolar combination of reagents **T**, **CS1-3**, and **RS1-3**, at a final concentration of 2.0 μM in 1xTAMg. The solution was hybridized from 95°C to 4°C over 3.5 hours to maximize clean product formation. Native PAGE (8%, 1xTAMg running buffer, stained with StainsAll®) confirmed the clean hybridization of each product, as shown in Figure 2.7.

2.7.2.3 DNA linker pillars (L) Assembly and Characterization

Double-stranded linker pillars were prepared by mixing the corresponding strands in a 1:1 ratio at a scale of 7.0 pmol (1.2 μM) in 1xTAMg buffer (L1= LS1 + DS1, L2 = LS2 + DS23, L3 = LS3 + DS23). These three mixtures were hybridized from 95°C to 4°C over 3.5 hours to maximize clean product formation.

2.7.3 Ensemble Instrumentation

Standard automated oligonucleotide solid-phase synthesis was performed on a BioAutomation MerMade MM6 DNA synthesizer. UV-Vis measurements were performed with a BioTek Synergy HT microplate reader. Gel electrophoresis was carried out on an acrylamide 20 x 20 cm vertical Hoefer 600 electrophoresis unit. Thermal hybridizations and enzymatic digestions were conducted using a Flexigene Techne 96 well thermocycler.

2.7.4 Single Molecule Sample Preparation and Imaging

Coverslips were soaked in piranha solution (25% H_2O_2 and 75% concentrated H_2SO_4) and sonicated for 1 h, followed by multiple water (molecular biology grade), and acetone (high-performance liquid chromatography (HPLC) grade) rinsing cycles. Dry and clean coverslips were then treated with vectabond/acetone 1% v/v solution for 5 min and then rinsed with H_2O and left in dried state until used. In order to prevent non-specific adsorption of biomolecules onto the glass surface, coverslips were functionalized prior to use with a mixture of poly(ethylene glycol) succinimidyl valerate, MW 5000 (mPEG-SVA) and biotin-PEG-SVA at a ratio of 99/1 (w/w), in a 0.1 M sodium bicarbonate solution for 3 h. Excess PEG was rinsed with water, and the coverslips were dried under a N_2 stream.[3,4] In order to reduce photobleaching events, oxygen scavenger solution was prepared consisting of a triplet quencher agent, β-mercaptoethanol 1% v/v and an oxygen scavenger system (D(+)glucose 3% w/v, glucose oxidase 0.1 mg/mL, and catalase 0.02 mg/mL).[5]

Imaging chambers (~8 μL) were constructed by pressing a polycarbonate film with an adhesive gasket onto a PEG-coated coverslip. Two silicone connectors were glued onto the predrilled holes of the film and served as inlet and outlet ports.[6] The surface was incubated with 10 μL of a 0.2 mg/mL streptavidin solution for 10 min. Excess streptavidin was then washed with 100 μL of 1xTAMg buffer.

The surface was next incubated with ~18 μL of the foundation rung flowed gently, to achieve a good surface density (~300 fluorescent spots per 70 μm × 35 μm region). Unbound DNA structures were then flushed out with 30μL of 1×TAMg buffer. For our growth experiment, four solutions of 100 μL each were prepared in four different syringes: DNA Linkers (120 nM), Cy3-tagged DNA rung (39 nM), oxygen scavenger and 1×TAMg buffer. Prior to image acquisition, a tubing was inserted into the inlet port, connecting the chamber to a syringe placed on a syringe pump. Each of the solutions was flowed at a rate of 10 μL/min for 3 minutes (~30 μL) in the following order:

The plunger of the syringe containing DNA linkers was first pushed. After a 5 minutes incubation time, unbound DNA structures were flushed out with 30 μL of 1×TAMg buffer. Subsequently, we pumped the solution containing Cy3-tagged rungs, upon incubation for 5 minutes, the solution containing 1×TAMg buffer and oxygen scavenger was pumped in, removing unbound Cy3-tagged rungs and providing a convenient media for single molecule imaging. A movie (5Hz, 1500 frames) of the region was acquired at this stage. The same cycle of steps is then repeated to achieve a six rung nanotube on the surface.

2.7.4.1 Single Molecule Raster-scan Fluorescence Microscopy

The confocal setup consisted of an Olympus IX-71 inverted microscope provided with a closed-loop sample scanning stage (Nano LP100, Mad City Labs, Madison, WI) used for imaging and sample positioning. Samples were excited continuously employing the 514 nm (1.0 kW/cm^{-2}) or the 633 nm (6.6 kW/cm^{-2}) output from a HeNe laser. The circularly polarized laser beam was introduced via a single mode fiber optic and directed by a dichroic beamsplitter (z514-633rdc DCLP, Chroma, Rockingham, VT) to the sample via a high numerical aperture (N.A. = 1.40) oil immersion objective (Olympus U PLAN SAPO 100X). Fluorescence emission was

collected through the same objective and then transmitted or reflected by a beam splitter (640DCXR Chroma, Rockingham, VT) to two avalanche photodiode detectors (Perkin Elmer Optoelectronics SPCM-AQR-14, Vaudreuil, Quebec, Canada). The emission was cleaned from any residual laser excitation by a 514 nm or 633 nm holographic Raman notchplus filter (Kaiser Optical Systems, Ann Arbor, MI) or a HQ685/80M and a HQ590/70 (Chroma, Rockingham, VT). Images 30 μm x 30 μm consisting of 256 by 256 pixels were acquired by collecting the intensity for 1 ms at each pixel. A home built LabView routine was used for data acquisition and stage positioning. A National Instruments NI-PCI-6602 board was used as a counter board.

2.7.4.2 TIRF Microscopy and Image Analysis

Fluorescence single molecule experiments were carried out using a total internal reflection fluorescence microscope (TIRFM) and a confocal fluorescence microscope. The TIRF microscope consisted of an inverted microscope (IX71, Olympus) equipped with a laser-based TIRFM illumination module (IX2-RFAEVA-2, Olympus) coupled to two diode-pumped solid-state green and red lasers (532 nm, 641 nm CrystaLaser). The beam position was adjusted using the illuminator to attain total internal reflection through an oil-immersion objective (N.A. 1.45, Olympus PLAN APO N 60x). Fluorescence emission was collected through the objective and images were captured with an EMCCD camera (CascadeII: 512B, Photometrics, Roper Scientific). For Cy5 imaging, the laser beam was coupled into the microscope objective using a beam splitter (FF660-Di01-25×36, BrightLine, Semrock). Fluorescence light was spectrally filtered with a (HQ685/70, Chroma Technology) emission filter. For imaging of Cy3 the laser beam was coupled into the microscope objective using a beam splitter (FF562-Di02 25x36, BrightLine, Semrock). The emission is then refocused by a lens with a focal length equal to 150 mm. Emission was chromatically separated using dichroic mirrors (640dcxr, Chroma Technology) with the ‘green’ and ‘red’ emission filtered through band pass filters (HQ590/70M and HQ685/80M, respectively, Chroma Technology) before being captured each by one half of the EMCCD camera chip. The camera was controlled using Image-Pro Plus 5.1 (Media Cybernetics), capturing 8-bit 512 x 512 pixel images with an exposure time of 200 ms, a conversion gain of 3, and multiplication gain of 4095. Excitation was carried out at a full power setting (25 mW) with a power output of 9.1 mW at the objective for the green (532 nm) laser.

The excitation power of the red laser ranged between 3 and 7 mW at the objective based on the experiment. We observe typically ~150-300 spots over one field of view (35μm × 70μm). Fluorescence intensity time traces of individual molecules were extracted from the videos using a self-written algorithm in IDL and Matlab defining a square region of 3×3 pixels around the centers of the spots captured. The steps in intensity-time traces were evaluated and counted manually. The steps within every trace were very similar in amplitude, but vary from trace to trace due to the Gaussian profile of the laser beam.

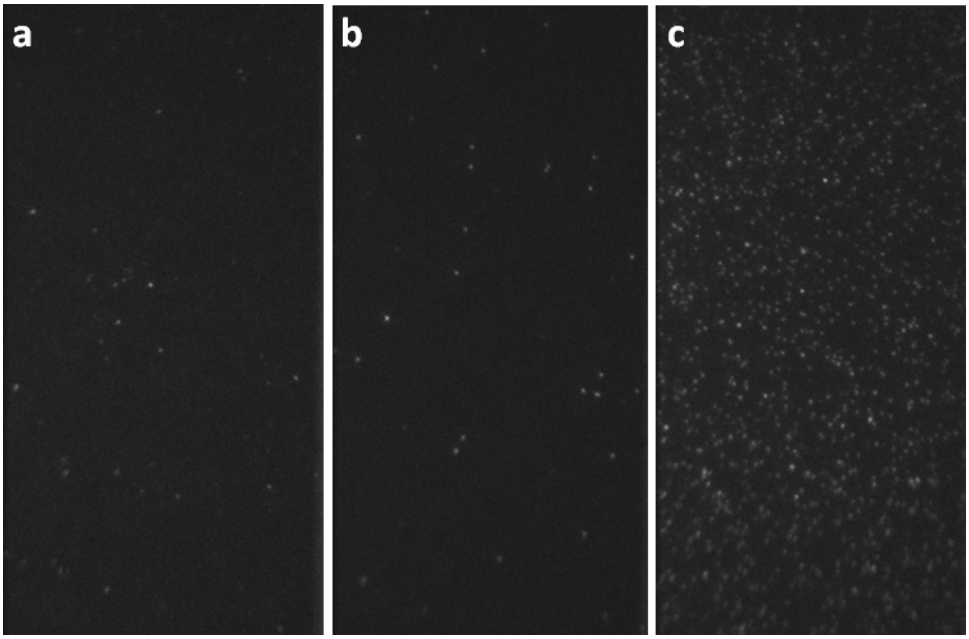

Figure 2.10: TIRFM control experiments to test the binding specificity of the foundation rung and the Cy3-tagged rung. a. The Cy3-tagged DNA rung flown on a streptavidin-surface shows negligible binding. **b.** The foundation rung flown on a biotin-surface (no streptavidin added) shows negligible binding. **c.** The foundation rung flowed on a streptavidin-coated shows binding. Images are 35 x 70 μm^2.

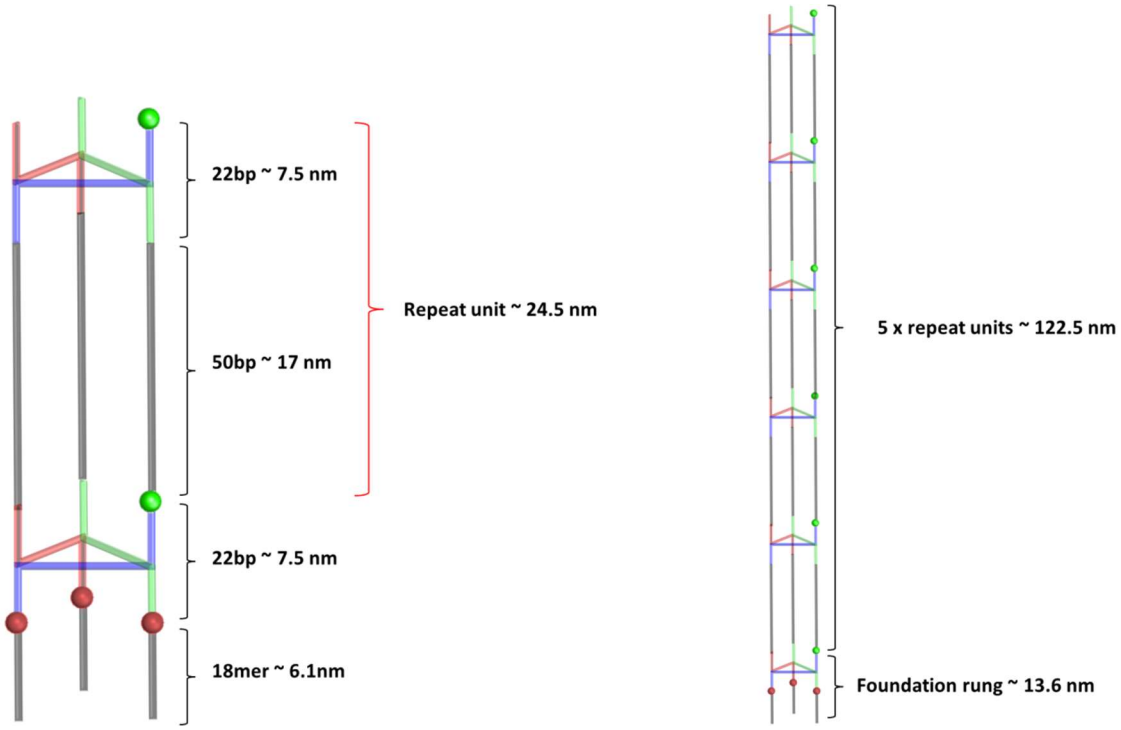

Figure 2.11: Cartoon illustrating the dimensions of the DNA nanotube following the first and up to 5 addition cycles of L and R. Each addition cycle contributes 24.5 nm to the nanotube length, growing away from the surface. Note that for simplicity the cartoon portrays in color (green, red and blue) the double-stranded segments of **CS#** (and **CS#-cap** for **FR**) hybridized to the triangular DNA scaffold **T** and rigidifying strands **RS#**. The gray segments (except those in **FR**) illustrate the linker pillars **L**. The full length of the linking strands (**LS#)** in **L** are shown, consisting of 50 bases, however 10 bases at the top and bottom of **LS#** in **L** are actually connected to 10 bases of the complementary strands **CS#** in **R**. Not shown in **a** or **b** are the 10 base-long single-stranded DNA sticky ends of the last repeat unit **R** in the nanotubes.

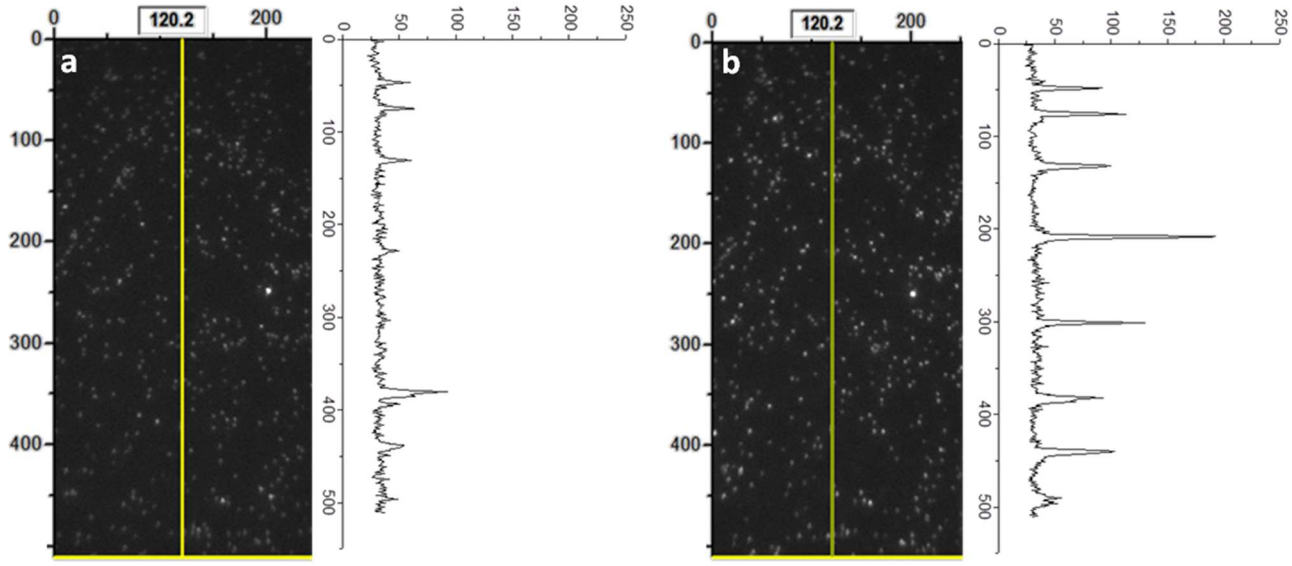

Figure 2.12: Line-scan on TIRFM images acquired prior and after the first addition cycle: **a.** Before the addition (emission due to Cy3 in the foundation rung); **b. A**fter the addition**.** Images are 35 x 70 μm^2.

2.7.4.3 Binomial distribution calculations

The theoretical distribution of Cy3 dyes attached to the foundation rungs was obtained by solving the following equation based on a binomial model[10]:

$$f(n; M, P) = \binom{M}{n} P^n (1-P)^{M-n} = \left(\frac{M!}{n!\,(M-n)!}\right) P^n (1-P)^{M-n}$$

Given n_{rungs}, the probability of n_{dye} attached is:

$$f(n_{dye}; n_{rung}, P_{dye}) = \binom{n_{rung}}{n_{dye}} {P_{dye}}^{n_{dye}} (1-P_{dye})^{n_{rung}-n_{dye}}$$

Where n_{rungs} is the number of rungs added (n_{rungs}= 1, 2,…6), n_{dye} is the number of bleaching steps (number of dyes), and P_{dye}=0.86 is the experimentally determined labeling efficiency for the Cy3 dye based on the measured absorbance and reported extinction coefficient of the dye-labeled DNA. The same model will describe the theoretical distribution of Cy5 dyes, however P_{dye}=0.91 in this case.

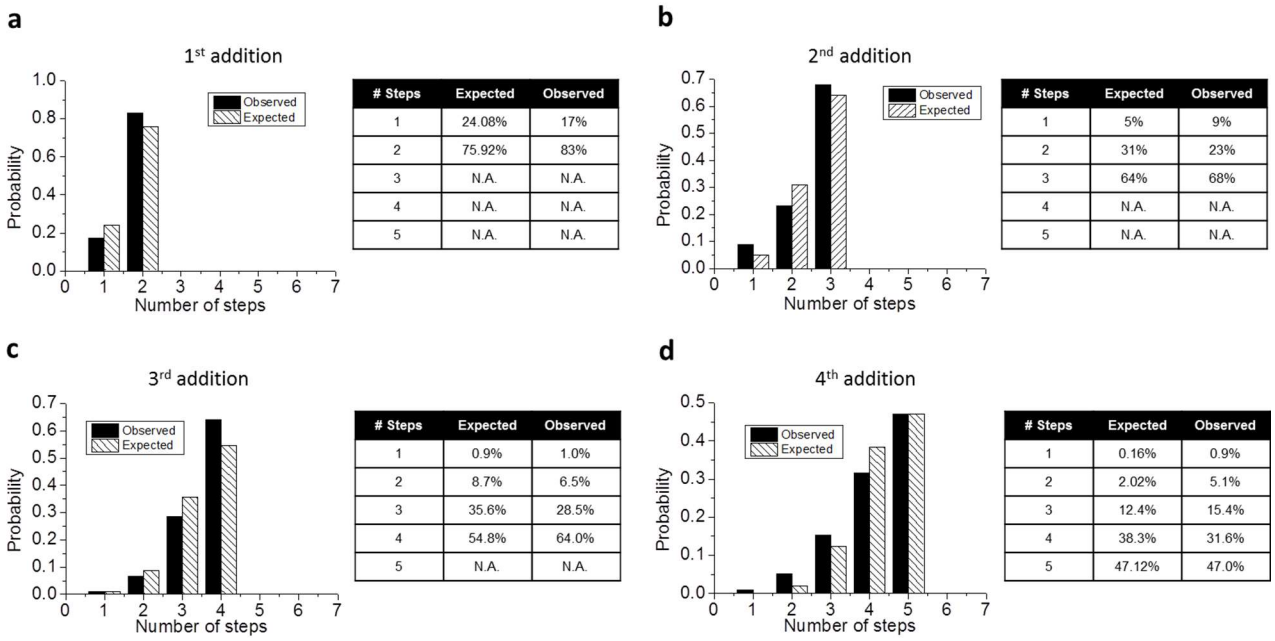

# Steps	Expected	Observed
1	24.08%	17%
2	75.92%	83%
3	N.A.	N.A.
4	N.A.	N.A.
5	N.A.	N.A.

# Steps	Expected	Observed
1	5%	9%
2	31%	23%
3	64%	68%
4	N.A.	N.A.
5	N.A.	N.A.

# Steps	Expected	Observed
1	0.9%	1.0%
2	8.7%	6.5%
3	35.6%	28.5%
4	54.8%	64.0%
5	N.A.	N.A.

# Steps	Expected	Observed
1	0.16%	0.9%
2	2.02%	5.1%
3	12.4%	15.4%
4	38.3%	31.6%
5	47.12%	47.0%

Figure 2.13: TIRF images acquired after an increasing number of addition cycles following immobilization of the foundation rung. Panels a, b, c, and d show the experimentally obtained probability distribution for number of Cy3 dyes (and photobleaching steps) per surface-grafted DNA nanotube following the addition cycles, overlaid for comparison with the theoretical expectations. Both estimated and experimental percentiles are also listed.

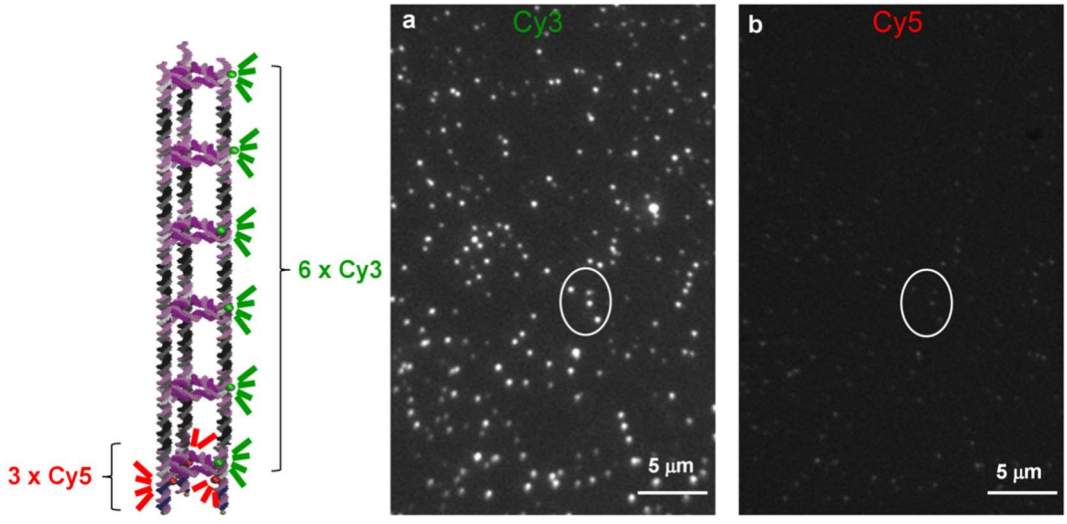

Figure 2.14: TIRFM images of surface-grafted DNA nanotubes assembled following 5 cycles of addition of repeat units. The images were acquired for the same region upon

excitation and emission collection of Cy5 first and Cy3 next. Suitable bandpass filters and excitation with laser diodes with 641 nm output (Cy5 excitation) and 532 nm output (Cy3 excitation) ensured there is no cross talk between green and red channels.

2.7.4.4 Imaging of nanotubes bearing 20 rungs alternating Cy3 and Atto647N

A total of around 150 bright fluorescent spots were observed in any given imaged region, with Cy3 and Atto647N emissions co-localizing in space, an indication that the imaged DNA nanotubes contained both Cy3 and Atto647N fluorophores (Fig. 5b). It is important to mention that in our analysis we only considered molecules colocalizing in the red and green channels. Due to the rare yet possible non-specific binding of the DNA labeled rungs, 12 % of the imaged single molecules did not show colocalization and further showed a single step photobleaching pattern (i.e. one rung structures). These traces were excluded from the analysis. We note that non-specifically bound structures may be washed after in subsequent additions and would not lead to truncated nanotubes.

Our choice of Atto647N over Cy5 for the photobleaching experiment reflects on the need to have trajectories characterized by long enough intervals of steady intensity in-between photobleaching steps. Atto647N has significantly improved photostability over Cy5 or Alexa 647 under our experimental conditions, desired for these experiments where rapid photobleaching and/or blinking may compromise the counting of rungs. We found that the average survival time for Atto647N (55s) was one order of magnitude larger than that for Cy5 (2s) in the absence of oxygen scavenger (Fig. 2.15), conditions that we chose to minimize any blinking due to e.g. reactions with thiols or formation of long lived intermediates.[11] Given the above result, we may also conclude that the 3 Cy5 dyes labeling the foundation rung will photobleach fast enough to not interfere with the counting of Atto647N via photobleaching steps.

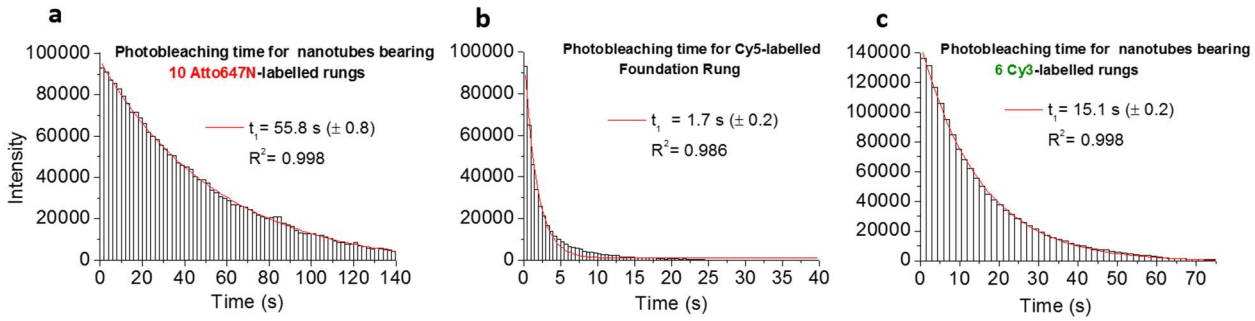

Figure 2.15: Histograms assembled from the photobleaching time recorded for a. Atto647N-labeled nanotubes, **b.** Cy5-labeled foundation rung. **c.** Nanotubes containing 6 Cy3 labeled rungs acquired with conditions similar to those reported in Figure 5. Imaging was conducted in the absence of oxygen scavenger.

Binomial distributions recorded for two different Cy3 labeling efficiencies (91% and 80%)

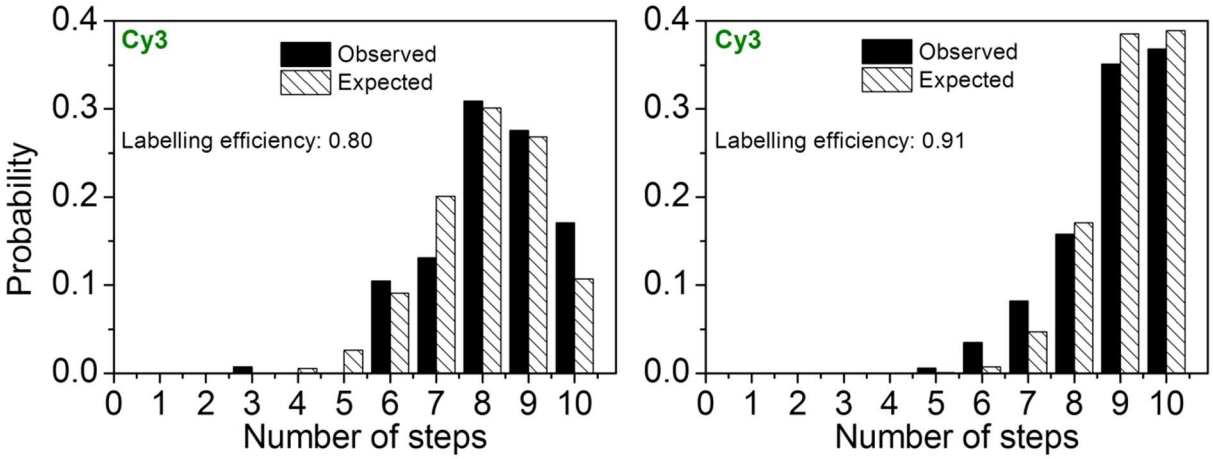

Figure 2.16: Experimentally obtained probability distribution for the number of Cy3 dyes. Two samples of long DNA nanotubes bearing 20 rungs (10 labeled with Cy3 and 10 labeled with Atto647N) were monitored. Nanotubes were prepared with two different batches of Cy3 labeled rigidifying strand (RS). **a.** Data obtained for nanotubes prepared from a batch with an experimentally determined Cy3 labeling efficiency of 80%. **b.** Data obtained for nanotubes prepared from a batch with an experimentally determined Cy3 labeling efficiency of 91%. Overlaid for comparison is the theoretical expectation.

2.7.5 Super-Resolution STORM[7-9] Imaging

Fluorescence imaging was carried out using an inverted Nikon Eclipse Ti microscope equipped with the Perfect Focus System (PFS) implementing an objective-type TIRF configuration with a Nikon TIRF illuminator and an oil-immersion objective (CFI SR Apo TIRF 100× Oil Immersion Objective Lens, numerical aperture (NA) 1.49). 3D images were acquired with a cylindrical lens inserted in the detection pathway.[8] The effective pixel size was 160 nm. With these settings, two lasers were used for excitation (Agilent MLC400B Monolithic Laser Combiner): 561 nm (1 mW, measured out of the objective) and 647 nm (30 mW, measured out

of the objective). For Cy3 imaging, the laser beam was passed through a multiband cleanup filter (ZET405/488/561/647x, Chroma Technology) and coupled into the microscope objective using a multiband beam splitter (ZT405/488r/561/640rpc, Chroma Technology). Fluorescence light was spectrally filtered with a (ET600/50m, Chroma Technology) emission filter. For Cy5 imaging, the laser beam was coupled into the microscope objective using a beam splitter (ZT647rdc, Chroma Technology). The emission from Cy3 was spectrally filtered with emission filters (HHQ665lp and ET705/72m, Chroma Technology). All movies were recorded onto a 256×256 pixel region of a back-illuminated electron-multiplying charge-coupled device (EMCCD) camera (iXon X3 DU-897-CS0-#BV, Andor Technology). STORM movies were analyzed with the N-STORM module of the NIS element from Nikon.

2.7.5.1 Calibration for 3D localization

Calibration for the 3D localization was performed with a coverslip containing immobilized beads (FluoSpheres Carboxylate-Modified Microspheres, 0.02 µm, dark red fluorescent (660/680), Life Technologies). The calibration was carried out using the NIS element AR routine. The sample was mounted on top of a z nanopositioning system (Mad City Labs, Inc. Nano-Drive^{TM}) with a travel range of 100 µm controlled by the NIS element in the Nikon software.

2.7.5.2 Buffer for STORM Imaging of Cy5

STORM measurements were carried out in an oxygen-depleted buffer. The pH 7.3 buffer was prepared with 10 mM HEPES (Fischer), 20 mM NaCl (Ambion), 0.8% W/V β-D(+) Glucose (Sigma-Aldrich), 165 units/mL Glucose Oxidase (Sigma-Aldrich) and 142 mM 2-mercaptoethanol (Sigma-Aldrich). The Buffer was flowed at a rate of 2 µL/min. All experiments were conducted at room temperature (22-23 ^{o}C).

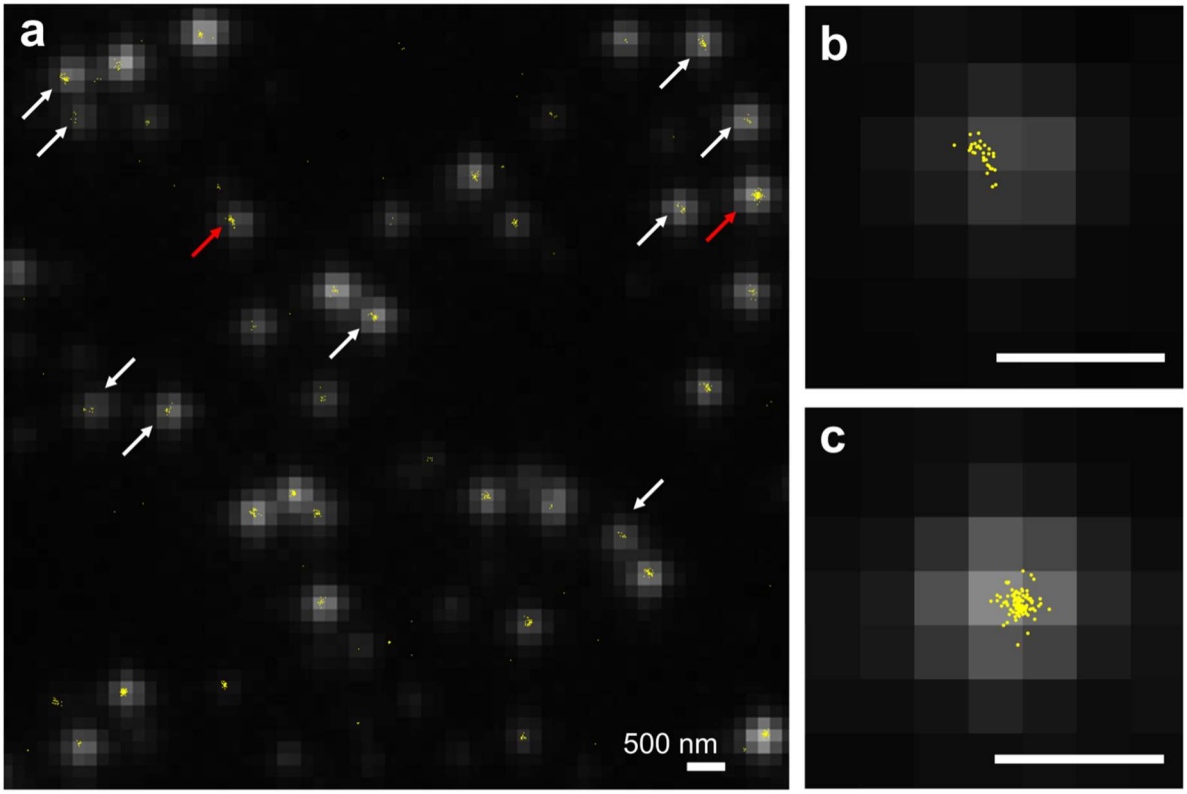

Figure 2.17: STORM Super-resolution image of nanotubes bearing 20 rungs alternating Cy3 and Cy5: Shown is the reconstructed image obtained in the red (Cy5) channel. Every localization event is recorded as a yellow marker. The yellow markers trace the multiple fluorophores along a nanotube. The reconstructed super resolution image is superimposed over the standard diffraction limited TIRF image obtained in the green channel upon directly exciting Cy3 (gray scale image with black background). The superposition enables observing the nanotubes in standard (gray scale) and STORM super resolution (yellow markers) confirming the colocalization of the dyes. Arrows point to elongated structures. Panels b and c show enlarged views of an elongated and a circular looking structures (red arrows in panel a). Scale bars are 500 nm.

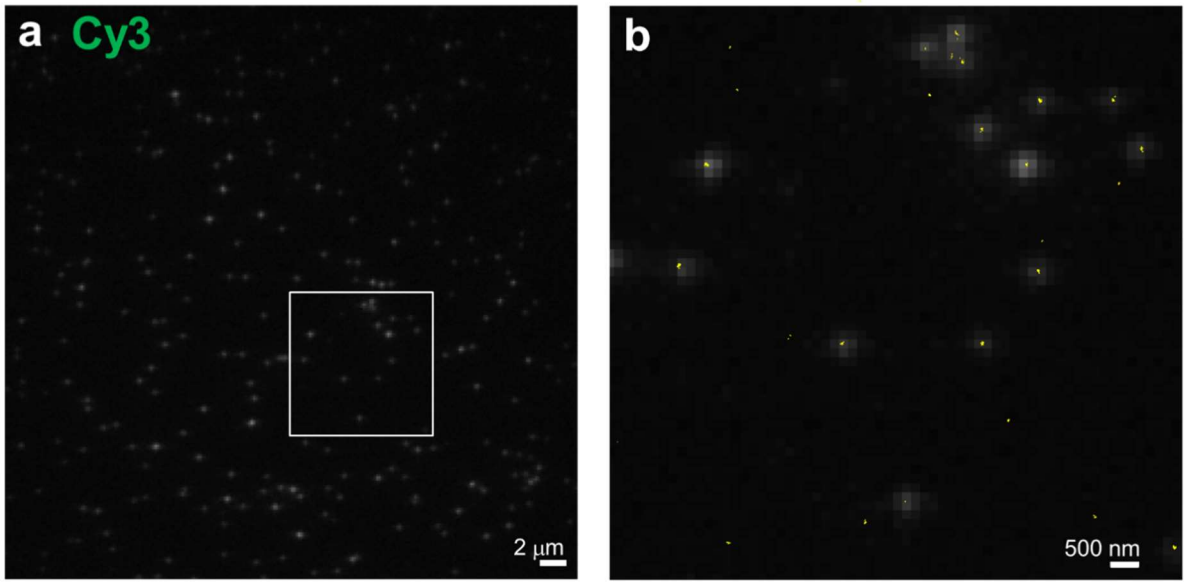

Figure 2.18: STORM Super-resolution image of the foundation rung labeled with 1 Cy3 and 3 Cy5 dyes: a. Image acquired upon direct excitation of Cy3, scale bar is 2 µm. **b**. Magnification of the highlighted region (4x) showing the reconstructed image obtained in the red (Cy5) channel (yellow dots) superimposed over the image obtained upon directly exciting Cy3 (pixels in gray scale). Specifically, every localization event recorded during STORM imaging is recorded as a yellow marker. The yellow markers trace the multiple fluorophores along a nanotube. The reconstructed super resolution image is superimposed over the standard diffraction limited TIRF image obtained in the green channel upon directly exciting Cy3 (gray scale image). The superposition enables observing the nanotubes in standard (gray scale) and STORM super resolution (yellow markers) confirming the colocalization of the dyes. Arrows point to elongated structures. Scale bar is 500 nm.

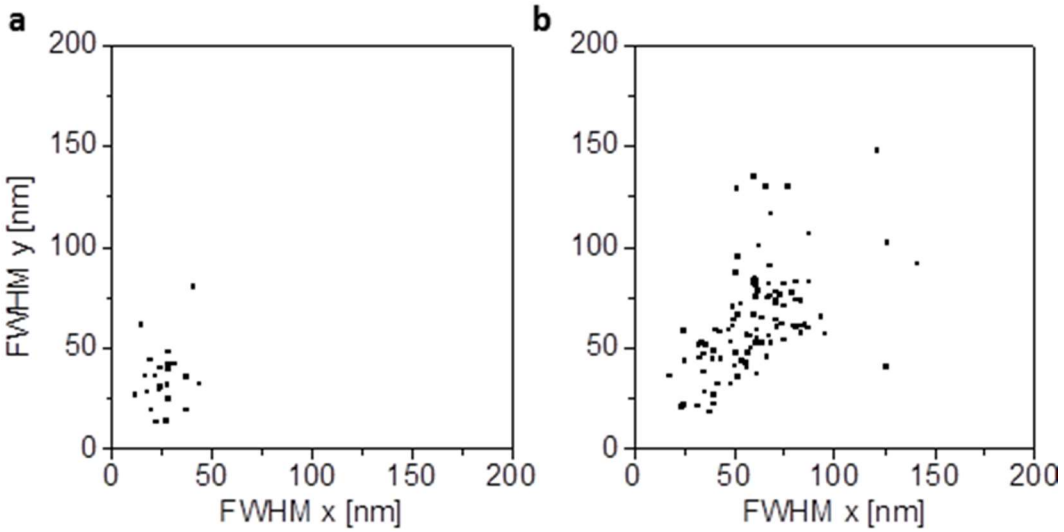

Figure 2.19: Correlation of FWHM in x and y axis. a. FWHM correlation of x v/s y axis acquired for individual foundation rungs. **b.** FWHM correlation for nanotubes bearing 20 rungs alternating Cy3 and Cy5.

Table 2.4: Statistical analysis of localizations: Average standard deviation (sd) and full width at a half maximum (FWHM) recorded for the foundation rungs and the 20 rung-long nanotubes in x, y and z.

	Foundation Rung		***Nanotube***	
Axis	*sd [nm]*	*FWHM [nm]*	*sd [nm]*	*FWHM [nm]*
X	11.2	26.4	27.0	63.6
Y	14.8	34.8	27.8	65.5
Z	37.0	87.2	45.1	106.1

A total of 27 and 105 clusters were analyzed for the foundation rung and the nanotubes, respectively.

2.8 References

1. Aldaye, F.A. et al. Modular construction of DNA nanotubes of tunable geometry and single- or double-stranded character. *Nature Nanotechnology* **4**, 349-352 (2009).

2. Lo, P.K. et al. Loading and selective release of cargo in DNA nanotubes with longitudinal variation. *Nat Chem* **2**, 319-328 (2010).

3. Roy, R., Hohng, S. & Ha, T. A practical guide to single-molecule FRET. *Nat Meth* **5**, 507-516 (2008).

4. Ngo, A.T., Karam, P., Fuller, E., Burger, M. & Cosa, G. Liposome Encapsulation of Conjugated Polyelectrolytes: Toward a Liposome Beacon. *J. Am. Chem. Soc.* **130**, 457-459 (2007).

5. Ha, T. Single-Molecule Fluorescence Resonance Energy Transfer. *Methods* **25**, 78-86 (2001).

6. Karam, P., Ngo, A.T., Rouiller, I. & Cosa, G. Unraveling electronic energy transfer in single conjugated polyelectrolytes encapsulated in lipid vesicles. *Proc. Natl. Acad. Sci. USA* **107**, 17480-17485 (2010).

7. Dempsey, G.T., Vaughan, J.C., Chen, K.H., Bates, M. & Zhuang, X.W. Evaluation of fluorophores for optimal performance in localization-based super-resolution imaging. *Nat. Methods* **8**, 1027-1036 (2011).

8. Huang, B., Wang, W., Bates, M. & Zhuang, X. Three-Dimensional Super-Resolution Imaging by Stochastic Optical Reconstruction Microscopy. *Science* **319**, 810-813 (2008).

9. Rust, M.J., Bates, M. & Zhuang, X.W. Sub-diffraction-limit imaging by stochastic optical reconstruction microscopy (STORM). *Nat. Methods* **3**, 793-795 (2006).

10. Hastie, P. et al. AMPA receptor/TARP stoichiometry visualized by single-molecule subunit counting. *Proc. Natl. Acad. Sci. USA* **110**, 5163-5168 (2013).

11. Ha, T. & Tinnefeld, P. Photophysics of Fluorescent Probes for Single-Molecule Biophysics and Super-Resolution Imaging. *Annu. Rev. Phys. Chem.* **63**, 595-617 (2012).

3 Stoichiometry and dispersity of DNA nanostructures using single molecule photobleaching pair correlation analysis.

Author contributions: **Amani A. Hariri** performed the single molecule photobleaching measurements and carried out the data analysis. **Amani A. Hariri** designed experiments and wrote the manuscript with **Prof. Sleiman** and **Prof. Cosa**. **Jean Francois DesJardens** programmed the automated MATLAB routine for the photobleaching step counting. **John Hardwick** assisted **Amani A. Hariri** in the optimization of the photobleaching steps, characterization and purification of the foundation rung. **Amani A. Hariri** and **Graham Hamblin** carried out the DNA synthesis. **Robert Godin** performed the MATLAB simulations on nanotubes with different labelling efficiencies. **Prof. Wiseman**, **Prof. Sleiman** and **Prof. Cosa** supervised the work.

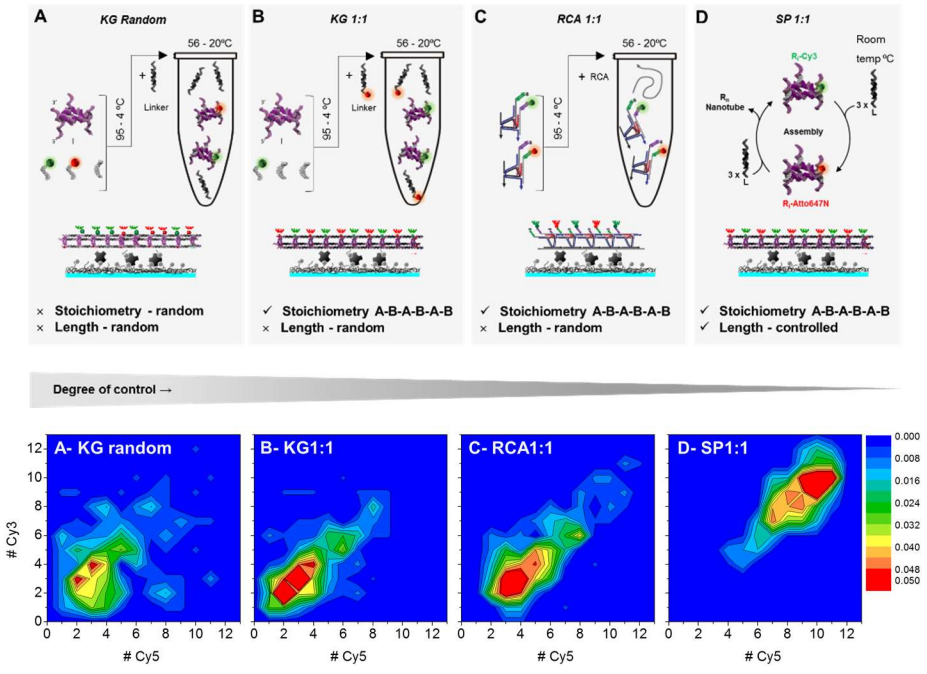

3.1 Introduction

The synthetic power towards building highly complex chemical assemblies that incorporate organic and/or biological building blocks has tremendously advanced in the past decade.[1] Both top-down and bottom-up approaches have enabled the systematic and rapid fabrication of numerous symmetric or periodic nanostructures with precisely organized features.[2] However, the development of larger and more robust constructs is accompanied with many technical challenges, the most significant of which is the high error rate in assembly.[3] This constitutes a major hurdle for the application of nanostructures in dynamic devices and nanomachines where even small defects can drastically affect performance. Currently, we are lacking powerful methods at the analytical level to better inspect and correct the structure and validate the composition of large nanoscale objects in order to facilitate their applications in areas such as photonics, medicine and energy.[4]

Single molecule fluorescence methodologies are uniquely poised to unravel the structural properties and dynamics of complex supramolecular systems.[5] A number of systems of key biological relevance have been explored involving oligomeric proteins, protein-DNA and protein-RNA, as well as protein-lipid interactions.[6] Learning from our own work in this area, we have expanded single molecule fluorescence strategies towards the characterization of synthetic supramolecular structures and more particularly, DNA-based nanostructures.[7] By careful design of the labeling schemes utilized to fluorescently tag supramolecular structures of interest and following a judicious choice of imaging conditions including surface passivation, excitation power, frame capture rate, fluorophore choice, buffer media, and antifading agents, we have built a robust protocol to rapidly dissect the structure and dynamics of synthetic DNA nanotubes that we postulate will be extendable to supramolecular systems in general.

Here, we describe a single molecule fluorescence method that enables us to assign polydispersity, sequence pattern and stoichiometry for different DNA nanotubes. Working with fluorescence intensity-time trajectories acquired from images of single molecules of doubly labeled DNA nanotubes bearing a green Cy3 and red Cy5/or ATTO647N fluorescent dyes along their backbone, and upon monitoring single photobleaching steps in both colors, we successfully retrieved key structural parameters of four DNA nanotube systems differing in their preparation method. An algorithm that automatically counts photobleaching steps in both channels and assigns

them to a given nanotube was built to facilitate selection and interpretation of the data. Automation allowed analysis of large two-color datasets consisting of hundreds of nanotubes monitored in parallel over time through thousands of frames. Utilizing our approach, we are capable of selecting and isolating every nanostructure with its molecular profile and providing a rapid and systematic way to accurately assess the outcome of synthetic work building supramolecular systems. We postulate that the method described herein, while developed for DNA nanotubes, will be instrumental to many research groups synthesizing large supramolecular structures or studying naturally occurring ones.

3.2 Results and Discussion

3.2.1 Single molecule photobleaching study

Several groups have previously employed one-color single molecule photobleaching studies to elucidate the stoichiometry of plasma membrane protein aggregates, RNA or DNA structures and synthetic nanomachines.[8] A major complexity in photobleaching data analysis lies in that with increasing copy number, there is an increasing probability that two or more fluorophores will bleach either simultaneously or within a short period of time (few frames), which may skew the step size distribution and complicate the estimation of a unitary photobleaching step size. In addition, the dynamic range of current EMCCD cameras prevents the accurate resolution of photobleaching steps from noise as the number of dyes recorded (and steps expected) is increased beyond ca. 10. For this reason, the number of countable steps reported in the literature has, to our knowledge, not exceeded 11 steps in size.[8b, 9]

These limitations make the application of photobleaching analysis to larger assemblies significantly challenging. We reasoned that by tagging repeat units in supramolecular systems of interest with an increasing number of spectrally distinguishable fluorophores[10], one may proportionally increase the number of units accurately counted. Additionally, colocalization of the different labels may validate the success of the assembly. [8c, 11] Key to our method is the implementation of a two-color (green and red emission) single-molecule photobleaching technique in order to unequivocally count the number of green and red repeat units in each of the structures.

3.2.2 Single molecule imaging set-up

In order to acquire fluorescence intensity time trajectories of dually-labelled (green Cy3 and red Cy5 or ATTO647N) individual supramolecular structures, we utilized a total internal reflection fluorescence microscope (TIRFM) equipped with an EMCCD camera. Polycarbonate film imaging chambers were assembled onto glass coverslips pre-coated with a mixture of polyethylene glycol (PEG) and biotin-tagged PEG to prevent nonspecific adsorption. Individual dye-labeled DNA nanotubes were next specifically immobilized on the chambers via biotin streptavidin interactions (Figure 3.1A, and See Experimental Section 3.4.2). A low surface density was sought to minimize the possibility of having two nanotubes within a diffraction-limited region. Excitation in the form of an evanescent field employed the 638 nm output of a diode laser first until all red dyes were bleached followed by the 532 nm output of a second diode laser next. Photobleaching events were thus recorded sequentially to avoid artifacts in the analysis of photobleaching trajectories arising from bleeding of Cy5/ATTO647N emission into the green channel and of Cy3 emission into the red channel. Exciting the red emissive fluorophore first further prevented its premature photobleaching when recording the green channel emission upon 532 nm excitation as Cy5/ATTO647N may be partially excited with this wavelength. About 200 bright fluorescent spots were observed in any given image, with green and red emissions co-localizing in space, an indication that the two fluorophores resided within the same volume and that the imaged DNA nanotubes contained both units (Figure 3.1B). For each single nanotube imaged, the fluorescence intensity-time trajectory was observed to decrease stepwise over time, giving a descending "staircase" photobleaching pattern with a measurable number of discrete intensity levels (Figure 3.1C-D).

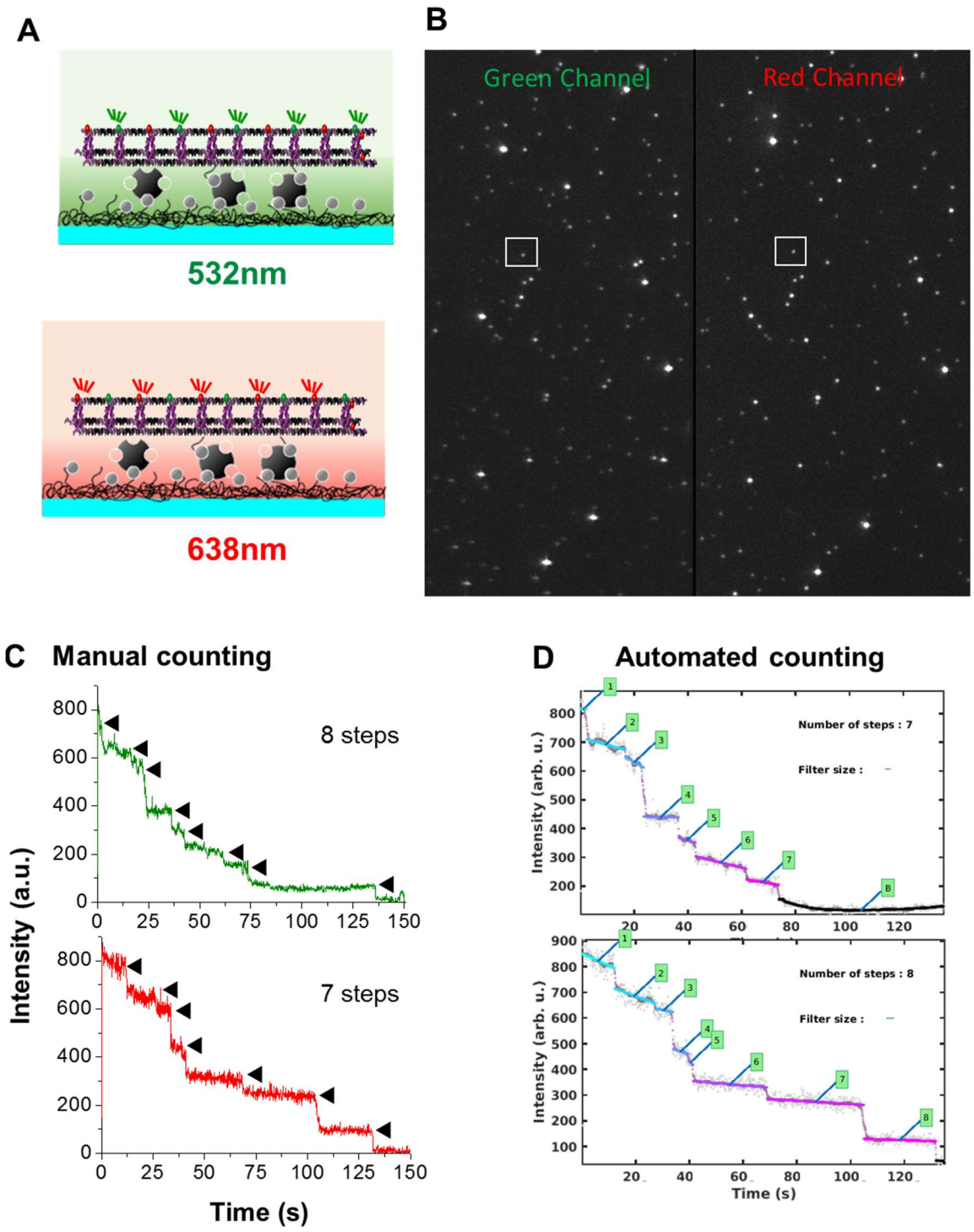

Figure 3.1: Photobleaching analysis of DNA nanotubes. A. Illustration of the surface bound DNA nanotubes under different laser excitation (641nm, top and 532nm, bottom). B. Typical two-color TIRF images of the dually-labelled DNA nanostructures showing the colocalization of the green and red emission signals in space to emphasize the co-existence of both fluorophores in one structure (scale: 35 µm × 70 µm). C. Manual counting: Fluorescence intensity-time trajectories showing the photobleaching steps of the Cy3 and Cy5 labels colocalized in space (black arrows).

D. Automated counting: Fluorescence intensity-time trajectories showing the photobleaching steps of the Cy3 and Cy5 labels colocalized in space (Green squares).

3.2.3 DNA nanotubes design and preparation

We utilized different DNA structures, assembled via synthetic strategies yielding increasing levels of control in structure, stoichiometry and polydispersity, to validate our method. A total of four different synthetic strategies were explored based on previously published protocols[7, 12]. By organizing triangular DNA polygons on top of one another using linking strands, we generated a variety of nanotube systems with tunable rigidity and porosity. Common to all of the nanotubes is the DNA rung, a building block constructed from a closed triangular single-stranded DNA scaffold characterized by orthogonal sequences in each of its three sides. The rung was completed after the hybridization of three strands (CS1-2-3), each complementary to a triangle side and presenting an extended non-complementary region at the ends for subsequent functionalization along the vertices ('sticky ends'). Next, three rigidifying strands were hybridized at the vertices to render the rung sticky ends better oriented in space. Fluorescence studies required the two sets of rungs to be fluorescently tagged (green and red). One rung was assembled with one Cy3-labelled rigidifying strand, and the other with either a Cy5 or an ATTO647N labelled rigidifying strand. Linking pillar strands (LS) were then used to connect the rungs and generate elongated DNA nanotubes (See Experimental section 3.4.1).

The different assembly strategies are outlined in figure 3.2 (See Experimental section 3.4.1, Figures 3.7-8). A solution-based growth approach, which gives little control over length, was adopted for samples A, B, and C. Sample A (KG Random) consisted of randomly mixing Cy3 and Cy5 labelled DNA rungs that would polymerize in the presence of linkers, with no control over the length or sequence pattern of the end-product (Figure 3.2A). For sample B (KG1:1), the nanotube was designed bearing Cy3 labelled DNA rungs and Cy5 labelled DNA linkers that were randomly polymerized as for sample A; this yields nanotubes with a 1:1 sequence pattern of dyes as shown in Figure 3.2B. Sample C (RCA1:1) used the rolling circle amplification (RCA), an enzymatic process that produces long and highly polydisperse single-stranded DNA backbones (∼1400−15000 bases long) from a cyclic template. This gives a long repeating strand that replaces one of the struts and guides the nanotube assembly, as described in reference [7b]. The backbones

are produced with alternating regions binding Cy3 and Cy5 labelled DNA rungs to form templated DNA nanotubes with 1:1 sequence patterns as shown in Figure 3.2C. Another assembly approach exploited a solid-phase synthesis towards a sequential construction to control the length and patterns on every position of DNA nanotubes. We applied this approach to sample D (SP1:1), where we built the tubes step by step on the surface by adding, in an alternating fashion, Cy3 and ATTO674N labelled DNA rungs with DNA linkers in between to generate nanotubes with controlled length and 1:1 sequence pattern (Figure 3.2D).

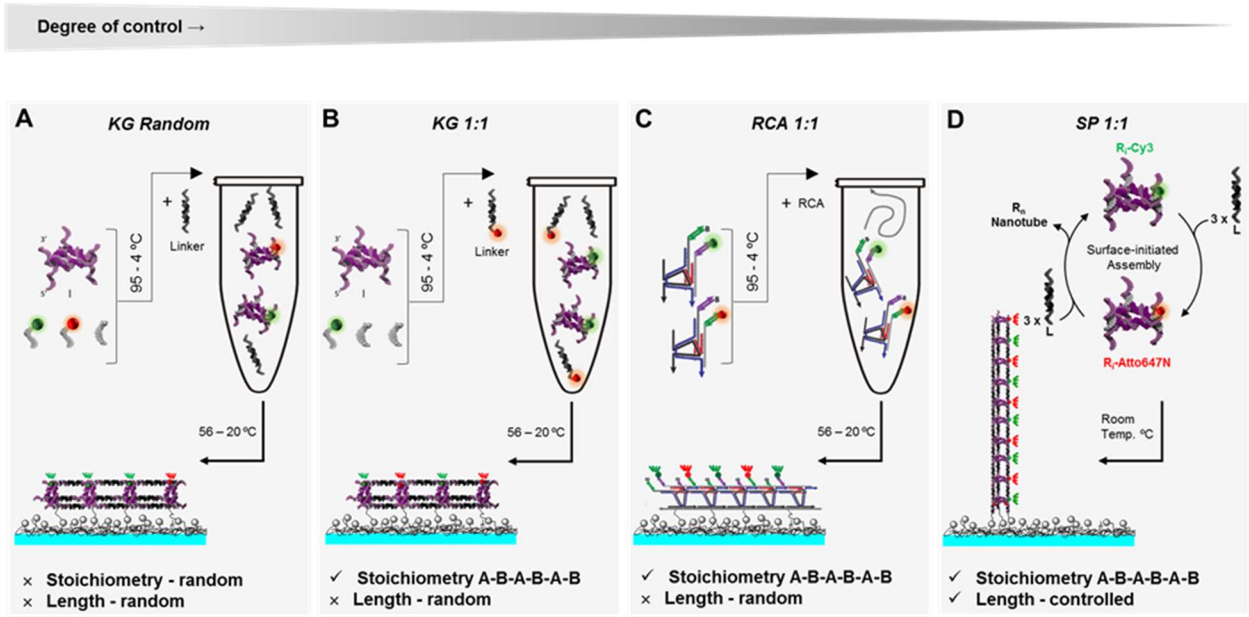

Figure 3.2: Description of DNA nanotubes systems with different level of control over their polydispersity and stoichiometry: A. DNA nanotubes assembled in solution following a random polymerization of Cy3 and Cy5 labelled-DNA rungs with linkers, (random length and stoichiometry). B. (left) DNA nanotubes assembled in solution following a random polymerization of Cy3-labelled DNA rungs and Cy5-labelled DNA linkers (random length and 1:1 stoichiometry); (right) DNA nanotubes assembled by the hybridization of Cy3 and Cy5 labelled DNA rungs on an ABAB enzymatically produced DNA backbone, (random length but controlled stoichiometry 1:1 Cy3:Cy5). C. DNA nanotubes assembled by a stepwise growth synthesis on the surface of Cy3 and Cy5 labelled DNA rungs, (controlled length and controlled stoichiometry 10:10 Cy3:Cy5).

3.2.4 Data acquisition optimization

In order to obtain good trajectories with discrete, clearly observable steps, two requirements must be fulfilled: i) a sufficiently long time interval should exist prior to a photobleaching event; ii) the intensity should be large enough such that each photobleaching step may be distinguishable from shot noise fluctuations. To this end, it was crucial to maximize photon collection, in a given time period, while minimizing possible saturation in the image. Optimizing parameters such as excitation power, exposure time, camera gain, camera frame rate, fluorophore choice, and antifading agents was thus of paramount importance for the method success.

3.2.4.1 Imaging acquisition parameters. The signal to noise ratio (SNR) is defined as:

$$SNR = \frac{N}{\sqrt{N}} = \sqrt{N}$$

With *N* being the number of photons collected. SNR is therefore improved with signal intensity (larger N). Because the signal intensity increases linearly with excitation power, the laser power employed has to be high enough to obtain a satisfactory signal to noise ratio (SNR) with the largest possible amplitude. However, one needs to keep the power relatively low to increase the average fluorophore survival time and avoid saturation. Alternatively, improving the signal can be realized by increasing the exposure time. Yet, the right exposure time can be more critical to optimize as a balance between short exposures to be able to capture all photobleaching events, particularly those occurring at very proximate time intervals, and longer exposures to minimize shot noise. To minimize the saturation of the detector and maximize the dynamic range, the gain should be set at the lowest possible value at which the read noise is minimal. It is equally important that the camera's readout rate and gain be optimized so that the low read noise is maintained.

3.2.4.2 Fluorophores choice, buffer media and antifading agents. Because rapid photobleaching and/or blinking of the dyes may compromise the counting of the steps in a trajectory, the choice of the fluorophore and the photoprotection media is critical. From the cyanine family, two of the sulfoindocyanine dyes, Cy3 and Cy5 are extensively used in single molecule studies, given their high absorption coefficient (ca. 150,000 $M^{-1}cm^{-1}$ and 250,000 $M^{-1}cm^{-1}$, respectively) and modest fluorescence quantum yield (0.15 and 0.3, respectively). We selected Cy3 for the green channel, as it proved relatively photostable (15-19 s, typical fluorescence trajectory emission period) without the need for addition of any photoprotection system. For the red channel, we tested Cy5 and ATTO647N with a number of anti-fading conditions. We

ultimately established that the combination of ATTO647N and Trolox in 1x TAMg buffer yields the best result in terms of photostability (emission time period of 55 s), blinking behaviour (minimal) and favorable conditions for the paired green dye Cy3. All the components were prepared in molecular water except for the triplet quencher Trolox, we dissolved it in ultra-grade methanol (MeOH) and filtered it in order to minimize impurities.

3.2.4.3 Fluorophore emission period optimizations. Given the stochastic nature of photobleaching, we estimated a reasonable fluorophore average emission period (τ) of ca. 20 s. This τ value would ensure that on average, on a 10 dye structure, 6 dyes would bleach in 20 s and by 5τ (ca. 100 s), photobleaching would be almost complete, or complete in a large fraction of the structures imaged. From our experimental results, a range of τ of 20-55 s was ideal for Cy3 and ATTO647N dyes.

3.2.4.4 Automated routine for step counting. In order to automatically retrieve the number of bleaching steps for multiple fluorophores in a given nanotube, we developed a step detection algorithm, capable of automatically counting photobleaching steps in intensity-time trajectories in two color channels simultaneously and assigning them to a given nanotube. This step detection algorithm tracked and counted photobleaching events by applying a novel segmentation technique based on point concentration segmentation. The software localized the fluorescent spot positions in the image using a 2D derivative peak detection algorithm over the average image of the recorded movie. It measured the peak shape by fitting it to an elliptic Gaussian and then calculated the point spread function (PSF) radius by averaging the peak radii. The fluorescence intensity-time trajectory was extracted by summing up the intensity of pixels within a region corresponding to three times the radius of the PSF size centred on the peak centroid. The accuracy of the step detection algorithm was initially evaluated using simulated trajectories purposefully designed to exhibit the characteristics observed in the experimental data. The main task of the algorithm was to distinguish bleaching steps of different amplitude from noise or blinking events. The algorithm was able to detect a maximum of six steps. Accuracy dropped for a larger number of steps due to the intrinsic noise arising from the emission of multiple fluorophores which complicates the discrimination of adjacent bleaching steps (see Experimental section 3.5.7). The software is still under optimization.

3.2.5 Single molecule photobleaching: Ratiometric analysis

After processing and retrieving the number of photobleaching steps for each nanotube, we adopted an analysis relying on the distribution of the ratio of green and red steps, i.e., histogram of the green steps/red steps values, in order to assess the stoichiometry of the sample. More than 100 single nanotubes were analyzed in this way for each of the four samples. We first compared two structures differing in the expected distribution of green to red dyes, specifically $RCA_{1\text{-}2}$ and $RCA_{1\text{-}2\text{-}2\text{-}2}$ consisting of nanotubes with 1:1 and 1:3 sequence patterns, respectively (See Figure 3.3AB). As expected, a distribution centered at around 1 with a standard deviation (SD) of 0.49, was observed for sample $RCA_{1\text{-}2}$. Sample $NT_{1\text{-}2\text{-}2\text{-}2}$, with an expected 1:3 ratio yielded a distribution centered at 0.3 with a SD of 1.22. The larger standard deviation in the latter case indicated a higher degree of defectiveness of the patterns generated using RCA 3:1.

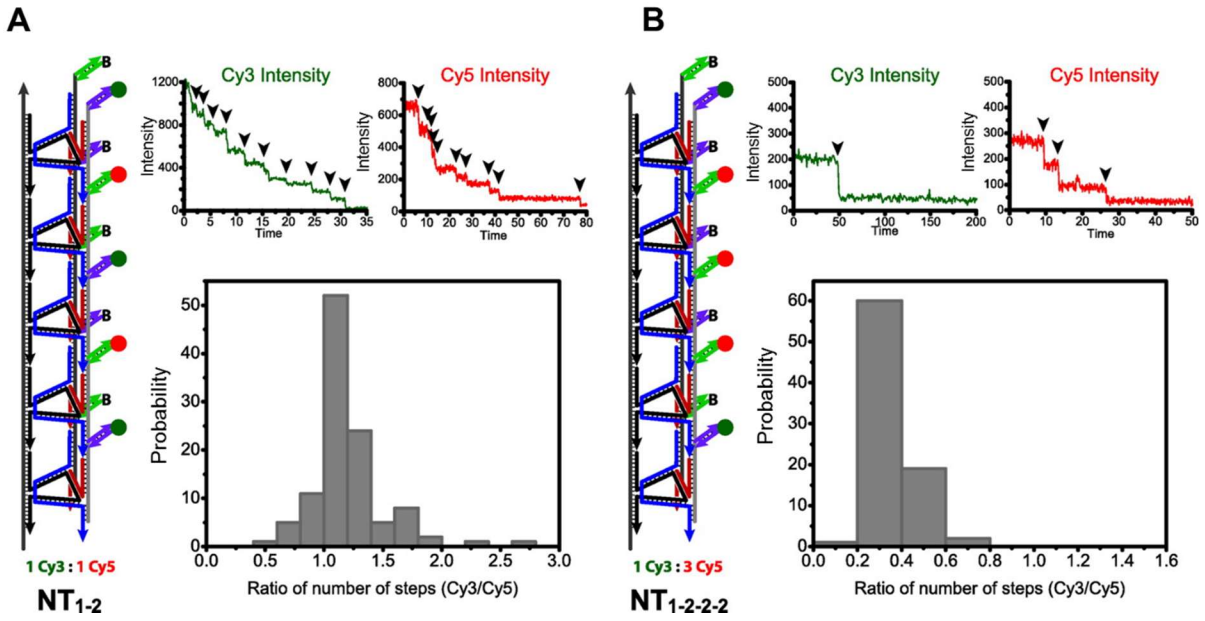

Figure 3.3: Dye-quantized photobleaching analysis on immobilized RCA-DNA nanotubes. Dye-quantized photobleaching analysis of immobilized nanotubes. A. NT1-2, with an expected 1:1 Cy3:Cy5 ratio. Typical photobleaching transients for a single nanotube are shown (arrows indicate bleaching events). A histogram displaying the distribution of the ratio of green steps to red steps for individual DNA nanotubes is also shown. The distribution is centered at 1, as expected. B. NT1-2-2-2, with an expected 1:3 Cy3:Cy5 ratio yields a distribution centered at 0.3 as expected. (Copyright © 2013 American Chemical Society).

Looking at all four constructs depicted in figure 3.2 including $RCA_{1\text{-}2}$, all characterized by having a hypothetical alternating pattern, we recorded mean values close to 1 for the Cy3/Cy5 step

ratio (See Figure 3.4, inset). However, standard deviation (SD) values showed a marked drop in going from sample KG random to SP1:1 signifying the increasing level of control/precision in the structure stoichiometry.

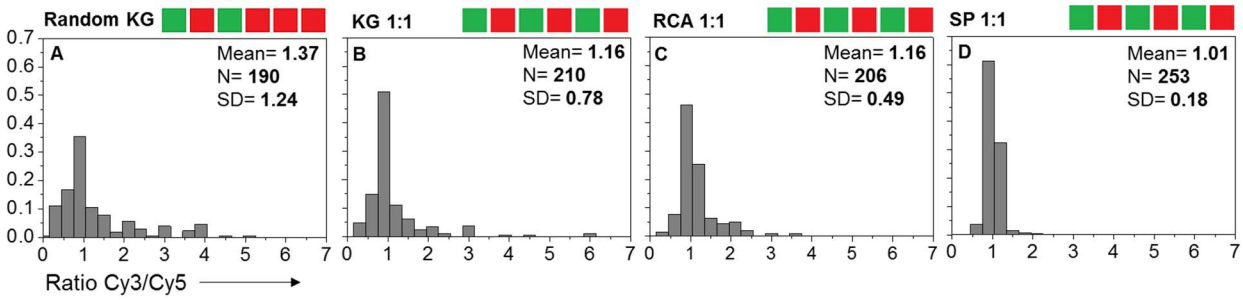

Figure 3.4: Dye-quantized photobleaching analysis on four systems of DNA nanotubes assembled using different strategies. A. Histogram displaying the probability distribution of the ratio of green steps to red steps for a control sample with a random combination of red and green dyes, centered at 1.37 and a standard deviation (SD) of 1.24. (B-D) Histograms displaying the probability distribution of the ratio of green steps to red steps for a DNA sample with 1:1 stoichiometry of the red and green emitters, centered at around 1 (1.16, 1.16, 1.01, respectively) with decreasing SD values (0.78, 0.49, 0.18, respectively). In each case, N is the total number of nanotubes analyzed.

3.2.6 Single molecule photobleaching: Pair correlation analysis

We next conducted a correlation analysis on the number of steps recorded for the green dye versus the red dye in the four nanotube samples. A surface contour plot was subsequently built to facilitate the data visualization (Figure 3.5). We first simulated, a perfectly monodisperse sample of DNA nanotubes composed of 10 green and 10 red rungs/nanotube, with a 100% labelling efficiency of the dye-tagged DNA strands and created a contour plot as a guide. The resulting correlation displayed a single peak whose coordinates are 10:10 (Figure 3.5B1). Deviations from this ideal point would be attributed to various structural characteristics of the nanotubes which we identified by simulating the expected distribution upon varying the 1) dispersity, 2) stoichiometry and 3) labeling efficiency of the sample.

By postulating that the growth of nanotubes is driven by independent processes of rungs accumulating on both the top and bottom of the growing stacks of rungs, then the nanotube size would be expected to follow a Gaussian distribution (See Experimental section 3.4.4 and 3.4.5.1). Given that the nanotubes were observed to grow up to a maximum size of 20 rungs (assuming a

100% labelling efficiency), we generated in MATLAB the dataset of a 2D Gaussian with the range of [x; y] (Cy3; Cy5) being [0;10] in each case and centered at [5;5]. Only values that correspond to the cross-section x=y were plotted to illustrate the 1:1 stoichiometry of the structures (See Experimental section 3.4.5, Figure 3.13). The polydispersity of the sample may be hence assessed by the degree of dispersion along the diagonal as shown in Figure 3.5A1. By considering the case wherein the stoichiometry of dyes in a structure is not controlled, we next computed the theoretical dye distribution (green and red) for the sample of a given size population of DNA nanotubes (monodisperse). For instance, for a monodisperse nanotube population of 20 rungs, the Cy3/Cy5 stoichiometry within DNA nanotubes follows a Gaussian distribution perpendicular to the diagonal (x=y) as shown in figure 3.5A2. The resultant plot of the two characteristics, polydispersity and random stoichiometry, displayed a pronounced deviation along and from the diagonal as illustrated in Figure 3.5A3.

It is critical to generate a theoretical model taking into account the labelling efficiency of the sample in order to deconvolute the effect of the incomplete labeling efficiency of the dye-labeled DNA strands, utilized for the nanotube assembly, on the shape of the distribution and the resulting surface contour plot. The theoretical distribution of the dyes attached to the structure can be obtained by solving a binomial equation:

$$\mathrm{f(n; M}, P) = \binom{\mathrm{M}}{\mathrm{n}} P^{\mathrm{n}}(1-P)^{\mathrm{M-n}} = \left(\frac{\mathrm{M!}}{\mathrm{n!\,(M-n)!}}\right) P^{\mathrm{n}}(1-P)^{\mathrm{M-n}}$$

Given n_{block}, the probability of n_{dye} attached is:

$$\mathrm{f}\left(\mathrm{n_{dye}; n_{block}, P_{dye}}\right) = \binom{n_{block}}{n_{dye}} {P_{dye}}^{n_{dye}}(1-P_{dye})^{n_{block}-n_{dye}}$$

where n_{block} is the number of building blocks in a structure (n_{blocks}= 1, 2,…20), n_{dye} is the number of bleaching steps (number of dyes), and P_{dye} is the experimentally determined labeling efficiency based on the measured absorbance and reported extinction coefficient of the dye-labeled DNA. DNA nanotubes were generated *in silico* using a Monte Carlo method written in the MATLAB environment. In each simulation, 10000 nanotubes were initialized. Next, 20 sequential additions of nanotube rungs were simulated, bearing a green dye or a red dye. The largest possible nanotubes are thus 20 rungs long and contain 10 green dyes and 10 red dyes (Figure 3.5B2-3). For each addition, the success of binding a new nanotube rung was determined by obtaining a random

number (1 representing success, 0 representing failure) from the binomial distribution. The probability of success, physically representing the reaction yield of rung addition, was set to 90% or 100% to explore different outcomes. After each successful addition, the simulation verified whether the added rung was labeled with a dye. Another random number was generated from the binomial distribution and the probability of success, either 90% or 100%, represents the reaction yield of rung labelling with a dye. A 2D histogram was finally built by counting the number of green and red dyes present in each of the 10000 nanotubes simulated. Clearly, while the interplay of sample dispersity and stoichiometry (Figure 3.5A3) may lead to a broad correlation of Cy3 and Cy5, adding the effect of inefficient dye labeling to the constitutive DNA strands may result in an intractable data set. However, a narrow dispersity, defined stoichiometry and efficient labeling should approach an ideal situation as that illustrated in Figure 3.5B1.

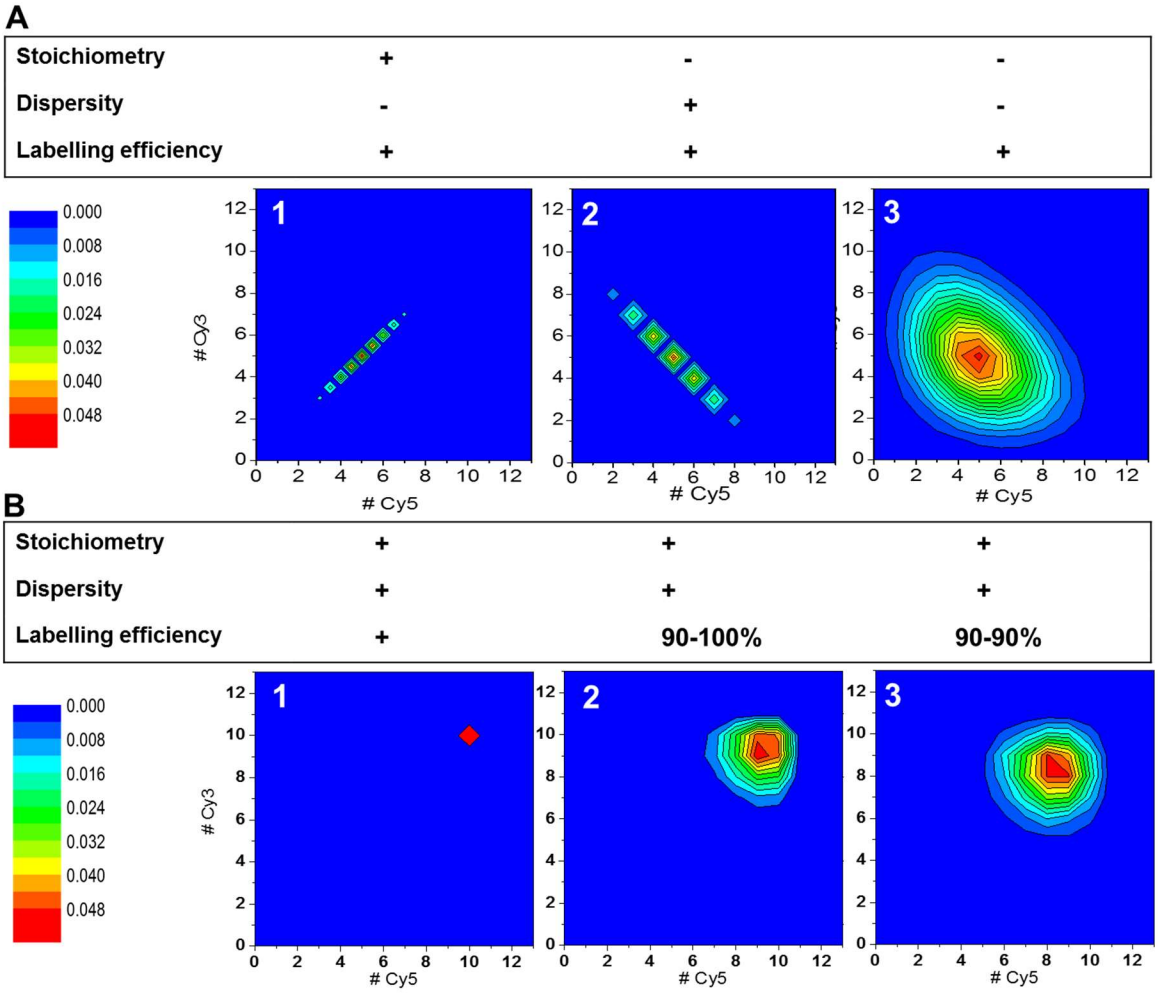

Figure 3.5: 3D color map of simulated DNA nanotubes. A. 3D color map of DNA nanotubes with 100% labelling efficiency (+) but (1) polydisperse (-) and stoichiometric (+), (2) monodisperse (+) and non-stoichiometric (-), (3) polydisperse (-) and non-stoichiometric (-). B. 3D color map of a monodisperse and stoichiometric nanotube sample with 100%-100% labelling efficiency (1), 100:90% labelling efficiency and (2) 90:90% labelling efficiency (3). A color coding shown on the left (blue to red) help reveal the probability of counts (0 to > 0.05) calculated for each given sample.

Figure 3.6 displays the correlation analysis for the four DNA constructs described in figure 3.2. The slope of the linear fit revealed the average stoichiometry of the sample while the corresponding R^2 value indicated the degree of deviation from the average stoichiometry. The values of the slope (a_0) and R^2 extracted from the plots (See Table 3.1) diverged from 1 in going from sample SP1:1 to KG random confirming the decreasing level of precision in the structure stoichiometry, similarly to the results obtained with the ratiometric analysis. This can be attributed to the incomplete dye-labelling of DNA strands, as well as structural defects during the nanotube assembly or to the random nature of rung incorporation (KG random, with poor correlation). On the other hand, the spread along the line provided a measure of the degree of dispersity in the samples (Figure 3.5A1). We quantified this parameter by computing the standard deviation of the distribution along the diagonal (x=y cross section, See Experimental section 3.4.6, Figure 3.19). Nanotubes built sequentially on the surface with complete control over their length presented the lowest spread value (1.62) while those built using a highly polydisperse backbone RCA1:1, showed the largest dispersity along the diagonal (2.40). From the simulations obtained, we note that the spread caused by labeling efficiency is equal in all directions (Figure 3.5B). This indicates that the pronounced spread along the diagonal in the contour plots of the sample SP1:1 is not due to labelling efficiency, but rather to shorter tubes resulting possibly from truncation due to the washing steps throughout the synthesis or strained structures. Alternatively, shorter nanotubes may also arise during the synthesis as some would have failed to incorporate a key substrate or incorporated a defective unit (or dormant units) causing an irreversible structural failure, terminating hence the growth of the tubes. Nanotubes with 95% reaction yield, 95% labelling efficiency and with or without 5% termination yield were simulated (Figure 3.16, Experimental section). While adding the termination factor does elongate the distribution along the diagonal, we observe more tubes with less dyes (say 1 or 2) than with an intermediary (around 5) amount of each dyes. The absence of small tubes may be an indication that the operating mechanism is that larger tubes are more prone

to errors in the addition. The collapse of the larger structures on the surface can reduce the availability of the capture strands on the top rung.

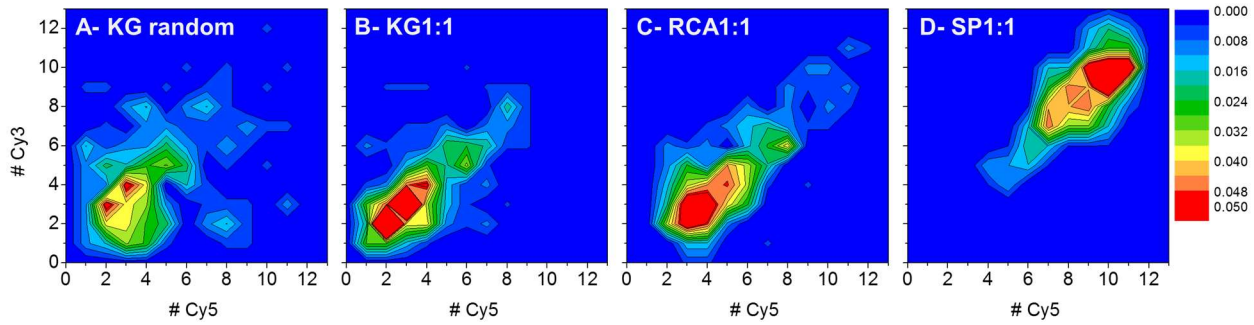

Figure 3.6: 3D color map showing a 2-color correlation of the number of photobleaching steps in green versus red dyes for samples: KG-random (A), KG1:1 (B), RCA1:1 (C), and SP1:1 (D).

Table 3.1: Slope, R2 and standard deviation values extracted from the 3D contour plots.*

Sample	Slope (a_0)	R^2	$SD_{diagonal}$
KG random	**0.821** (0.027)	**0.7128**	**1.84**
KG 1:1	**0.923** (0.038)	**0.8501**	**1.92**
RCA 1:1	**1.022** (0.020)	**0.9246**	**2.40**
SP 1:1	**0.993** (0.010)	**0.9740**	**1.62**

***Figure 3.18, Experimental section 3.4.6**

3.2.7 From single molecule to bulk measurements: PDI values

In addition to the shape and momentum of the distributions established from the two-color single molecule analysis, we can also retrieve bulk measurements upon combining single molecule data and by implementing the fundamental characterization parameters commonly encountered in the polymer chemistry literature (Table 3.2). Using the total number of rungs (M_x= green rungs +

red rungs), we calculated (1) the number average molecular weight (M_n), (2) the weight average molecular weight (M_w) and (3) the polydispersity index (PDI), as defined by the equations below:

$$[1] \quad M_n = \frac{\sum N_x M_x}{\sum N_x} \quad ; \quad [2] \quad M_w = \frac{\sum N_x M_x^2}{\sum N_x M_x} \quad ; \quad [3] \quad PDI = \frac{M_w}{M_n}$$

where N_x, is the number of nanotubes of weight (size) M_x. We note that the molecular weight in this case, is proportional to the number of rungs (steps in green + steps in red) in a given tube. Upon combining single molecule data, an average length size of 10 rungs and an average PDI value of 1.3 were computed for the three solution-based (KG random, KG1:1 and RCA1:1) constructs, indicative of the pre-dominance of short monodisperse structures in these samples. Conversely, for typical step polymerization, which is the mechanism attributed to the solution-based nanotubes elongation, the most probable PDI value is around 2. The lower PDI observed is an indication of a preferential binding of a shorter population of nanotubes, whereas larger structures remain in solution due to the possible unavailability of the biotin molecules (See Experimental section 3.4.8). On the other hand, the solid-phase constructs (SP1:1) presented an average length size of 18 rungs with a PDI value of 1.1, which underlines the advantage of the solid phase approach in producing highly monodisperse samples with a precise length, in comparison with solution-based approaches.

Table 3.2: Bulk quantities extracted from single molecule data sets*

Sample	$\sum N_x$	$\sum N_x M_x$	$\sum N_x M_x^2$	M_w	M_n	PDI
KG random	215	1640	16764	7.62	10.22	**1.34**
KG 1:1	235	1596	14504	6.79	9.08	**1.33**
RCA 1:1	231	2155	25865	9.32	12.00	**1.28**
SP 1:1	278	4402	78628	15.83	17.86	**1.13**

***(includes the monomer units).**

3.3 Conclusion

In this work, we have demonstrated how single molecule-based methods can unravel the structure of nanomaterials through a simple protocol centered on the use of photobleaching steps. Using multiple fluorophores expands the maximum number of repeat units that may be monitored in a supramolecular structure. Every new color, by virtue of having its own detection channel, enables increasing the number of detectable units by ca. 11 steps. By offering a unique combination of the photobleaching and multiple color colocalization features, our approach enables molecular analysis beyond what is possible with the one-color photobleaching method. Additionally, the 3D contour plots provide the fullest representation of the 2-color sets of data and allow a rigorous comparison of contour patterns among the different samples. Using this approach, samples of different dyes composition were readily distinguishable on the basis of the correlated number of steps in the two color analysis: on one hand, the graphs display the slope and deviations of the distribution to evaluate the stoichiometry of the sample, while on the other hand, the spread of the distribution along the diagonal revealed the dispersity of the size of our assembled nanostructures. Together, the different values extracted from the plots provide collaborative information about the characteristics of the structures prepared. This method enables a consistent and systematic way of assessing the polydispersity and stoichiometry of different structures and designs which we posit, will be instrumental for sample characterization, in the new age of complex assemblies at the nanoscale and mesoscale.

3.4 Experimental section

3.4.1 Materials and Methods

3.4.1.1 DNA nanotube synthesis. Acetic acid, boric acid, cyanogen bromide (5M in acetonitrile), EDTA, urea, 4-morpholineethanesulfonic acid (MES), magnesium chloride, StainsAll, GelRed and tris(hydroxymethyl)-aminomethane (Tris) were purchased from Aldrich. 1000Å nucleoside-derivatized LCAA-CPG solid support with loading densities of 25-40 μmole/g, Sephadex G-25 (super fine DNA grade) and reagents were used for automated DNA synthesis as purchased from BioAutomation. 1000Å Phosphate-CPG was purchased from ChemGenes Incorporated. 40% acrylamide/bis-acrylamide 19:1 solution and agarose were purchased from BioShop.

The strands were deprotected and cleaved from the solid support in the presence of concentrated ammonium hydroxide solution (60°C, 16 hours). Polyacrylamide gel electrophoresis (PAGE: 20 x 20 cm vertical Hoefer 600 electrophoresis unit) was employed to purify crude products (8-20% polyacrylamide/8M urea at constant current of 30 mA for 2 hours, with 1xTBE as a running buffer). The desired bands were then excised, crushed and incubated in 11 mL of autoclaved water at 60°C for at least 12 hours. After drying the samples to 1.5 mL, size exclusion chromatography (Sephadex G-25) was used to desalt the solution. The strands were quantified (OD260) by UV/vis spectroscopy with a NanoDrop Lite Spectrophotometer and using IDT's extinction coefficient at 260. ATTO647N/Cy5/Cy3-tagged DNA strands were purchased from IDT and Cy5-Biotin DNA strand was purchased from TriLink Biotechnologies. Gels containing dye-labelled oligonucleotides were visualised (Bio-Rad GelDoc XR+ controlled with the Image Lab software package) using the appropriate excitation wavelength before being stained with GelRed (Biotium). 1xTBE buffer is composed of 90 mM Tris and boric acid, 1.1 mM EDTA, with a pH of ~8.3. 1xTAMg buffer is composed of 45 mM Tris, 7.6 mM $MgCl_2$, with pH adjusted to 8.0 using glacial acetic acid. It is important to note that buffers used in single molecule experiments are prepared with molecular water and are filtered afterwards. 1xMESMg buffer is composed of 250 mM MES, 20 mM $MgCl_2$, with pH 7.6. DNA sequences and designs utilized in constructing the different samples of DNA nanotubes including rungs and linkers used as repeating units are based on published references[7, 12b].

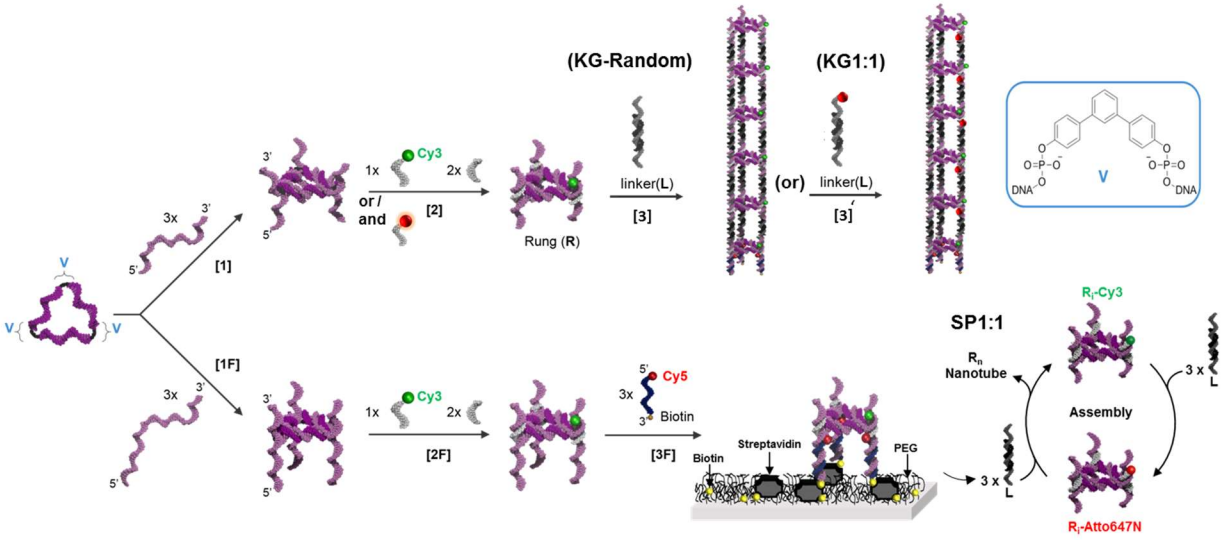

Figure 3.7: Schematic representation of the assembly of the DNA nanotubes. A triangular DNA strand (shown in dark purple) that bears synthetic aromatic corner units (V) at the three

vertices to yield orientation and rigidity is first prepared as previously described. The sequences for each side of the triangle are designed to be orthogonal to each other. Each side is then hybridized to give a complementary sequence (shown in light purple, 1 and 1F); see top for **R** bottom for **FR**). The complementary strands bear long overhang segments at both ends. In the next step (2 and 2F) the overhangs are partially hybridized to three short single-stranded DNA rigidifying segments (shown in light grey). One of these contains a fluorophore of choice (Cy3 in this figure or Cy5). The remaining single-stranded regions of the overhangs provide the rung **R** and **FR** with sticky ends above and below the triangular plane, which enable connection of the rungs to the linker pillars **L** (with no dye 3, and with dye 3'). In the case of **FR** the three sticky ends below the triangular plane are hybridized with three 18-mer single-stranded DNA sequences (shown in dark blue, 3F) that are functionalized at their 3′ end with a biotin moiety, which enables grafting to a substrate through biotin–streptavidin interactions and hence a sequencial addition of labelled rungs (R) and linkers to form nanotubes.

3.4.1.2 DNA nanotubes sample preparation. The four DNA designs used in the manuscript have each a different mode of preparation. The sample design of (A), (B) and (D) is based on the protocol described in reference [7]. For all these cases, the DNA rung (R) and linkers were generated upon the equimolar combination of reagents T, CS1-3, and RS1-3 on one hand for the rung, and on the other hand LS1-DS1, LS23-DS23 for the linkers at a scale of 7.0 pmol (1.2 μM) in 1xTAMg buffer. The solution was hybridized from 95°C to 4°C over 3.5 hours to maximize clean product formation. On one hand, samples (A) and (D) had two different sets of rungs, each with a dye label (Cy3 or Cy5/ATTO647N) on the RS1 strand, mixed with a set of double-stranded linker pillars L1, L2 and L3. On the other hand, sample (B) had one type of DNA rung with a Cy3 label on the RS1 strand, mixed with a set of linkers Cy5-labelled-L1 (Cy5-DS1), L2 and L3. For sample (A) and (B) the different building blocks were annealed in a one pot mixture whereas for sample (D) they were incorporated one by one on the surface in a stepwise fashion (Figure 3.7). Sample C, on the other hand, is based on the RCA patterned nanotubes protocol described in figure 3.8. For further details on this system of nanotube please consult reference [7b].

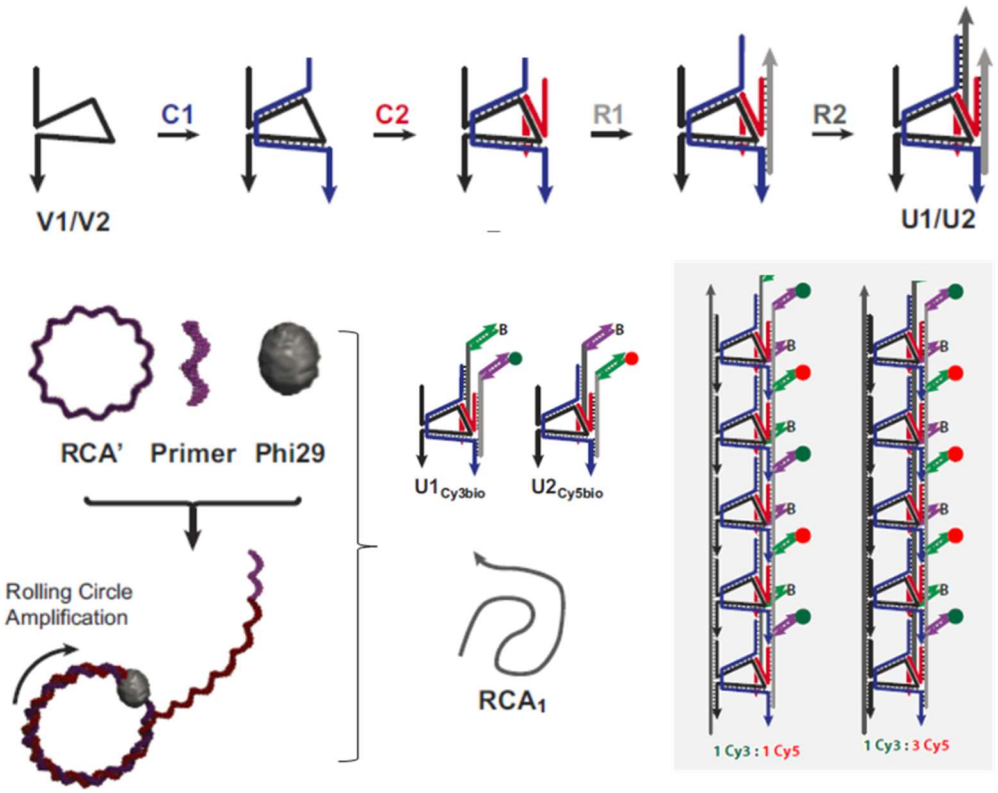

Figure 3.8: Design of triangular rungs (U1-2) units and nanotubes using RCA_1. (Top) A variable strand V1 (black) can bind with complementary strand C1 (blue), which spans the internal section and brings the two variables together creating a unique variable region for binding. Complementary, strand C2 (red) binds the third edge. Rigidifying strands R1 and R2 (grey) bind the overhang C1 and C2. (Bottom) RCA, a long strand with repeating units for (U1-2), produced by rolling circular amplification, is combined with the rungs to produce the patterned DNA nanotubes.

In this case, we synthesized an enzymatically produced backbone (RCA) with repeating attachment sites (1:1 or 3:1 patterns) on which two sets of dye labelled DNA-rungs (Cy3 or Cy5) can be hybridized together with DNA linkers and produce nanotubes. The choice of the labelled strands was such that the distance between the dyes is large enough to minimize FRET (Figure 3.9).

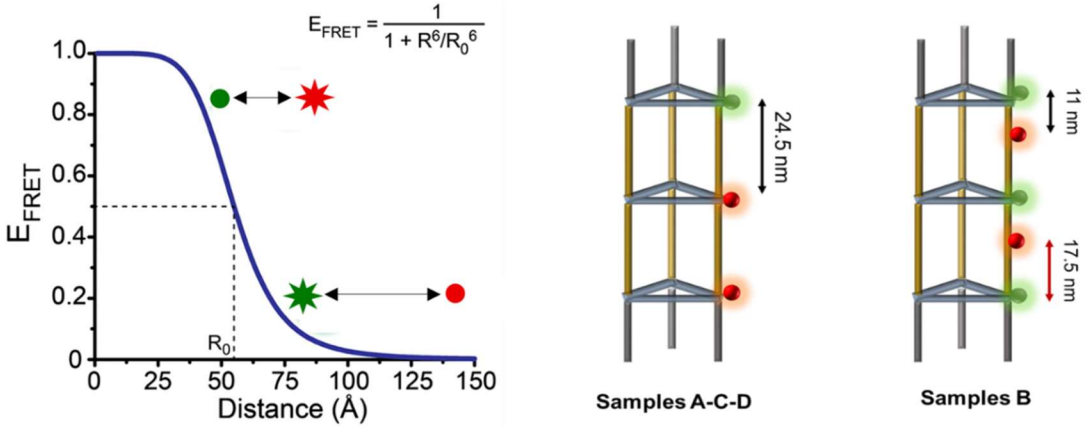

Figure 3.9: Scheme showing the distances between the two dyes (Green-Red) in the different DNA samples. Samples (A, C and D) incorporate the fluorophores on the DNA rungs while sample (B) include them on the rungs and linkers.

3.4.2 Single molecule sample preparation and imaging

3.4.2.1 Coverslip functionalization procedure. Coverslips were soaked in piranha solution (25% H_2O_2 and 75% concentrated H_2SO_4) and sonicated for 1 h, followed by multiple water (molecular biology grade), and acetone (high-performance liquid chromatography (HPLC) grade) rinsing cycles. Dry and clean coverslips were then treated with vectabond/acetone 1% v/v solution for 5 min and then rinsed with H_2O and left in dried state until used. In order to prevent non-specific adsorption of biomolecules onto the glass surface, coverslips were functionalized prior to use with a mixture of poly(ethylene glycol) succinimidyl valerate, M.W. 5000 (mPEG-SVA) and biotin-PEG-SVA at a ratio of 99/1 (w/w), in a 0.1 M sodium bicarbonate solution for 3 h. Excess PEG was rinsed with water, and the coverslips were dried under a N_2 stream. Imaging chambers (~8 µL) were constructed by pressing a polycarbonate film with an adhesive gasket onto a PEG-coated coverslip. Two silicone connectors were glued onto the predrilled holes of the film and served as inlet and outlet ports. The surface was incubated with 10 µL of a 0.2 mg/mL streptavidin solution for 10 min. Excess streptavidin was then washed with 100 µL of 1xTAMg buffer. Next, DNA samples were added and incubated at a concentration of 500pM of DNA nanotubes, to achieve a good surface density (~300 fluorescent spots per 70 µm × 35 µm region). Unbound DNA structures were then flushed out with 50µL of 1x TAMg buffer. Prior to image acquisition, a tubing was inserted into the inlet port, connecting the chamber to a syringe placed on a syringe pump. Oxygen

scavenger solution was flowed at a rate of 5 μL/min throughout the experiment. Movies (200ms, 1500 frames) of the region were acquired at this stage.

3.4.2.2 TIRF Microscopy. Fluorescence single molecule experiments were carried out using a total internal reflection fluorescence microscope (TIRFM) and a confocal fluorescence microscope. The TIRF microscope consisted of an inverted microscope Olympus equipped with a laser-based TIRFM illumination module (IX2-RFAEVA-2, Olympus) coupled to two diode-pumped solid-state green and red lasers (532 nm and 641 nm, respectively from CrystaLaser). The beam position was adjusted using the illuminator to attain total internal reflection through an oil-immersion objective (N.A. 1.45, Olympus PLAN APO N 60x). For Cy5 imaging, the laser beam was coupled into the microscope objective using a beam splitter (FF660-Di01-25x36, BrightLine, Semrock). For imaging of Cy3 the laser beam was coupled into the microscope objective using a beam splitter (FF562-Di02 25x36, BrightLine, Semrock). Fluorescence emission was collected through the objective. The emission was then refocused by a lens with a focal length equal to 150 mm. Images were captured with an EMCCD camera (CascadeII: 512B, Photometrics, Roper Scientific). Emission was chromatically separated using dichroic mirrors (640dcxr, Chroma Technology) with the 'green' and 'red' emission filtered through band pass filters (HQ590/70M and HQ685/80M, respectively, Chroma Technology) before being captured each by one half of the EMCCD camera chip. The camera was controlled using ImagePro Plus 5.1 (Media Cybernetics), capturing 8-bit 512 x 512 pixel images with an exposure time of 100-200ms, a conversion gain of 3, and multiplication gain of [3200-4000]. Excitation was carried out with a power output of 7-9 mW at the objective for the green (532 nm) laser. The excitation power of the red laser ranged between 5-7 mW at the objective based on the experiment. We observe typically ~150-300 spots over one field of view (70 μm × 35 μm).

3.4.3 Single molecule analysis using MATLAB-Origin software

3.4.3.1 Intensity-time trajectories extraction and analysis. Fluorescence intensity-time trajectories of paired molecules (green and red) were extracted from the Tiff movies using a self-written algorithm in IDL and MATLAB defining a square region of 3x3 pixels around the centers

of the spots captured and colocalized. The steps in intensity-time trajectories were evaluated and counted manually. The steps within every trajectory were very similar in amplitude. Different amplitudes are however recorded for different molecules due to the non-homogenous exciting beam (Gaussian shape) resulting in some molecules receiving a slightly stronger excitation intensity. (Figure 3.10)

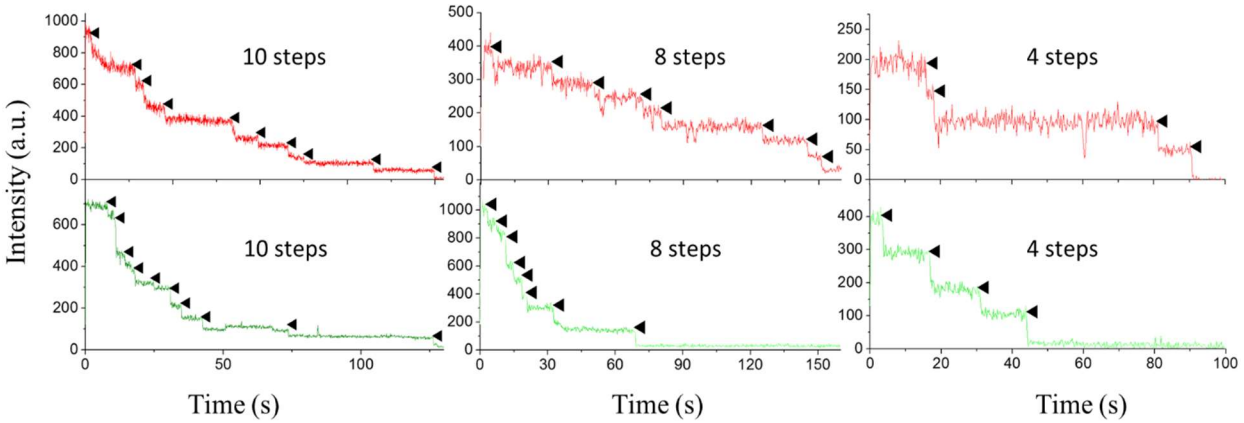

Figure 3.10: Typical photobleaching trajectories of the red and green emitters with optimized conditions for a fast and accurate manual counting.

3.4.3.2 Rejection criteria. Trace files are open and evaluated in MATLAB. A small percentage (10-15% of the trajectories) was rejected due to the following reasons (Figure 3.11): 1) Aggregated tubes (if exponentially decaying trajectories), 2) Molecules with very high intensity that saturate the detector (more than 256 counts/pixel), 3) Trajectories with incomplete photobleaching, 4) Shot noise and 5) Blinking events masking the bleaching steps. Additionally, trajectories that present only one color (no colocalization) possibly due to the non-specific adsorption of dyes or impurities caused by an inhomogeneous surface passivation, were also discarded.

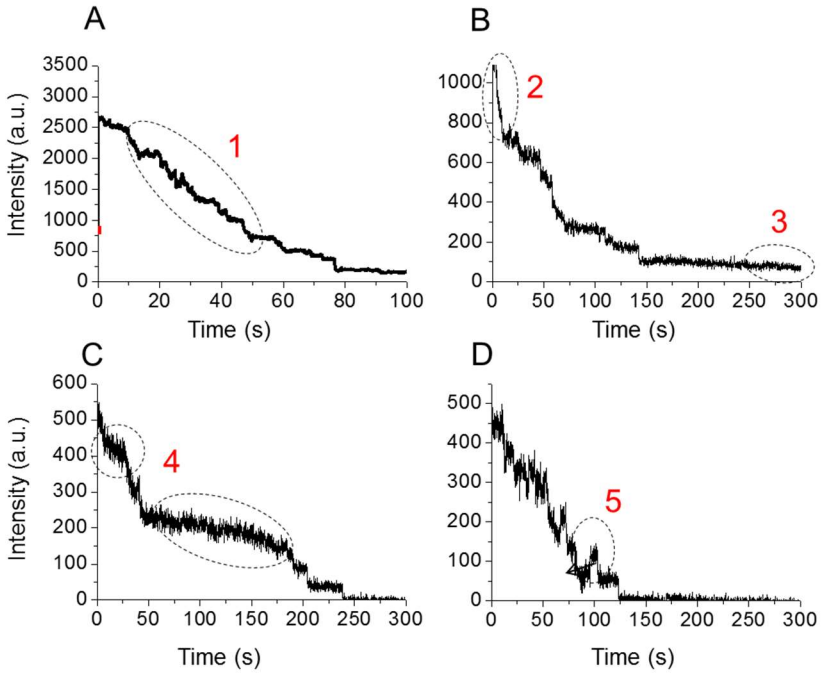

Figure 3.11: Examples of problematic intensity-time trajectories that include (1) exponential bleaching, (2-3) saturation and incomplete photobleaching, (4) shot noise, and (5) blinking events.

3.4.3.3 Sources of errors. Many parameters before and after acquisition affect the accuracy and precision of quantitative fluorescence microscopy: Firstly, errors could be introduced by the microscope (drifting), the detector (noise) and coverslips (impurities). Additionally, errors could be introduced during the analysis process such as: i) missing of steps in the counting process (under or over estimating the number of steps observed and counted); ii) poor labelling efficiencies of the strands (< 100%); iii) Simultaneous bleaching of two or more dyes which has increasing probability with an increasing number of dyes; iv) photobleaching occurring before starting the acquisition.

3.4.4 Analysis of single molecule intensity-time trajectories.

3.4.4.1 Dye-count histogram. Ensemble histograms frequently used in the literature display simply the dispersion of the number of steps in the two different colors separately. Applying this strategy to the different data sets obtained for each DNA sample, we extracted parameters such as the mean, standard deviation and shape of the distributions. It is clear from the plots that in the absence of control over the assembly of the tubes, and by relying on their random polymerization

in solution, a preference for short nanotubes is observed with an average of 4 subunits in each color for samples A, B and C (KG random, KG1:1 and RCA1:1). However, for sample D (SP1:1), when 10 rungs of each color were incorporated sequencially on the surface[7a], the distrubution confirmed the expected outcome with a main population centered at 9 for each color (See Figure 3.12, inset). The standard deviation (SD) values showed a marked increase in going from sample SP1:1 to KG random signifying the decreasing level of control/precision in the structure length size. The good overlap observed upon overlaying the distribution of the green and red dyes in all the samples (Figure 3.12B) demonstrated qualitatively the correlation between the two colors in the various systems. Importantly, we noticed that the shape of the distributions is characterized with a skew towards i) smaller structures in the first 3 samples (A, B and C) and ii) larger structures in the case of sample D. While sample D, synthesised in a stepwise fashion, fits a binomial model as explained earlier, a quantitative fitting is not possible for the other three samples given the lack of understanding of the mechanism underlying the assembly of the tubes. We speculate that a Poissonian model would best describe the system if we assume a step-growth polymerization of the tubes, however, clarifying the mechanism of the nanotubes polymerization requires a larger set of molecules and is beyond the scope of this thesis. More rigorous studies are underway in our laboratory to elucidate the details of the growth of these nanotubes and only preliminary results are outlined in the next chapter (4).

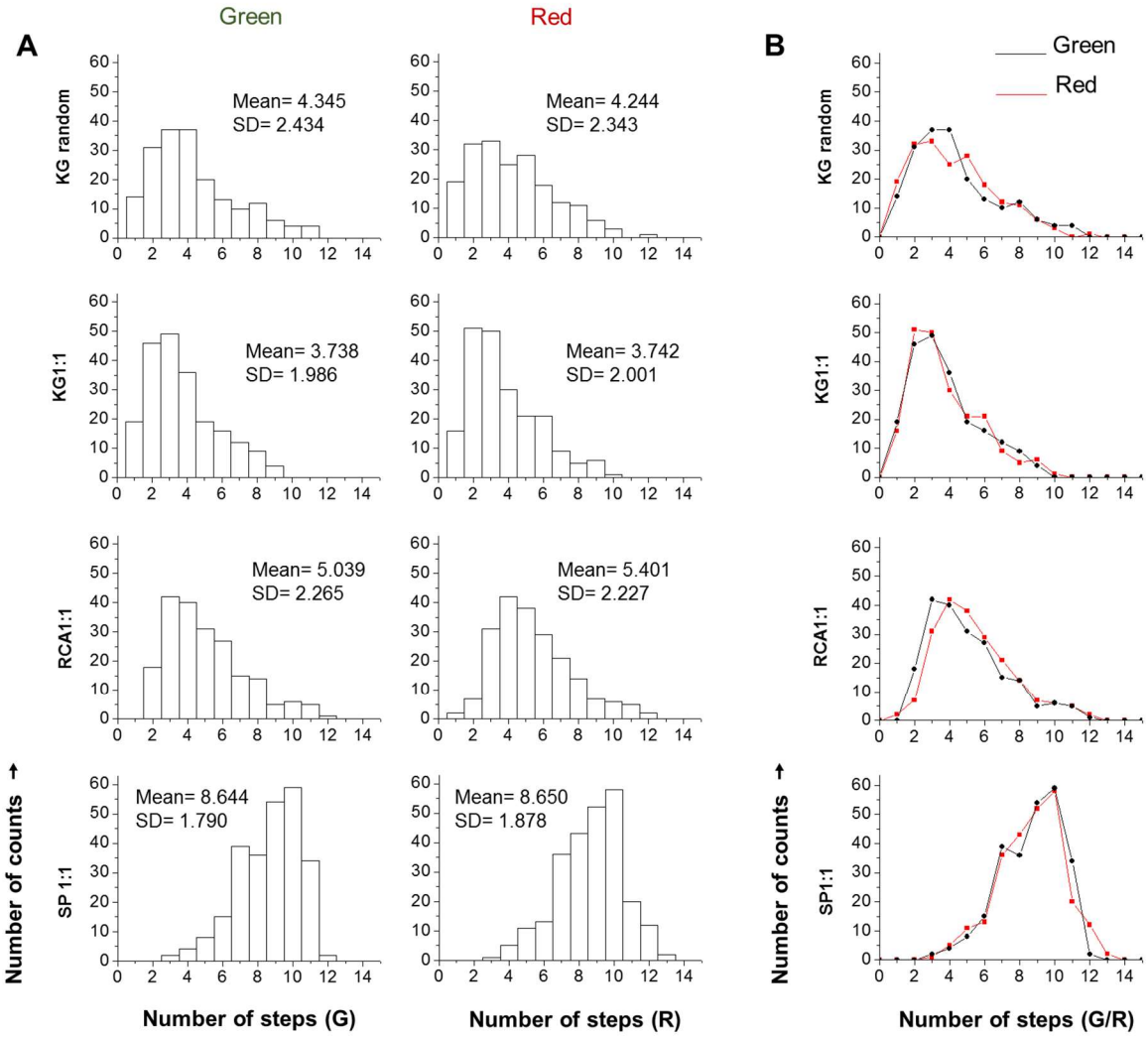

Figure 3.12: Ensemble histogram. Histograms showing the distributions of photobleaching steps for the green and red emitters independently (A) and overlaid (B) in the four different samples of nanotubes with the corresponding mean and standard deviation values.

3.4.5 Single molecule correlation analysis

3.4.5.1 Simulations on the expected nanotube size distribution and dye composition

3.4.5.1.1 Polydisperse DNA nanotubes with a 1:1 dye stoichiometry. The random nanotube growth model involves triangular rungs being stacked in tube-like structures. Growth is driven by independent processes of blocks accumulating on top or bottom of the growing stacks of blocks. Each nanotube evolves independently (i.e., with no spatial correlation) while its size would be governed by the Gaussian distribution. We thus expect the theoretical size distribution of nanotubes (assuming a 100% labelling efficiency) to follow a 2D Gaussian profile defined by the following equation:

$$f(x;y) = Ae^{-\left(\frac{(x-x_0)^2}{2\sigma_x^2}+\frac{(y-y_0)^2}{2\sigma_y^2}\right)}$$

where A is the amplitude of the curve, x_0 and y_0 are the coordinates of the peak value, σ is the variance of the distribution. Given that the nanotubes were observed to grow to a maximum size of about 20 rungs, we generated in MATLAB a dataset for a 2D Gaussian with the range of x (Cy3) and y (Cy5) being [0;10] in each case, centered at [5;5] with a standard deviation of 2.5. Only values that correspond to the cross-section x=y were extracted to illustrate the 1:1 stoichiometry of the structures (Figure 3.13).

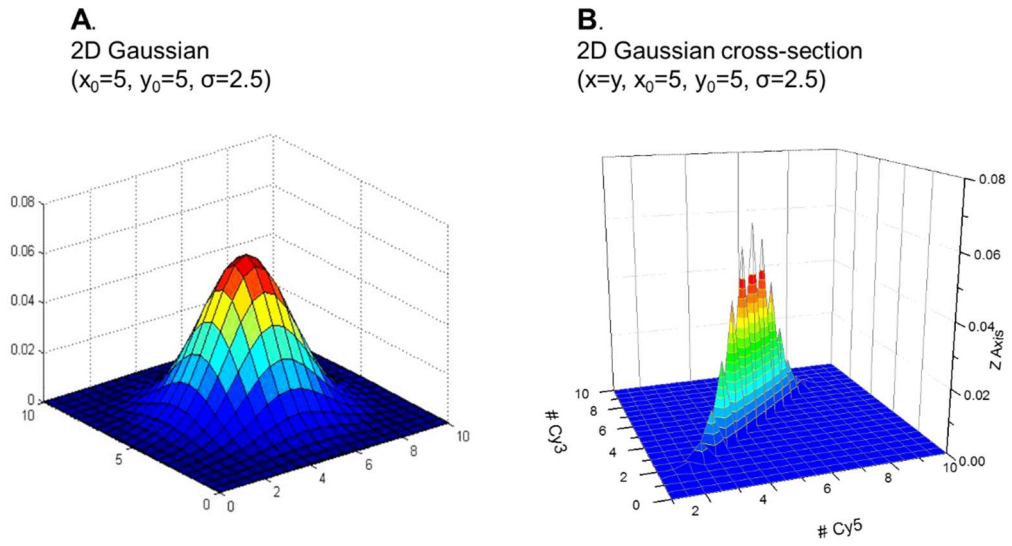

Figure 3.13: 2D Gaussian simulation. A. 2D Gaussian generated in MATLAB to simulate the size distribution of DNA nanotubes given a random solution growth. B. (x=y) cross section of the Gaussian to represent a polydisperse sample of nanotubes with a perfect 1:1 stoichiometry.

3.4.5.1.2 Monodisperse DNA nanotube with a random dye stoichiometry. For each size population of DNA nanotubes (from the smallest composed of 1 rung to the largest possible composed of 20 rungs), the theoretical distribution of green versus red dyes (assuming a 100% labelling efficiency) can be obtained by solving a binomial model:

$$f(n; M, P) = \binom{M}{n} P^n (1-P)^{M-n} = \left(\frac{M!}{n!\,(M-n)!}\right) P^n (1-P)^{M-n}$$

Given n_{block}, the probability of n_{Cy3} attached is:

$$f(n_{Cy3}; n_{block}, P_{Cy3}) = \binom{n_{block}}{n_{Cy3}} {P_{Cy3}}^{n_{Cy3}} (1-P_{Cy3})^{n_{block}-n_{Cy3}}$$

where n_{block} is the number of building blocks in a structure and hence the size of the nanotube (n_{blocks}= 1, 2,…20), n_{Cy3} is the number of Cy3-labelled rungs incorporated, and P_{Cy3} is the probability of Cy3-labelled rungs to be incorporated in the structure. Assuming that the nanotube formation results from a random attachment of the different building blocks (rungs) in solution, the probability of Cy3-rungs incorporation is therefore 50%, while the probability of the Cy5-rungs incorporation is '1-0.5= 50%'. Figure 3.14 below shows the dye (Cy3 versus Cy5) composition in a given size of nanotubes (1, 2,...20 rungs) after computing in each case $n_{Cy5} = n_{block} - n_{Cy3}$ and then plotting n_{Cy3} versus n_{Cy5} with their corresponding probabilities.

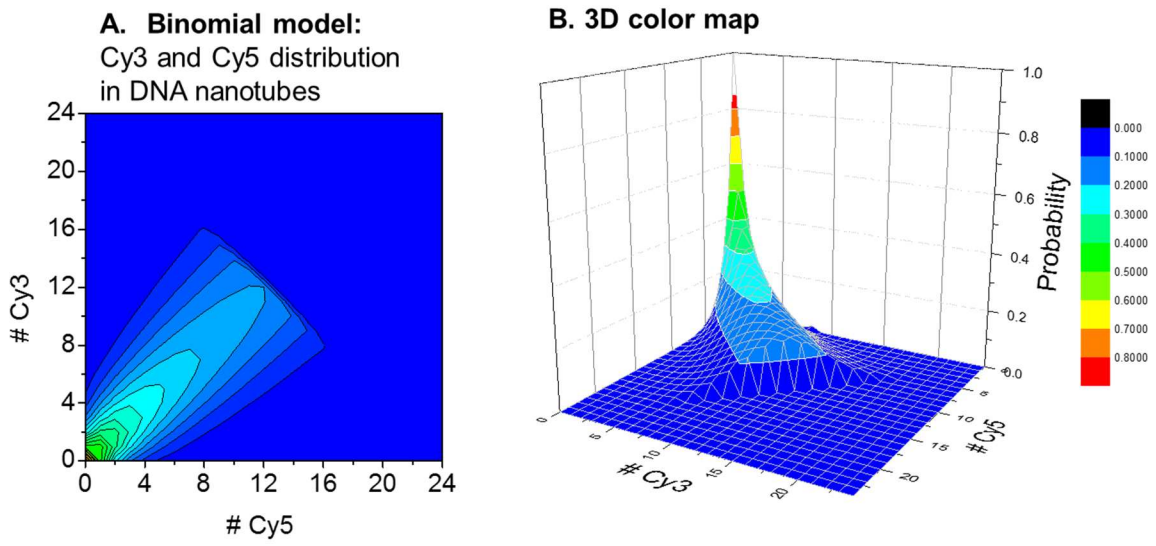

Figure 3.14: Probability distribution of Cy3/Cy5 in monodisperse DNA nanotubes based on a binomial model.

3.4.5.1.3 Monodisperse DNA nanotubes with incomplete dye labelling efficiency.

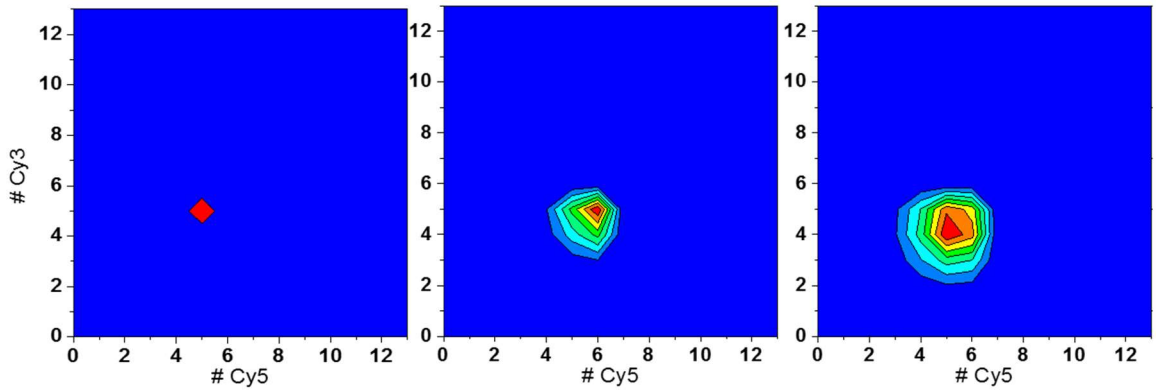

Figure 3.15: Complete/Incomplete labelling efficiency simulations in DNA nanotubes built step by step (5 red: 5 green) on the surface. A. Simulated distribution on a 100% labelling efficiency sample. B. Simulated distribution on a 90% labelling efficiency sample.

3.4.5.1.4 Monodisperse DNA nanotubes with incomplete dye labelling efficiency with a probability of irreversible damage (termination).

To prove that the pronounced spread along the diagonal in the contour plots of the sample SP1:1 is due to a termination step occurring for a fraction of the tubes, we simulated nanotubes with 95% reaction yield with 95% labelling efficiency, with or without 5% termination yield (Figure 3.16). While adding the termination factor does elongate the distribution along the diagonal, we observe more tubes with less dyes (say 1 or 2) than with an intermediary (around 5) amount of each dyes. The absence of small tubes may be an indication that the operating mechanism is that larger tubes are more prone to errors in the addition. This can be explained by the collapse of the tubes on the surface, which would reduce the availability of the capture strands on the top rung.

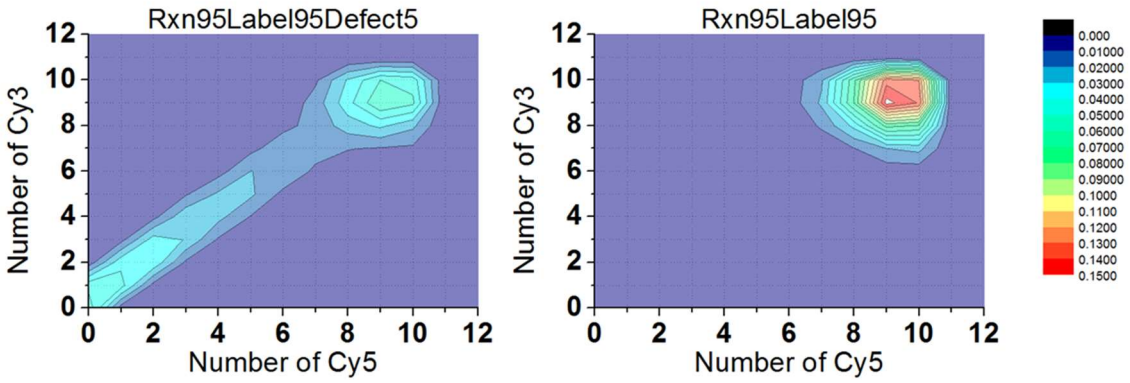

Figure 3.16: Incomplete labelling efficiency simulations in DNA nanotubes built step by step (10 red: 10 green) on the surface with (left) /without (right) 5% termination yield.

3.4.6 3D correlation plots of DNA nanotube samples

We next computed the frequency count of each pair of number of steps to generate a matrix and build a 3D contour plot in Origin 8.1. We performed this analysis for the four samples of nanotubes described in the chapter in addition to the RCA sample (NT1-2-2-2), with an expected 1:3 Cy3:Cy5 ratio as shown in Figure 3.17 below.

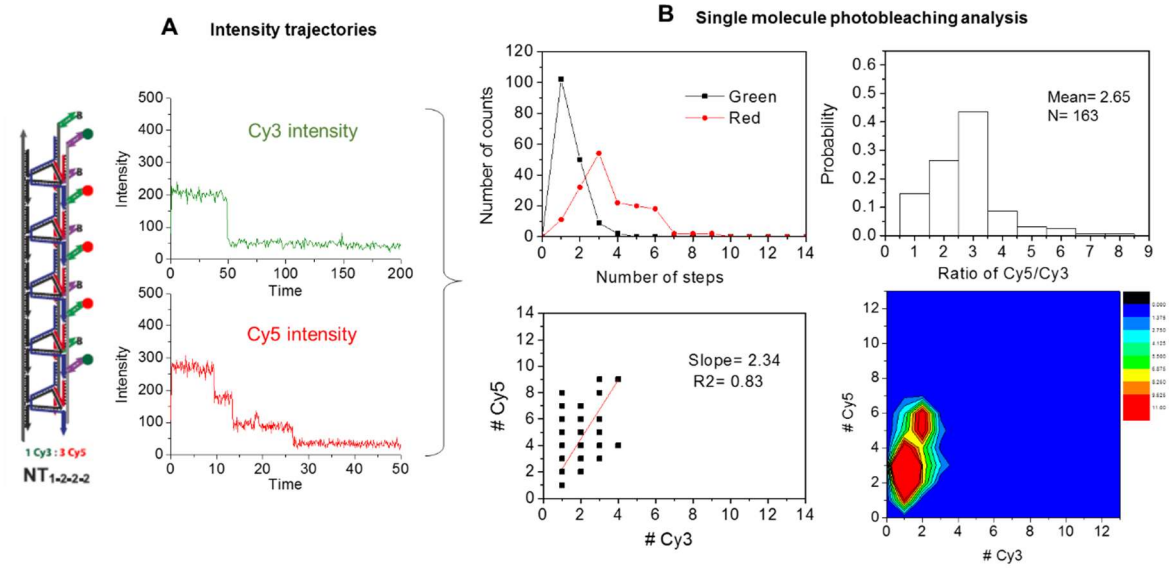

Figure 3.17: Quantitative information extracted from simple intensity-time trajectories from a 3:1 stoichiometric DNA nanotube sample. A. Intensity-time trajectories of Cy3 (top, 1 step) and Cy5 (bottom, 3 steps) dyes incorporated in a DNA nanotubes with a 3:1 sequence pattern. B. (Top left) An ensemble histogram displaying the distribution of the number of steps in each color, green and red, independently. (Top right) A Histogram showing the distribution of the ratio of Cy5/Cy3 ratio centered at 2.65. (Bottom left) A 2D correlation of the number of steps for the green and red dyes with a slope of 2.34 and a R^2 value of 0.83. (Bottom right) A 3D correlation

color surface showing the dispersion of the number steps for the green and red dyes and illustrating the polydispersity index of the 3:1 sample of nanotubes.

Next, by fitting each scatter of points to a linear function, we extracted the slopes and standard error of each sample (Figure 3.18).

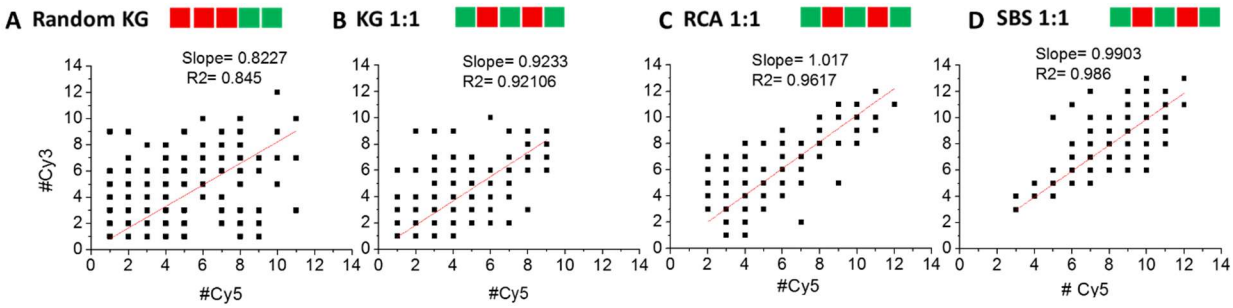

Figure 3.18: 2D correlation display. 2D correlation analysis of the number of steps in green and red within colocalized nanotubes. (Red line) Linear regression fitting ($y= a_0x+b_0$) for the four different nanotube samples with the corresponding slopes (a_0) and R^2 values.

Additionally, from the 3D matrix, the dispersion (or spread) along the diagonal can be calculated by extracting the standard deviation of the corresponding 1D distribution. Therefore, using the values of the cross-section x=y (diagonal of the matrix), we plot the 1D distributions of the four samples and calculate the corresponding standard deviations as shown in figure 3.19.

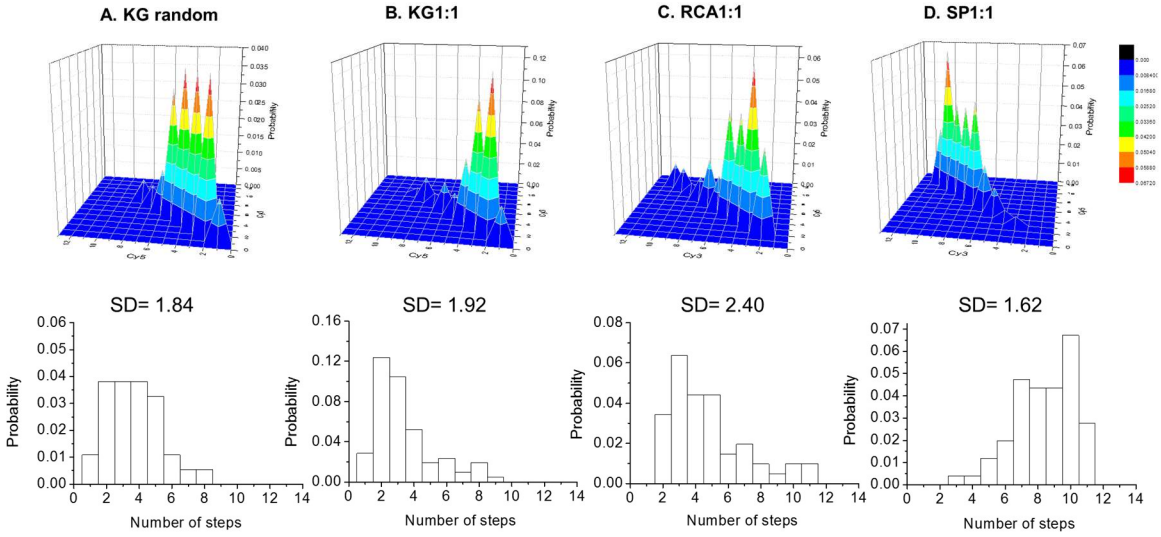

Figure 3.19: Cross-section x=y from the 3D matrices. (Top) 3D Histograms displaying the x=y cross-section (diagonal) in the 4 different samples. (Bottom) 1D distribution of the x=y values with the corresponding standard deviations.

Because the number of bleaching steps can infer the number of fluorophores in the nanotube and therefore the number of units incorporated, the size of the nanotubes can be computed and correlated rather than the number of steps. Size per unit can be determined from figure 3.20 showing the distance between the building blocks.

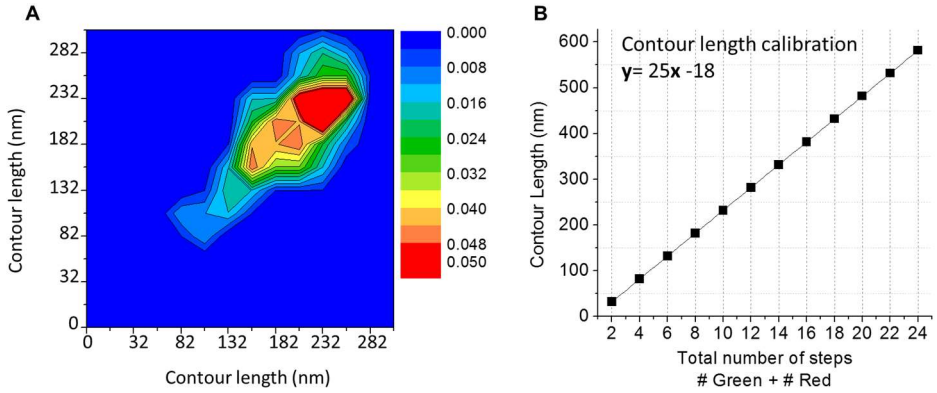

Figure 3.20: Conversion of photobleaching steps into size (nm). A. Example of a 3D correlation plot with the x-y coordinate being the contour length of the structure in each color after the number of steps was converted to size of the DNA in nm. B. Calibration curve displaying the contour length in (nm) as a function of the total number of steps with the linear fitting y= 25x -18 corresponding to the equation for converting from steps to length (nm).

3.4.7 Automated analysis using MATLAB

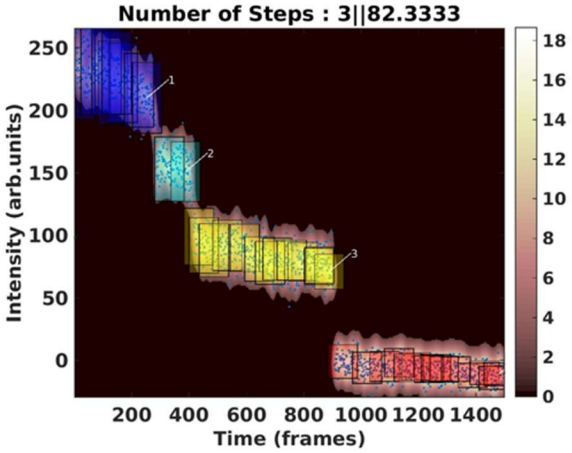

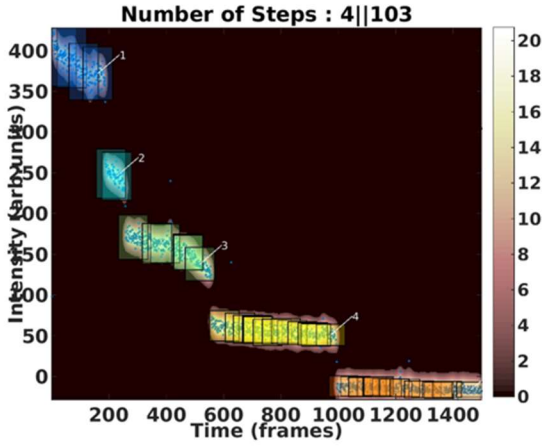

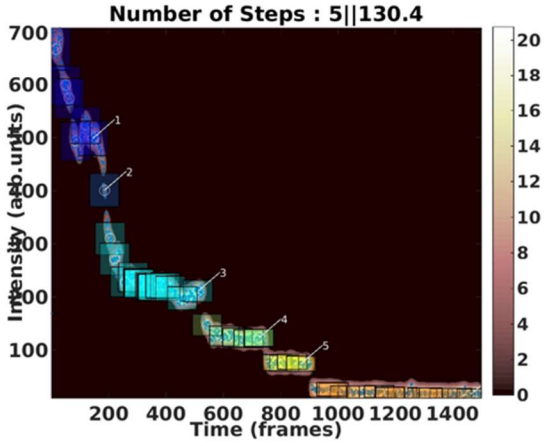

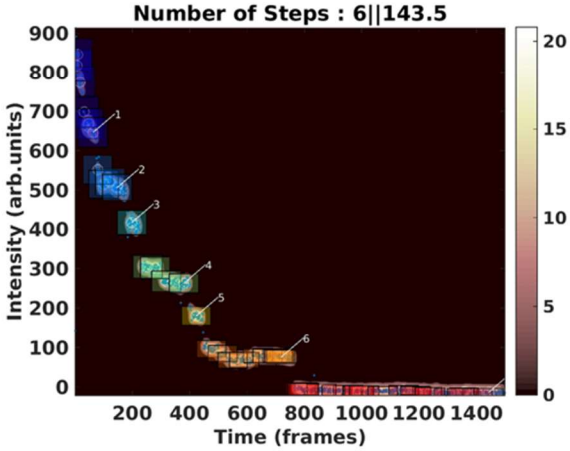

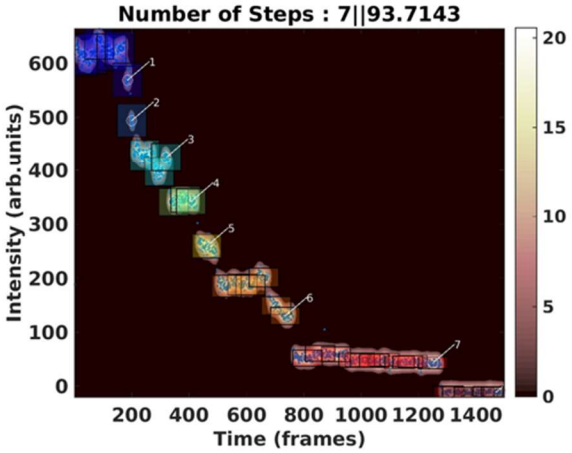

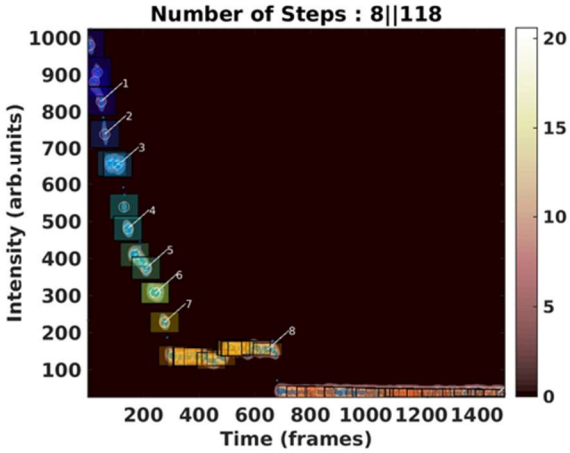

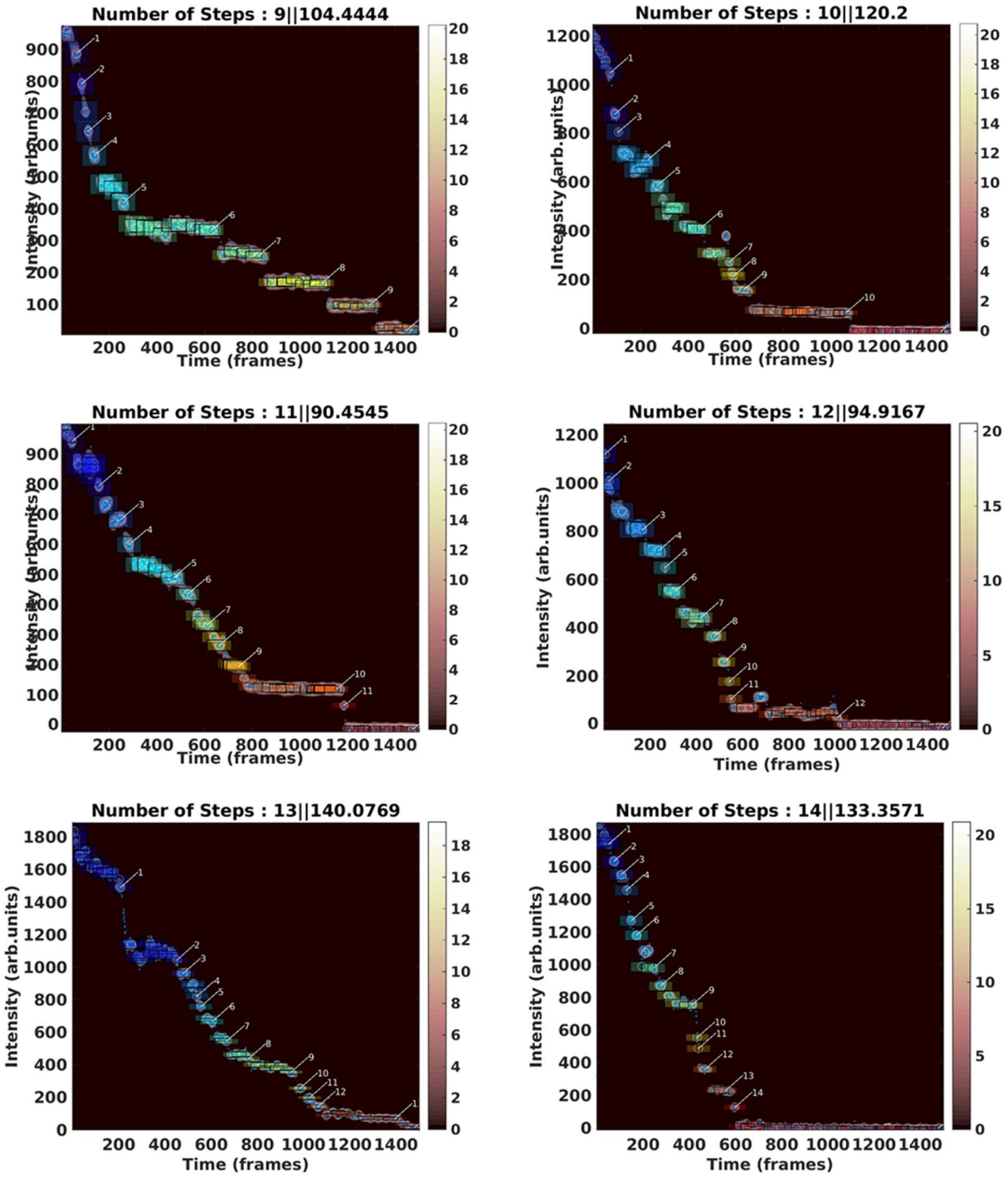

Figure 3.21: Twelve examples of photobleaching trajectories (3-14 steps) detected and counted automatically by the routine from a simple TIRF image.

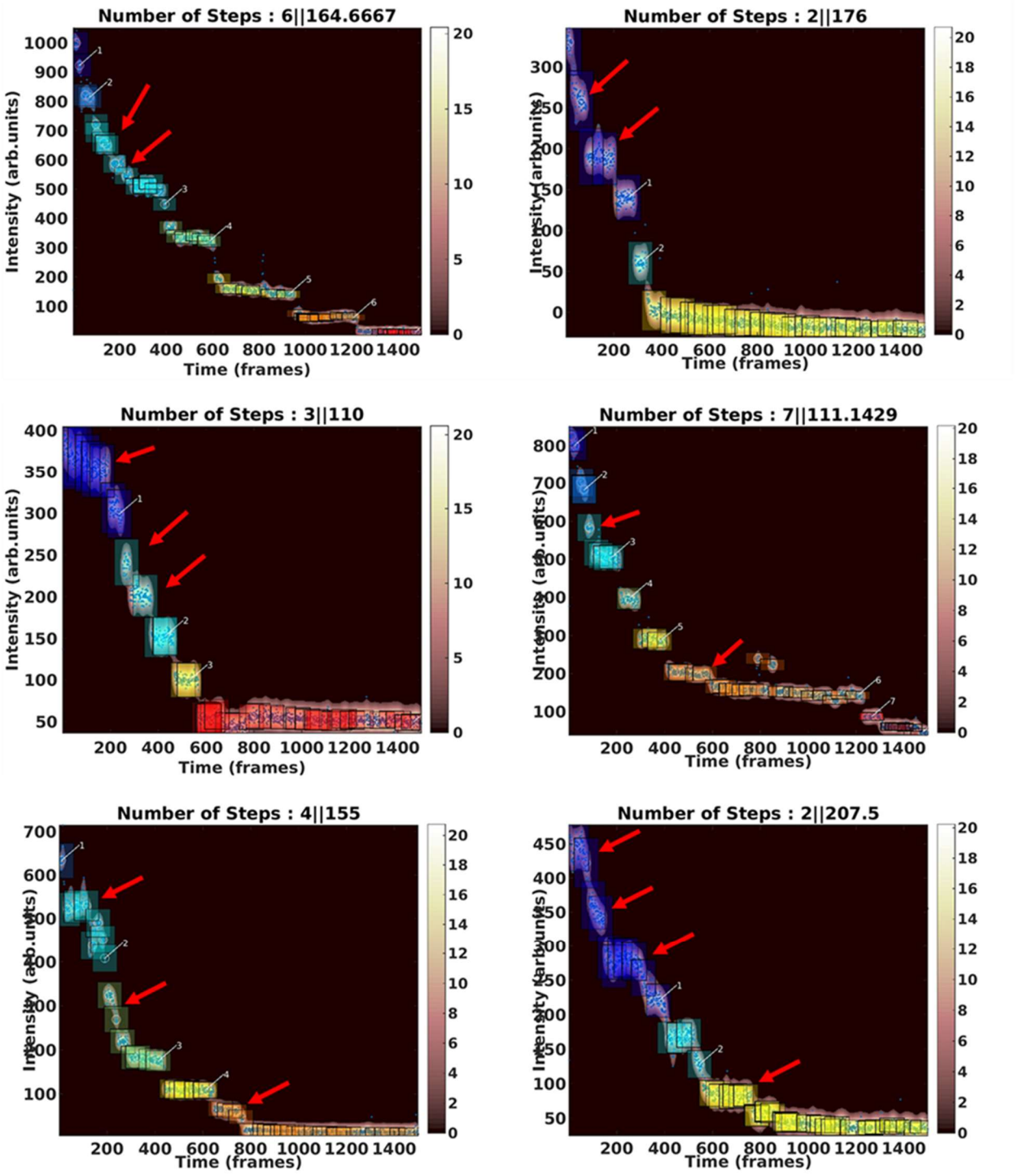

Figure 3.22: Six examples of photobleaching trajectories showing clear steps not detected by the automated routine.

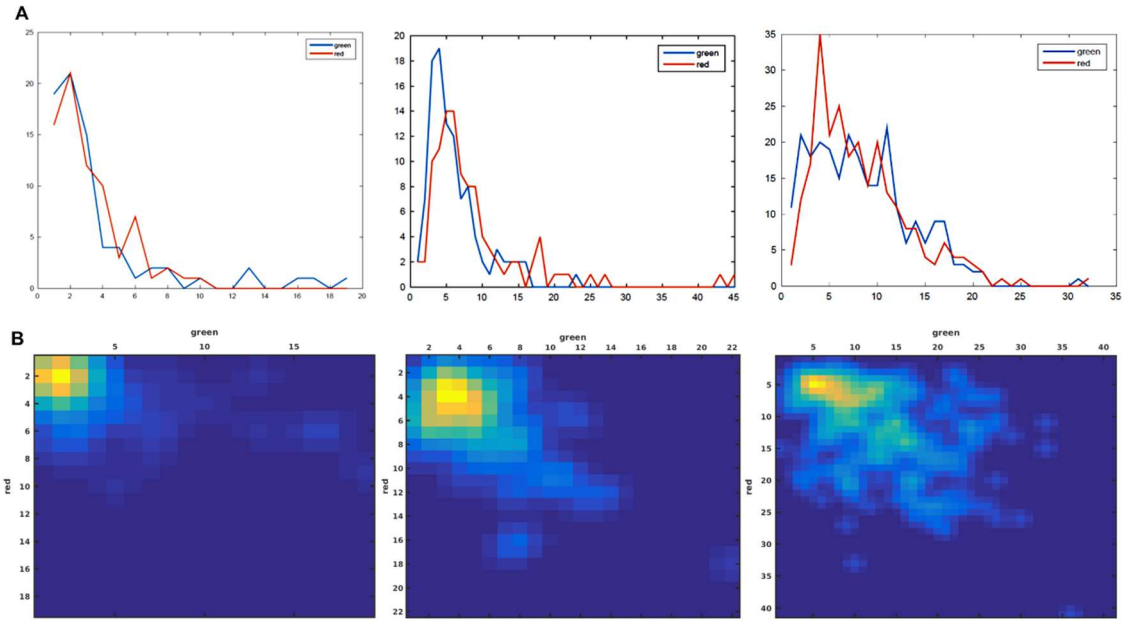

Figure 3.23: Histograms and plots generated by an automated routine. A. Ensemble histogram showing the distribution of the step photobleaching number for green and red emitters overlaid generated by the automated MATLAB routine for samples KG-RCA-SBS. B. 3D correlation color surface plots generated for samples KG-RCA-SP 1:1.

3.4.8 Bulk measurements: PDI calculations including larger nanotubes

Knowing that a theoretical PDI of 2 is calculated for an ideal step polymerization whose yield reaches 100%, a lower PDI indicates that we may preferentially be immobilizing a specific population of nanotube, particularly the short ones, rather than all of them. We re-calculated the PDI values after including a small subset (ca. 4%) of large nanotubes with ca. 60 subunits, which results in values closer to 2, as expected for a step-growth mechanism (Table 3.3). Based on this result, we postulate that large nanotubes, which constitute a small fraction of the sample, remain in solution due to the possible globular state of the structure and the hindrance of the biotin within it making it less available for surface binding.

Table 3.3: Bulk quantities extracted from single molecule data sets including hypothetical large nanotubes*

Sample	$\sum N_x$	$\sum N_x M_x$	$\sum N_x M_x^2$	M_w	M_n	PDI
KG random	219	1880	28764	8.58	15.3	1.80
KG 1:1	239	1836	26504	7.68	14.43	1.91
RCA 1:1	235	2395	37865	10.19	15.81	1.55
SP 1:1	282	4642	90628	16.46	19.52	1.18

***Grey selection calculation is not taken into account since SP1:1 nanotubes do not follow a step polymerization.**

3.5 References

1. (a) Grayson, S. M.; Fréchet, J. M. J., Convergent Dendrons and Dendrimers: from Synthesis to Applications. *Chemical Reviews* **2001,** *101* (12), 3819-3868; (b) Geary, C.; Rothemund, P. W. K.; Andersen, E. S., A single-stranded architecture for cotranscriptional folding of RNA nanostructures. *Science* **2014,** *345* (6198), 799-804; (c) Langecker, M.; Arnaut, V.; Martin, T. G.; List, J.; Renner, S.; Mayer, M.; Dietz, H.; Simmel, F. C., Synthetic Lipid Membrane Channels Formed by Designed DNA Nanostructures. *Science* **2012,** *338* (6109), 932-936; (d) Le Meins, J. F.; Schatz, C.; Lecommandoux, S.; Sandre, O., Hybrid polymer/lipid vesicles: state of the art and future perspectives. *Materials Today* **2013,** *16* (10), 397-402; (e) Crowley, J. D.; Goldup, S. M.; Lee, A.-L.; Leigh, D. A.; McBurney, R. T., Active metal template synthesis of rotaxanes, catenanes and molecular shuttles. *Chemical Society Reviews* **2009,** *38* (6), 1530-1541.

2. (a) Chong, T. C.; Hong, M. H.; Shi, L. P., Laser precision engineering: from microfabrication to nanoprocessing. *Laser & Photonics Reviews* **2010,** *4* (1), 123-143; (b) Seeman, N. C.; Belcher, A. M., Emulating biology: Building nanostructures from the bottom up. *Proceedings of the National Academy of Sciences* **2002,** *99* (suppl 2), 6451-6455; (c) Rothemund, P. W. K., Folding DNA to create nanoscale shapes and patterns. *Nature* **2006,** *440* (7082), 297-302.

3. (a) Pinheiro, A. V.; Han, D.; Shih, W. M.; Yan, H., Challenges and opportunities for structural DNA nanotechnology. *Nat Nano* **2011,** *6* (12), 763-772; (b) Schulman, R.; Wright, C.; Winfree, E., Increasing Redundancy Exponentially Reduces Error Rates during Algorithmic Self-Assembly. *ACS Nano* **2015,** *9* (6), 5760-5771.

4. Tsukanov, R.; Tomov, T. E.; Liber, M.; Berger, Y.; Nir, E., Developing DNA Nanotechnology Using Single-Molecule Fluorescence. *Accounts of Chemical Research* **2014,** *47* (6), 1789-1798.

5. Moerner, W. E.; Fromm, D. P., Methods of single-molecule fluorescence spectroscopy and microscopy. *Review of Scientific Instruments* **2003,** *74* (8), 3597-3619.

6. (a) Schuler, B.; Lipman, E. A.; Eaton, W. A., Probing the free-energy surface for protein folding with single-molecule fluorescence spectroscopy. *Nature* **2002,** *419* (6908), 743-747; (b) Zhuang, X.; Bartley, L. E.; Babcock, H. P.; Russell, R.; Ha, T.; Herschlag, D.; Chu, S., A Single-Molecule Study of RNA Catalysis and Folding. *Science* **2000,** *288* (5473), 2048-2051; (c) Evans, G. W.; Hohlbein, J.; Craggs, T.; Aigrain, L.; Kapanidis, A. N., Real-time single-molecule studies of the motions of DNA polymerase fingers illuminate DNA synthesis mechanisms. *Nucleic Acids Research* **2015,** *43* (12), 5998-6008; (d) Funatsu, T.; Harada, Y.; Tokunaga, M.; Saito, K.; Yanagida, T., Imaging of single fluorescent molecules and individual ATP turnovers by single myosin molecules in aqueous solution. *Nature* **1995,** *374* (6522), 555-559; (e) Hastie, P.; Ulbrich, M. H.; Wang, H.-L.; Arant, R. J.; Lau, A. G.; Zhang, Z.; Isacoff, E. Y.; Chen, L., AMPA receptor/TARP stoichiometry visualized by single-molecule subunit counting. *Proceedings of the National Academy of Sciences* **2013,** *110* (13), 5163-5168; (f) Marko, R. A.; Liu, H.-W.; Ablenas, C. J.; Ehteshami, M.; Götte, M.; Cosa, G., Binding Kinetics and Affinities of Heterodimeric versus Homodimeric HIV-1 Reverse Transcriptase on DNA–DNA Substrates at the Single-Molecule Level. *The Journal of Physical Chemistry B* **2013,** *117* (16), 4560-4567.

7. (a) Hariri, A. A.; Hamblin, G. D.; Gidi, Y.; Sleiman, H. F.; Cosa, G., Stepwise growth of surface-grafted DNA nanotubes visualized at the single-molecule level. *Nat Chem* **2015,** *7* (4), 295-300; (b) Hamblin, G. D.; Hariri, A. A.; Carneiro, K. M. M.; Lau, K. L.; Cosa, G.; Sleiman, H. F., Simple Design for DNA Nanotubes from a Minimal Set of Unmodified Strands: Rapid, Room-Temperature Assembly and Readily Tunable Structure. *ACS Nano* **2013,** *7* (4), 3022-3028.

8. (a) Ulbrich, M. H., Counting Molecules: Toward Quantitative Imaging. In *Far-Field Optical Nanoscopy*, Tinnefeld, P.; Eggeling, C.; Hell, W. S., Eds. Springer Berlin Heidelberg: Berlin, Heidelberg, 2015; pp 263-291; (b) McGuire, H.; Aurousseau, M. R. P.; Bowie, D.; Blunck, R., Automating Single Subunit Counting of Membrane Proteins in Mammalian Cells. *The Journal of Biological Chemistry* **2012,** *287* (43), 35912-35921; (c) Reyes-Lamothe, R.; Sherratt, D. J.; Leake, M. C., Stoichiometry and architecture of active DNA replication machinery in Escherichia coli. *Science (New York, N.Y.)* **2010,** *328* (5977), 498-501; (d) Yu, Y.; Ulbrich, M. H.; Li, M.-h.; Dobbins, S.; Zhang, W. K.; Tong, L.; Isacoff, E. Y.; Yang, J., Molecular mechanism of the assembly of an acid-sensing receptor ion channel complex. *Nature communications* **2012,** *3*, 1252-1252.

9. Leake, M. C.; Chandler, J. H.; Wadhams, G. H.; Bai, F.; Berry, R. M.; Armitage, J. P., Stoichiometry and turnover in single, functioning membrane protein complexes. *Nature* **2006,** *443* (7109), 355-358.

10. Wu, R. A.; Dagdas, Y. S.; Yilmaz, S. T.; Yildiz, A.; Collins, K., Single-molecule imaging of telomerase reverse transcriptase in human telomerase holoenzyme and minimal RNP complexes. *eLife* **2015,** *4*, e08363.

11. Leake, M. C., Shining the spotlight on functional molecular complexes: The new science of single-molecule cell biology. *Communicative & Integrative Biology* **2010,** *3* (5), 415-418.

12. (a) Aldaye, F. A.; Lo, P. K.; Karam, P.; McLaughlin, C. K.; Cosa, G.; Sleiman, H. F., Modular construction of DNA nanotubes of tunable geometry and single- or double-stranded character. *Nat Nano* **2009,** *4* (6), 349-352; (b) Lo, P. K.; Karam, P.; Aldaye, F. A.; McLaughlin, C. K.; Hamblin, G. D.; Cosa, G.; Sleiman, H. F., Loading and selective release of cargo in DNA nanotubes with longitudinal variation. *Nat Chem* **2010,** *2* (4), 319-328.

4 | Effect of base deletion in DNA nanotubes: A single molecule study.

Reproduced in part with permission from: "Dynamic DNA Nanotubes: Reversible Switching between Single and Double-Stranded Forms, and Effect of Base Deletions", Janane F. Rahbani, **Amani A. Hariri**, Gonzalo Cosa & Hanadi F. Sleiman, ACS nano **2015**, *9* (12), pp 11898–11908.

Author Contributions: DNA sequence design, synthesis and purification were carried out by **Janane F. Rahbani.** Single molecule experiments were carried out by **Amani A. Hariri**. The DNA nanotubes structural schemes were generated by **Alex Rousina-Webb.**

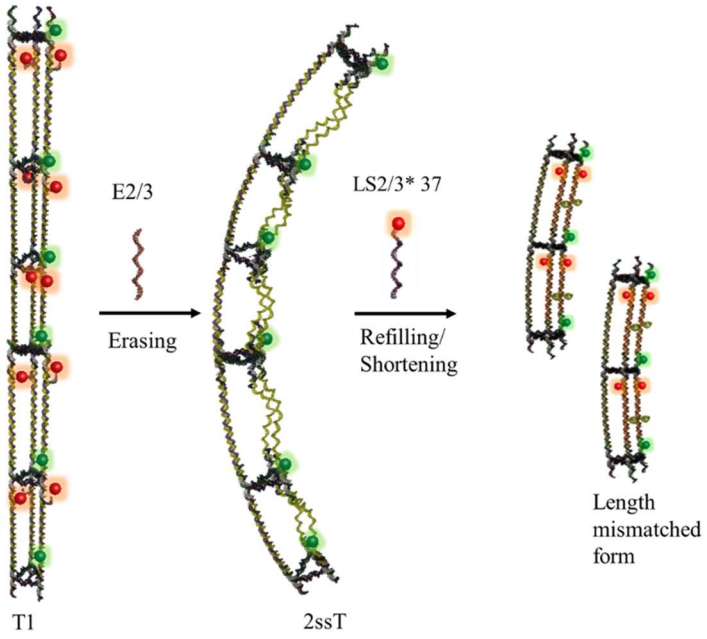

4.1 Introduction

By taking it out of its biological role, DNA has served as a robust and versatile building block to assemble a variety of two-dimensional and three-dimensional discrete nanometer-sized structures with arbitrary shapes and designs.[1] These molecularly addressable materials could serve as platforms for the site-specific hybridization of cargos at the nanometer precision.[2] Besides structural complexity, DNA objects evolved to comprise an intrinsic dynamic character allowing them to respond to surrounding stimuli in a predictable manner.[3] The idea was first proposed by Mao et al., who developed a DNA nanostructure that took advantage of the B–Z transition of DNA to switch states.[4] Soon after, efforts to fabricate dynamic DNA systems have primarily focused on strand displacement approaches in which two strands with full or partial complementarity hybridize and displace in the process pre-hybridized strands.[5] This strategy can be combined with static structures to execute nanometer scale motions such as opening DNA containers, controlling molecular binding, or reconfiguring structures.[6] Alternatively, the use of stored mechanical energy to design deformed nanostructures was demonstrated by Dietz and co-workers who locally deleted or added base-pairs between DNA origami cross-over connections to introduce stresses that caused bending or twist of the overall structure.[7] The degree of bending or twist could be programmed by controlling the amount of the number of base-pairs added or deleted. However, progress toward practical applications of DNA nanodevices in numerous areas of materials science and medicine will require more DNA-economic and rapid fabrication methods.[8]

The need to simplify assembly while maintaining programmability and dynamic character is exemplified by the construction of DNA nanotubes using different well-established methodologies.[9] Notably, Sleiman et al. introduced a simple and efficient synthesis of DNA nanotubes from 11 short unmodified strands, yielding robust structures with controlled geometry and circumference, and site-specific addressability.[10] Although DNA nanotubes are typically portrayed as large and rigid struts, they are potentially capable of structural switching by dynamically adjusting one or several of the edge lengths between the building blocks using a combination of strand displacement and loops.[3] Yet, a detailed understanding of their collective structural changes in response to modifications within their repeat unit is still a challenge.[8]

A rational design of dynamic DNA nanotubes requires analytical tools in order to provide an informative feedback on the final product.[11] Gel electrophoresis, atomic force microscopy (AFM)

and transmission electron microscopy (TEM) are typically used to give useful structural information on a resulting DNA construct. However, these tools are not *in situ* techniques, in that DNA samples are not investigated in the preferable aqueous environment. Alternatively, single-molecule immobilization-based total internal reflection fluorescence (TIRF) techniques enable the continuous observation of individual structures in solution. The method also enables the detection of small distinct populations and side products rather than just the average distribution.[12] The real-time observation of discrete steps in the fluorescence intensity, resulting from the sequential photobleaching of all fluorophores attached to different building blocks, enables the quantification of the number of repeat units within a structure.[13] Additionally, when coupled with two color-laser excitation, this technique allows the determination of the presence or absence of multiple building blocks.[14] In combination with a flow-cell, it also enables the fast replacement of the surrounding solution to facilitate the introduction of building blocks and the washing of excess material. From this perspective, TIRFM-based single molecule approaches land themselves as the method of choice for DNA nanotube characterization and manipulation.[15]

In this work, we employ SM-based TIRF microscopy methods to investigate the programmable introduction of DNA structural changes within the dye-labelled repeat units of DNA nanotubes designed and synthesized in the Sleiman lab. By performing single molecule photobleaching studies on surface-immobilized surface nanotubes, we first quantified the number of Cy3-tagged repeat units within a nanotube structure at the initial (open tube) and the final (fully assembled tube) stages of the tube-assembly, to shed light on a plausible assembly mechanism. Our analysis showed that open structures would form short closed tubes, geometrically well-aligned, which would possibly grow and elongate through base pairing of the sticky ends. Second, we investigated the effect of base-deletion on the nanotube structure. We site-specifically introduced DNA strands that shorten two sides of the nanotubes, while keeping intact and strain free the length of the third side. We hypothesize that a length mismatch in each repeat unit could induce distortion/bending of the nanotubes generated in solution, until it is significant enough to compromise the stability and shorten the nanotube, as measured by photobleaching experiments. Using two-color single molecule photobleaching studies and strand displacement experiments, we validated the presence of the loop strand within the structures, and verified that an initially long single-stranded nanotube can be fragmented and shortened upon addition of length mismatched strands. We are currently investigating whether the resulting nanotube length can be correlated with the extent of distortion

introduced in the DNA strands within the repeat unit: this would allow the nanotube to act as a reporter of small molecule- or protein-induced DNA binding events.

4.2 Results and discussion

4.2.1 Design of DNA nanotube assembly

The nanotube design and synthesis is based on the work of the Sleiman lab described in depth in the published protocols[16]. Briefly, the assembly starts with a triangular "core" unit (U), composed of 6 unmodified DNA strands (Figure 4.4A, Experimental section 4.4.1). The mixture is annealed at 95 °C then slowly cooled down to 4°C over 4 h to give (U) in quantitative yield. The core structure (U) possesses extensions from the top and bottom of the triangular plane, in order to hybridize *via* sticky-end cohesion to three linking strands (LS1–3), which result in nanotube formation (Figure 4.4B, Experimental section 4.4.1). To maximize the yield of fully formed nanotubes and prevent cross-linking, our method uses linking strands that are different from one another. The first, LS1 is designed with longer sticky-ends (14 nucleotides, nt), and the other two (LS2, LS3) with shorter sticky-ends (10 nt). The nanotubes T1 are formed through a stepwise, hierarchical mechanism. Linking strand LS1 is first added (heating to 56 °C then cooling to 22 °C), resulting in the formation of an open structure T_{op} with the triangular rungs positioned on top of one another. Then linking strands LS2 and LS3 are added (44 to 22 °C) to close the structure T_{op} with pre-organized triangles, into the full nanotube. These DNA nanotubes were studied and characterized by non-denaturing AGE, AFM under dry conditions and TIRFM. This chapter will focus solely on the single molecule fluorescence imaging and analysis. For details on these techniques, please consult reference [16].

4.2.2 Single molecule surface preparation and experimental design

Single-molecule total internal reflection fluorescence microscopy (TIRFM) was used to obtain quantitative information on the mechanism of nanotube formation and resulting structural characteristics. In order to immobilize the nanotubes on a coverslip surface, 5% of one of the strands within the triangular core was labeled with biotin. The 5% average biotin labeling represents a compromise between specifically immobilizing the nanotubes on the coverslip surface and maintaining their dynamic character. To this end, we extended one of the rigidifier strands (R3ov) by 20 bases and we synthesized its complementary strand decorated with a biotin moiety

(Bio-R3ov*). Since the interaction of biotin on our constructs with strepdavidin on the surface determined the dynamics and the stability of the tubes during the TIRFM measurements, we varied the amount of biotin attached to our nanotubes from 100% to 5%. A 100% biotin was referred to a 1:1 ratio of the biotinylated strand with respect to the rung. On the other hand, a percentage of 5% for example, 5% of the rigidifier (R3) were hybridized to the strand tagged with biotin and to the triangular core while the remaining 95% consisted of R3 lacking the 20 base sticky-end. Since the rigidifier R1 was labelled with a Cy3 dye, the emission of nanotubes bearing 100%, 80%, 60%, 40%, 20%, 10% and 5% biotin molecules was detected into the green channel (Figure 4.5B, Experimental section 4.4.4). Interestingly, visualization of the tubes was possible even at the lowest percentage tested indicating that a minimal percentage of biotin label is sufficient to deposit the tubes on the surface (see Experimental section 4.4.4). Next, polycarbonate film imaging chambers were assembled onto glass coverslips, coated with a mixture of polyethylene glycol (PEG) to prevent nonspecific adsorption and biotin-tagged PEG to provide specific binging sites (Figure 4.5A, Experimental section 4.4.4). Individual dye-labeled nanotubes were next specifically immobilized on the coverslips *via* biotin–streptavidin interactions. We expect most nanotubes to bind partially in a side-on manner to the PEG-streptavidin surface. Optimization of nanotube binding to this surface is described in the experimental section 4.4.2 and 4.4.5. Regions were excited using a TIRF setup with an evanescent field employing the 532 nm output of a diode laser. Images corresponding to a field of view of *ca*. 70 μm × 35 μm were acquired on an EMCCD camera. Typically, 150 single DNA nanotubes were simultaneously imaged within this field of view (See Experimental section 4.4.3).

We used single molecule photobleaching to count the number of Cy3 dyes, and thus the number of repeat units in each single nanotube imaged. Here, images were acquired for extended periods of time enabling visualizing the intensity-time profile of individual nanotubes. Conditions were optimized to work under the full dynamic range of the imaging camera, avoiding pixel saturation by the larger and brighter structures. Considering that the structures are ∼2 μm long on average by AFM, we expect an average of 70 Cy3 dyes per nanotube. Given the noise in single molecule trajectories, we have observed that when the number of dyes is equal or smaller than 10 dyes, discrete photobleaching steps in the intensity-time trajectory can be resolved, essentially a "staircase" photobleaching pattern. The number of intensity steps may be counted as the number of Cy3 repeats and thus the nanotube length can be quantified in this manner. Nanotubes with more

than ca. 11 dyes exhibit, however, steps that are too small, and insufficiently separated over time, to be unambiguously assigned. In this case, and an exponential decay, consistent with the stochastic nature of the process is obtained.

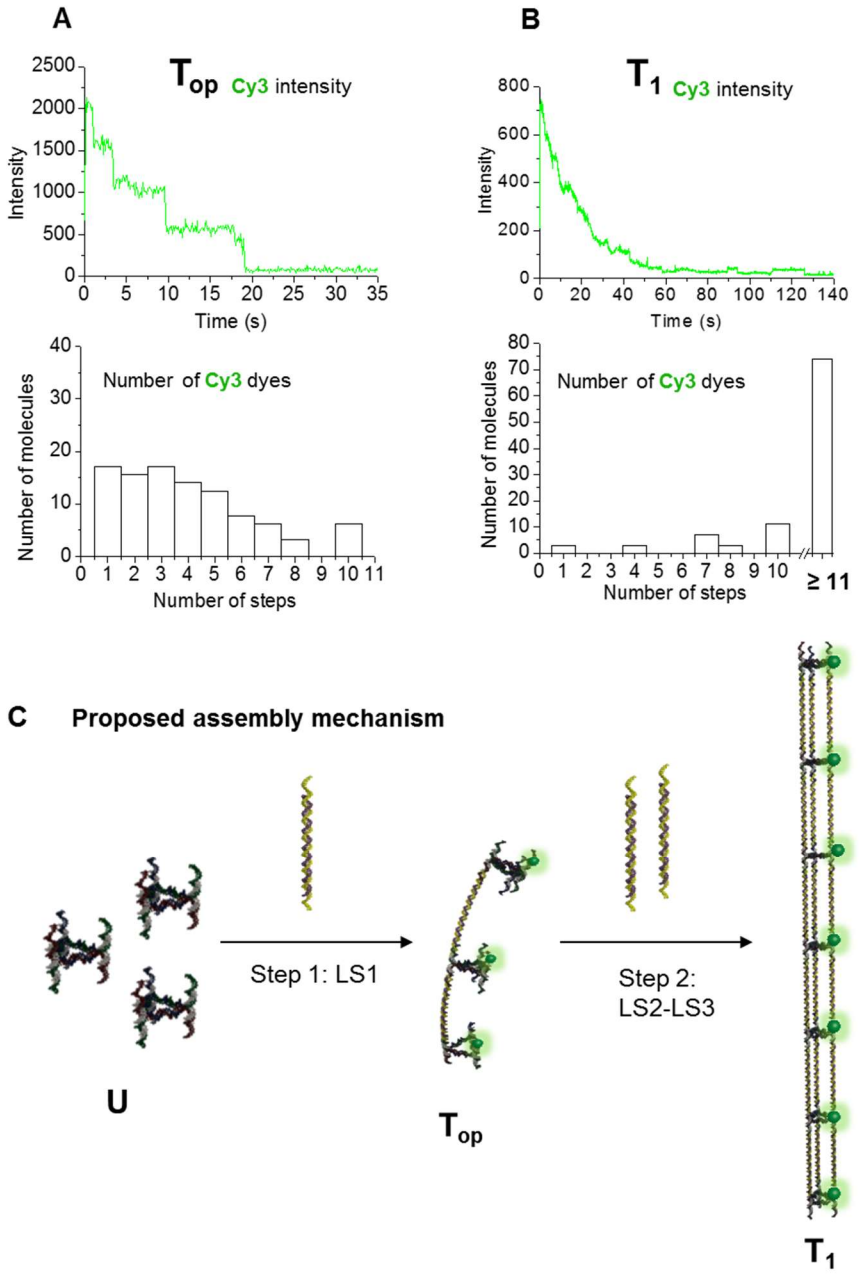

Figure 4.1: Single molecule characterization of the open tube and fully assembled tube. (A) Top: Typical intensity-time trajectory acquired for a single open nanotube, displaying 4 steps (dyes/units). Bottom: Histogram showing the distribution of the number of steps (dyes/units) obtained from photobleaching curves of the open nanotube samples. (B) Top: Typical intensity-time trajectory acquired for a single nanotube. Bottom: Histogram showing the distribution of the

number of steps (Cy3 dyes) obtained from photobleaching curves. (C) Schematic illustration of the suggested elongation mechanism showing the Cy3-labeled units (U) which assemble into short open tubes (T_{op}) upon the addition of LS1 in step 1, then elongate into closed tubes T_1 upon the addition of linking strands LS2-3.

4.2.3 Photobleaching studies: Nanotube elongation mechanism

We performed single molecule photobleaching studies to determine whether the elongation of the nanotubes into micron-sized structures occurs in the first step of their formation (upon LS1 binding) or in the second step (upon LS2/3 binding). For this, we assembled the 5%-biotin and Cy3-labeled nanotubes by annealing the components with LS1 only (without LS2 and LS3) in the solution. This is expected to give a Cy3-labeled open, intermediate structure Top (Figure 4.1C). Attachment of these open forms onto the coverslip surface and examination of their length by single-molecule TIRFM photobleaching analysis revealed a maximum of 10 rungs in the histograms, and the complete absence of structures displaying exponential intensity decrease in the intensity-time trajectories (Figure 4.1A). These observations are consistent with the formation of relatively short structures in the first step. We then created the fully assembled Cy3-tagged nanotube T1 upon the addition of the LS2 and LS3 linking strands (LS2 and LS3 have the same sequence in the middle, double-stranded portions, but different sequences at their sticky-end regions). In the case of tube T1, we observed photobleaching patterns with an exponentially decreasing intensity for the majority (90%) of the single nanotubes imaged. A histogram reflecting the Cy3 count distribution is displayed in Figure 4.1B. Based on the above results, we speculate that LS2 and LS3 may bind the open structures to form short closed tubes that are geometrically well-aligned, which then grow and elongate through base pairing of the sticky ends (Figure 4.1C). That is, following nucleation and formation of short structures, they then oligomerize and elongate via base-pairing. Tile-based nanotubes have been shown to form through a nucleation-elongation mechanism, with a relatively high barrier for the assembly of a few tiles into a short nanotube core, followed by facile elongation of the nuclei.

4.2.4 Photobleaching studies: Effect of base-deletion on the nanotube structure

We next examined the dynamic switching of nanotubes between different states of torsional strain along the backbone achieved through base-pair mismatch along the linking strands. The length mismatch between the tube sides serves as a strategy to introduce a local DNA structural change in the repeat unit (distortion/bending as a result of protein or small molecule binding). We were interested to probe whether this mismatch results in morphological changes in the nanotubes,

and at which point this bending/distortion would disrupt nanotube formation. To achieve this, we modified the length of the strand complementary to the two linking strands (LS2/3*) as shown in Figure 4.2A, by removing 2 to 6 bases. By hybridizing to LS2/3*, the newly prepared shorter strands likely cause the formation of internal loops of 2 to 6 bases. As a result, on one side of the nanotube, two consecutive triangular cores are separated by 84 bases (~28.6 nm) and on the other two sides they are separated by shorter DNA stretches: 82 for T2 (~27.9 nm), 81 for T3 (~27.5 nm), 80 for T4 (~27.2 nm), 79 for T5 (~26.9 nm) and 78 bases for T6 (~26.5 nm), respectively. This size mismatch repeats over the whole length of the nanotube at each constitutive polygon considering that a 1 μm nanotube has ~35 repeat units.

First, the nanotubes were preassembled in solution by mixing and annealing all strands (Figure 4.1A). As described earlier (Figure 4.1B), fully double-stranded T1 tubes exhibit exponential traces in intensity-time trajectories (>12 rungs). However, as the length difference between the tube sides increases (T2–T6), a population with a smaller number of steps appeared, consistent with shorter nanotubes (Figure 4.2B-C). Single molecule TIRFM photobleaching experiments for T2 and T3 showed an exponential decay of fluorescence intensity for the majority of the tubes, with a slight increase in the population of shorter tubes made up of 5 to 10 repeat units (Figure 4.2Ca-b). With a 4 base difference between LS1 and LS2/3, T4 exhibits a large increase in the population of shorter tubes ranging from 4 to 10 rungs, with only ~33% of the tubes showing an exponential decay (Figure 4.2Cc). A difference between the three sides of the tubes of 5 and 6 bases induced the assembly of small features of at most ~150 nm in length (~5 rungs, Figure 4.2Cd-e). Using single-molecule intensity trajectories (Figure 4.7, Experimental section), we generated histograms of the distribution of the number of bleaching steps in the nanotubes, where tubes T5 and T6 showed short nanotubes with no more than 5 repeat units (Figure 4.2Cd-e). AFM of T2-T6 confirmed these results, and in addition, showed increased bending as the length mismatch increases. Thus, the introduction of length mismatches in the repeat units of DNA nanotubes results in bending for differences of 2–3 bases, with relative maintenance of the tube length. On the other hand, a mismatch greater than 4 bases introduces sufficient distortion to cause nanotube shortening, which becomes significant for differences of 5–6 bases.

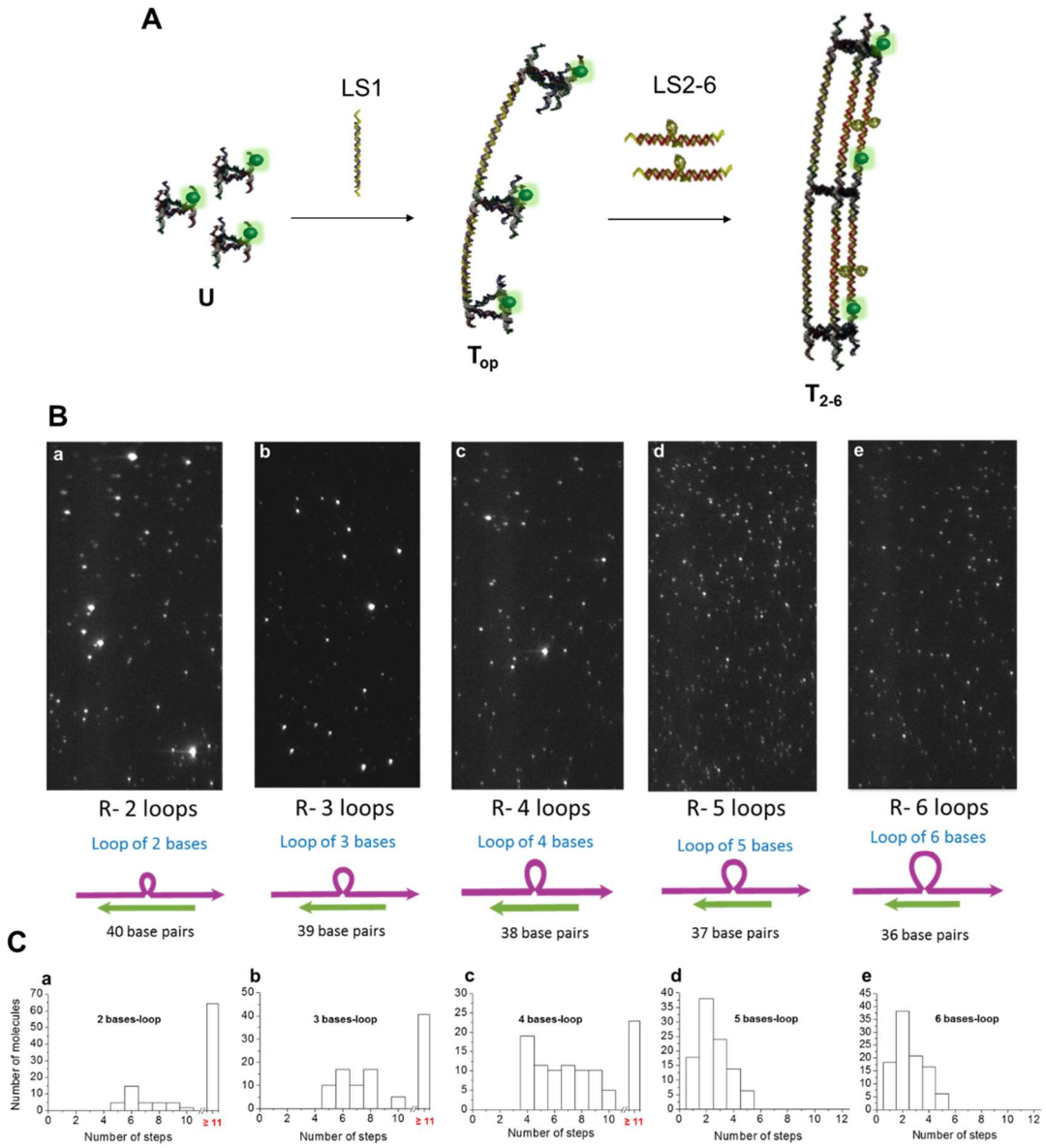

Figure 4.2. Study of the robustness of the tubes by increasing length mismatches between the vertical strands of the repeat units. (A) Schematic representing the introduction of a size mismatch between LS2-3 strands and LS2/3* through a gradual decrease of the length of LS2/3* strand. (B) a-e Typical TIRF images displaying the emission signal of Cy3-tagged DNA nanotubes (Scale 70 µm × 35 µm) upon the introduction of the size mismatch between LS2-3 strands and LS2/3* through a gradual decrease of the length of LS2/3* strand (2 to 6 bases). (C) a-e Histograms displaying the distribution of the number of steps in the traces of the different samples to show the effect of these mismatches on the size distribution of the tubes. The average length of the tubes decreases with increasing the mismatch length; a mismatch of 5 bases is enough to break the tubes into small pieces of 5 rungs at most.

4.2.5 Two-color single-molecule photobleaching experiment: Confirming structural details

In order to validate the presence of the loop strand within the structures, and confirm that the shortening of the nanotubes is caused by the length mismatched strand, we performed two-color single-molecule photobleaching experiments. In particular, we were interested to see if an initially long single-stranded nanotube can be fragmented and shortened upon addition of length mismatched strands, even under mild conditions. A strand displacement strategy can be applied to erase the complementary strands of LS1, LS2 and LS3 in solution and generate partially or fully single-stranded tubes. A detailed study of the switching of the nanotube from double- to single-stranded forms on the surface is presented in the experimental section 4.4.7 (Figure 4.9). A more in depth discussion of this topic will be provided in Chapter 5. In the present nanotubes, the linking strands LS1, LS2, and LS3 can be independently addressed (note that LS2 and LS3 have the same sequence in their middle, double-stranded portions, but different sequences at their sticky-end regions). To accomplish this experiment, the tubes were assembled using extended linking strands LS1–3*, bearing the same sequence as the original LS1–3, but additionally carrying a 10 base overhang. Addition of a fully complementary strands (eraser strands E1–3) that are expected to bind to each of LS1–3* displaced LS1-3 one by one from the nanotube (Figure 4.3A) leaving the nanotube single-stranded on either one or two or three sides respectively (1ssT, 2ssT and 3ssT). Using this strategy, we generated 2ssT with Cy3 and 5% biotin, by starting with double-stranded T1 and strand displacement of LS2/3 (Figure 4.3A). We then refilled the tube with the 5-bases shorter complements (LS2/3* 37) labeled with the red emitting dye Atto647N, in solution at room temperature (1 h incubation). Using two different diode lasers, regions were excited with an evanescent field, first at 641 nm and then at 532 nm. This sequential recording of the frames minimized artifacts that arise from the bleeding of Atto647N emission into the green channel and of Cy3 emission into the red channel. Single frames (200 ms) were acquired to prevent the photobleaching of the dyes. Little FRET was expected between the dyes because of their large separation (~7 nm, Figure 4.8, Experimental section 4.4.6). Immobilization of these preformed nanotubes T5 followed by TIRF microscopy showed the colocalization of Cy3 and Atto647N in the expected 1:2 ratio, which confirms the presence of the loop strand in the tube. Cy3 photobleaching revealed the presence of short nanotubes, with no more than 5 repeat units (Figure 4.3B-C). Thus, pre-annealing nanotubes T5 with length mismatch, or generating them from single-stranded forms produce similar populations of shortened nanotubes.

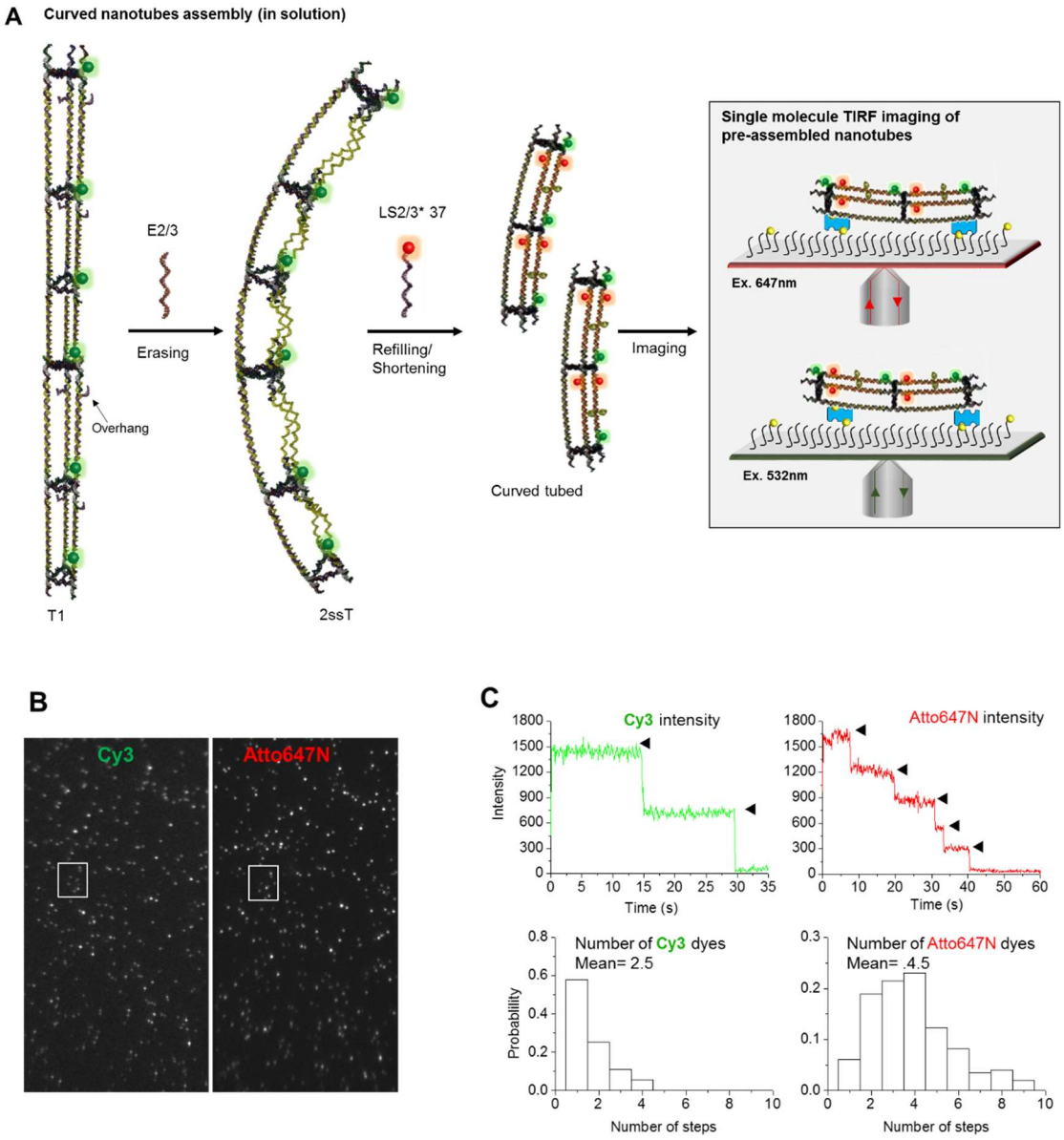

Figure 4.3: Single-molecule characterization of tubes T1 treated in solution with E2/3, then refilled with 5-base length mismatched LS2/3*, resulting in T5. This is followed by immobilization on the coverslip surface and TIRF measurement. (A) Schematic of the experiment whereby a partially single-stranded nanotube 2ssT is generated from the dually labelled Cy3-ATTO647N tube T1 upon "erasing" with E2-3 strands; then short and curved tubes are formed from "refilling" 2ssT with the mismatched length strands LS23*37. (B) TIRF images displaying the colocalization of the two dyes Cy3 and Atto647N (70 μm × 35 μm). Photobleaching traces and histograms of the probability distribution of the number of steps in the traces of refilled T5 for the Cy3 and ATTO647N dyes showing that the majority of the tubes consist of two or three rung units.

4.3 Conclusion

The newly simplified assembly design of nanotubes allows a rapid and scalable production of dynamic nanotubes using a minimal number of component strands, for potential applications as biophysical probes, tools for drug delivery, materials organization, plasmonic scaffolds and nanowire growth. *In situ* single molecule fluorescence microscopy enabled us to quantitatively characterize structural changes upon the introduction of an additional morphological modification into the nanotubes: an increasing size mismatch between the vertical strands of each repeat unit. This results in nanotube bending, until the introduced distortion disrupts the formation of long nanotubes as confirmed by one- and two-color single-molecule photobleaching studies. Because they have a large number of repeat units down their length, these nanotubes have the potential to amplify biologically relevant DNA distortions. In fact, due to the periodic nature of nanotubes, a single trigger could result in amplified motion across hundreds of nanometers by acting at each site along the length of the tube. This could be interesting for sensing applications, with an analyte producing large scale, detectable structural changes, or for design of molecular muscles, capable of extension and contraction under external stimuli.

4.4 Experimental section

4.4.1 Materials

Details on the sequences of the strands and the nanotube design and synthesis, in addition to AFM characterization and gel electrophoresis can be found in the published manuscript [16]. The strands were synthesized via automated solid-phase synthesis carried on a BioAutomation MerMade MM6 DNA synthesizer at 1 μmol scale. Labeled strands were ordered from Integrated DNA Technologies (IDT). The strands were deprotected and cleaved from the solid support in the presence of concentrated ammonium hydroxide solution (60°C, 16 hours). Polyacrylamide gel electrophoresis (PAGE: 20 x 20 cm vertical Hoefer 600 electrophoresis unit) was employed to purify crude products (8-20% polyacrylamide/8M urea at constant current of 30 mA for 2 hours, with 1xTBE as a running buffer). Following electrophoresis, the desired bands were excised then crushed and incubated in 11 mL of autoclaved water at 60°C for at least 12 hours. After drying the samples to 1.5 mL, we used size exclusion chromatography (Sephadex G-25) to desalt the solution. The strands were quantified (OD260) by UV/vis spectroscopy with a NanoDrop Lite Spectrophotometer and using IDT's extinction coefficient at 260.

Acetic acid, boric acid, EDTA, urea, magnesium chloride, GelRed, tris(hydroxymethyl)aminomethane (Tris), D(+) glucose, 2-betamercaptoethanol, and streptavidin were purchased from Aldrich. Nucleoside (1000 Å)-derivatized LCAACPG solid support with loading densities of 25-40 μmol/g, Sephadex G-25 (super fine DNA grade), and reagents for automated DNA synthesis were used as purchased from BioAutomation. Acrylamide (40%)/bis-acrylamide 19:1 solution and agarose were purchased from BioShop. For TIRFM sample preparation, 1% v/v Vectabond/acetone was purchased from Vector Laboratories, while poly-(ethylene glycol) succinimidyl valerate MW 5000 (mPEG-SVA) and biotin-PEG-SVA were purchased from Laysan Bio, Inc. Imaging chamber components were purchased from Grace Bio-Lab. TBE buffer is composed of 90 mM Tris and boric acid and 1.1 mM EDTA, with a pH of ~8.3. TAMg buffer is composed of 45 mM Tris and 12.5 mM $MgCl_2$ with a pH of ~7.8 adjusted by glacial acetic acid.

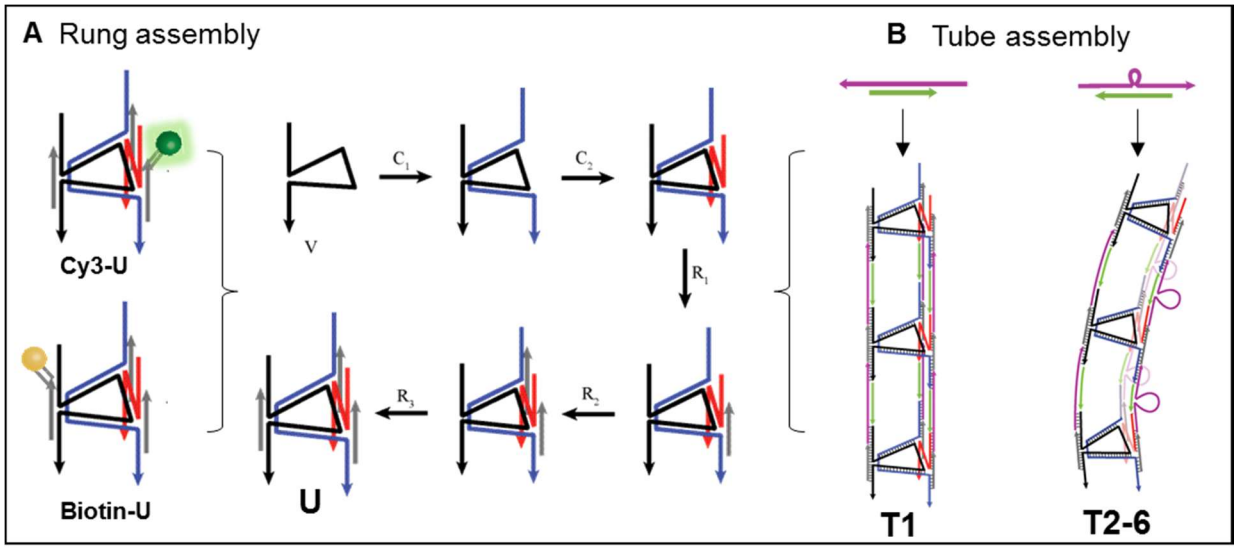

Figure 4.4: DNA nanotube design. (A) Assembly of the triangular core unit U from 5 unmodified DNA strands. (Right) Design of U: Strand V (black) binds with complementary strand C1 (blue), which spans its internal section and creates a core triangular frame. Complementary strand C2 (red) binds the third edge. Rigidifying strands R1, R2 and R3 (gray) bind the overhangs of C1 and C2, holding them out of plane from the triangular core, to create the vertical sticky-ends of the rung. Rigidifying strands can include an additional overhang to hybridize a Cy3 or biotin tagged DNA strand. (B) Nanotube formation through sticky-end cohesion of the rung units to linking strands; LS1-3 (right), or by introducing a size mismatch between LS2-3 strands and LS2/3* through a gradual decrease of the length of LS2/3* strand.

4.4.2 Surface and sample preparation

Coverslips were immersed in piranha solution (25% H_2O_2 and 75% concentrated H_2SO_4) and sonicated for 1h, followed by multiple water (molecular biology grade), and acetone (high-performance liquid chromatography (HPLC) grade) rinsing cycles. Dry and clean coverslips were then treated with Vectabond/Acetone 1% v/v solution for 5 min and then rinsed with H_2O and left in dried state until used. In order to prevent non-specific adsorption of biomolecules onto the glass surface, coverslips were functionalized prior to use with a mixture of poly(ethylene glycol) succinimidyl valerate, MW 5000 (mPEG-SVA) and biotin-PEG-SVA at a ratio of 99/1 (w/w), in a 0.1 M sodium bicarbonate solution for 3h. Excess PEG was rinsed with water, and the coverslips were dried under a N_2 stream. In order to reduce photobleaching rate, oxygen scavenger solution was prepared consisting of a triplet quencher agent, β-mercaptoethanol 1% v/v and an oxygen scavenger system (D(+)glucose 3% w/v, glucose oxidase 0.1 mg/mL, and catalase 0.02 mg/mL).

Imaging chambers (~8 μL) were constructed by pressing a polycarbonate film with an adhesive gasket onto a PEG-coated coverslip. Two silicone connectors were glued onto the predrilled holes of the film and served as inlet and outlet ports. The surface was incubated with 10 μL of a 0.2 mg/mL streptavidin solution for 10 min. Excess streptavidin was then washed with 100 μL of 1xTAMg buffer. 10 μL of the 680pM DNA nanotube solution was injected in the chamber. (136nM solution diluted 200×; ~100 fluorescent spots per 30 μm × 30 μm region). Unbound DNA structures were then flushed out with 50 μL of 1xTAMg buffer.

4.4.3 Imaging set-up and analysis

Fluorescence single-molecule experiments were carried out using a total internal reflection fluorescence microscopy (TIRFM) setup. The TIRFM setup consisted of an inverted microscope (IX71, Olympus) equipped with a laser-based TIRFM illumination module (IX2-RFAEVA-2, Olympus) coupled to a diode-pumped solid-state green laser (both 532 nm and 638 nm outputs were used, lasers from CrystaLaser). The beam position was adjusted using the illuminator to attain total internal reflection through an oil-immersion objective (N.A. 1.45, Olympus U PLAN SAPO 60x,). Fluorescence emission was collected through the objective and images were captured with an EMCCD camera (CascadeII: 512B, Photometrics, Roper Scientific). Emission was chromatically separated using dichroic mirrors (640dcxr, Chroma) with the 'green' and 'red' emission filtered through band pass filters (HQ590/70M and HQ685/80M, respectively, from Chroma) before being captured by the EMCCD camera. The camera was controlled using Image-Pro Plus 5.1 (Media Cybernetics), capturing 8-bit 512 x 512 pixel images with an exposure time of 150-200 ms, a conversion gain of 3, and multiplication gain of 3750-4095. To image the Cy3/Atto647N DNA nanotube sample, excitation was carried out with a power output of 6.5 mW (532 nm) and 4.6 mW (638 nm) measured from the objective. Fluorescence intensity-time trajectories of individual molecules were extracted from the movies using an automated IDL and Matlab algorithm built in-house.

4.4.4 Optimization of the DNA nanotubes surface binding

In order to immobilize the nanotubes on a streptavidin coated coverslip surface as described in the previous section, 5% of one of the strands within the triangular core were labeled with biotin. The 5% average biotin labeling represents a compromise between specifically immobilizing the nanotubes on the coverslip surface and maintaining their dynamic character. For this end, we extended one of the rigidifier strands (R3ov) by 20 bases and we synthesized its complementary strand decorated with biotin moiety (Bio-R3ov*). Since the interaction of biotin on our constructs with strepdavidin on the surface determined the dynamics and the stability of the tubes during the TIRFM measurements, we varied the amount of biotin attached to our nanotubes from 100% to 5%. A 100% biotin was referred to a 1:1 ratio of the biotinylated strand with respect to the rung. However, at a percentage of 5% for example, 5% of the rigidifier (R3) were hybridized to the strand tagged with biotin and to the triangular core while the remaining 95% consisted of R3 lacking the 20 base sticky-end. Since the rigidifier R1 was labelled with a Cy3 dye, the emission of nanotubes bearing 100%, 80%, 60%, 40%, 20%, 10% and 5% of biotin molecules was detected into the green channel (Figure 4.5B). The visualization of the tubes was possible even at the lowest percentage tested indicating that a minimal percentage of biotin label is sufficient to deposit the tubes on the surface. Because the biotin-streptavidin interaction can restrain the movement of the tubes, 5% biotin labels were employed in all studies in order to allow a certain degree of freedom of the tubes on the surface. Interestingly, with a lower biotin percentage, we started observing a wiggling behavior of the partially anchored structures observed in real time using TIRF microscopy. This observation confirms that nanotubes are not fully immobilized on the surface but present a certain degree of freedom.

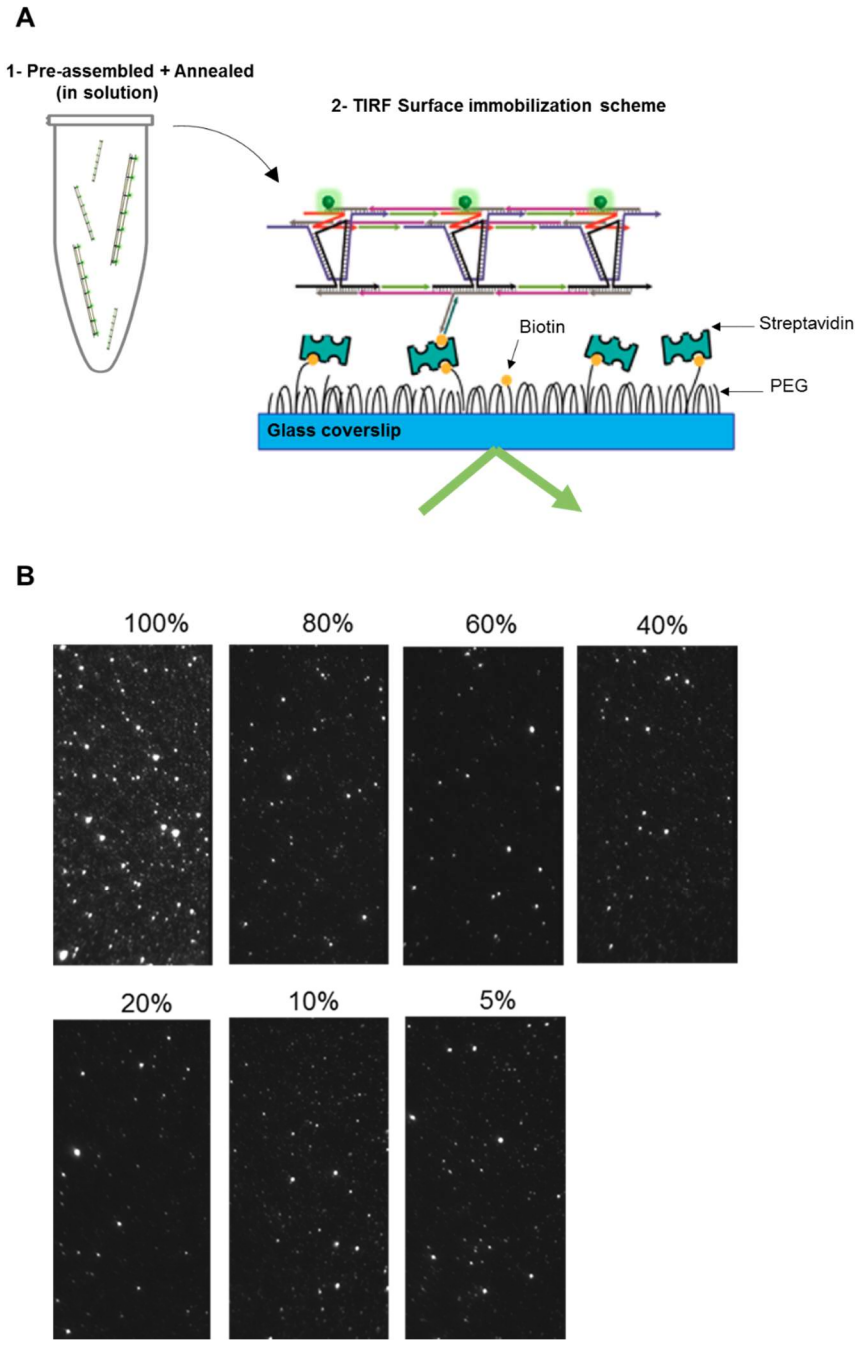

Figure 4.5: Single-molecule surface immobilization of pre-assembled DNA nanotubes. (A) 1. Illustration of the nanotubes pre-formed and annealed in solution. 2. Illustration of the glass coverslip functionalization with PEG, PEG-biotin and streptavidin with a biotinylated DNA nanotube bound specifically on the surface via biotin streptavidin interactions. (B) Typical TIRF images (70 µm × 35 µm) displaying the Cy3 signal of DNA nanotubes with different biotin concentration on a streptavidin coated- PEG-PEG-biotin surface.

4.4.5 A possible ether-like chelating effect of Mg^{2+} on the PEG surface

We note that after the many attempts to bind the biotinylated nanotubes on the streptavidin coated PEG surface, we observed that the amount of buffer (1x TAMg, Magnesium containing buffer) used to flush the surface before adding the nanotubes is critical for the binding of the structures. Importantly, control experiments with no streptavidin added were performed to confirm the specificity of the binding we were observing. For the conditions of our experiments, we determined the minimum volume to be 100µL of a 1x TAMg buffer below which no binding was observed (except for the 10% non-specific binding caused by the surface defects) (Figure 4.6A). We speculated, based on literature, that an excess of Mg^{2+}, after certain volume of buffer flushed, might be chelating the PEG chain and cyclizing it similarly to a crown-ether compound. This phenomenon would make the streptavidin, originally buried among the PEG chains, more available for binding the tubes (Figure 4.6B).

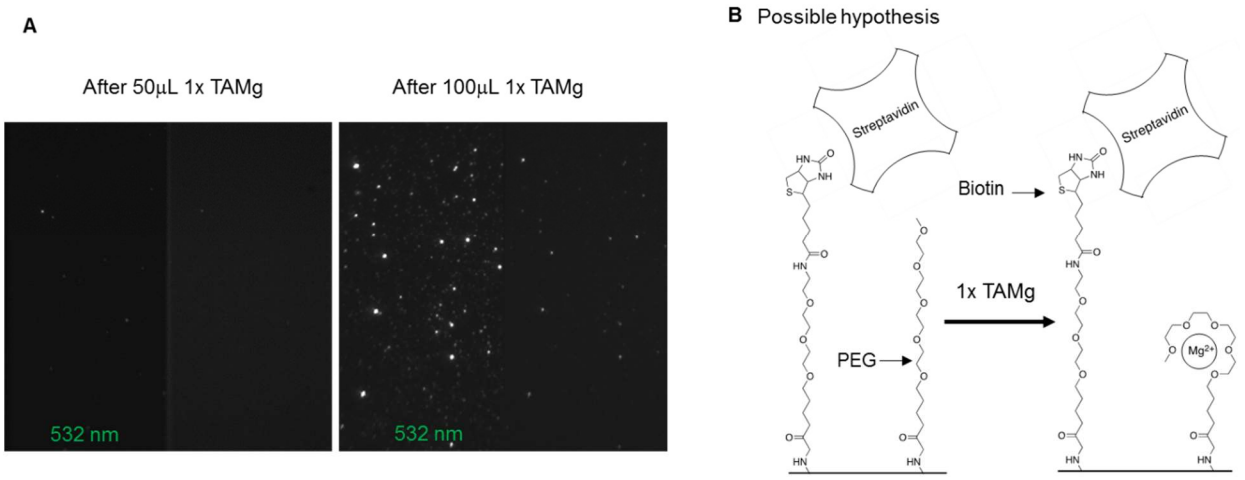

Figure 4.6: Magnesium ether-like chelating effect. (A) Typical TIRF images (scale: 70 × 70 µm) showing the surface density of the bound nanotubes after 50 µL (left) and after 100 µL (right). (B) Scheme showing the possible crown-ether-like chelating effect causing the PEG chain to collapse in the presence of a certain excess of Mg^{2+} and exposing hence the streptavidin.

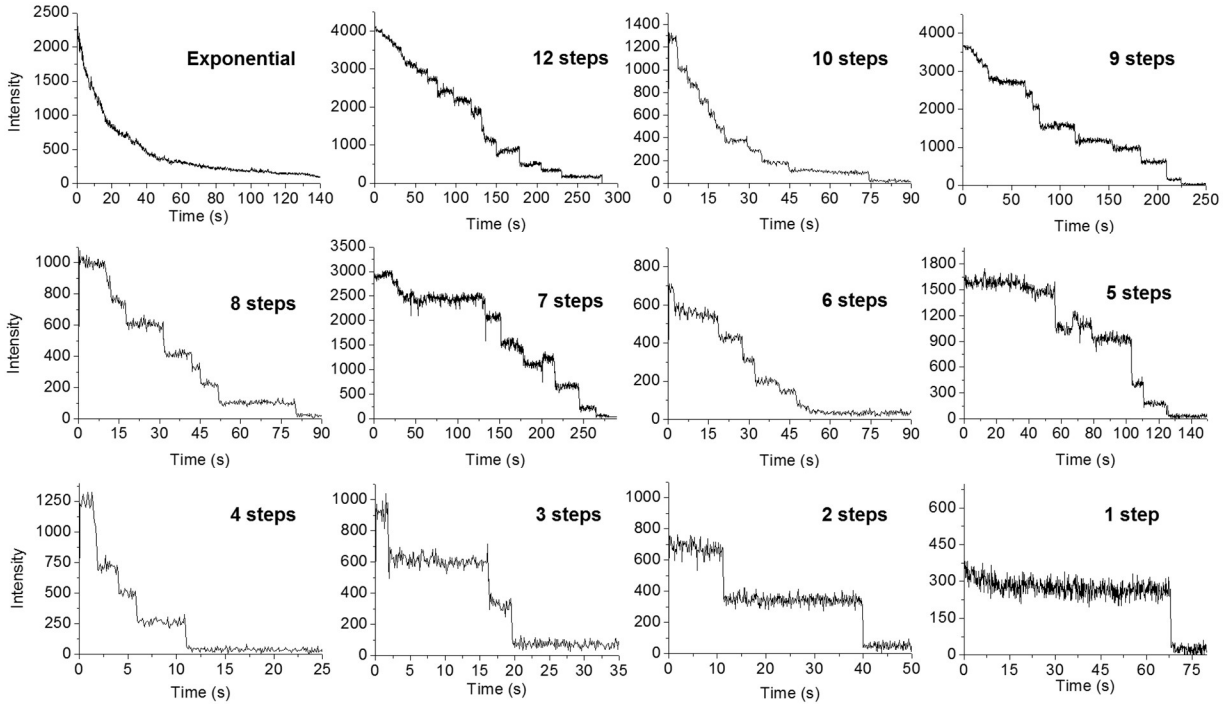

Figure 4.7: Typical single molecule photobleaching traces. Examples of the different number of steps observed in intensity-time trajectories and counted for the imaged samples of DNA nanotubes (T1 to T6).

4.4.6 Fluorescence Resonance Energy Transfer (FRET)

The figure below shows the distances between the ATTO647N and the two neighboring Cy3 dyes. Given the fact that the ATTO647N-tagged overhang is single-stranded (10 bases) and has a high degree of flexibility, it will then rotate on a sphere of 4.2nm radius, an average distance calculated based on FRET studies by Ha's group.[17] We calculated the distances at the two extreme ends at which the ATTO647N dye could possibly be (the closest side to Cy3 and the farthest from it, ends at 180° angle difference). In either of the two cases, the distance is at least 6.68 nm, which implies that the FRET expected at this proximity is minimal as mentioned in the text.

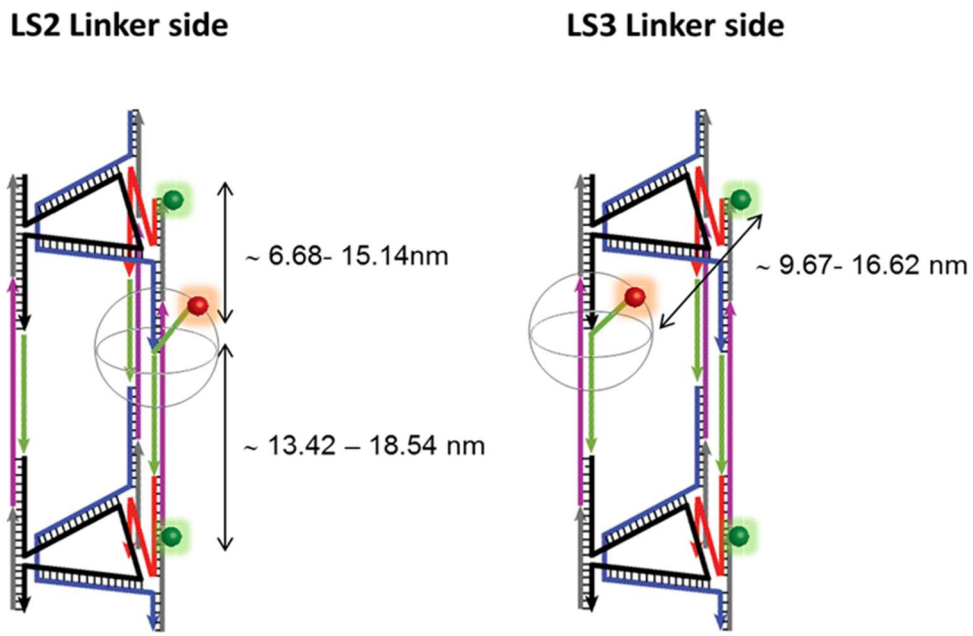

Figure 4.8: Illustration showing the distances between ATTO647N (red) and the two neighboring Cy3 (green) dyes: (left) when ATTO647N linker is LS2 or (right) when ATTO647N linker is LS3.

4.4.7 Switching between single- and double-stranded forms of the nanotube

In addition to solution-based assembly, we also applied the strand displacement strategy to erase and refill the complementary strands of LS2 and LS3 on the surface. Chapter 5 includes a detailed single-molecule study of the underlying dynamics. First, we built the tubes using extended linking strands LS2–3*, bearing the same sequence as the original LS2–3, but additionally carrying a 10-base overhang. We then added fully complementary strands (eraser strands E2–3) that are expected to bind to each of LS2–3* thus displacing them one by one from the nanotube. This leaves the nanotube single-stranded on two sides (2ssT) (Figure 4.9A). We examined each state of these tubes *in situ* by TIRFM. We immobilized the nanotubes T1 labeled with Cy3 and 5% biotin as before, but we used in this case ATTO647N-labeled LS2/3*, containing 10-base overhangs. We once again observed the spatial colocalization of the two dyes in most of the imaged structures (Figure 4.9B). We then added the erasing strand E2/3 at a concentration of 500 nM (in excess), to form the immobilized, partially single-stranded nanotube 2ssT. This was followed by a washing step with 1× TAMg buffer (50 µL). Consistent with two sides of the nanotube losing the labeled LS2/3* and becoming single-stranded, no emission was detected in the red channel (Atto647N) following the above 2 steps. We next added and incubated fresh ATTO647N-LS2/3* solution at a

concentration of 500 nM (in excess) followed by a washing step with 1× TAMg buffer (50 μL). Colocalization of the two dyes indicated that the refilling experiment was successful (Figure 4.9B). Interestingly, refilling the partially single-stranded tube 2ssT with strands was qualitatively slow, taking tens of minutes, in contrast with the near immediate removal of the strands from double-stranded tube T1. Chapter 5 explores the erasing and refilling dynamics in greater detail. When we compare the intensity ratios of the two dyes before and after erasing/refilling, we notice a high refilling percentage after 1 h incubation. These observations provide evidence of the stability of the tubes in both single- and double-stranded forms and their ability to restore the initial design without degradation. We note the difference in the background between panel 2 and panel 3, and between panel 2 and panel 4 in Figure 4.9B. This difference is due to the incubation of the Atto647N labeled DNA strand in the chamber (panel 2) giving higher background, which is rinsed thoroughly (panel 3) after erasing. Panel 4 also shows a refilling experiment with Atto647N labeled DNA but in this case imaging was done after rinsing thoroughly, rather than during incubation as in panel 2.

The above experiments are consistent with the ability to reversibly cycle the nanotube system between double-stranded, partially single-stranded and fully single-stranded forms. Our preliminary evidence shows that the surface attached single-stranded nanotubes are slower to re-hybridize into their double-stranded form (TIRF), possibly consistent with increased DNA deformation and/or compaction and decreased accessibility. Additionally, the switching processes are reversible and the nanotube retains its length and robustness as it changes between these forms.

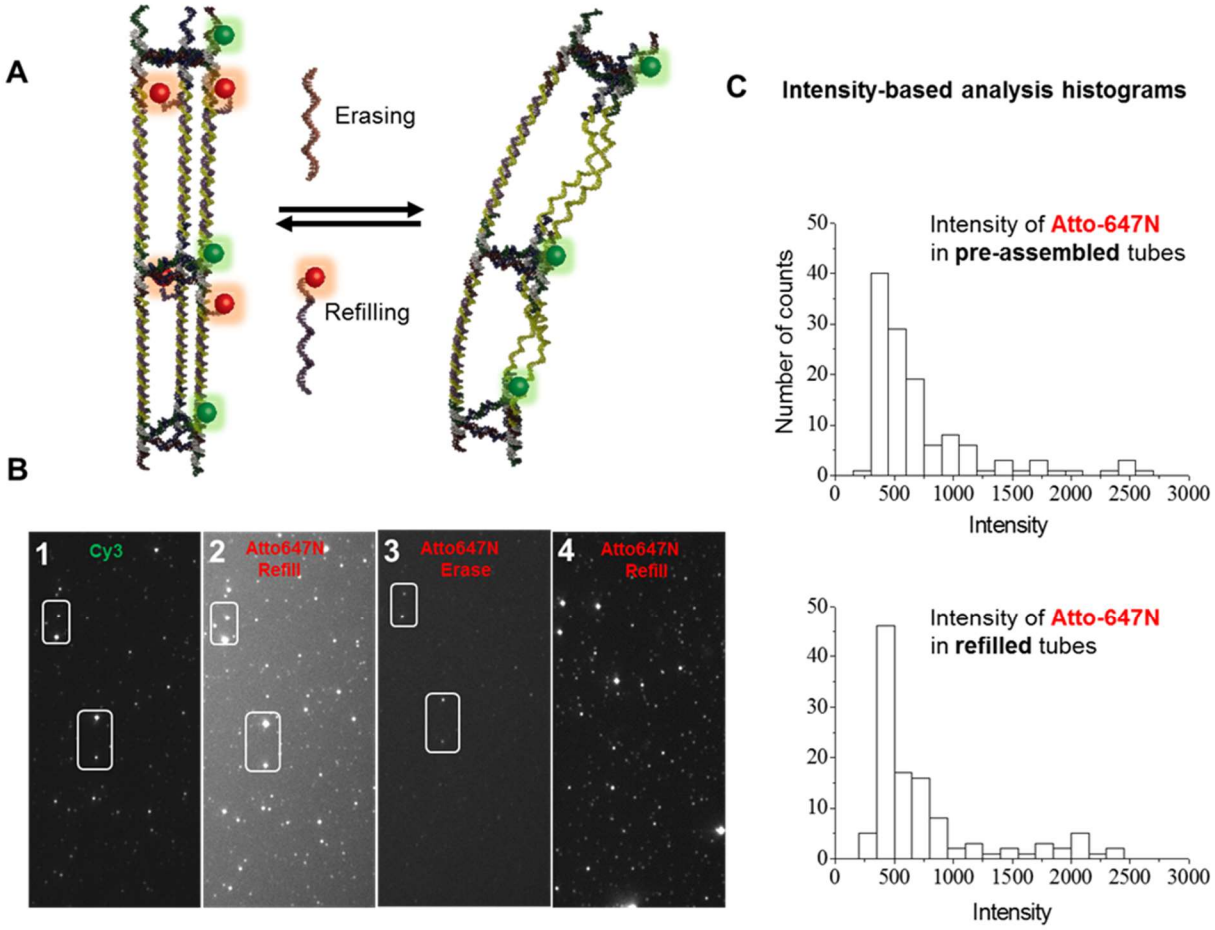

Figure 4.9: Single-molecule characterization of the reversible switching between tubes T1 and 2ssT, immobilized on coverslips using biotin-streptavidin interactions. (A) Schematic showing the removal of the strands labeled with Atto647N and their re-addition. (B) Series of TIRFM images (70 μm × 35 μm) displaying the colocalization of the two dyes prior to the removal of the labeled LS2/3* (panels 1 and 2), the disappearance of the Atto647N emission upon adding E2/3 (panel 3) and its reappearance after LS2/3* hybridization (panel 4). (C) Histograms depicting the intensity distribution of Atto647N in preassembled versus refilled tubes T1, consistent with efficient refilling with LS2/3*.

4.5 References

1. (a) Seeman, N. C., DNA in a material world. *Nature* **2003,** *421* (6921), 427-431; (b) Aldaye, F. A.; Palmer, A. L.; Sleiman, H. F., Assembling Materials with DNA as the Guide. *Science* **2008,** *321* (5897), 1795-1799; (c) Liu, H.; Chen, Y.; He, Y.; Ribbe, A. E.; Mao, C., Approaching The Limit: Can One DNA Oligonucleotide Assemble into Large Nanostructures? *Angewandte Chemie International Edition* **2006,** *45* (12), 1942-1945; (d) Shih, W. M.; Lin, C., Knitting complex weaves with DNA origami. *Current opinion in structural biology* **2010,** *20* (3), 276-282.

2. (a) Lin, C.; Liu, Y.; Yan, H., Self-Assembled Combinatorial Encoding Nanoarrays for Multiplexed Biosensing. *Nano Letters* **2007,** *7* (2), 507-512; (b) Yan, H.; Park, S. H.; Finkelstein, G.; Reif, J. H.; LaBean, T. H., DNA-Templated Self-Assembly of Protein Arrays and Highly Conductive Nanowires. *Science* **2003,** *301* (5641), 1882-1884.

3. Rothemund, P. W. K.; Ekani-Nkodo, A.; Papadakis, N.; Kumar, A.; Fygenson, D. K.; Winfree, E., Design and Characterization of Programmable DNA Nanotubes. *Journal of the American Chemical Society* **2004,** *126* (50), 16344-16352.

4. Mao, C.; Sun, W.; Shen, Z.; Seeman, N. C., A nanomechanical device based on the B-Z transition of DNA. *Nature* **1999,** *397* (6715), 144-146.

5. (a) Zhang, D. Y.; Seelig, G., Dynamic DNA nanotechnology using strand-displacement reactions. *Nat Chem* **2011,** *3* (2), 103-113; (b) Nielsen, P.; Egholm, M.; Berg, R.; Buchardt, O., Sequence-selective recognition of DNA by strand displacement with a thymine-substituted polyamide. *Science* **1991,** *254* (5037), 1497-1500; (c) Yurke, B.; Turberfield, A. J.; Mills, A. P.; Simmel, F. C.; Neumann, J. L., A DNA-fuelled molecular machine made of DNA. *Nature* **2000,** *406* (6796), 605-608.

6. Castro, C. E.; Su, H.-J.; Marras, A. E.; Zhou, L.; Johnson, J., Mechanical design of DNA nanostructures. *Nanoscale* **2015,** *7* (14), 5913-5921.

7. Dietz, H.; Douglas, S. M.; Shih, W. M., Folding DNA into Twisted and Curved Nanoscale Shapes. *Science (New York, N.Y.)* **2009,** *325* (5941), 725-730.

8. Pinheiro, A. V.; Han, D.; Shih, W. M.; Yan, H., Challenges and opportunities for structural DNA nanotechnology. *Nat Nano* **2011,** *6* (12), 763-772.

9. (a) Aldaye, F. A.; Lo, P. K.; Karam, P.; McLaughlin, C. K.; Cosa, G.; Sleiman, H. F., Modular construction of DNA nanotubes of tunable geometry and single- or double-stranded character. *Nat Nano* **2009,** *4* (6), 349-352; (b) Wilner, O. I.; Orbach, R.; Henning, A.; Teller, C.; Yehezkeli, O.; Mertig, M.; Harries, D.; Willner, I., Self-assembly of DNA nanotubes with controllable diameters. *Nat Commun* **2011,** *2*, 540.

10. Hamblin, G. D.; Hariri, A. A.; Carneiro, K. M. M.; Lau, K. L.; Cosa, G.; Sleiman, H. F., Simple Design for DNA Nanotubes from a Minimal Set of Unmodified Strands: Rapid, Room-Temperature Assembly and Readily Tunable Structure. *ACS Nano* **2013,** *7* (4), 3022-3028.

11. Tsukanov, R.; Tomov, T. E.; Liber, M.; Berger, Y.; Nir, E., Developing DNA Nanotechnology Using Single-Molecule Fluorescence. *Accounts of Chemical Research* **2014,** *47* (6), 1789-1798.

12. (a) Moerner, W. E.; Fromm, D. P., Methods of single-molecule fluorescence spectroscopy and microscopy. *Review of Scientific Instruments* **2003,** *74* (8), 3597-3619; (b) Waters, J. C., Accuracy and precision in quantitative fluorescence microscopy. *The Journal of Cell Biology* **2009,** *185* (7), 1135-1148.

13. (a) Das, S. K.; Darshi, M.; Cheley, S.; Wallace, M. I.; Bayley, H., Membrane Protein Stoichiometry Determined from the Step-Wise Photobleaching of Dye-Labelled Subunits. *ChemBioChem* **2007,** *8* (9), 994-999; (b) Ulbrich, M. H., Counting Molecules: Toward Quantitative Imaging. In *Far-Field Optical Nanoscopy*, Tinnefeld, P.; Eggeling, C.; Hell, W. S., Eds. Springer Berlin Heidelberg: Berlin, Heidelberg, 2015; pp 263-291.

14. (a) Coffman, V. C.; Wu, J.-Q., Counting protein molecules using quantitative fluorescence microscopy. *Trends in biochemical sciences* **2012,** *37* (11), 499-506; (b) Chen, Y.; Bharill, S.; Isacoff, E. Y.; Chalfie, M., Subunit composition of a DEG/ENaC mechanosensory channel of Caenorhabditis elegans. *Proceedings of the National Academy of Sciences* **2015,** *112* (37), 11690-11695.

15. (a) Trache, A.; Meininger, G. A., Total Internal Reflection Fluorescence (TIRF) Microscopy. In *Current Protocols in Microbiology*, John Wiley & Sons, Inc.: 2005; (b) Zhuang, X.; Bartley, L. E.; Babcock, H. P.; Russell, R.; Ha, T.; Herschlag, D.; Chu, S., A Single-Molecule Study of RNA Catalysis and Folding. *Science* **2000,** *288* (5473), 2048-2051.

16. Rahbani, J. F.; Hariri, A. A.; Cosa, G.; Sleiman, H. F., Dynamic DNA Nanotubes: Reversible Switching between Single and Double-Stranded Forms, and Effect of Base Deletions. *ACS Nano* **2015,** *9* (12), 11898-11908.

17. Murphy, M.; Rasnik, I.; Cheng, W.; Lohman, T. M.; Ha, T., Probing single-stranded DNA conformational flexibility using fluorescence spectroscopy. *Biophysical Journal* **2004,** *86* (4), 2530-2537.

5 DNA nanotube dynamics at the single molecule level

Author Contributions: Single molecule protocols and experimental design were developed by **Amani A. Hariri** in assistance with **Jesse Gordon** (summer student, 2015). Single molecule experiments were carried by **Amani A. Hariri** in assistance with **Jesse Gordon** and **Casey Platnich**. Data analysis was interpreted by **Amani A. Hariri** with the help of **Prof. G. Cosa, Prof. H.F. Sleiman** and **Yasser Gidi**. DNA sequence design, nanotube synthesis and purification were carried out by **Janane F. Rahbani.** The work was conducted under the supervision of **Prof. G. Cosa** and **Prof. H. F. Sleiman.**

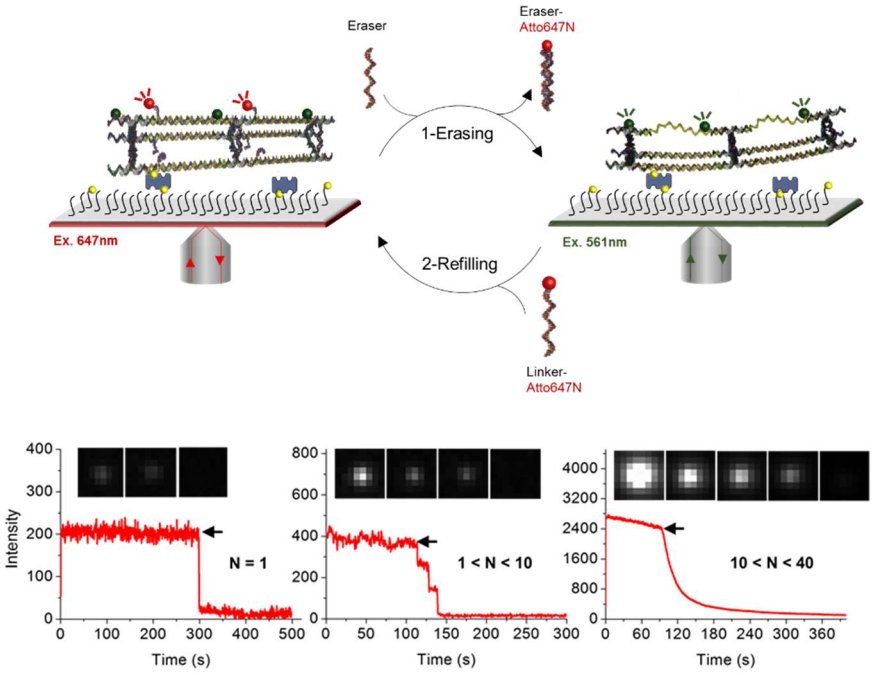

5.1 Introduction

Dynamic DNA nanotechnology uses weak and reversible interactions to generate higher-order supramolecular structures with multiple molecular components.[1] Additionally, exchange reactions among the different building blocks induce increasingly complex spatial and temporal dynamics.[2] Due to the highly complex and dynamic features of DNA nanoarchitectures[3], a key challenge is to develop analysis tools and kinetic methods for a better understanding of their collective structural behaviour in response to modifications in their molecular elements.[4] A comprehensive study of the interplay of thermodynamics and dynamics is desired as it will ensure building architecturally precise and structurally robust nanomaterials.[5] This understanding will also provide the conceptual underpinning towards developing dynamic functional activity, extending and diversifying the current paradigms of dynamic DNA structures.[6]

Single molecule fluorescence (SMF) methodologies have been utilized in recent years to extract structural and dynamic information on protein complexes as well as protein DNA or protein RNA complexes.[7] These methods are performed *in situ* where samples are investigated in their natural aqueous environment.[8] More particularly, single-molecule fluorescence imaging of immobilized substrates enables the continuous observation of individual structures for an extended period of time, and the detection of small intermediate populations and side-products, which are obscured in bulk measurements where only the average distribution is recorded.[9] In combination with a flow-cell, SMF enables real-time monitoring while replacing the surrounding solution to facilitate the introduction of building blocks and chemical actuators.[10]

Here, we adapt existing SMF methods and develop new SMF strategies to investigate the dynamics of DNA nanostructures. Working with structures efficiently synthesized through a minimal set of 11 strands only[11], robust nanotubes with controlled geometry and site specific addressability were built. This unique structure enabled to reversibly switch the linkers within the DNA nanotubes from a double-stranded to a single-stranded form using strand displacement strategies. We employed a total internal reflection fluorescence microscope to examine, in real time, the "peeling off" of 1 and 2 fluorescently-labelled linking strands from surface-bound DNA nanotubes. Computing the fluorophores survival lifetimes, we observed that the rate of releasing DNA strands in a dimer structure (ca. 9.5s) is half that recorded for an oligomer structure (ca. 20s). This is possibly indicative of a negative cooperativity within the oligomer structures. In addition

to structural cooperativity, our work addressed the robustness of DNA assembly using single molecule two-colour colocalization analysis. In doing so, we showcase how SMF methodologies are uniquely poised to understand and tackle the vexing dynamics of DNA nanostructures providing unsurpassable information towards the fabrication of DNA-based actuators with improved performance.

5.2 Results and discussions

Key to our dynamic studies is the adaptation of state-of-the-art single-molecule fluorescence methodologies to monitor and characterize the relaxation time of the ATTO647N emission intensity in single nanotubes under a constant flow of the "eraser" strand. Two-colour imaging experiments enabled us to report unequivocally the robustness and structural fidelity of the constructs following the erasing process.

5.2.1 DNA nanotube design and synthesis

Dynamic studies involved two types of DNA nanotube structures, dimers and oligomers, designed to switch between double-stranded and single-stranded form upon the removal of the linking strands using strand displacement strategies. The nanotube design and synthesis is based on a protocol recently reported by us and described in chapter 4. The design involved a modular synthesis of a triangular "core" unit (U) and three different linking strands (LS1, LS2 and LS3). The core structure (U), composed of six unmodified DNA strands, possessed extensions from the top and bottom of the triangular plane, in order to hybridize *via* sticky-end cohesion to the three linking strands resulting in nanotube formation. It is important to note that the linking strands LS1, LS2, and LS3 are independently addressable. Additionally, LS2 and LS3 have the same sequence in their middle double-stranded portions (complementary to LS2/3*), but different sequences at their sticky-end regions. To convert the structure into the single stranded form, we modified the strands LS2/3*, by adding 10-base overhangs in the DNA backbone. Strand displacement strategies could then be exploited to erase LS2/3* with E2/E3 strands.
In order to prepare a control sample consisting of a dimer, we introduced two types of triangular cores. For the top rung, the three sticky-end overhangs above the plane were removed while the three sticky-ends below remained. Additionally, the three overhangs below the plane of the bottom rung were removed. Subsequently, all dimers were constructed through the addition of LS1 first

then LS2 and LS3 as described before. For details on gel and AFM studies, please consult reference [11].

Nanotubes were immobilized on a coverslip surface for fluorescence studies (Figure 5.1A). Glass coverslips were coated with a mixture of polyethylene glycol (PEG) and biotin-tagged PEG to prevent nonspecific adsorption. Individual nanotubes were specifically grafted on the coverslips through biotin-streptavidin interactions. To this end, we modified the core of the tubes (U) by labelling one of the rigidifying strands (RS1) with a biotin at an average of 5% biotin-labeling. We chose this biotin concentration to ensure mobility on the surface and thus make the hybridization dynamics more easily perceived. We note that the biotin loading was 100% for dimers.

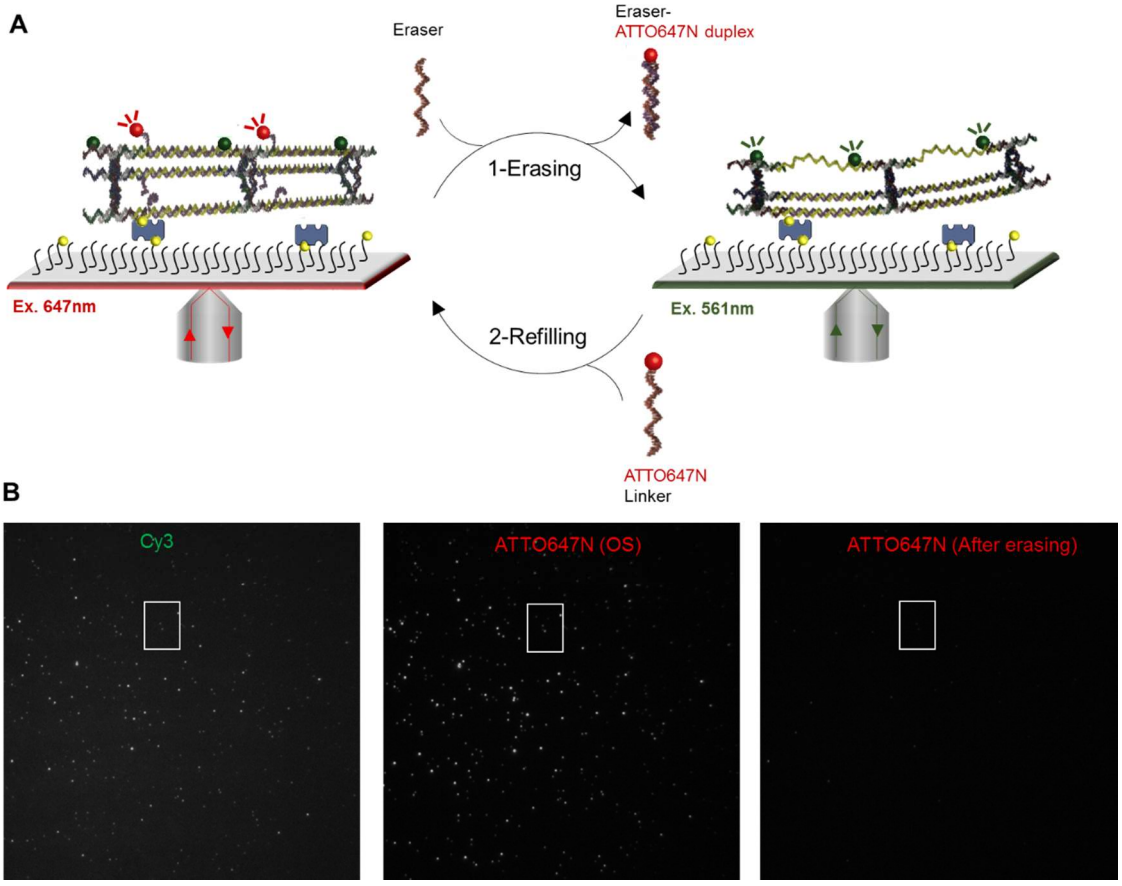

Figure 5.1: In-situ TIRF imaging of reversible double stranded-single stranded switching along the linkers of DNA nanotubes. (A) Schematic showing the two-color TIRF imaging experimental design for monitoring the emission of surface bound DNA nanotubes bearing ATTO647N and Cy3 dyes. The introduction of an eraser strand to remove ATTO647N linkers from the surface bound DNA nanotubes is also illustrated. (B) Typical TIRF images (70µm×70µm) acquired following 647nm (ATTO647N) or 561nm (Cy3) excitation before (left and middle panels) and after (right panel) the addition of the eraser strand. Geometric figures assist in qualitatively visualizing the colocalization, quantified using our homebuilt software.

5.2.2 Single molecule fluorescence studies

Single-molecule fluorescence imaging enabled us to visualize real-time the "peeling off" of ATTO647N linker in different numbers and locations within the nanotubes. For fluorescence studies, we modified i) the core of the tube (U) by labelling another component rigidifying strand (RS2) with the fluorophore Cy3; and ii) the linking strands by labelling LS2/3* with an ATTO647N fluorophore (ATTO647 linker).

Single particle fluorescence imaging was carried out in our flow-through imaging chambers using an inverted microscope implementing an objective-type TIRF configuration and employing a 561nm and a 647nm lasers. Fluorescence emission was spectrally filtered with the adequate emission filters to record emission on the green and red channels. Images corresponding to a field of view of ca. 70 μm×70 μm were acquired onto a 512×512 pixel back-illuminated electron-multiplying charge-coupled device (EMCCD) camera. Prior to image acquisition, a tubing was inserted into the inlet port, flowing solutions at a rate of 5 μL/min. Data acquisition was initiated synchronously with the pump flowing the eraser strand.

In order to record the erasing process over time in each bound nanotube, 6000 frames were collected for the ATTO647N emission. Single frame captures in the green channel (150ms) were acquired prior to and after the erasing process. Typically around 200 single molecules were simultaneously imaged within a field of view (See Experimental Section). Figure 5.1B shows fluorescent spots observed upon the subsequent excitation of the two dyes (Cy3 and ATTO647N) with their emissions colocalizing in space, which confirms that DNA nanotubes bind on the surface as integral units. Only colocalizing molecules were considered for the analysis.

5.2.2.1 Single molecule intensity-time trajectories.

We utilized two types of structures for our kinetics experiments: DNA nanotube dimers and oligomers. Using single molecule immobilization-based TIRF imaging, we monitored in real-time the erasing of either one or two ATTO647N linkers in each repeat unit along the DNA backbone from surface bound nanotubes (Figure 5.1A). An excess of the eraser strand (33nM) in oxygen scavenger solution was flowed while simultaneously recording the intensity over time for each nanotube (see Experimental section). One step and two steps were observed in the intensity time trajectories for the erasing of a dimer structure with 1 and 2 ATTO647N linkers, respectively; while only an exponentially decaying behaviour was observed for the oligomer tubes.

Representative intensity-time trajectories showing the erasing of the two different sets of nanotubes with 1 and 2 ATTO647N linkers are shown in panel 1, 2 and 3 (Figure 5.2B, see also Experimental Section). To confirm that the intensity drop is due to the erasing of the ATTO647N linkers and not caused by the photobleaching of the dye, control experiments were carried out with oxygen scavenger alone (in the absence of the eraser), for which we observed long steady intensity-time trajectories as shown in panel 4 (Figure 5.2B) with an average lifetime of 1264 s (See Experimental Section).

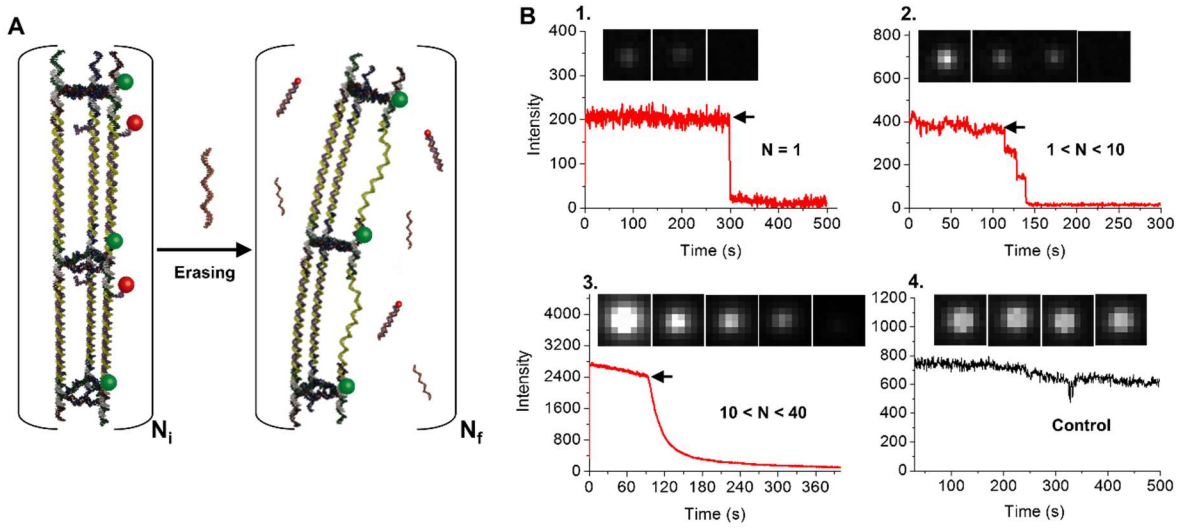

Figure 5.2: Single molecule intensity-time trajectories for the visualization of the erasing process upon 647nm excitation. (A) Scheme showing the erasing reaction occurring within a single DNA nanotube. (B) Representative intensity–time trajectories recorded for single DNA nanotubes in the presence of the eraser strand (E2/3) in oxygen scavenger solution. Panel 1: dimer structure showing a single step (N=1), panel 2: short tubes with 1<N<10, and panel 3: long tubes with N> 10. The arrows on the plots indicate the arrival of the eraser upon initiation of its flow. Panel 4: control showing the intensity–time trajectory recorded for a nanotube under a continuous flow of oxygen scavenger solution in the absence of the eraser. Images (9×9 pixels) on the top of each trajectory show the intensity within a single nanotube over time.

5.2.2.2 Single molecule survival time fittings.

We quantified the erasing rates by measuring the emission decay lifetime of ATTO647N for each single nanotube (Figure 5.10, Experimental Section). Single intensity-time trajectories for nanotubes with 1 and 2 ATTO647N linkers were fitted with an exponential decay function, and time constants were extracted (See Figure 5.3A-C, inset). In order to study the size effect of the nanotubes on the erasing rates, we studied the correlation between the survival time and initial

intensity of a given nanotube (size). Additionally, the initial intensity retrieved from each trajectory gave us information on the relative size of the structures, given that the signal intensity increases with the number of labelled-building blocks. As the scatter plot obtained indicated a constant value of y= 25.4 (0.6) for the erasing of 1 ATTO647N linker and y= 17.5 (0.8) for 2 ATTO647N linkers (Figure 5.3B-D), we established that the rate of erasing is independent of the size of the structure.

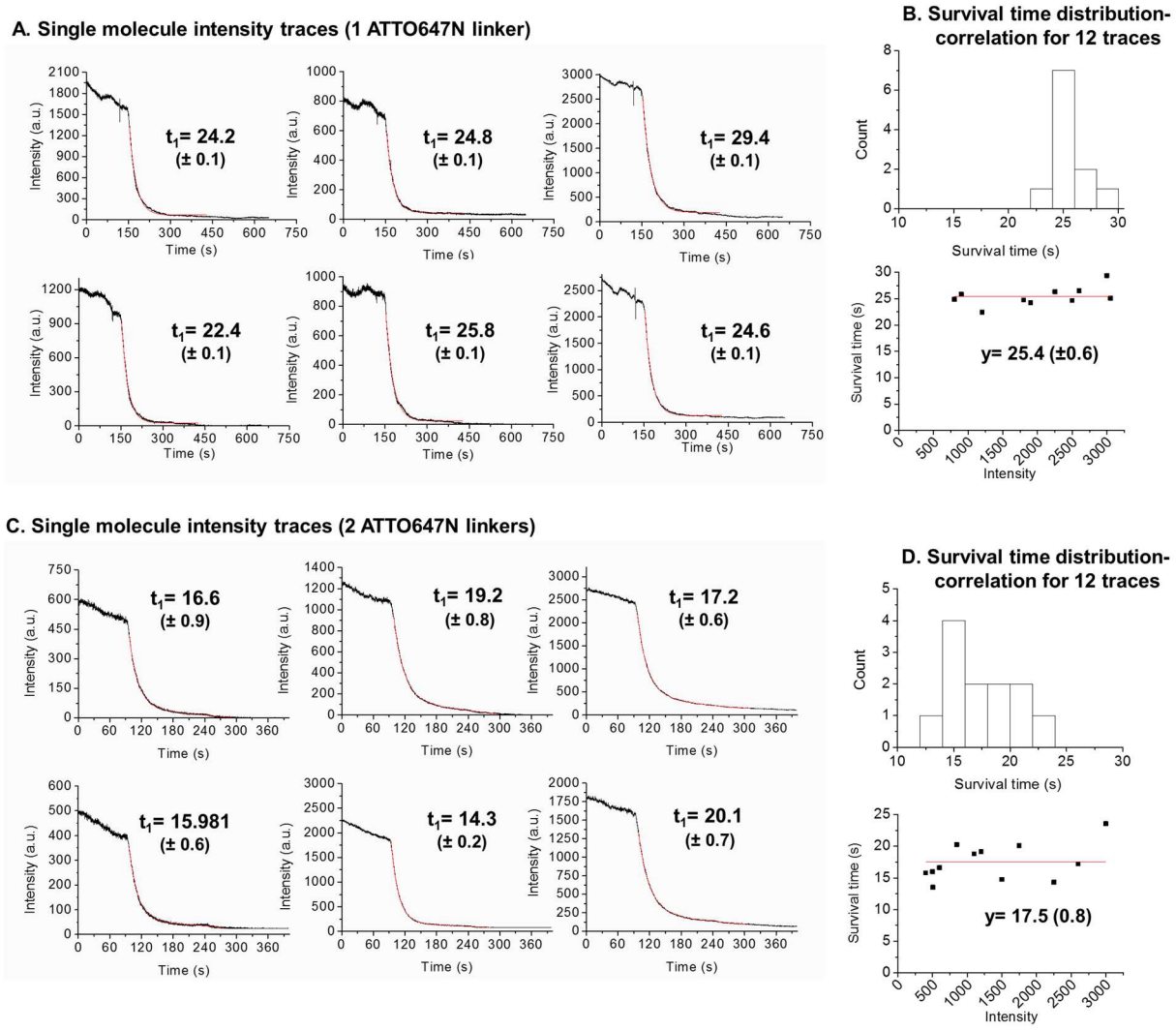

Figure 5.3: Single molecule survival time recorded for: (A-B) Erasing of 1 ATTO647N and (C-D) Erasing of 2 ATTO647N. (A-C) Single nanotube intensity time trajectories recorded for ATTO647N during eraser addition. Data was fit with a bi-exponential function (red trace). (B-D) A histogram of the survival time distributions of ATTO647N strands erasing in 12 single nanotube (top) along with a correlation of survival times with their corresponding intensities (bottom) with y=25.4s and y=17.5s best fit lines.

5.2.2.3 Ensemble survival times of ATTO647N.

An ensemble intensity-time trajectory was next built by combining the individual single molecule trajectories. By fitting the ensemble trajectory obtained for dimer structures following the erasing of one or two ATTO647N linkers to mono-exponential decay functions, we extracted an average survival time of 6.32s (0.11) and 13.62s (0.19) for one and two strands, respectively (Figure 5.4, A-B). In contrast, the trajectories obtained for oligomeric nanotube structures upon erasing one and two strands were best fitted to bi-exponential functions. We note that the origin of the double exponential for the nanotube fittings results from two competing processes, erasing and photobleaching. The fast decays with time constants of 22.77s (0.03) and 17.12s (0.03) were attributed to the erasing processes of 1 and 2 ATTO647N linkers, respectively (Figure 5.4, C-D). The larger time constants 297.9s (1 ATTO647N linker) and 142.5s (2 ATTO647N linkers), being in the same range of those recorded in control photobleaching experiments (in the absence of the eraser), were assigned to photobleaching of the dyes. As opposed to the dimer ensemble fitting where no photobleaching occurred, the photobleaching accounted for in the survival time fitting of the nanotubes (tail) may be caused by an unerasable fraction of structures (Figure 5.11-12, Experimental section).

By comparing the average survival times of the ATTO647N linkers, the erasing of the nanotubes (20s) was observed to be slower than dimers (9s) which could be arguably the result of a negative cooperativity within the nanotube structure. By assuming that the ATTO647N linkers are equally available to the invader strands, an excess of eraser added to many dimer structures incorporating each a single ATTO647N linker, or to a single nanotube including several ATTO647N linkers, should result in a comparable rate of erasing. We hypothesize that the removal of a few erasing strands in the oligomeric structures induces intrinsic bending and kinks within the nanotube, which would adopt a more collapsed morphology, thus hindering a subset of the linkers and making them less accessible to the eraser.

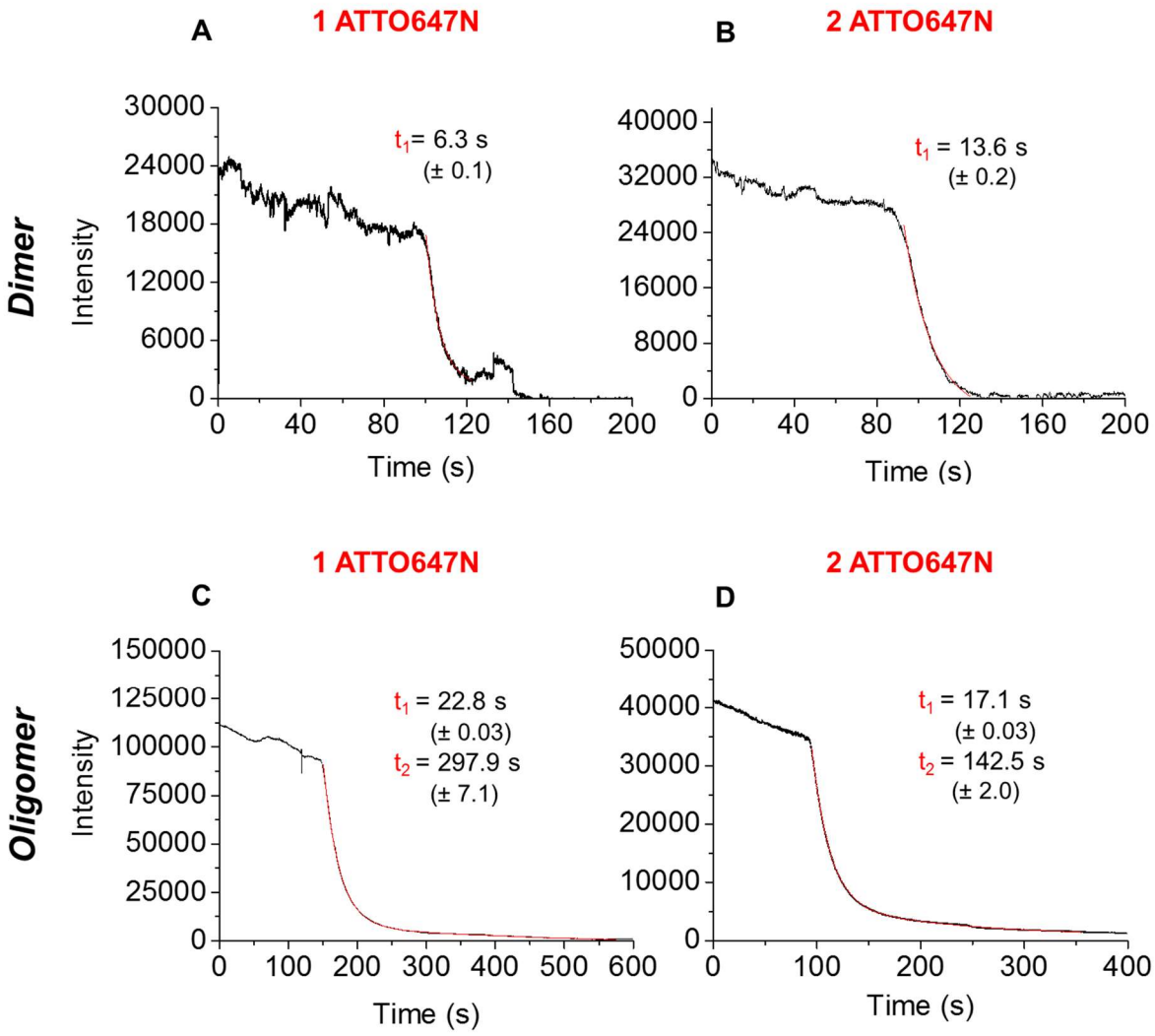

Figure 5.4: Ensemble trajectories assembled from the intensity-time trajectories. Data was recorded upon erasing 1 and 2 ATTO647N linkers in single dimers (A,B) and oligomers (C,D) acquired using TIRF microscopy. Imaging was conducted in the presence of oxygen scavenger in all cases. Intensity jumps observed in some of the trajectories are due laser fluctuations.

5.2.3 Colocalisation analysis

5.2.3.1 Quantifying erasing efficiency: ATTO647N intensity drop

In order to evaluate the efficiency of the ATTO647N strands erasing process, we designed a correlation routine resorting to Cy3 as an internal standard and involving monitoring the relative intensities of ATTO647N (red) versus Cy3 (green) before and after erasing (Figure 5.5A-D). We note that this correlation would follow a linear regression model where the slope would depend on the excitation power and efficiency of the emission collection for both channels, and, importantly to our experiment, on the number of green and red emissive fluorophores in a structure, assumed to be the same given the periodic nature of the designed nanotubes (Experimental section 5.4.1.4). Erasing experiments were performed on samples with 1 and 2 ATTO647N linkers (Figure 5.5E, panels 2-3, red and black). The fitting slopes dropped from 1.078 and 1.323 to 0.074 and 0.008 for one and two ATTO647N linkers erasing, respectively which corresponds to larger than 92% drop. This is indicative that the eraser strand displaced most of the ATTO647N linkers. Importantly, we observe, in the case of the 2 ATTO647N linker erasing, an additional population with a slightly higher slope of 0.283 corresponding to the possible "un-erasable" fraction of the ATTO647N linkers which remained in small and large structures (Figure 5.5E, panel 3, black). We speculate that the removal of two linking strands would result in a more flexible conformation of the tube, more susceptible to collapse on the surface and hinder the availability of a subset of strands. In order to confirm that the drops in the slope values are due to the erasing of the ATTO647N linkers and not to the photobleaching of the dye, a control experiment was performed in the absence of the eraser. In this case, the slope of the linear regression fitting dropped from 1.330 to 0.9034 which corresponds to a 30% drop and is attributed to photobleaching of the ATTO647N dye or sample manipulation (Figure 5.5E, panel 1, red and black).

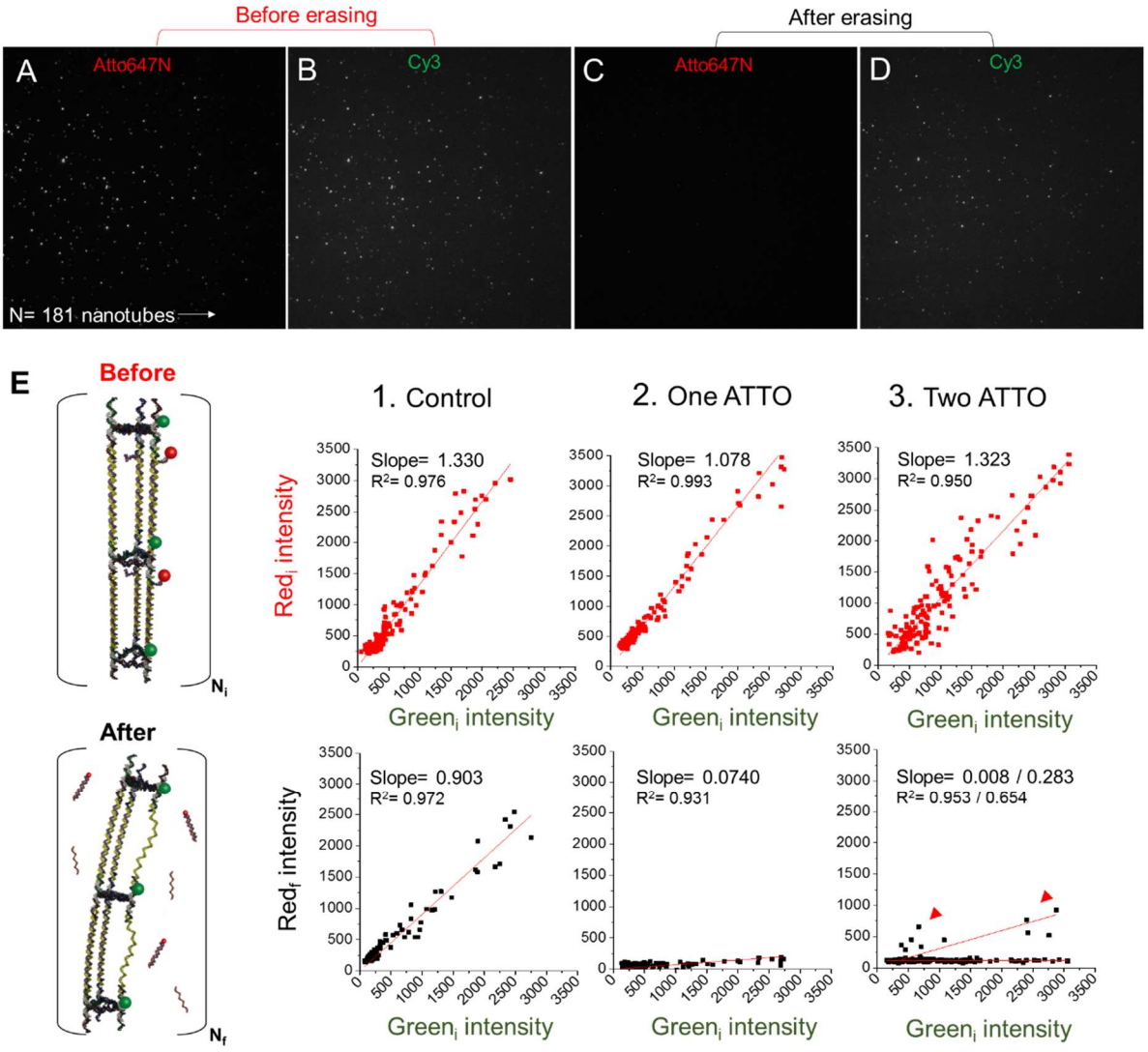

Figure 5.5: Intensity correlation analysis of Cy3-ATTO647N intensity before and after erasing. (A-B-C-D). Typical TIRF images of the same region (scale 70 µm×70 µm) showing the same nanotubes upon 561nm and 647nm laser excitation before and after erasing. A total of 181 nanotubes were detected and analyzed. (E). Correlation plots of the green (x-axis) and red (y-axis) intensities before erasing (top red section) and after erasing (bottom black section) upon (1) Irradiation of the ATTO647N dye in the absence of eraser (2) Erasing 1 ATTO647N linker (3) Erasing 2 ATTO647N linkers. Red arrows point out the un-erasable fraction.

5.2.3.2 Quantifying structural integrity: Cy3 intensity drop

In order to assess the structural fidelity of the tube upon undergoing morphological changes, we resorted to the green channel and performed a colocalization analysis of the Cy3 intensity before and after erasing. The nanotubes are assembled with a Cy3-labelled core, which is not expected to be compromised by the removal of the ATTO647N linker (i.e. loss of fragment ATTO647N labelled linker strand in figure 5.1) except in case of the tube degradation or Cy3 photobleaching. From the TIRF images, one may qualitatively appreciate the persistence of the Cy3 intensity before and after the erasing of ATTO647N linkers, which in contrast, has resulted in a sharp drop in the ATTO647N intensity as shown earlier (Figures 5.4 and 5.5).

If the data is to be consistent with the assumption that the nanotubes remained intact throughout the erasing process, the intensity of the Cy3 would be unchanged ($I_{initial} = I_{final}$) and the correlated points should lie on a straight line with a slope of 1. Any drop in the slope following the flowing of the eraser is indicative of a loss of material (nanotube degradation) and/or photobleaching. In the absence of the eraser, we observed a linear trend fitted with a slope of 1.023 indicating that photobleaching of the Cy3 dyes did not occur under these experimental conditions (Figure 5.6.1). The slight increase in the green intensity can be attributed to laser fluctuations. Remarkably, a drop in the green intensity of ca. 20% was recorded after erasing one strand, and the drop was of ca. 30% upon the removal of two ATTO647N (Figure 5.6.2-3). We note that in the latter case, the correlation data shows another minimal population that lost completely the green signal (ca. 100% drop) which occurred in 11% of the nanotubes as shown in Figure 5.6.3 (red arrow). This would indicate that the tubes are not fully preserved after erasing and some of the structures shed out some of their Cy3-labelled core components possibly due to a strain induced within the structure, while a small fraction undergo a full degradation upon erasing (catastrophic) possibly due to the presence of defective structures in the sample, such as tubes that are not fully assembled. This thorough analysis of the structural robustness of the nanotubes upon conformational changes and strand displacement reactions occurring within the structures underlines the importance of single molecule analysis in uncovering the degrees of defectiveness and anomalies detected in nanostructures samples that may not be rendered by bulk measurements. A ratiometric intensity analysis to compute the relative change in the green intensity before and after the erasing can be alternatively performed on the given data set (Figure 5.14, Experimental section 5.4.1.4).

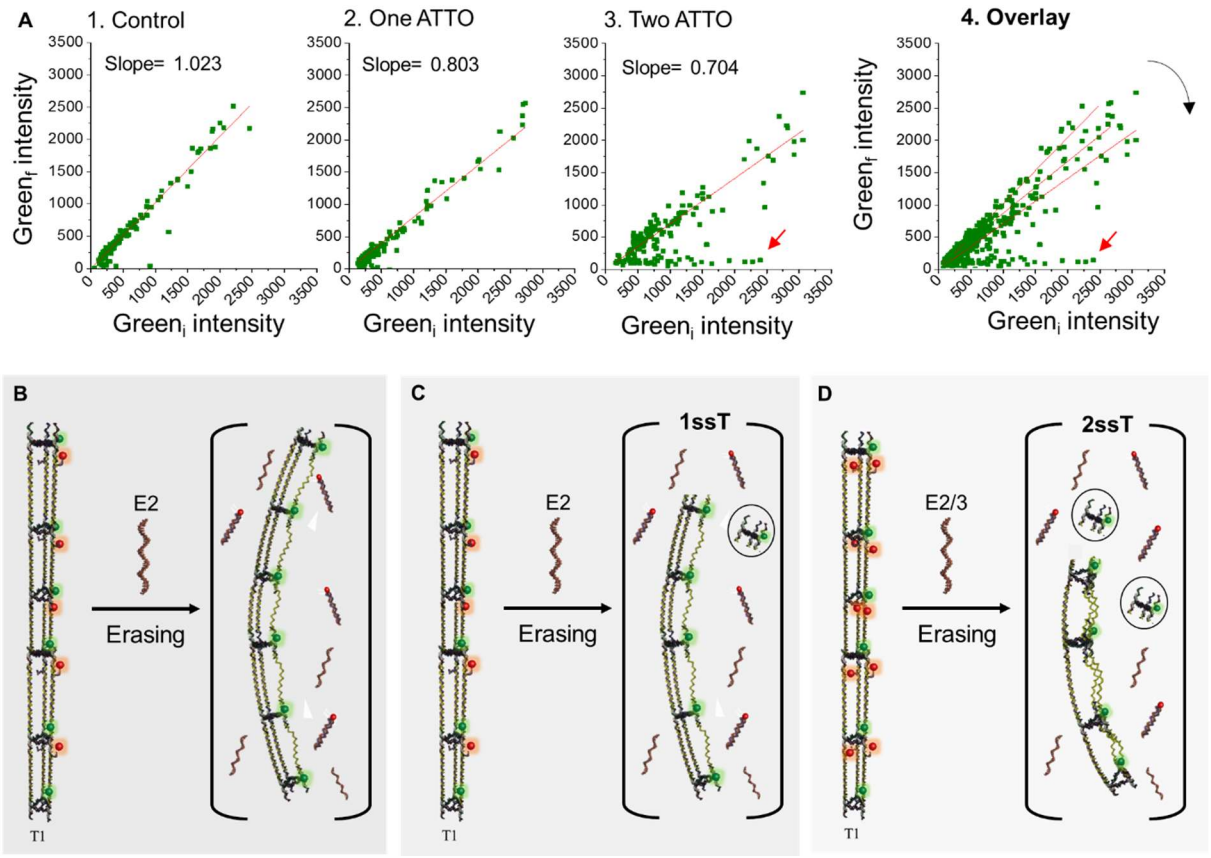

Figure 5.6: Intensity correlation analysis for the green dye (Cy3) before and after erasing. (A) Correlation plots of the green intensities before erasing (x-axis) and after erasing (y-axis) upon 1) irradiation of the ATTO647N dye in the absence of eraser; 2) erasing one ATTO647N linker; 3) erasing 2 ATTO647N linkers; 4) Overlay of the different green intensity correlations showing the drop in the slope after erasing (black arrow). Red arrows point out the fully degraded nanotubes. (B) Previously proposed mechanistic scheme for the erasing (from chapter 4) whereby the tube's structure was thought to remain pristine during the conversion. (C-D) Corrected mechanistic scheme based on the green intensity correlation analysis.

5.3 Conclusion

To conclude, we have established in the present work a method to assess the robustness of DNA nanostructures, reconfigured in response to site-specific deletion of DNA strands, at the single molecule level. Using *in situ* two-color single molecule fluorescence microscopy and strand displacement strategies, we switched the tethered Cy3-tagged nanotubes between double and single-stranded forms, and examined the stability of the single-stranded version of the design. By monitoring the intensity of the dye-labelled tubes, one at a time, we were able to extract time constants which revealed that releasing DNA strands in a dimer structure (ca. 9s) is two-fold faster than in an oligomer structure (ca. 20s). We hypothesized that during the conversion to the single form, nanotubes undergo morphological changes and collapse/fold on the surface, which would reduce the availability of the erasable strands. In addition, colocalisation intensity analysis enabled us to discover anomalies and defectiveness in the partially single stranded nanotubes where 8% of the tubes included an "un-erasable fraction" while 11% were destabilized and got fully degraded. This underlines the importance of single molecule fluorescence as a powerful methodology to assist in advancing the field of DNA nanotechnology, by enabling the production of well-defined high-quality objects that can meet the designer's compositional and dynamic specifications. Current studies are underway to explore the rates of "refilling" of the partially single stranded nanotubes with ATTO647N linkers, the effect of the biotin concentration and position on the erasing and refilling processes and the effect of the invader strand concentration on the erasing rates.

5.4 Experimental section

5.4.1 Materials and methods

Details on the nanotube design and synthesis, in addition to AFM characterization and gel electrophoresis can be found in reference [11]. The strands (Table 5.1) were synthesized via automated solid-phase synthesis carried on a BioAutomation MerMade MM6 DNA synthesizer at 1 μmol scale. Labelled strands were ordered from Integrated DNA Technologies (IDT). The strands were deprotected and cleaved from the solid support in the presence of concentrated ammonium hydroxide solution (60°C, 16 hours). Polyacrylamide gel electrophoresis (PAGE: 20 x 20 cm vertical Hoefer 600 electrophoresis unit) was employed to purify crude products (8-20% polyacrylamide/8M urea at constant current of 30 mA for 2 hours, with 1xTBE as a running buffer). Following electrophoresis, the desired bands were excised then crushed and incubated in 11 mL of autoclaved water at 60°C for at least 12 hours. After drying the samples to 1.5 mL, we used size exclusion chromatography (Sephadex G-25) to desalt the solution. The strands were quantified (OD260) by UV/vis spectroscopy with a NanoDrop Lite Spectrophotometer and using IDT's extinction coefficient at 260.

Acetic acid, boric acid, EDTA, urea, magnesium chloride, GelRed, tris(hydroxymethyl)aminomethane (Tris), D(+) glucose, 2-betamercaptoethanol, and streptavidin were purchased from Aldrich. Nucleoside (1000 Å)-derivatized LCAACPG solid support with loading densities of 25-40 μmol/g, Sephadex G-25 (super fine DNA grade), and reagents for automated DNA synthesis were used as purchased from BioAutomation. Acrylamide (40%)/bis-acrylamide 19:1 solution and agarose were purchased from BioShop. For TIRFM sample preparation, 1% v/v Vectabond/acetone was purchased from Vector Laboratories, while poly-(ethylene glycol) succinimidyl valerate MW 5000 (mPEG-SVA) and biotin-PEG-SVA were purchased from Laysan Bio, Inc. Imaging chamber components were purchased from Grace Bio-Lab. TBE buffer is composed of 90 mM Tris and boric acid and 1.1 mM EDTA, with a pH of ~8.3. TAMg buffer is composed of 45 mM Tris and 12.5 mM $MgCl_2$ with a pH of ~7.8 adjusted by glacial acetic acid.

Table 5. 1: Sequences of all the strands used (Copyright © 2015 American Chemical Society).

Name	Seuquence 5' to 3'	ε_{260} (L.mole^{-1}.cm^{-1})
V	CTCAGCAGCGAAAAACCGCTTTACCACATTCGAGGCACGTTGTACGTC CAC ACT TGGAACCTCATCGCACATCCGCCTGCCACGCTCTTAGCATAGGACGGC GGC GTT AAA TA	1062100
C1	CGGTGCATTTCGACGGTACTTCGTACAACGTGCCTCGAATGTAGAGCGTGGCAGG CGGATGTGAAGCAGTTGCAGCGTACTCGT	803900
C2	TCGGCAGACTAATACACCTGTCGATGAGGTTCCAAGTGTGGATAGCTAGGTAACG GATTGAGC	623300
R1	TGCAACTGCTACCAGGTGTATT	207400
R2	TTACCTAGCTCCAGTACCGTCG	202000
R3	GTCCTATGCTTTGTAAAGCGGT	207400
LS1	TTTTCGCTGCTGAGGTAAGCCTTCGGCGAGCATCTATCTATGTCTCCG TAT TTA ACG CCG CC	563700
LS1*	CGGAGACATAGATAGATGCTCGCCGAAGGCTTA C	337000
LS1*ov	CGACTTCGAGCGGAGACATAGATAGATGCTCGCCGAAGGCTTAC	430500
LS2	AGTCTGCCGACACAGAGATCAGTCGGAAGCATAATATCTTATGTTCGT GAT AAC GAGTACGC	618800
LS3	AAATGCACCGCACAGAGATCAGTCGGAAGCATAATATCTTATGTTCGT GAT AGC TCAATCCG	615100
LS2/3*	TATCACGAACATAAGATATTATGCTTCCGACTGATCTCTGTG	406900
LS2/3*ov	TTTTTTTTTTTATCACGAACATAAGATATTATGCTTCCGACTGATCTCTGTG	487900
E1	GTAAGCCTTCGGCGAGCATCTATCTATGTCTCCGCTCGAAGTCG	409100
E2/3*	CACAGAGATCAGTCGGAAGCATAATATCTTATGTTCGTGATAAAAAAAAAAA	546300
R3ov	GTCCTATGCTTTGTAAAGCGGTGCCTGGCCTTGGTCCATTTG	379700
Bio-R3ov*	biotin-CAAATGGACCAAGGCCAGGC	198100
LS2/3*24	TATCACGAACATCTGATCTCTGTG	227600
LS2/3*36	TATCACGAACATAAGATATTCCGACTGATCTCTGTG	352500
LS2/3*37	TATCACGAACATAAGATACTTCCGACTGATCTCTGTG	358700
LS2/3*38	TATCACGAACATAAGATATCTTCCGACTGATCTCTGTG	367800
LS2/3*39	TATCACGAACATAAGATATTCTTCCGACTGATCTCTGTG	375900
LS2/3*40	TATCACGAACATAAGATATTGCTTCCGACTGATCTCTGTG	384800

5.4.1.1 Surface and sample preparation

5.4.1.1.1 Coverslip preparation

Coverslips were soaked in piranha solution (25% H_2O_2 and 75% concentrated H_2SO_4) and sonicated for 1h, followed by multiple water (molecular biology grade), and acetone (high-performance liquid chromatography (HPLC) grade) rinsing cycles. Dry and clean coverslips were then treated with Vectabond/acetone 1% v/v solution for 5 min and then rinsed with H_2O and left in dried state until used. In order to prevent non-specific adsorption of biomolecules onto the glass surface, coverslips were functionalized prior to use with a mixture of poly(ethylene glycol) succinimidyl valerate, MW 5000 (mPEG-SVA) and biotin-PEG-SVA at a ratio of 99/1 (w/w), in a 0.1 M sodium bicarbonate solution for 3h. Excess PEG was rinsed with water, and the coverslips were dried under a N_2 stream.

5.4.1.1.2 Sample preparation

Imaging chambers (~8 μL) were constructed by pressing a polycarbonate film with an adhesive gasket onto a PEG-coated coverslip. Two silicone connectors were glued onto the predrilled holes of the film and served as inlet and outlet ports. The surface was incubated with 10 μL of a 0.2 mg/mL streptavidin solution for 10 min. Excess streptavidin was then washed with 100 μL of 1xTAMg buffer. 10 μL of the 680pM DNA nanotube solution was injected in the chamber. (136nM solution diluted 200×). Unbound DNA structures were then flushed out with 50 μL of 1xTAMg buffer. For our erasing experiment, two solutions of 300 μL each were prepared in two different syringes: oxygen scavenger solution (control sample in the absence of the eraser) and DNA erasers (33 nM) diluted with an oxygen scavenger solution. Prior to image acquisition, a tubing was inserted into the inlet port, connecting the chamber to a syringe placed on a syringe pump. Each of the solutions was flowed at a rate of 5 μL/min in the following order: The plunger of the syringe containing oxygen scavenger solution was first pushed. A movie of 6000 frames of the region was acquired upon 647nm excitation for 10 minutes upon flowing the scavenger solution to photostabilize the ATTO647N dyes. We next pumped the solution containing the erasing strands (E2-3) in oxygen scavenger. In this case, the frame acquisition (5Hz, 6000 frames) was started simultaneously with the beginning of the flow. The dead volume of the tubing contains around 7.5 μL, delaying the arrival of the eraser by around 2 minutes. We note that a snap of 1 frame (150ms) is taken for the green channel before and after the movie to check for colocalization

(Figure 5.7). A control sample with oxygen scavenger only was always performed in the absence of the eraser, to account for the rate of photobleaching for a possible deconvolution of the two competing processes, photobleaching and erasing of the dyes.

5.4.1.1.3 Photoprotection system: Oxygen scavenger + Trolox

Our choice of ATTO647N over Cy5 or Alexa647 for the photobleaching experiment reflects on the need to have trajectories characterized by long enough intervals of steady intensity to be able to visualize a clear drop upon the arrival of the erasing strand. ATTO647N has significantly improved photostability over Cy5 or Alexa 647 under our experimental conditions, desired for these experiments where rapid photobleaching and/or blinking may compromise the clear distinction between erasing and photobleaching. The photoprotection system used in this experiment includes an oxygen scavenger solution and a triplet quencher and is composed of Glucose oxidase / Glucose / Catalase / Trolox. (165 units mL^{-1} Glucose oxidase, 3% Glucose w/v, 1600 units mL^{-1} / Catalase and 2mM Trolox in 1 x TAMg buffer). All the components were prepared in molecular biology grade water except for the triplet quencher Trolox, dissolved it in ultra-grade methanol (MeOH) and filtered before usage.

5.4.1.2 Single molecule TIRF Imaging and analysis

5.4.1.2.1 TIRF microscope

Fluorescence imaging was carried out using an inverted Nikon Eclipse Ti microscope equipped with the Perfect Focus System (PFS) implementing an objective-type TIRF configuration with a Nikon TIRF illuminator and an oil-immersion objective (CFI SR Apo TIRF 100× Oil Immersion Objective Lens, numerical aperture (NA) 1.49). The effective pixel size was 160 nm. With these settings, two lasers were used for excitation (Agilent MLC400B Monolithic Laser Combiner): 561 nm (2 mW, measured out of the objective) and 647 nm (2mW for the dimers and 0.75 mW for the oligomers, measured out of the objective). For Cy3 imaging, the laser beam was passed through a multiband cleanup filter (ZET405/488/561/647x, Chroma Technology) and coupled into the microscope objective using a multiband beam splitter (ZT405/488r/561/640rpc, Chroma Technology). Fluorescence light was spectrally filtered with an emission filter (ET600/50m, Chroma Technology). For ATTO647N imaging, the laser beam was coupled into the microscope

objective using a beam splitter (ZT647rdc, Chroma Technology). The emission from ATTO647N was spectrally filtered with emission filters (HHQ665lp and ET705/72m, Chroma Technology). All movies were recorded onto a 512x512 pixel back-illuminated electron-multiplying charge-coupled device (EMCCD) camera (iXon X3 DU-897-CS0-#BV, Andor Technology).

5.4.1.2.2 Image analysis

Frames were acquired with the NIS element software from Nikon (nd2 files) and then converted to TIFF image files using Image J. Fluorescence intensity time trajectories of individual molecules were extracted from the series of frames using a self-written algorithm in IDL and Matlab. In order to ensure that the selected molecules are nanotubes and not artifacts or non-specifically bound aggregates, we adopted a two color detection strategy. In our image analysis, we took the Cy3 channel (green) as the reference from which the homebuilt software would generate a matrix with the coordinates of all the nanotubes detected, and find their match in frames acquired in the red channel before and after erasing (Figure 5.7).

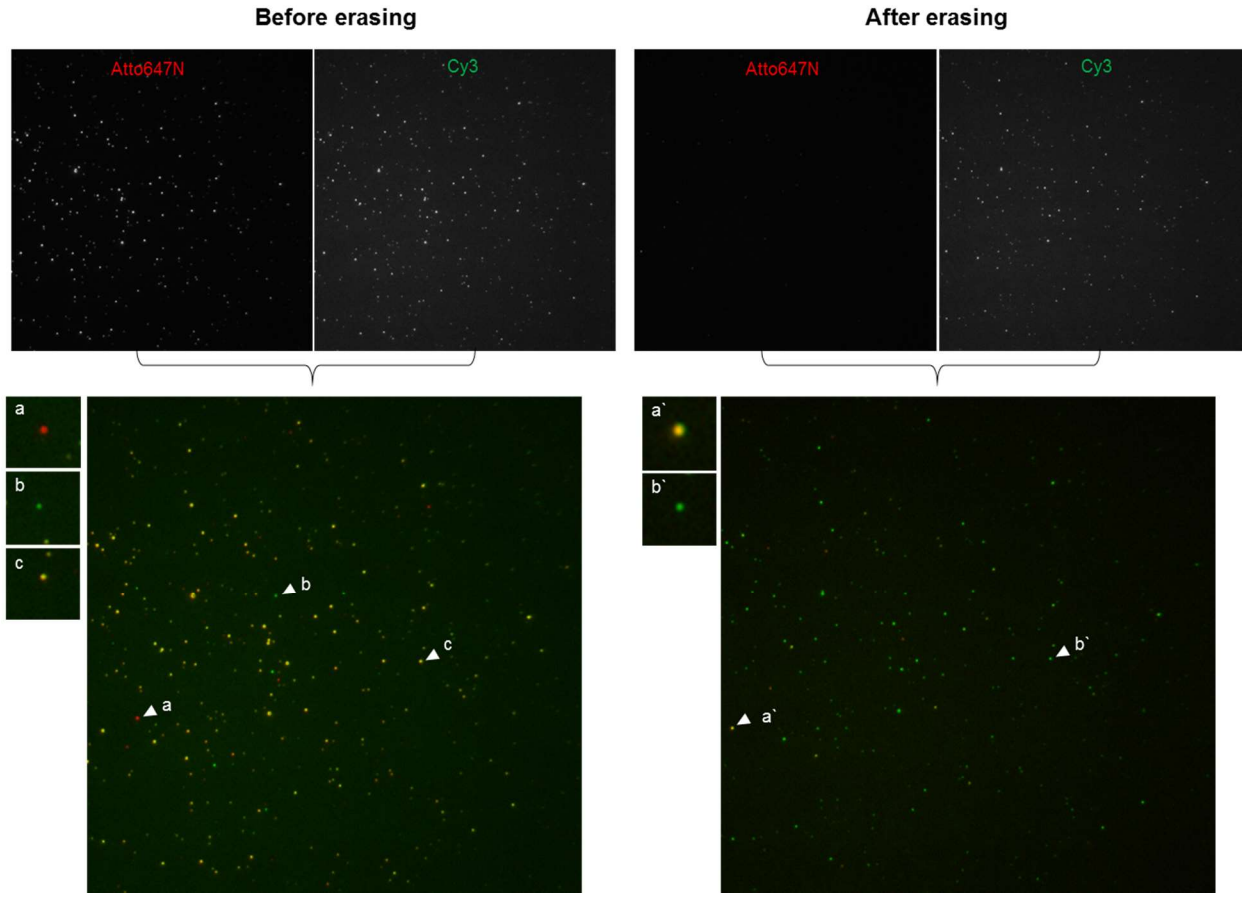

Figure 5.7: TIRF images of surface bound dye labelled nanotubes before and after erasing. Typical TIRF images (scale 70 µm×70 µm) showing the same nanotubes in both colors, upon

561nm and 647nm laser excitation before and after erasing. A total of 181 nanotubes were detected and analyzed. A two color overlay of the Cy3-ATTO647N emission before (left) and after (right). Before erasing: Non-specifically bound molecules appear in either red (a) ATTO647N strands, or in green (b) Cy3-labelled strands or rungs. A yellow color (c) indicates colocalization of the ATTO647N and Cy3 emission intensities in a double stranded nanotube. Only yellow molecules were considered for analysis. After erasing: Yellow (a') indicates colocalisation of Cy3 and the remaining ATTO647N (un-erasable fraction), green (b') single stranded Cy3-labelled nanotubes.

5.4.1.2.3 Intensity-time trajectories of nanotube dimers (1 and 2 ATTO647N)

In the absence of the eraser, long steady intensity-time trajectories were observed (ca. 83%) whereas discrete steps were detected following the addition of the eraser (Figure 5.8). In some of the cases, due to a possible aggregation of 2 dimers, we observe 2 steps in the dimer with 1 ATTO647N, and 4 steps with those having 2 ATTO647N strands. Our survival time analysis, only trajectories with 1 step (dimer with 1 ATTO647N) and 2 steps (dimer with 2 ATTO647N) were considered.

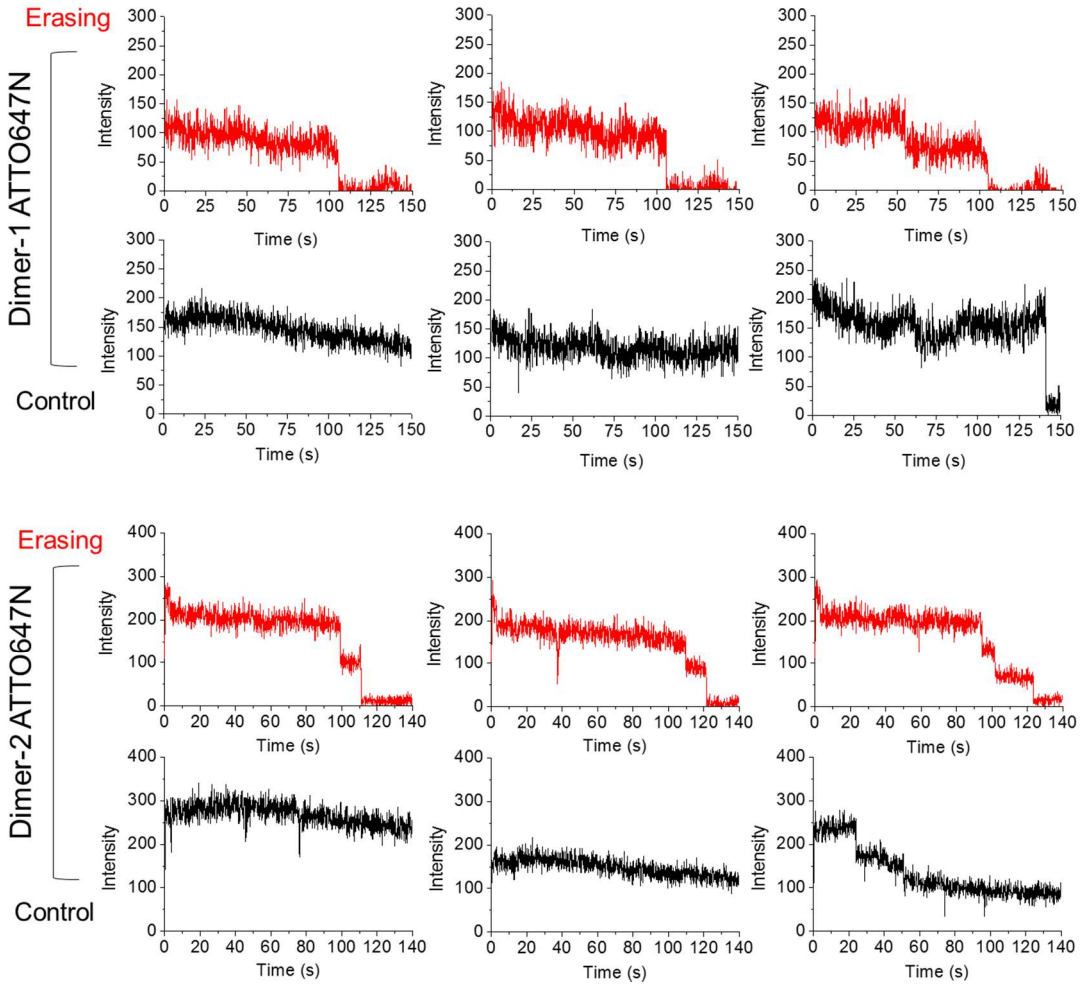

Figure 5.8: Intensity time trajectories for DNA nanotube dimers. Representative intensity–time trajectories recorded for Atto647N upon 647nm excitation of single DNA nanotube dimers bearing either 1 ATTO647N linker (Top) or 2 ATTO647N linker (bottom) per repeat unit, under a continuous flow of oxygen scavenger solution in the presence of an excess of erasers (red) and absence of an eraser (black).

5.4.1.2.4 Intensity-time trajectories of nanotube multi-mers

Oligomeric nanotube samples are highly polydisperse due to their uncontrolled polymerization resulting in a shorter population size of nanotubes. This was confirmed from the intensity-time trajectories extracted which presented steps upon erasing ATTO647N strands as illustrated in figure 5.9A below. A histogram of the number of intensity steps counted (drops) showed a distribution ranging from single to twelve steps (Figure 5.9A). In the absence of the eraser, trajectories were observed to present mostly a long steady intensity (zero step in the histogram) or a single step (78% of the trajectories), as shown in the control trajectories and the distribution of steps (Figure 5.9B). This confirms that every step observed is an erasing event and not photobleaching.

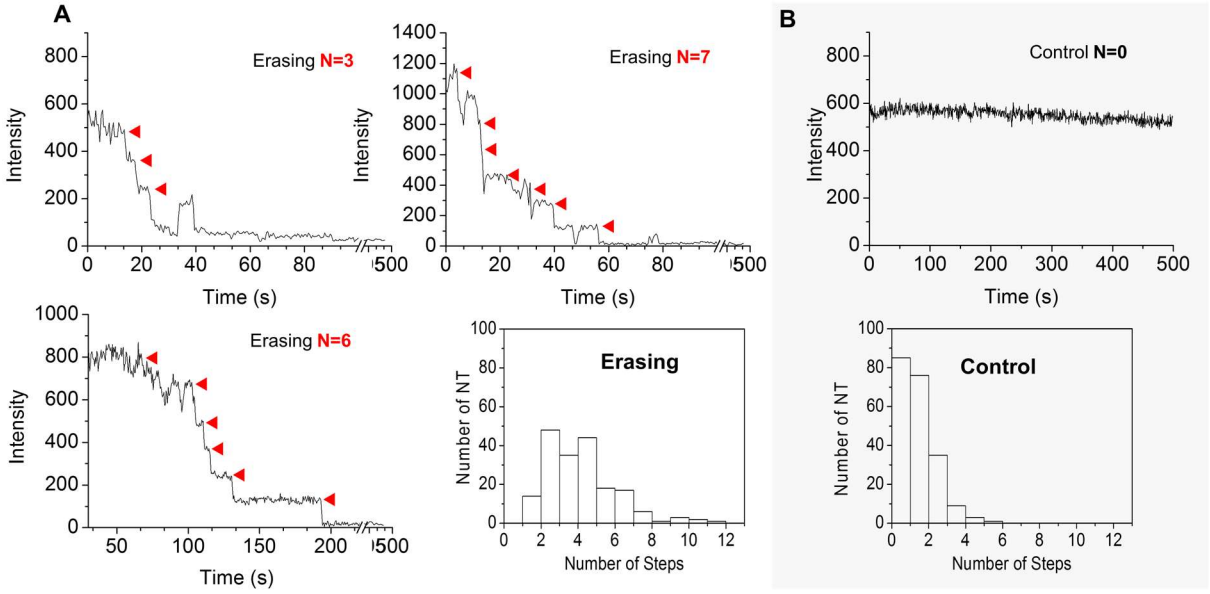

Figure 5.9: Intensity-time trajectories of DNA nanotube multi-mers. A. Representative intensity–time trajectories recorded for ATTO647N in our TIRFM set-up upon 647nm excitation of single DNA nanotube multi-mers under a continuous flow of oxygen scavenger solution following the addition of an excess of eraser B. Control showing the intensity-time trajectory recorded for a nanotube under a continuous flow of oxygen scavenger solution in the absence of the eraser (top). Histogram of the number of steps computed for the control sample (bottom).

5.4.1.2.5 Ensemble survival time fittings

We integrated all the individual intensity-time trajectories extracted from a series of frames for a given sample of DNA nanotube oligomers using Origin 8.5 (Figure 5.10). We then fitted the curve to a bi-exponential decay function [1] to get the time constants of the photobleaching and erasing events. The different fittings are compared below in figure 5.11.

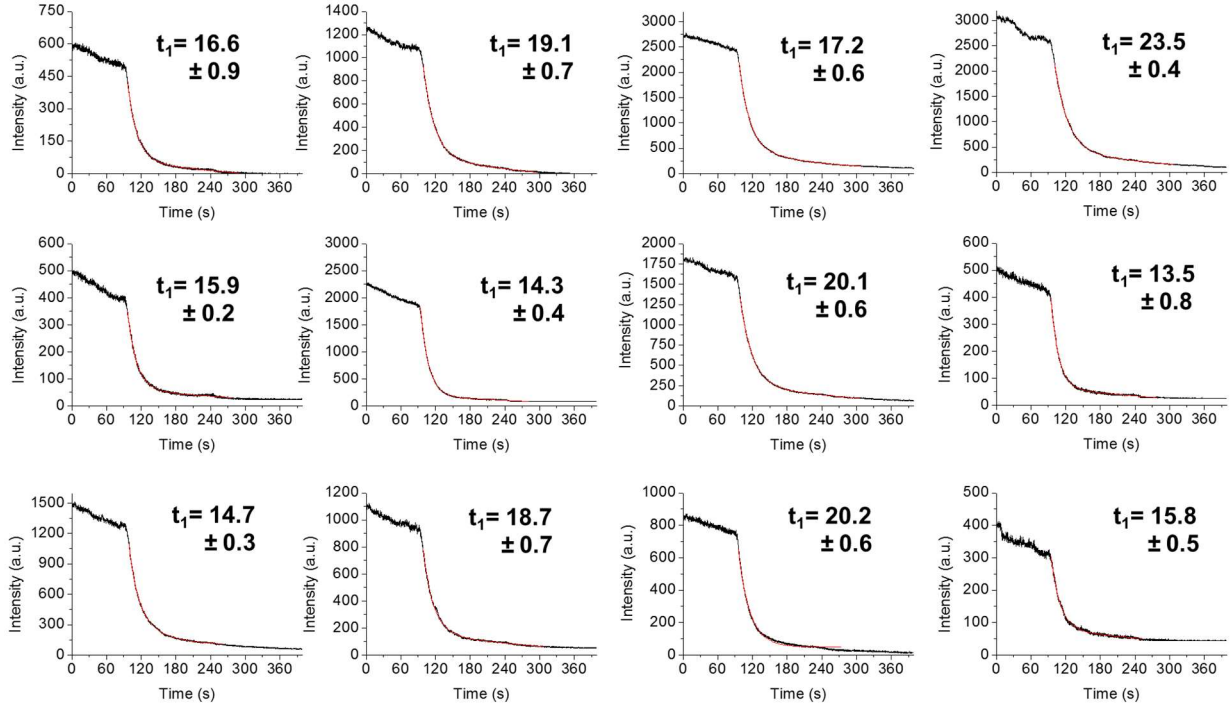

Figure 5.10: Intensity-time trajectories of DNA nanotube oligomers. Single nanotube intensity- time trajectories recorded for ATTO647N during eraser addition. Data was fit with a bi-exponential function (red trace).

Scheme 5. 1: Proposed kinetic model of the erasing process: Pseudo-first order reaction

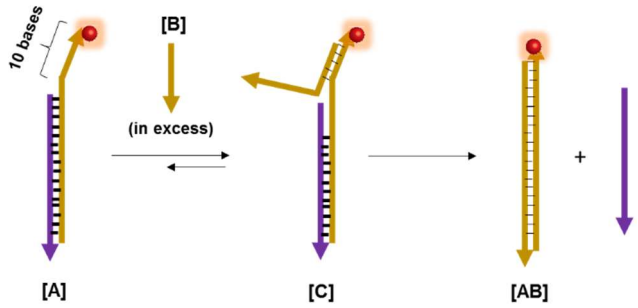

$$r = k_1[A][B]$$

$$\frac{dC}{dt} = 0 = k_1[A][B] - k_2[C]$$

$$\leftrightarrow k_1[A][B] = k_2[C]$$

$$r = k_2[C] = k_1[A][B] = \boldsymbol{k'_1[A]}$$

$$with\ k'_1 = k_1[B]\ ([B]\ is\ in\ exces$$

Bi-exponential decay equation:

$$y = y_0 + A_1 e^{-\frac{x}{t_1}} + A_2 e^{-\frac{x}{t_2}} \qquad [1]$$

where y_0 is the y off-set, A is the amplitude and t_1 and t_2 are the time constants.

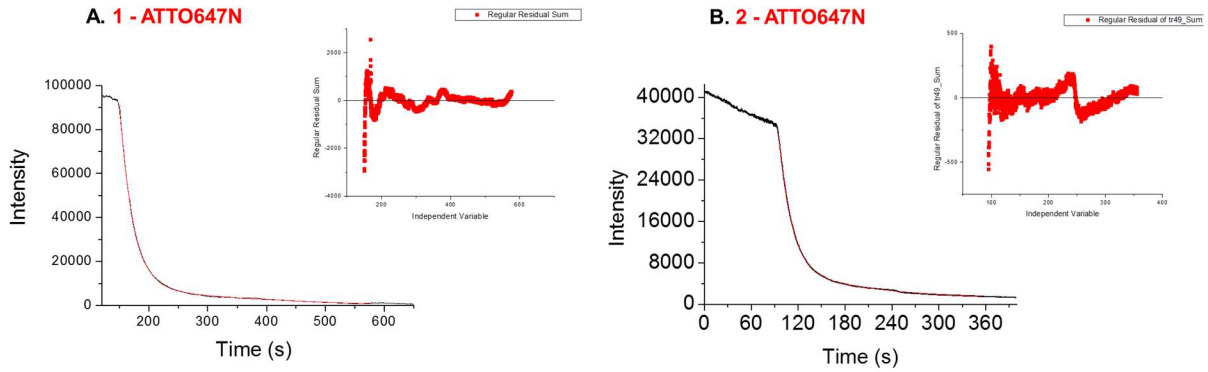

Figure 5.11: Ensemble survival time histogram for the erasing of 1 (A) and 2 (B) ATTO647N linkers from nanotubes. Bi-exponential fitting (with a small residual value) was a good fitting of the data.

5.4.1.2.6 Control samples: Photobleaching of ATTO647N

Control samples in the absence of the eraser were performed to account for the time constant of the ATTO647N photobleaching. By fitting the ensemble trajectories to a mono-exponential decay [2], we extracted the average survival time of ATTO647N in the dimers (117.46s) and oligomers (1264s) (Figure 5.12). We note that the dimers were excited with around twice the power used for the oligomers (2mW versus 0.75mW) which could explain the faster photobleaching rate in the dimer control. Additionally, the photobleacching rate would vary from sample to sample given i) its high dependence of the TIRF angle (which vary from sample to sample); ii) the environment of the dyes ; iii) oxygen scavenger solutions. This control experiment confirmed that photobleaching is at least an order of magnitude slower than the erasing process which enabled to deconvolute the two different processes in the erasing experiments performed. We note that jumps in the intensity observed in some cases are due to laser fluctuations (systematic error in the Nikon set-up).

Mono-exponential decay equation:

$$y = y_0 + Ae^{-\frac{x}{t_1}} \qquad [2]$$

where y_0 is the y off-set, A is the amplitude and t_1 is the time constant.

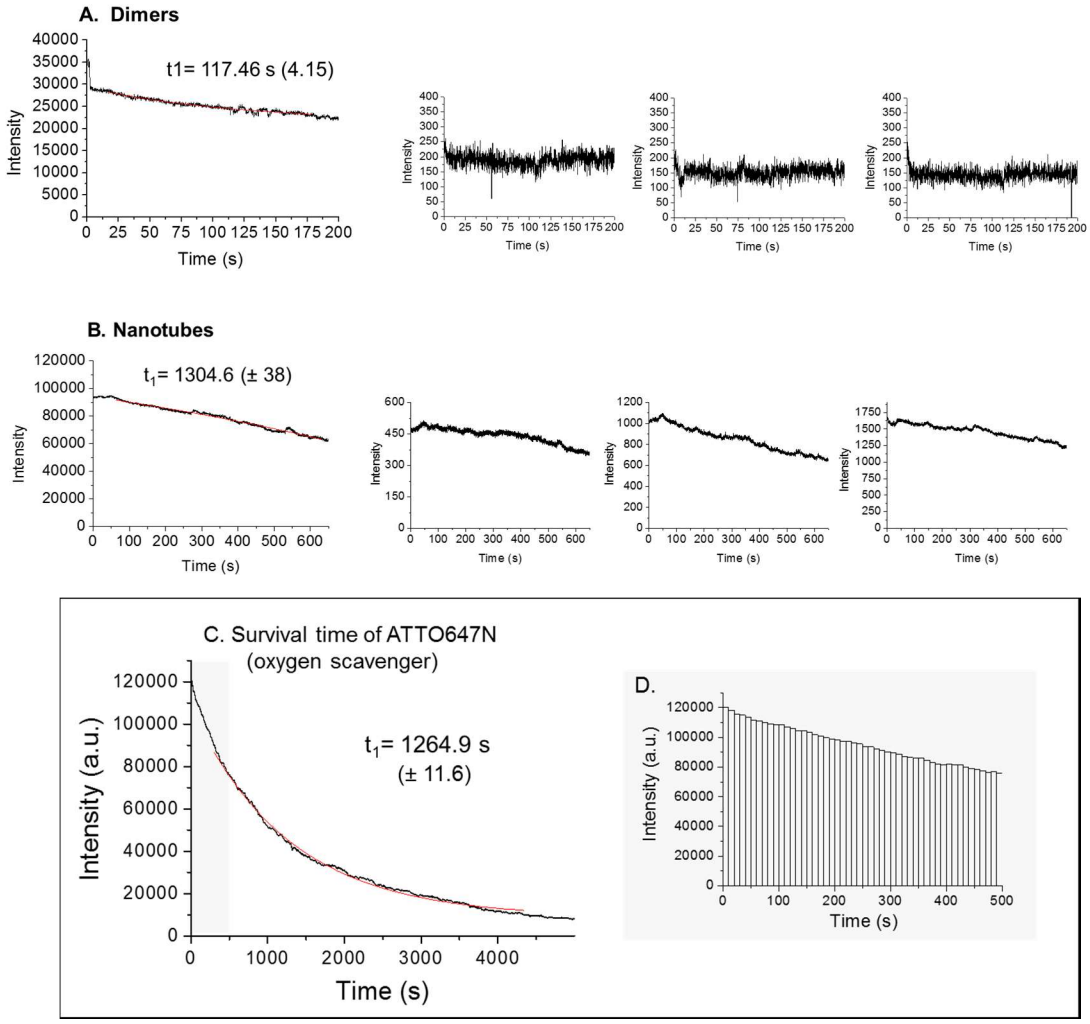

Figure 5.12: Ensemble and single molecule intensity-time trajectories of the photobleaching of ATTO647N under oxygen scavenger, in the absence of eraser. (A) Ensemble trajectories of ATTO647N in nanotube dimers with examples of single dimer trajectories. (B) Ensemble trajectories of ATTO647N in nanotube oligomers with examples of single oligomer trajectories. (C) Ensemble trajectories of ATTO647N dyes in nanotube oligomers upon complete photobleaching. (D) A zoom in into the time interval of photobleaching (0-500s) comparable to the time it took for erasing to occur.

5.4.1.3 Intensity-based and colocalization analysis

5.4.1.3.1 Single molecule intensity histograms

From the initial intensities extracted from single molecule intensity-time trajectories, a distribution was obtained for each sample studied. As expected, the intensity distribution for the dimer has a smaller average intensity (ca. 197) than a nanotube oligomer (ca. 905) (Figure 5.13). Given that the power employed for dimer excitation was ca. 2.5 fold greater than the one used for the nanotube oligomers (section 5.4.1.2), the mean intensity for the oligomer structures was multiplied by a factor of 2.5 (ca.2262) for comparison purposes. This enabled us to quantify the number of building blocks in the nanotubes using the dimer intensity as the standard (ca. 2262/197 = 12 linkers per nanotube). Surprisingly, while dimers with 2 ATTO647N linkers showed an intensity ca. 2 fold greater than that of dimers with 1 ATTO647N linker, a comparable average intensity was observed for the two different nanotubes (1 and 2 ATTO647N). This is indicative of an assembly failure following the addition of two strands bearing an ATTO647N labelled overhangs, which possibly resulted in a shorter population of nanotubes.

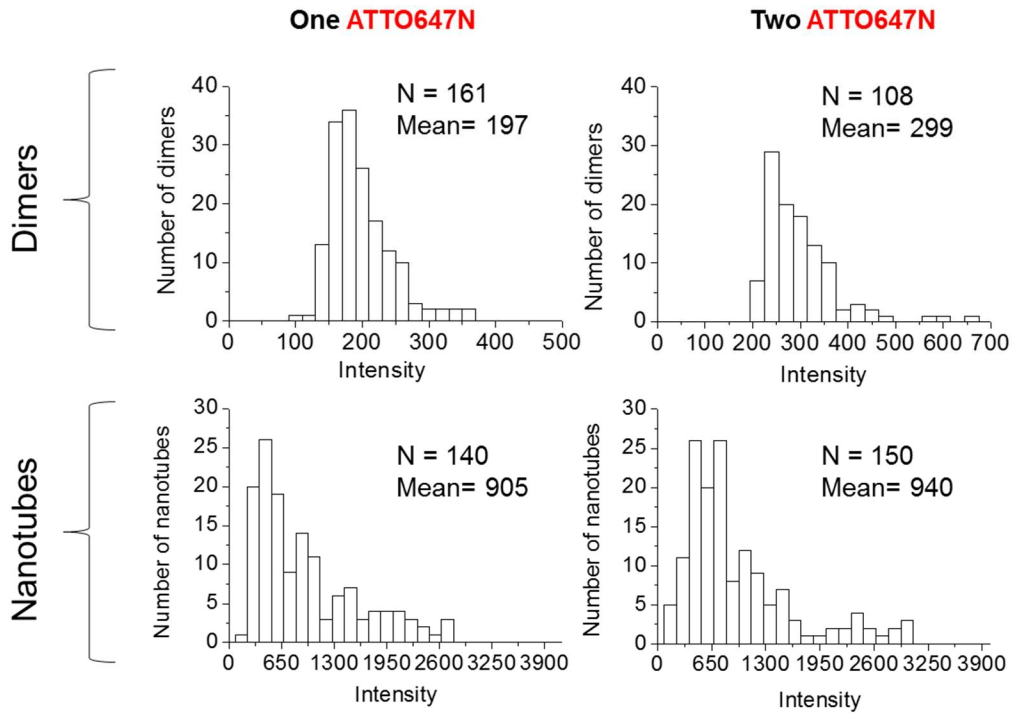

Figure 5.13: Histograms showing the intensity distribution of dimers versus oligomers of nanotubes.

5.4.1.3.2 Single molecule ratiometric intensity analysis

After computing the ratio I_{green} [3] accounting for the relative change in the green intensity before and after the erasing (efficiency), the resulting values reflected on the robustness of the structures where the closer the factor is to 0, the less degraded the structures are and hence the more robust as shown in the calculation below. Particularly, comparing the red intensity (Red_f) to the green efficiency (I_{green}), the un-erasable fraction of ATTO647N linkers can be assigned to the partially degraded tubes (Figure 5.14). This observation may confirm that the structures that shed out rungs have experienced the most pronounced conformational changes (or collapse) resulting in the hindrance of a subset of their linking strands.

$$I_{green} = \frac{I_{green(i)} - I_{green(f)}}{I_{green(i)}} \quad [3]$$

- $If \quad I_{green} = 0 = \frac{I_{green(i)} - I_{green(f)}}{I_{green(i)}}$

  $I_{green(i)} - I_{green(f)} = 0$

  $I_{green(i)} = I_{green(f)} \leftrightarrow \boldsymbol{Intact\ tubes}$

- $If \quad I_{green} = 1 = \frac{I_{green(i)} - I_{green(f)}}{I_{green(i)}}$

  $I_{green(i)} - I_{green(f)} = I_{green(i)}$

  $I_{green(f)} = 0 \leftrightarrow \boldsymbol{Degraded\ tubes}$

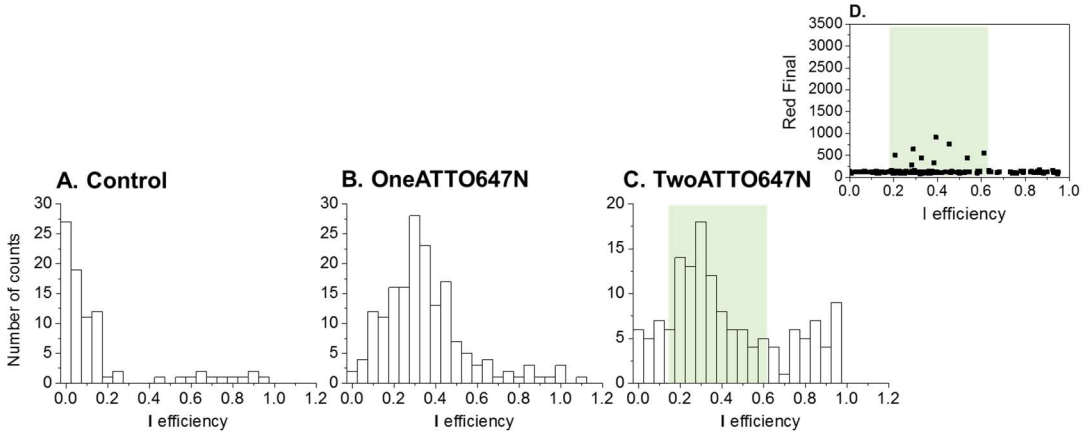

Figure 5.14: Histograms showing the green efficiency ratio distribution for the different samples of DNA nanotubes studied.

5.5 References

1. (a) Shih, W. M., Exploiting weak interactions in DNA self-assembly. *Science* **2015,** *347* (6229), 1417-1418; (b) Yurke, B.; Turberfield, A. J.; Mills, A. P.; Simmel, F. C.; Neumann, J. L., A DNA-fuelled molecular machine made of DNA. *Nature* **2000,** *406* (6796), 605-608.

2. Zhang, D. Y.; Seelig, G., Dynamic DNA nanotechnology using strand-displacement reactions. *Nat Chem* **2011,** *3* (2), 103-113.

3. (a) Wei, B.; Dai, M.; Yin, P., Complex shapes self-assembled from single-stranded DNA tiles. *Nature* **2012,** *485* (7400), 623-626; (b) Zhang, F.; Nangreave, J.; Liu, Y.; Yan, H., Structural DNA Nanotechnology: State of the Art and Future Perspective. *Journal of the American Chemical Society* **2014,** *136* (32), 11198-11211.

4. Pinheiro, A. V.; Han, D.; Shih, W. M.; Yan, H., Challenges and opportunities for structural DNA nanotechnology. *Nat Nano* **2011,** *6* (12), 763-772.

5. (a) Dunn, K. E.; Dannenberg, F.; Ouldridge, T. E.; Kwiatkowska, M.; Turberfield, A. J.; Bath, J., Guiding the folding pathway of DNA origami. *Nature* **2015,** *525* (7567), 82-86; (b) Sorgenfrei, S.; Chiu, C.-y.; Gonzalez, R. L.; Yu, Y.-J.; Kim, P.; Nuckolls, C.; Shepard, K. L., Label-free single-molecule detection of DNA-hybridization kinetics with a carbon nanotube field-effect transistor. *Nat Nano* **2011,** *6* (2), 126-132; (c) Hariadi, R. F.; Yurke, B.; Winfree, E., Thermodynamics and kinetics of DNA nanotube polymerization from single-filament measurements. *Chemical Science* **2015,** *6* (4), 2252-2267; (d) van der Zwaag, D.; Pieters, P. A.; Korevaar, P. A.; Markvoort, A. J.; Spiering, A. J. H.; de Greef, T. F. A.; Meijer, E. W., Kinetic Analysis as a Tool to Distinguish Pathway Complexity in Molecular Assembly: An Unexpected Outcome of Structures in Competition. *Journal of the American Chemical Society* **2015,** *137* (39), 12677-12688.

6. (a) Rothemund, P. W. K.; Ekani-Nkodo, A.; Papadakis, N.; Kumar, A.; Fygenson, D. K.; Winfree, E., Design and Characterization of Programmable DNA Nanotubes. *Journal of the American Chemical Society* **2004,** *126* (50), 16344-16352; (b) Saaem, I.; LaBean, T. H., Overview of DNA origami for molecular self-assembly. *Wiley Interdisciplinary Reviews: Nanomedicine and Nanobiotechnology* **2013,** *5* (2), 150-162; (c) Gerling, T.; Wagenbauer, K. F.; Neuner, A. M.; Dietz, H., Dynamic DNA devices and assemblies formed by shape-complementary, non–base pairing 3D components. *Science* **2015,** *347* (6229), 1446-1452.

7. (a) Funatsu, T.; Harada, Y.; Tokunaga, M.; Saito, K.; Yanagida, T., Imaging of single fluorescent molecules and individual ATP turnovers by single myosin molecules in aqueous solution. *Nature* **1995,** *374* (6522), 555-559; (b) Saccà, B.; Ishitsuka, Y.; Meyer, R.; Sprengel, A.; Schöneweiß, E.-C.; Nienhaus, G. U.; Niemeyer, C. M., Reversible Reconfiguration of DNA Origami Nanochambers Monitored by Single-Molecule FRET. *Angewandte Chemie International Edition* **2015,** *54* (12), 3592-3597.

8. (a) Moerner, W. E.; Fromm, D. P., Methods of single-molecule fluorescence spectroscopy and microscopy. *Review of Scientific Instruments* **2003,** *74* (8), 3597-3619; (b) Lu, H. P.; Xun, L.; Xie, X. S., Single-Molecule Enzymatic Dynamics. *Science* **1998,** *282* (5395), 1877-1882; (c) Evans, G. W.; Hohlbein, J.; Craggs, T.; Aigrain, L.; Kapanidis, A. N., Real-time single-molecule studies of the motions of DNA polymerase fingers illuminate DNA synthesis mechanisms. *Nucleic Acids Research* **2015,** *43* (12), 5998-6008.

9. (a) Marko, R. A.; Liu, H.-W.; Ablenas, C. J.; Ehteshami, M.; Götte, M.; Cosa, G., Binding Kinetics and Affinities of Heterodimeric versus Homodimeric HIV-1 Reverse Transcriptase on DNA–DNA Substrates at the Single-Molecule Level. *The Journal of Physical Chemistry B* **2013,** *117* (16), 4560-4567; (b) Peterson, E. M.; Manhart, M. W.; Harris, J. M., Single-Molecule Fluorescence Imaging of Interfacial DNA Hybridization Kinetics at Selective Capture Surfaces. *Analytical Chemistry* **2016,** *88* (2), 1345-1354.

10. Tsukanov, R.; Tomov, T. E.; Liber, M.; Berger, Y.; Nir, E., Developing DNA Nanotechnology Using Single-Molecule Fluorescence. *Accounts of Chemical Research* **2014,** *47* (6), 1789-1798.

11. Rahbani, J. F.; Hariri, A. A.; Cosa, G.; Sleiman, H. F., Dynamic DNA Nanotubes: Reversible Switching between Single and Double-Stranded Forms, and Effect of Base Deletions. *ACS Nano* **2015,** *9* (12), 11898-11908.

6 Conclusions and Future Work

6.1 Conclusions and contributions to original knowledge

The work described in this thesis aimed to develop single molecule fluorescence methodologies to study and advance the structure, dynamics and integrity of DNA-assemblies. Overall, we demonstrated that these techniques may enable the production of well-defined high-quality DNA structures that meet the designer's compositional and dynamic specifications.

The research presented in chapter 2 provided an assembly methodology reminiscent of the principles and methods of solid-phase synthesis for the synthesis of DNA nanotubes. Here, the nanotubes were assembled from prefabricated building blocks that were delivered and then removed from a flow-through chamber in a controlled fashion. Single-molecule fluorescence imaging further assisted in the inspection and the validation of the assembly process. The sequential introduction of prefabricated building blocks in controlled amounts provided a unique opportunity to customize the backbone sequence one rung at a time. We may fully exploit the hierarchical control of information/organization in which the base sequence for component strands is dictated by the design constraints that require the strands to hybridize and form rungs and linkers, and for which the nanotube code along its backbone may be dictated a priori by the controlled sequential delivery of predesigned rungs. Our proof-of-concept experiments, rooted in the exploitation of single-molecule fluorescence photobleaching and super-resolution techniques (STORM), showed that the nanotubes were produced with both high yield and structural fidelity.

In chapter 3 we have demonstrated how single molecule-based methods can be used to unravel the structure of nanomaterials through a simple protocol centered on counting photobleaching steps. Because the probability of missing bleaching events increases with the number of fluorophores in a given structure, the number of countable steps reported in the literature was limited to ca. eleven. Using multiple fluorophores expands the maximum number of repeat units that may be monitored in a supramolecular structure. Every new color, by virtue

of having its own detection channel, enables the number of detectable units to be increased by ca. 11 steps. By offering a combination of the photobleaching and multiple color colocalization features, our approach enables molecular analysis beyond what is possible with the one-color photobleaching method. Additionally, the construction of 3D contour plots provide the fullest representation of the 2-color sets of data and allow a rigorous comparison of contour patterns among the different samples. Using this approach, samples of different dye composition were readily distinguishable on the basis of the correlated number of steps in the two color analysis: on one hand, the graphs display the slope and deviations of the distribution to evaluate the stoichiometry of the sample, while on the other hand, the spread of the distribution along the diagonal revealed the dispersity of the size of our assembled nanostructures. Together, the different parameters extracted from the collection of single molecule data give an overall view of the characteristics of the structures prepared.

In Chapter 4, a simple method for the scalable production of dynamic nanotubes using a minimal number of component strands was introduced. *In situ* single molecule fluorescence microscopy enabled the quantitative characterization of the structural changes that occurred upon the introduction of an additional morphological modification into the nanotubes: an increasing size mismatch between the vertical strands of each repeat unit. The size mismatch induced nanotube bending until at one point the distortion disrupted the formation of long nanotubes, as confirmed by one and two color single molecule photobleaching studies. Because they have a large number of repeat units down their length, these nanotubes have the potential to amplify biologically relevant DNA distortions. In fact, due to the periodic nature of nanotubes, a single trigger could result in amplified motion across hundreds of nanometers by acting at each site along the length of the tube.

In chapter 5, a method to assess the dynamics and robustness of DNA reconfigurable nanostructures was established. Using *in situ* two-color single molecule fluorescence microscopy and strand displacement strategies, surface tethered dye-labelled DNA nanotubes were switched between double and single-stranded forms, and the cooperativity and the stability of the single-stranded version of the design was examined. By monitoring the intensity of the dye-labelled nanotubes in the two colors, one at a time, morphological changes, anomalies and defects were uncovered in the partially single stranded nanotubes. This work underlines the importance of

single molecule methodologies as a powerful set of tools to assist in advancing the field of DNA nanotechnology by providing a detailed informative feedback on the designs and structures.

6.2 Suggestions for future work

The application of DNA-based structures in dynamic devices such as machines, motors and robots, requires minimizing errors in assembly which can otherwise drastically affect performance. This will in turn demand not only development of novel synthetic approaches, but also novel quantitative tools to be applied.

From the viewpoint of novel synthetic strategies, we anticipate that by using the methodology we had developed in ***Chapter 2***, it will be possible to fine-tune the assembly at every step. The solid-phase method described in this work to construct and visualize DNA nanotubes one rung at a time will pave the way towards the production of custom-made materials scaffolded onto DNA nanotubes that bear distinct orthogonally addressable rungs laid out in a predetermined manner. This method may be extended to the construction of other DNA or macromolecular nanostructures assembled in a stepwise, controlled manner, rather than relying on their spontaneous assembly in solution. In an attempt to manufacture nanotubes for potential applications in molecular scale electronics and nanomedicine, this methodology should be pursued further to develop strategies in order to cleave the structures from the surface. For instance, a DNA displacement strategy (e.g. adding an overhang to the foundation rung or bottom linkers), an excess of biotin (i.e. to displace the biotynilated DNA nanotubes bound to streptavidin) or a tween-based surface (i.e. which is prone to degradation) may be used for this purpose. Preliminary experiments suggested that the nanotubes prepared herein are interacting with the PEG surface and might be collapsed, which may result in a hindered ability of the invading DNA strands or molecules to reach and displace the tubes. However, further optimization and controls for reproducibility are still needed to confirm this hypothesis. An alternative strategy to detach the nanotubes from the surface would be to design the foundation rung with a recognition/restriction site (specific DNA sequence) recognized/cleaved by a restriction endonuclease (or restriction enzyme).

The ability to analyze the incorporation of modules at each stage of the assembly in real time will allow an in-depth analysis of the growth mechanism and help uncover at what stage assembly errors occur. To achieve control at the finest level, another important opportunity to be considered for the optimization of this technique is to employ a different fluorescence-based method for the *in situ* characterization of the assembly product such as a FRET-based beacon (design illustrated in the figure below). In this case, each rung will bear both a fluorophore and a fluorescence quencher. The capture of the linker by the rung will release the quencher and light up the dye upon its addition, just like the DMT-step in DNA synthesis uncovers the incorporation of a new base to a grown DNA polymer backbone. Dissecting every step of the assembly will pave the way for the production of nanotubes with fewer structural flaws than the spontaneous-assembly method.

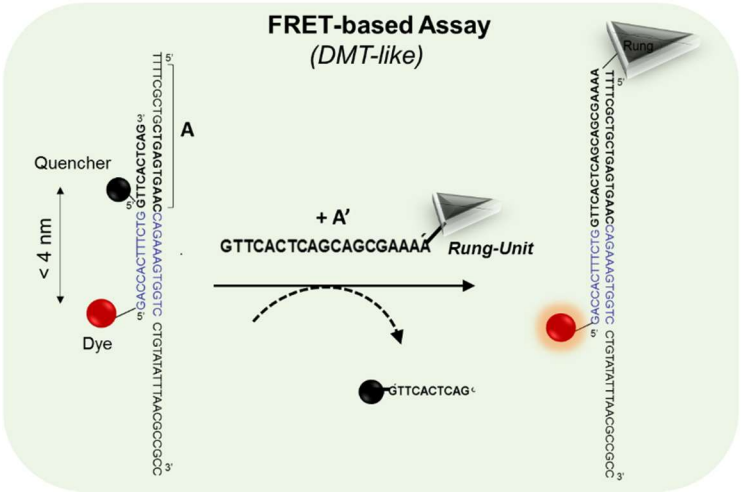

Our ability to monitor the growth on the surface step-by-step will assist in the progress towards building larger nanostructures by offering a mature understanding of the kinetics and thermodynamics of self-assembly within and between DNA building-blocks. For this purpose, changing buffer conditions (Mg^{2+}, Na^{+}, EDTA, etc.), viscosity, substrate concentration, and temperature to determine the relevant thermodynamic and kinetic parameters will lay the groundwork for future studies.

One of the downsides of the stepwise technique described in chapter 2 is the picomolar synthesis products that precludes their use for manufacturing purposes. In order to scale up the process in a future work, one may make use of streptavidin coated magnetic beads with a higher seeding density to grow the tubes. This may provide a route for scalable production of custom-

made nanotubes for promising applications in different areas. One potential application of these nanotubes is to use them as fluorescent nanobarcodes. Our exquisite control over the positioning of the dye-labelled rungs along the backbone of the nanotube enables the generation of numerous distinct barcodes that can be tagged to receptors for the identification and differentiation of a large number of distinct molecular species.

The two-color photobleaching technique described in ***chapter 3*** enables a consistent and systematic way of assessing the polydispersity and stoichiometry of different structures and designs which we posit will be instrumental for sample characterization in the new age of complex assemblies at the nanoscale and mesoscale. However, it will be of a great interest to automate this method and have a simple image analyzer to extract all of the plots with the click of a button. This work is already underway in our lab with the collaboration of Prof. Paul Wiseman (McGill University) and his student Jean-Francois DesJardens (McGill University). Additionally, the field of nanotechnology has tremendously advanced in the past few decades, rendering possible the assembly of bigger and much more complex synthetic nanoscale devices. From this perspective, extending the method to multiple-color photobleaching and establishing protocols for a variety of fluorophores to obtain good photobleaching steps is crucial.

In ***chapter 4***, using *in situ* two-color single molecule fluorescence imaging, we introduced a dynamic character to the surface-bound nanotubes by incorporating a "loop" strand within the structure. Using the temporal growth method published recently in the Sleiman lab or the stepwise method described in chapter 2, where each sequence of the tube's backbone is addressable, we can modify one specific rung with the loop sequence and observe the possible amplification of the bending across the whole structure. This could be interesting for sensing applications, with an analyte producing large scale, detectable structural changes, or to create "molecular muscles" that are capable of extension and contraction under external control. To this end, a more quantitative method to measure the bending is needed. In order to achieve this goal, single molecule FRET studies are one possibility to quantify the resulting curvature upon the loop strand addition. Because of their nanometer scale size ranging from 200nm to 800nm, the nanotubes studied in this thesis are suitable for further structural studies using super-resolution methods such as STORM or DNA-PAINT. These studies may be readily undertaken given the availability of the instrumentation and software in the Cosa lab. The application of super-

resolution methods may eventually permit the direct visualization of the bending in addition to counting the number of subunits within the structure.

On the other hand, the *in situ* nanotube editing enables us to modify the nanotubes on the surface in a controlled fashion with different tags without any side product that might form in the solution-based synthesis. The loop strand can alternatively be replaced with any other functionality, such as gold-labelled sequences to create a plasmonic fiber, drug-labelled sequences to produce a multi-drug delivery capsule and a variety of other tags.

Finally, in ***chapter 5*** we utilized *in situ* single molecule fluorescence as a tool to build a better understanding of the nanotubes' collective structural behaviour in response to modifications in their linking strands. A comprehensive study of the interplay of thermodynamics and structural dynamics is desirable as this information may assist in building architecturally precise and structurally robust nanotubes. Such a study may be tackled by manipulating different parameters during the erasing or refilling processes on the surface-bound nanotubes, such as: i) buffer medium (viscosity by adding glycerol, or ionic strength by changing the Mg^{2+} concentration), ii) concentration of erasers (invading strands), iii) concentration of the biotin (modify the mobility of the structure and its interaction with the surface), iv) position of the biotin moiety (could be on one end of the tube, which can be achieved by building the tubes in a stepwise fashion on the surface as shown in chapter 2), and v) temperature of the medium (buffer).

Two color ratiometric intensity and correlation analysis at the single molecule level enabled us to assess the quality and the fidelity of the product upon erasing. Again, automating this type of analysis by writing software to extract all the information from the given images will be crucial to generalize this technique to supramolecular chemists and make it easily accessible for scientists from different fields. We note that a comparison / correlation of the photobleaching (chapter 2-3) versus intensity-based counting (chapter 5) analysis will be interesting to study on DNA nanostructures of known composition (built using the stepwise assembly).

6.3 List of publications

1. Hamblin, G. D.; **Hariri, A. A.**; Carneiro, K. M. M.; Lau, K. L.; Cosa, G.; Sleiman, H. F., Simple Design for DNA Nanotubes from a Minimal Set of Unmodified Strands: Rapid, Room-Temperature Assembly and Readily Tunable Structure. *ACS Nano* **2013**, 7 (4), 3022-3028.
2. Karam, P.; **Hariri, A. A.**; Calver, C. F.; Zhao, X.; Schanze, K. S.; Cosa, G., Interaction of Anionic Phenylene Ethynylene Polymers with Lipids: From Membrane Embedding to Liposome Fusion. *Langmuir* **2014**, 30 (35), 10704-10711.
3. **Hariri, A. A.**; Hamblin, G. D.; Gidi, Y.; Sleiman, H. F.; Cosa, G., Stepwise growth of surface-grafted DNA nanotubes visualized at the single-molecule level. *Nat Chem* **2015**, 7 (4), 295-300.

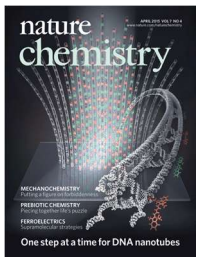

Journal Cover

4. Rahbani, J. F.; **Hariri, A. A**.; Cosa, G.; Sleiman, H. F., Dynamic DNA Nanotubes: Reversible Switching between Single and Double-Stranded Forms, and Effect of Base Deletions. *ACS Nano* **2015,** *9* (12), 11898-11908.
5. **Hariri, A. A.**; DesJardins, J.F.; Hardwick, J.; Hamblin, G.D.; Rahbani, J.; Godin, R.; Wiseman, P.; Sleiman, H. F.; Cosa, G., Stoichiometry and dispersity of DNA nanostructures using single molecule photobleaching pair correlation analysis. *To be submitted*.
6. **Hariri, A. A.**; Rahbani, J.; Gordon, J.; Platnish, C.; Sleiman, H. F.; Cosa, G., DNA nanotube dynamics at the single molecule level. *To be submitted*.

The End

”فقل لمن يدعي في العلم فلسفة حفظت شيئاً وغابت عنك أشياء“

ابو نواس